frontiers | Research Topics

The neural economy hypothesis: Changes with aging and disease to cones and other central nervous system visual neurons

Edited by
Ann E. Elsner, Phil Luthert, Jessica I. W. Morgan, Adam M. Dubis
and Ferenc Balazs Sallo

Published in
Frontiers in Aging Neuroscience
Frontiers in Neuroscience
Frontiers in Medicine

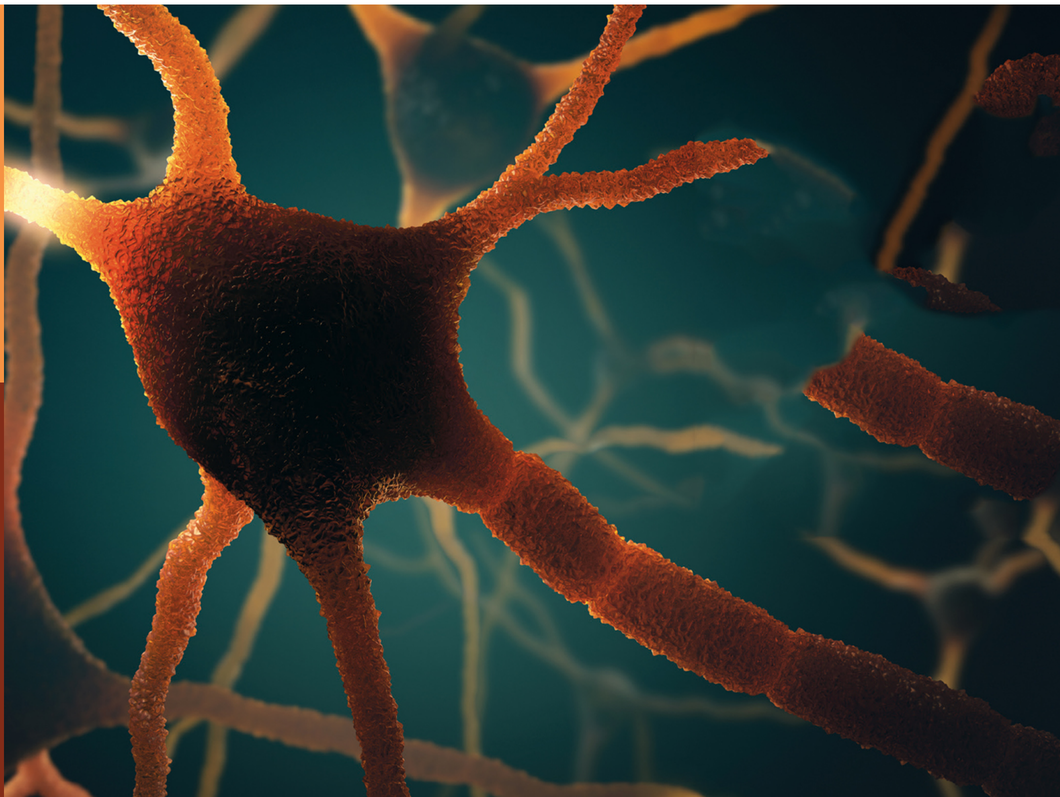

ISSN 1664-8714
ISBN 978-2-83250-971-5
DOI 10.3389/978-2-83250-971-5

About Frontiers

Frontiers is more than just an open access publisher of scholarly articles: it is a pioneering approach to the world of academia, radically improving the way scholarly research is managed. The grand vision of Frontiers is a world where all people have an equal opportunity to seek, share and generate knowledge. Frontiers provides immediate and permanent online open access to all its publications, but this alone is not enough to realize our grand goals.

Frontiers journal series

The Frontiers journal series is a multi-tier and interdisciplinary set of open-access, online journals, promising a paradigm shift from the current review, selection and dissemination processes in academic publishing. All Frontiers journals are driven by researchers for researchers; therefore, they constitute a service to the scholarly community. At the same time, the *Frontiers journal series* operates on a revolutionary invention, the tiered publishing system, initially addressing specific communities of scholars, and gradually climbing up to broader public understanding, thus serving the interests of the lay society, too.

Dedication to quality

Each Frontiers article is a landmark of the highest quality, thanks to genuinely collaborative interactions between authors and review editors, who include some of the world's best academicians. Research must be certified by peers before entering a stream of knowledge that may eventually reach the public - and shape society; therefore, Frontiers only applies the most rigorous and unbiased reviews. Frontiers revolutionizes research publishing by freely delivering the most outstanding research, evaluated with no bias from both the academic and social point of view. By applying the most advanced information technologies, Frontiers is catapulting scholarly publishing into a new generation.

What are Frontiers Research Topics?

Frontiers Research Topics are very popular trademarks of the *Frontiers journals series*: they are collections of at least ten articles, all centered on a particular subject. With their unique mix of varied contributions from Original Research to Review Articles, Frontiers Research Topics unify the most influential researchers, the latest key findings and historical advances in a hot research area.

Find out more on how to host your own Frontiers Research Topic or contribute to one as an author by contacting the Frontiers editorial office: frontiersin.org/about/contact

The neural economy hypothesis: Changes with aging and disease to cones and other central nervous system visual neurons

Topic editors
Ann E. Elsner — Indiana University, United States
Phil Luthert — University College London, United Kingdom
Jessica I. W. Morgan — University of Pennsylvania, United States
Adam M. Dubis — University College London, United Kingdom
Ferenc Balazs Sallo — Hôpital ophtalmique Jules-Gonin, Switzerland

Citation
Elsner, A. E., Luthert, P., Morgan, J. I. W., Dubis, A. M., Sallo, F. B., eds. (2022). *The neural economy hypothesis: Changes with aging and disease to cones and other central nervous system visual neurons*. Lausanne: Frontiers Media SA.
doi: 10.3389/978-2-83250-971-5

JM's lab receives financial support from AGTC. AE is the CEO and founder of Aeon Imaging.
The remaining authors declare that the research was conducted in the absence of any commercial or financial relationships that could be construed as a potential conflict of interest.

Table of contents

frontiers | Frontiers in Aging Neuroscience

TYPE Editorial
PUBLISHED 22 November 2022
DOI 10.3389/fnagi.2022.1054455

Editorial: The neural economy hypothesis: Changes with aging and disease to cones and other central nervous system visual neurons

Ann E. Elsner[1]*, Adam M. Dubis[2], Jessica I. W. Morgan[3] and Ferenc B. Sallo[4]

[1]School of Optometry, Indiana University, Bloomington, IN, United States, [2]Global Business School for Health, University College London, London, United Kingdom, [3]Scheie Eye Institute, Department of Ophthalmology, University of Pennsylvania, Philadelphia, PA, United States, [4]Hôpital Ophtalmique Jules-Gonin, University of Lausanne, Lausanne, Switzerland

OPEN ACCESS

EDITED AND REVIEWED BY
Kristy A. Nielson,
Marquette University, United States

*CORRESPONDENCE
Ann E. Elsner
aeelsner@indiana.edu

SPECIALTY SECTION
This article was submitted to Neurocognitive Aging and Behavior, a section of the journal Frontiers in Aging Neuroscience

RECEIVED 26 September 2022
ACCEPTED 10 November 2022
PUBLISHED 22 November 2022

CITATION
Elsner AE, Dubis AM, Morgan JIW and Sallo FB (2022) Editorial: The neural economy hypothesis: Changes with aging and disease to cones and other central nervous system visual neurons. *Front. Aging Neurosci.* 14:1054455. doi: 10.3389/fnagi.2022.1054455

KEYWORDS

cones, macula, risk to photoreceptors, vascular changes, fovea, cone distribution, retinal degeneration, diabetic retinopathy

Editorial on the Research Topic
The neural economy hypothesis: Changes with aging and disease to cones and other central nervous system visual neurons

Photoreceptors and other central nervous system cells are considered post-mitotic and at their maximum numbers before birth, although the human retina undergoes considerable developmental changes in the first few years of life (Hendrickson and Yuodelis, 1984). In the human fovea, the packing of cones becomes denser at the central fovea by migration, not by new cones being formed. Cone outer segments elongate by adding more segments over time, and the inner retinal cells move to more eccentric locations, reducing light scatter to enhance foveal acuity. To provide decades of vision these neurons and their networks must have inherent repair processes and be supported and renewed by glial and other cells. There are limitations to the extent of support available to visual system neurons, especially photoreceptors with their high metabolic rates, the assault by incident light on the retina, and the need for optical clarity that constrains the numbers and locations of blood vessels. Further, these support systems can fail with aging and disease, creating a harsh microenvironment for photoreceptors.

Cones have a remarkable ability to survive, compared with rods. Alterations in cone structure and function enable them to stay connected in their circuitry to provide at least some vision. This is the neural economy hypothesis, i.e., that neurons adapt to their environment and can modify their physiology to be economical (Elsner et al., 2020). Improving the microenvironment in aging and disease has the potential to preserve cones and visual system circuitry, thereby preserving vision.

Many possible changes to visual system neurons over the life span include cones reverting to having fewer outer segments, and even existing as mainly cell bodies as can be found in eyes with missing or damaged retinal pigment epithelium such as in age-related macular degeneration (Sarks et al., 1988), myopia (Jonas et al., 2013), or glaucoma (Dichtl et al., 1998). However, cone photopigment can increase to more normal levels over time following a retinal detachment (Elsner et al., 1992).

New technologies enable *in vivo* assessments of photoreceptor health with the added advantages of including younger subjects with earlier stage disease and longitudinal studies of disease progression. Histology for many human diseases such as age-related macular degeneration is often weighted toward old eyes and end-stage disease. This Research Topic inspects photoreceptors, their microenvironment, and visual pathways in health, disease, and aging, using a variety of techniques including histology, *in vivo* imaging, and function measures in both human eyes and animal models.

There are extreme differences in the changes in the retina when the initial insult is a genetic mutation as opposed to a metabolic challenge provided by aging or diseases such as diabetes. The effect of aging on the retina is spatially heterogeneous, as described in Zouache: the greater prominence of aging changes occur in the regions with the highest energy requirements. The environment of neurons changes more in the macula than in the periphery, and in the outer retina and choroid as compared to the inner retina. In one family of progressive retinal degenerations due to genetic defects, known as retinitis pigmentosa, damage to cones over time and space can be complex because of the viability factor provided by another neuron, the rods (Roberts). In a mathematical model for progressing cone degeneration caused by a reduction in rod derived cone viability factor (RdCVF), a simple formula is insufficient as both the amount of RdCVF produced and the amount of RdCVF the cones require to survive will vary with retinal location in different manners.

Longer term degeneration of cones is also described by Li et al., who evaluated long term cone structure in the inherited retinal dystrophy Oligocone Trichromacy. This condition results in decreased but usually stable cone function. Their work demonstrates that even though cone function is reduced, cones survive, shown by multimodal cellular imaging.

A more complex structure to function relationship was observed by Jolly et al., who evaluated the changes in color vision in patients with choroideremia. Their work shows that there is early loss of tritan (blue-yellow) loss, before loss of red-green discrimination. While the disease progresses, both chromatic axes had functional loss, even while visual acuity and OCT based structural parameters suggest that the retina remained intact. Their work suggests that the redundancy in the acuity system is likely maintained longer.

The structure to function relationship is also studied for aging by Baraas et al. looking at the first detected loss of red-green function and using the visual acuity of perifoveal L-cones. Their work confirms cone density did not decrease significantly in early age-related macular degeneration, through direct visualization of photoreceptors, even in areas with decreased L-cone visual function. Cones in patients with age-related macular degeneration had significantly shortened outer segments. Using visual function methods, the detection rate of photons by cones is proposed by Braham chaouche et al. to detect age-related macular degeneration. Using multi-modal imaging methods, Yuhas et al. propose that damage to cone axons may be detected by the combined use of directional OCT and scanning laser polarimetry or other polarization-sensitive imaging methods, demonstrating early changes to photoreceptor integrity in the central macula as a harbinger to ocular or to neurological disease.

Elsner et al. report that diabetic patients with vessel remodeling do not have a large decrease of cones and surprisingly have retinal thickness on OCT within normal limits. There is a greater variability in the reflectance and distributions of cones. Significantly low cone density is found in some patients, including younger patients, but the large variability of older controls makes difficult isolating metabolic damage.

Large changes with aging in more central neurons are described by Fiuza et al. for the rat non-image forming thalamus. The daily variations in neurons of calretinin expression that are important for calcium buffering and signaling decline progressively with age, with effects not restricted to particular regions suggesting this is a generalized process.

Taken together, these papers show how cones and other visual neurons survive, but with altered function. Imaging and function studies provide the potential for early detection and streamlining of treatment trials.

Author contributions

AE organized the topic review, wrote the initial call for papers, invited editors, edited manuscripts, contributed one manuscript to the topic, and led writing of the editorial. AD invited two editors, served as an editor and reviewer, contributed one manuscript to the topic, and contributed to the initial draft of the editorial. JM edited the call for papers, edited manuscripts, and contributed to the initial draft of the editorial. AE, AD, JM, and FS approved the submitted version.

Funding

The preparation of this article was supported by research grants from the AE National Eye Institute (EY024315 to FS), National Eye Institute (EY028601 and EY030227 to JM), and the NIHR Biomedical Resource Centre to Moorfields Eye Hospital NHS Trust and UCL Institute of Ophthalmology to AD.

Acknowledgments

We thank the many reviewers and also the independent editors assigned to review papers in our topic.

Conflict of interest

JM's lab receives financial support from AGTC. AE is the CEO and founder of Aeon Imaging.

The remaining authors declare that the research was conducted in the absence of any commercial or financial relationships that could be construed as a potential conflict of interest.

Publisher's note

References

Dichtl A., Jonas J. B., and Naumann, G. O. (1998). Histomorphometry of the optic disc in highly myopic eyes with absolute secondary angle closure glaucoma. *Br. J. Ophthalmol.* 82, 286–289. doi: 10.1136/bjo.82.3.286

Elsner, A. E., Burns, S. A., and Weiter, J. J. (1992) Retinal densitometry in retinal tears and detachments. *Clin. Vis. Sci.* 7, 489–500.

Elsner, A. E., Papay, J. A., Johnston, K. D., Sawides, L., de Castro, A., King, B. J., et al. (2020). Cones in ageing and harsh environments: the neural economy hypothesis. *Ophthalmic Physiol. Opt.* 40, 88–116. doi: 10.1111/opo.12670

Hendrickson, A. E., and Yuodelis, C. (1984). The morphological development of the human fovea. *Ophthalmol.* 91, 603–612. doi: 10.1016/s0161-6420(84)34247-6

Jonas, J. B., Ohno-Matsui K., Spaide, R. F., Holbach, L., and Panda-Jonas, S. (2013). Macular Bruch's membrane defects and axial length: association with gamma zone and delta zone in peripapillary region. *Ophthalmol. Vis. Sci.* 54, 1295–1302. doi: 10.1167/iovs.12-11352

Sarks, J. P., Sarks, S. H., and Killingsworth, M. C. (1988). Evolution of geographic atrophy of the retinal pigment epithelium. *Eye (Lond).* 2, 552–577. doi: 10.1038/eye.1988.106

frontiers
in Aging Neuroscience

ORIGINAL RESEARCH
published: 24 February 2021
doi: 10.3389/fnagi.2021.613305

Aging Alters Daily and Regional Calretinin Neuronal Expression in the Rat Non-image Forming Visual Thalamus

Felipe P. Fiuza*[1]*, *José Pablo G. Queiroz*[1], *Antônio Carlos Q. Aquino*[2], *Diego A. Câmara*[2], *Luiz Eduardo M. Brandão*[2,3], *Ramon H. Lima*[1], *José Rodolfo L. P. Cavalcanti*[4], *Rovena Clara G. J. Engelberth*[2] and *Jeferson S. Cavalcante*[2]

[1] Graduate Program in Neuroengineering, Edmond and Lily Safra International Institute of Neuroscience, Santos Dumont Institute, Macaíba, Brazil, [2] Laboratory of Neurochemical Studies, Department of Physiology, Biosciences Center, Federal University of Rio Grande do Norte, Natal, Brazil, [3] Department of Medical Sciences, Uppsala University, Uppsala, Sweden, [4] Laboratory of Experimental Neurology, Department of Biomedical Sciences, Health Science Center, University of State of Rio Grande do Norte, Mossoró, Brazil

Aging affects the overall physiology, including the image-forming and non-image forming visual systems. Among the components of the latter, the thalamic retinorecipient inter-geniculate leaflet (IGL) and ventral lateral geniculate (vLGN) nucleus conveys light information to subcortical regions, adjusting visuomotor, and circadian functions. It is noteworthy that several visual related cells, such as neuronal subpopulations in the IGL and vLGN are neurochemically characterized by the presence of calcium binding proteins. Calretinin (CR), a representative of such proteins, denotes region-specificity in a temporal manner by variable day–night expression. In parallel, age-related brain dysfunction and neurodegeneration are associated with abnormal intracellular concentrations of calcium. Here, we investigated whether daily changes in the number of CR neurons are a feature of the aged IGL and vLGN in rats. To this end, we perfused rats, ranging from 3 to 24 months of age, within distinct phases of the day, namely zeitgeber times (ZTs). Then, we evaluated CR immunolabeling through design-based stereological cell estimation. We observed distinct daily rhythms of CR expression in the IGL and in both the retinorecipient (vLGNe) and non-retinorecipient (vLGNi) portions of the vLGN. In the ZT 6, the middle of the light phase, the CR cells are reduced with aging in the IGL and vLGNe. In the ZT 12, the transition between light to dark, an age-related CR loss was found in all nuclei. While CR expression predominates in specific spatial domains of vLGN, age-related changes appear not to be restricted at particular portions. No alterations were found in the dark/light transition or in the middle of the dark phase, ZTs 0, and 18, respectively. These results are relevant in the understanding of how aging shifts the phenotype of visual related cells at topographically organized channels of visuomotor and circadian processing.

Keywords: aging, intergeniculate leaflet, ventral lateral geniculate nucleus, lateral geniculate body, calcium binding proteins, circadian rhythms, calretinin, stereology

Edited by:
Ann E. Elsner,
Indiana University, United States

Reviewed by:
Vanessa Castelli,
University of L'Aquila, Italy
Paul Gamlin,
University of Alabama at Birmingham,
United States

****Correspondence:***
Felipe P. Fiuza
felipe.fiuza@isd.org.br

Received: *01 October 2020*
Accepted: *01 February 2021*
Published: *24 February 2021*

Citation:
Fiuza FP, Queiroz JPG, Aquino ACQ, Câmara DA, Brandão LEM, Lima RH, Cavalcanti JRLP, Engelberth RCGJ and Cavalcante JS (2021) Aging Alters Daily and Regional Calretinin Neuronal Expression in the Rat Non-image Forming Visual Thalamus.
Front. Aging Neurosci. 13:613305.
doi: 10.3389/fnagi.2021.613305

INTRODUCTION

Aging is characterized, for most living organisms, as a time-dependent physiological decline associated with increases in mortality and decreases in fertility rates (Flatt and Partridge, 2018). A practical approach to understand how the aging phenotype is determined, as well as the relationship between normal aging and age-related pathologies, is to identify distinctive cellular alterations as hallmarks of the aging process (López-Otín et al., 2013). In the nervous system, for instance, despite there being few changes in the global neuronal numbers throughout life (Long et al., 1999; von Bartheld et al., 2016), neurochemical-specific subpopulations of cells are lost during aging (Bañuelos et al., 2013; Pal et al., 2019; Lamerand et al., 2020). Thus, given the diverse nature of brain neurochemistry, the characterization of age-related changes in a cellular level still poses a challenging endeavor for neuroscience.

There is clear evidence that age-related brain dysfunction and neurodegeneration are associated with abnormal intracellular concentrations of calcium (Ca^{2+}), as stated by the Ca^{2+} hypothesis of aging (Landfield, 1987; Khachaturian, 1994). Therefore, protein-mediated mechanisms of cytosolic Ca^{2+} buffering, such as the action of the EF-hand family of calcium binding proteins (CaBPs), may act as neuroprotective factors influencing age-related alterations (Alzheimer's Association Calcium Hypothesis Workgroup, 2017). Calretinin (CR), a representative of such CaBPs, seems to participate in the induction of long-term potentiation (Schurmans et al., 1997) and is present in neurons which are selectively resistant to the toxicity induced by β-amyloid protein, calcium overload, and excitatory amino acid stimulation in the brains of rodents (Lukas and Jones, 1994; Pike and Cotman, 1995). The CR and other CaBPs are often employed as histological markers due to their complementary distribution across brain regions and neuronal subclasses, being linked with region-specific vulnerability to aging effects (Fairless et al., 2019; Lamerand et al., 2020). Accordingly, the CR immunopositive (CR+) neurons are lost during aging in the cortical and subcortical regions of rodent and human brains (Villa et al., 1994; Bu et al., 2003; Bae et al., 2015; Ahn et al., 2017).

Aging affects the overall physiology, including visual, and circadian functions (Kondratova and Kondratov, 2012; Engelberth et al., 2013; Yan et al., 2020). After light reaches the retina, visual pathways to the brain nuclei are commonly grouped into image-forming and non-image forming visual systems (Lucas et al., 2014; Sondereker et al., 2020). A major retinorecipient zone lies in the thalamic lateral geniculate body, which is subdivided into dorsal lateral geniculate nucleus (dLGN), intergeniculate leaflet (IGL), and ventral lateral geniculate nucleus (vLGN) (Morin and Studholme, 2014). Apart from the clear subdivision of the vLGN in an external retinorecipient (vLGNe) and an internal non-retinorecipient (vLGNi) portions, there is no obvious cytoarchitectonic differences in these regions (Monavarfeshani et al., 2017). Unlike the dLGN, the classical component of the image forming visual system, the IGL and vLGN have no thalamocortical relays to any cortical areas (Harrington, 1997; Monavarfeshani et al., 2017). Instead, the IGL and vLGN widely innervate subcortical visuomotor related nuclei, such as pretectal and optic accessory system regions, being likely the main thalamic source of afferents to the superior colliculus in rats (Matute and Streit, 1985; Harrington, 1997). Also, the IGL is known to provide photic and non-photic (e.g., novel or metabolic conditions) inputs to the hypothalamic suprachiasmatic nucleus (SCN) that fine-tunes the circadian photo-entrainment (Morin, 2013). For all these reasons, the IGL and vLGN are classified as the thalamic components of the non-image forming visual system (Fox and Guido, 2011; Chengetanai et al., 2020).

It is noteworthy that several visual-related nervous cells, such as the retinal ganglion cells (RGCs), SCN, IGL, and vLGN neurons are neurochemically characterized by the presence of CR (Arai et al., 1992; Jeon and Jeon, 1998; Lee et al., 2010a,b; Lee et al., 2016; Moore, 2016). Interestingly, the day–night variations in the CR expression denote region-specificity (Campos et al., 2015a,b). For instance, the rat SCN presents a higher density of CR+ neurons in the light phase in comparison with the dark phase of the day (Moore, 2016). Notably, age-related alterations in the daily rhythmicity of other neurochemicals, such as serotonin, noradrenaline, dopamine, arginine vasopressin, and vasoactive intestinal polypeptide, are features of the brains of rodents and primates (Míguez et al., 1998; Cayetanot et al., 2005; Jagota and Kalyani, 2008). In fact, aging leads to a loss of rhythm in 90% of the hippocampal proteins that display circadian expression in mice (Adler et al., 2020). Thus, given the relationship among aging, calcium signaling, and circadian functions, one could hypothesize that daily changes in the CaBPs expression are markers of cellular aging and regional vulnerability. Here, we use unbiased stereology, the gold standard of cell quantification, to assess whether daily changes in the number of CR+ neurons occur in the IGL and vLGN of rats from different ages. In addition to presenting new data regarding this scarcely investigated issue, we discuss how the interpretation of morphometric data benefits from taking into consideration the chronobiologic context. Moreover, we present data supporting that a phase-dependent reduction in the amplitude of CR expression characterizes an age-related shift of neuronal phenotypes in the rat non-image forming visual thalamus.

MATERIALS AND METHODS

Experimental Subjects

A total of 48 male Wistar rats, ranging from 3 to 24 months of age, were housed in cages at 22°C and 50% humidity in a 12:12 h light/dark cycle with food and water freely available. Animals were divided into four groups ($n = 12$ per group) regarding

---

Abbreviations: asf, Area sampling fraction; CaBP, Calcium binding proteins; CB, Calbindin d-28k; CE, Coefficient of error; CR, Calretinin; CR+, Calretinin immunopositive; dLGN, Dorsal lateral geniculate nucleus; hsf, Height sampling fraction; IGL, Intergeniculate leaflet; opt, Optic tract; RGC, Retinal ganglion cell; SCN, Suprachiasmatic nucleus; ssf, Serial sampling fraction; vLGN, Ventral lateral geniculate nucleus; vLGNe, Ventral lateral geniculate nucleus external portion; vLGNi, Ventral lateral geniculate nucleus internal portion; ZT, Zeitgeber time; AU, Arbitrary units.

the photic condition, or zeitgeber, in which euthanasia was performed. By definition, the zeitgeber time (ZT) 12 corresponds to the lights-off hour in the animal housing facility. Specifically, animals were euthanized at ZT 0-dark/light transition, ZT 6-light phase, ZT 12-light/dark transition, and ZT 18- dark phase. All procedures were approved by local ethics committee (CEUA-UFRN number 054/2015) in accordance with Brazilian law number 11.794/2008 for animal experimentation.

Tissue Fixation

Following anesthesia with sodium thiopental (40 mg/kg), animals were submitted for a thoracotomy and transcardiac perfusion through the left ventricle with a 300 ml NaCl solution (0.9%) followed by 300 ml formalin (10%) in a 0.1 m phosphate buffer (PB, pH 7.4). These procedures were carried out in the beginning of each ZT. Following perfusion, the brains were removed, post-fixed with the same fixative overnight and cryoprotected in a 30% sucrose solution with 0.1 m PB (pH 7. 4) for 3 days. Then, brains were sectioned into 50 μm coronal slices in a cryostat (Leica Microsystems) and the sections were sequentially collected in 96-well plates filled with antifreezing solution to be stored at −20°C until use for immunohistochemistry. We further detailed tissue sampling under the Stereology topic.

Immunohistochemistry

Sections of IGL and vLGN were submitted to free-floating immunohistochemistry. Firstly, sections were blocked for endogenous peroxidase activity in 0.3% hydrogen peroxide. Then, sections were incubated overnight with rabbit anti-CR primary antibody (C7479, Sigma-Aldrich) in a 1:1,000 dilution with 2% bovine serum albumin and 0.1 m PB with 0.4% Triton X-100 (PBTX 0.4%). After rinsing, the sections were incubated with biotinylated goat anti-rabbit secondary antibody (111-065-003, Jackson ImmunoResearch) in a 1:1,000 dilution with PBTX 0.4%. Then, sections were incubated in a 0.5% avidin-biotin solution (Vectastain standard ABC kit, PK-4000, Vector Laboratories), with 2.3% NaCl addiction, for 120 min. Finally, sections were placed with a 2.5% solution of diaminobenzidine (DAB) diluted with 0.1 m PB. The final reaction was performed adding a 0.01% H_2O_2 solution, to reveal brown-stained areas resulting from DAB oxidation. All sections were simultaneously removed from the DAB solution after 2 min of reaction to minimize the staining variability. The brain sections were mounted on gelatinized slides, dried, dehydrated in graded ethanol solutions, cleared in xylene, and coverslipped with a DPX embedding matrix. Prior to histological processing, we performed a pilot study to establish optimal antibody concentration and incubation time. We confirmed internal positive controls by observing well-defined CR+ cell bodies in regions such as the cerebral cortex, the thalamic lateral posterior complex, and in the caudal zona incerta. Also, we addressed negative controls by incubating sections with no addition of primary antibody. In these cases, we observed no immunoreactivity.

Stereology

Unbiased stereological analyses were performed in an BX61 optical microscope (Olympus, Japan) fitted with a ProScan II X-Y-Z motorized stage (Prior Scientific, Rockland, MA, United States), a 0.5 μm resolution Heidenhain MT12 microcator (Heidenhain, Traunreut, Germany) and a Olympus DP-71 digital camera connected to a computer running the software NewCAST (Visiopharm, Hørsholm, Denmark). A pilot study was performed to establish optimal parameters of section fraction, counting frame area, grid-spacing size, and disector height for stereological analyses. Accordingly, we used a 1/4 section sampling fraction (ssf), corresponding to ∼5 IGL and 6 vLGN sections from an average of 24 sections identified with the aid of the seventh edition of the rat brain atlas in stereotaxic coordinates (Paxinos and Watson, 2014). We took into account, the anatomical considerations of Arai et al. (1992) and Harrington (1997), as well as previous observations of our group (Fiuza et al., 2016, 2017), to establish all stereological parameters and to trace the regional boundaries. Our systematic uniform random sampling was established by randomly choosing the first section and picking every following vLGN section in a 200 μm interval.

Regions of Interest

In the lateral geniculate body of the rat, the optic tract (opt) carries out retinal projections to the dLGN, IGL, and vLGN laterally bordering these nuclei (**Figure 1**). The dorsal and medial borders of IGL, namely the dLGN and superior thalamic radiation, were easily identified since there is little or no CR staining in its adjacent boundaries. As the dorsal most regions of the vLGNe and vLGNi are relatively spared from CR+ neurons, the IGL ventral borders can be distinguished from its adjacent vLGN nuclei. At rostral levels, the vLGNe presents a stronger background of CR staining which serves as a clear division from vLGNi (**Figure 1A**). At the middle and caudal levels, vLGNe enlarges and this stronger background is more pronounced in its surroundings, rather than in the center, still delineating the vLGNe/vLGNi border (**Figures 1B,C**). Also, the vLGNe neurons usually present a stronger CR cytoplasmic signal which aids in nuclei delineation.

Absolute Cell Number Estimation

We estimated absolute CR+ cell number bilaterally in an assumption-free manner for each nucleus following the optical fractionator method (West et al., 1991). Briefly, this methodology consists in overlaying a volumetric counting frame, the disector, in the histological material after the establishment of the ssf as well as area sampling fraction (asf) and height sampling fraction (hsf). The asf corresponds to the two-dimensional portion of the region of interest in which disectors are overlaid. The hsf comprehends the fraction of the Z plane that each disector probes. For our estimations, all samples were blind-coded so that the experimenter had no information regarding the age of the animal or its ZT group. First, we outlined the IGL and vLGN subdivisions with a low magnification objective (4x), and then counted the cells at high magnification (100x PlanApo oil lenses with 1.4 NA). We only counted the cells with the top of the nucleus clearly situated within the disector inclusion zone. Based on our pilot study, we determined a minimum of 100 counted cells to obtain reliable results with the coefficient of error (CE)

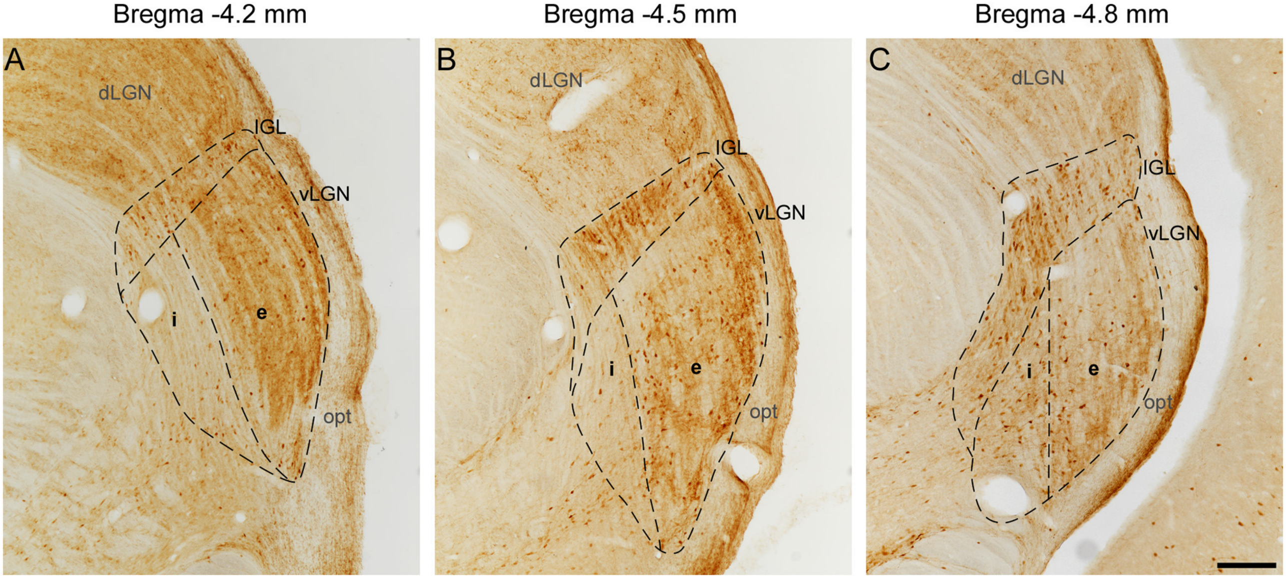

FIGURE 1 | Delineation of IGL, vLGNe, and vLGNe in CR immunolabeled sections at distinct rostrocaudal positions. Distance caudal (–) to Bregma 0.0 (in mm) are indicated at the top of each panel. In the rat lateral geniculate body, dLGN, IGL, and vLGN are bordered laterally by the opt. **(A)** At −4.2 mm, vLGNi weak background aids in the delineation of its boundary with vLGNe. **(B,C)** At −4.5 and −4.8 mm, the medial portion of IGL projects ventrally and stronger immunoreactivity in CR cell bodies denoting the vLGNe/vLGNi border. Scale bar = 200 μm.

below 0.1. To achieve this minimum cell number for counting, we used a 50 × 50 μm counting frame with a grid spacing size of 90 × 90 μm within our 1/4 ssf. We calculated the asf as a result of the counting frame area divided by grid-spacing area. The thickness of each post-shrinkage sections was calculated by focusing the topmost of tissue and slightly moving down to the bottommost focus point to measure the distance moved in the z-axis. As we observed that the tissue shrinks to an average value of 15 μm, the disector height was set at 12 μm with 1.5 μm guard zones above and below. Thus, the hsf was obtained through the division of the disector height by a number-weighted mean post-shrinkage section thickness. The CE was calculated with the smoothness class of m = 1 (Gundersen et al., 1999).

After obtaining cell counts (Q^-) from IGL and vLGN, the total number of cells (N) was estimated by the optical fractionator equation (West et al., 1991):

$$N = \sum Q^- \cdot \frac{1}{ssf} \cdot \frac{1}{asf} \cdot \frac{1}{hsf}$$

Evaluation of CR Spatial Distribution

We followed the approach of Sabbagh et al. (2020) to evaluate whether CR staining predominates particular vLGN portions in the lateral to medial axis at different ZTs. As there was no indication for the existence of any kind of such cellular organization in the IGL (Monavarfeshani et al., 2017), we did not evaluate this nucleus. For this evaluation, we developed a custom-line scan script that runs in the public domain software ImageJ FIJI version 1.52p (National Institutes of Health, USA). First, the image is calibrated into μm scale and the user contours the region of interest. Then, the image is transformed into 8-bit type, subtracted from the background and inverted, displaying the CR staining as pixel gray values. Finally, equally spaced lines are overlaid into the region of interest and plot profiles show the variation of pixel intensity along each line length. The data are plotted based on the average intensity of all lines within the section and every ssf section of the nucleus. Considering the variable stoichiometry in immunohistochemical procedures (Bishop et al., 2018), comparing intensities between the age and ZT groups could retrieve biased results. For this reason, we did not perform any direct statistical comparison with this dataset. Instead, we used its descriptive feature to evaluate the relative spatial predominance of CR staining in animals at earlier or later points of the lifespan.

Statistical Analysis

We performed a Kolmogorov–Smirnov test to assess the normality of our group distributions. After confirming that all distributions were normal, we computed Pearson's correlation coefficient and linear regression analysis to assess if there were any predictive relationships between age and CR cell numbers within each ZT group. Further, we divided our study population into three age groups, namely, young (3–7 months), middle-aged (12–18 months), and old (19–24 months) groups (**Table 1**). Then, we performed a two-way ANOVA followed by Tukey's test for *post-hoc* comparisons to compare the effects of age and ZT in CR cell numbers of each LGN nucleus. These analyses aided the identification of region-specific CR daily rhythmicity and to find whether the aging effects occurred in the earlier or later periods of animal lifespan. In all analyses, differences were considered significant at $p \leq 0.05$ and data are expressed as mean ± SD.

TABLE 1 | Mean CR+ neuronal number estimated in the IGL, vLGNe, and vLGNi in each ZT and age groups.

ZT group	Age group (Mean ± SD months)	Nucleus		
		IGL	vLGNe	vLGNi
0	Young (4 ± 1.15)	1,889 ± 516	2,999 ± 459	1,916 ± 375
	Middle-aged (16 ± 2.70)	1,777 ± 525	2,634 ± 721	1,770 ± 472
	Old (23.25 ± 2.70)	1,950 ± 443	2,763 ± 180	1,713 ± 695
6	Young (4.5 ± 1.91)	2,533 ± 111	4,055 ± 619	2,040 ± 393
	Middle-aged (15 ± 2.16)	2,279 ± 421	3,088 ± 209*	2,129 ± 395
	Old (23.5 ± 0.58)	1,963 ± 240*	3,163 ± 218*	1,729 ± 430
12	Young (4.75 ± 1.70)	2,572 ± 232	3,480 ± 256	2,831 ± 148
	Middle-aged (15.25 ± 2.36)	2,397 ± 170	3,212 ± 155	2,415 ± 459
	Old (22 ± 1.41)	1,796 ± 87*#	2,754 ± 272*	2,101 ± 274*
18	Young (3.75 ± 0.95)	1,926 ± 442	2,909 ± 702	2,146 ± 312
	Middle-aged (14 ± 1.87)	1,874 ± 203	2,849 ± 316	1,901 ± 472
	Old (20 ± 1)	2,149 ± 50	3,393 ± 245	1,558 ± 162

**$p \leq 0.05$ in comparison with the young group within the same ZT group. #$p \leq 0.05$ in comparison with the middle-aged group within the same ZT group. Data are expressed as mean ± SD.*

IGL, Intergeniculate leaflet; vLGNe, Ventral lateral geniculate nucleus external portion; vLGNi, Ventral lateral geniculate nucleus internal portion; ZT, Zeitgeber time.

Data analyses were performed with the GraphPad prism version 7.0 software.

RESULTS

Daily Rhythmicity of CR Expression

Representative IGL and vLGN CR immunolabeled sections of each ZT group in rats from distinct ages are shown in **Figure 2**. In **Figure 3**, we show CR+ cells in higher magnification at ZT 12. After employing the two-way ANOVA with light condition as an isolated factor, we observed a significant effect upon CR neuronal changes in the IGL [$F_{(3,36)} = 4.07$; $p = 0.01$], vLGNe [$F_{(3,36)} = 4.82$; $p = 0.006$], and vLGNi [$F_{(3,36)} = 5.99$; $p = 0.002$]. In the IGL, Tukey's test for *post-hoc* comparisons revealed that young animals present a higher number of CR+ neurons at ZT 6 (2,533 ± 111), and ZT 12 (2,572 ± 232) in comparison with ZT 0 (1,889 ± 516). Also, we observed a significant reduction at the ZT 18 (1,926 ± 442) in comparison with ZT 12. In the vLGNe, Tukey's test for *post-hoc* comparisons revealed that young animals present a higher number of CR+ neurons at ZT 6 (4,055 ± 619) in comparison with ZT 0 (2,999 ± 459) and ZT 18 (2,909 ± 702). In the vLGNi, Tukey's test for *post-hoc* comparisons revealed that young animals present a higher number of CR+ neurons at the ZT 12 (2,831 ± 148) in comparison with ZT 0 (1,916 ± 375) and ZT 6 (2,040 ± 393). In middle-aged and old animals, we observed no alterations in CR numbers at different ZTs in any nucleus (**Figure 4**).

Age-Related Changes in CR Cell Numbers of IGL and vLGN

Mean IGL, vLGNe, and vLGNi CR cell numbers of each age and ZT group are summarized in **Table 1**. In the IGL, two-way ANOVA with age as an isolated factor revealed no significant effects upon CR cell number alterations [$F_{(2,36)} = 2.44$; $p = 0.10$]. However, we found a significant effect between the interaction of age and ZT factors in the changes of CR cell numbers [$F_{(6,36)} = 2.334$; $p = 0.05$]. In the ZT 6, the Tukey's test for *post-hoc* comparisons revealed a significant CR cell number reduction in the old animals (1,963 ± 240) in comparison with the young ones (2,533 ± 111). In the ZT 12, we found a significant reduction of CR cells in old rats (1,796 ± 87) in comparison with both young (2,572 ± 232), and middle-aged (2,397 ± 170) groups (**Figure 4A**).

In the vLGNe, we observed CR cell numbers changed due to age factor [$F_{(2,36)} = 4.6$; $p = 0.01$] and the interaction between age and ZT factors [$F_{(6,36)} = 2.51$; $p = 0.04$]. In the ZT 6, Tukey's *post-hoc* test revealed a reduction in the CR cell numbers for the old (3,163 ± 218) and middle-aged (3,088 ± 209) groups in comparison with the young ones (4,055 ± 619). In the ZT 12, Tukey's *post-hoc* test revealed a significant reduction in CR cell numbers in the old (2,754 ± 272) animals in comparison with the young (3,480 ± 256) group (**Figure 4B**).

In the vLGNi, we observed CR cell numbers changed due to age factor [$F_{(2,36)} = 4.73$; $p = 0.01$] but the interaction between age and ZT factors had no significant effects [$F_{(6,36)} = 0.48$; $p = 0.8$]. In the ZT 12, Tukey's *post-hoc* test revealed a reduction in CR cell numbers of old (2,101 ± 274) rats in comparison with the young ones (2,831 ± 148) (**Figure 4C**).

Considering age as a continuous variable, we reported negative correlations between age and CR cell numbers in IGL ($r = -0.72$, $p = 0.008$) and vLGNe ($r = -0.63$, $p = 0.03$) at the ZT 6. Also, we found negative correlations between age and CR cell numbers in IGL ($r = -0.81$, $p = 0.002$), vLGNe ($r = -0.79$, $p = 0.002$), and vLGNi at the ZT 12 ($r = -0.73$, $p = 0.007$). We observed no correlations between these two variables in any nucleus in the other ZT groups (**Figure 5**).

Spatial Distribution of CR in the vLGN

Through line scan analysis, we distinguished four spatial vLGNe and one vLGNi domains marked by CR staining (**Figure 6**). We refer to those as e1, e2, e3, e4, and vLGNi zones. As different animals have slight differences in vLGN length, here we use approximations of average distances we found for the young group. From the lateral-most border to 50 μm, we observed that the e1 zone is relatively spared from CR (young: 16.34 ± 4.40; old: 14.36 ± 4.05). In young animals at the ZT 6, however, we found a higher predominance of CR staining in this area (35.17 ± 11.11). Between e1 and 190 μm, we observed the e2 CR rich area (young: 24.74 ± 5.15; old: 21.55 ± 3.69). Between e2 and 350 μm, we

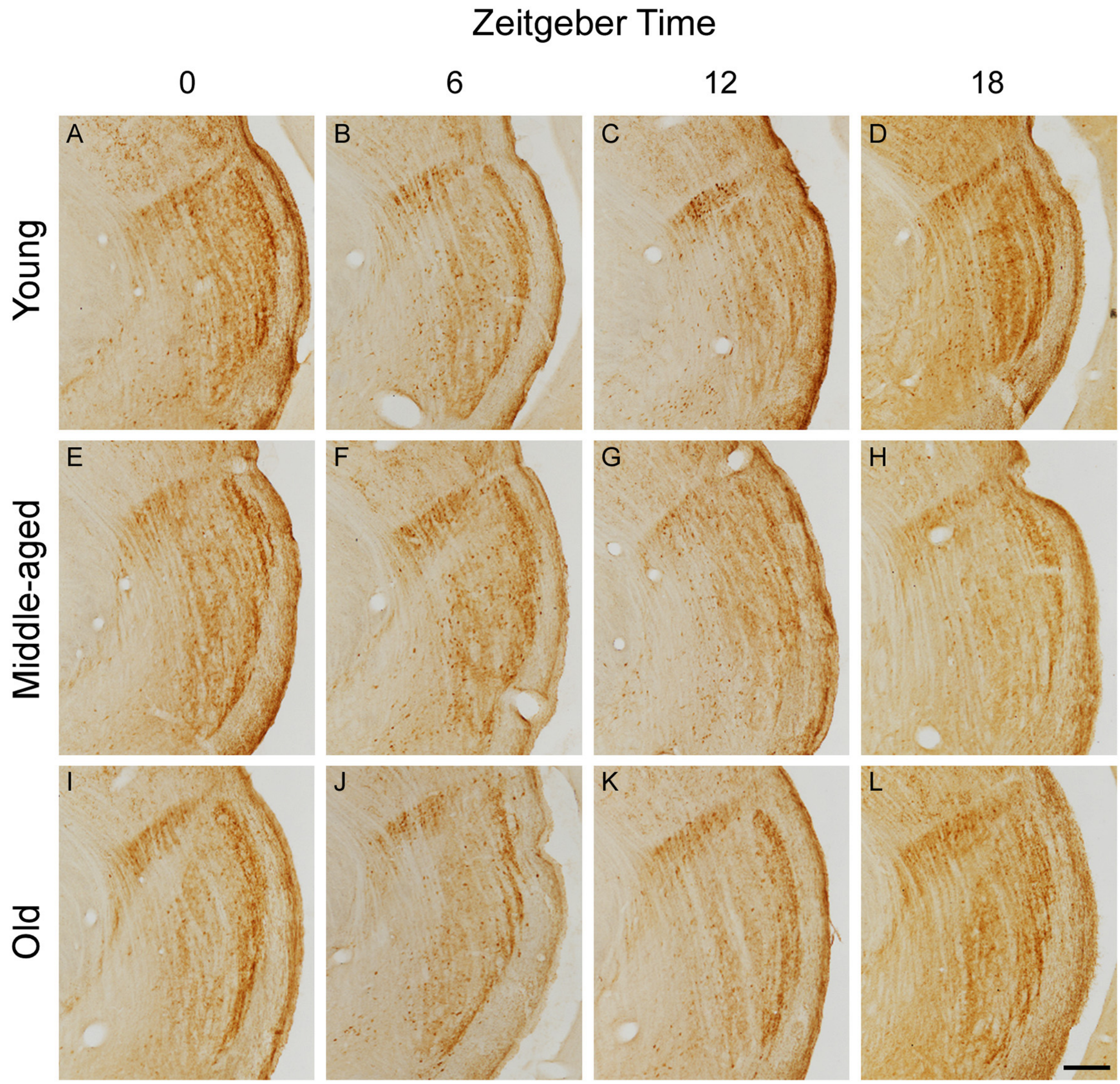

FIGURE 2 | Photomicrographs of CR immunolabeled histological sections containing the IGL, vLGNe, and vLGNi in animals from distinct age and ZT groups. CR sections are obtained after brain perfusion at ZTs 0 (dark/light phase), 6 (light phase), 12 (light/dark phase), and 18 (dark phase) from young **(A–D)**, middle-aged **(E–H)**, or old **(I–L)** animals. Scale bar = 225 µm.

found another CR-scarce zone that we refer as e3 (young: 16.54 ± 1.98; old: 14.93 ± 2.47). Between e3 and 420 µm, we report the e4 CR rich area highlighting the medial-most vLGNe border with vLGNi (young: 20.49 ± 4.36; old: 17.09 ± 4.04). From e4 to the medial-most boundary of vLGNi, we observed no particular pattern of CR staining (young: 11.62 ± 4.48; old: 10.20 ± 3.84). Data for CR intensity in each age group are presented here as the average of all ZTs, except for the e1 in which ZT 6 was isolated.

DISCUSSION

In this study, we describe how changes in the daily expression of the calcium binding protein, CR, marks region-specific patterns of cellular aging in the rat non-image forming visual thalamus. In a previous work, we quantified the total neuronal number for each of the subregions analyzed here using the same age-groups (Fiuza et al., 2017). Comparing these datasets, we can infer CR+ neurons correspond to 32–45% of the total neuronal population in the IGL, 16–23% in the vLGNe, and 13–20% in the vLGNi of rats. Considering CR is a known marker for GABAergic interneurons in other regions such as the cerebral cortex and amygdaloid complex (Tremblay et al., 2016; García-Amado and Prensa, 2021), it is likely that a sizeable portion of these neurons also composes GABAergic neuronal subpopulations. In fact, almost the entirety, if not all, of IGL cells are immunopositive for GAD, an enzyme that synthesizes GABA (Moore and Speh, 1993; Langel et al., 2018). Also, Gad1 and Gad2 mRNA, which translates the GAD 67 and GAD 65 isoforms, are expressed by

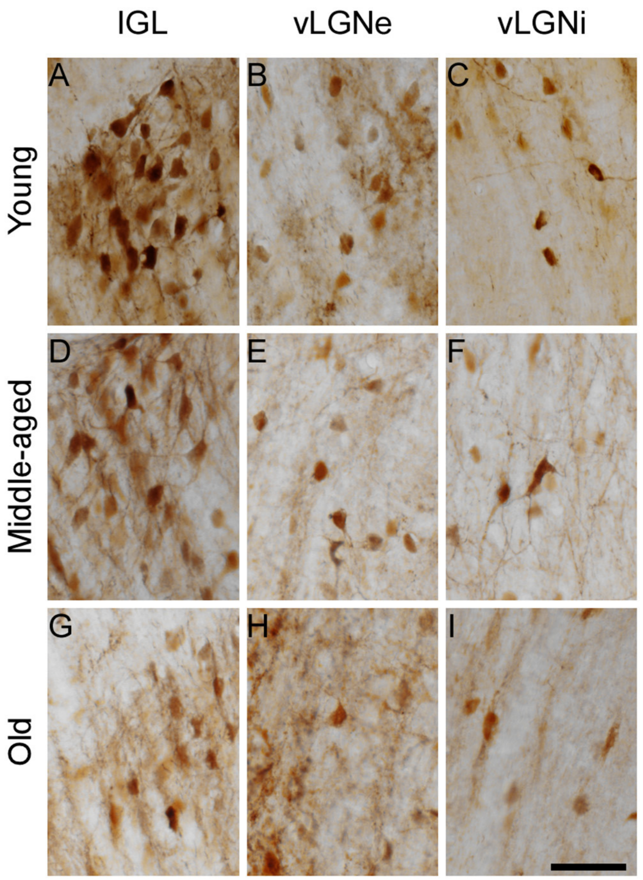

FIGURE 3 | High-magnification photomicrographs of CR immunolabeled cells of the IGL, vLGNe, and vLGNi at ZT 12. The IGL, vLGNe, and vLGNiCR+ neurons from young **(A–C)**, middle-aged **(D–F)**, and old **(G–I)** animals are shown in detail. Scale bar = 50 µm.

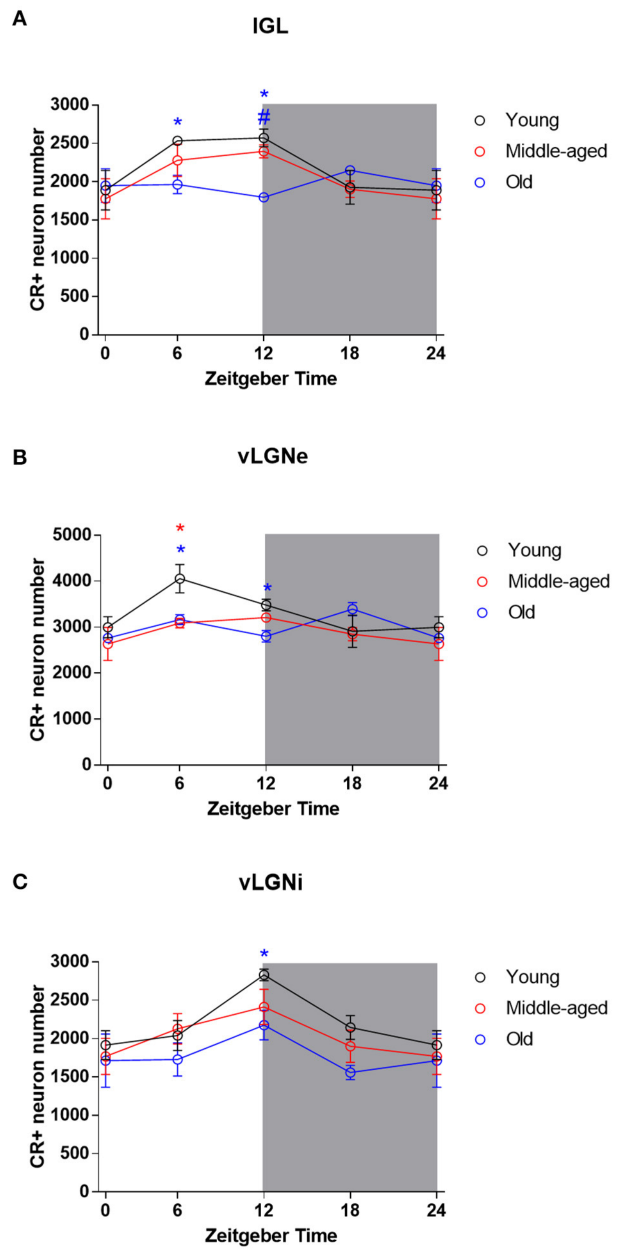

FIGURE 4 | Daily rhythmicity of CR expression in the IGL, vLGNe, and vLGNi. Stereological estimations of total CR cell number at each ZT in the IGL **(A)**, vLGNe **(B)**, and vLGNi **(C)** from young (black), middle-aged (red), or old (blue) animals. Data from ZT 0 are double plotted as ZT 24, to graphically represent the 24 h of the day. Shaded gray areas represent the dark phase. Blue *$p < 0.05$ in young vs. old comparison. Blue #$p < 0.05$ in middle-aged vs. old comparison. Red *$p < 0.05$ in young vs. old comparison. Data are analyzed by two-way ANOVA followed by Tukey's test for *post-hoc* comparison. Data are plotted as mean ± SD.

25 and 41%, respectively, of the total DAPI stained cells in the mouse vLGN (Sabbagh et al., 2020). It is important to highlight that CR+ neurons are also present in the geniculate body of lizard (Dávila et al., 2000), African wild dog (Chengetanai et al., 2020), banded mongoose, ferret (Pillay et al., 2020), marmoset, rock cavy (Cavalcante et al., 2008), and human brains (Münkle et al., 2000) denoting this characteristic is conserved, at some extent, during evolution. Since the IGL and vLGN contribute to visuomotor and circadian functions through projections to the superior colliculus, the pretectal nuclei, and suprachiasmatic nucleus in many species (Harrington, 1997; Morin, 2013), our findings could bring an interesting perspective for further translational aging studies.

We observed a phase-dependent CR expression in the IGL, vLGNe, and vLGNi of young rats. While every nucleus presented a higher number of CR cells during the light phase of the day, distinct phase-dependent patterns denoted a regional variability. In the IGL, we estimated higher numbers of CR+ cells in both ZTs 6 and 12 in comparison with ZT 18. However, CR+ cells peak only at ZT 6 in vLGNe and only at ZT 12 in vLGNi. Such a daily rhythmicity of CR expression, with higher CR+ counts at ZT 6 in comparison with ZTs 14 and 19, is also a feature of a neuronal subpopulation found in the rat suprachiasmatic nucleus (Moore, 2016). Additionally, in *Sapajus apella*, a diurnal primate, a similar

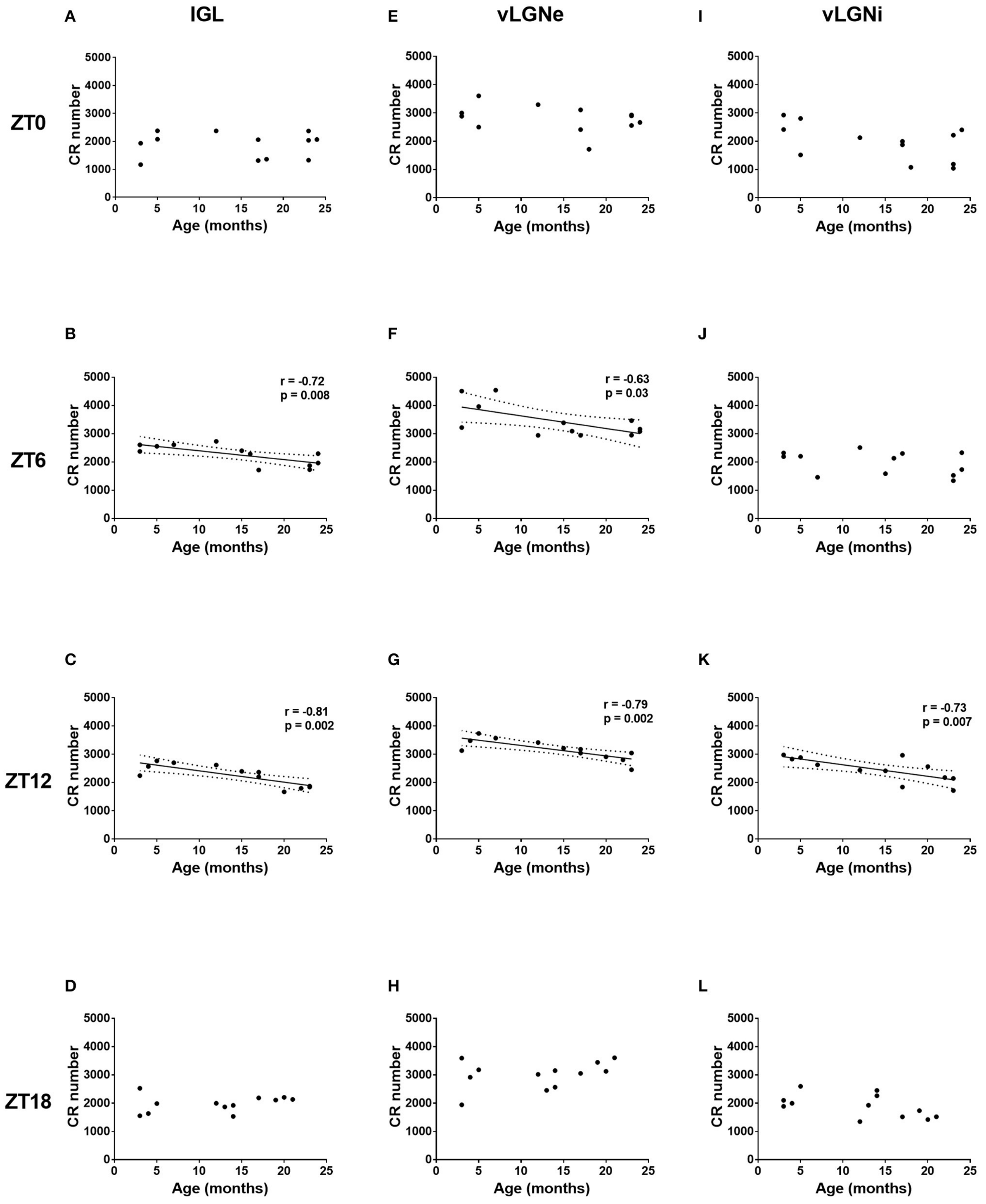

FIGURE 5 | Age-related changes in the CR expression of the IGL, vLGNe, and vLGNi. Total CR+ cell numbers of the IGL **(A–D)**, vLGNe **(E–H)**, and vLGNi **(I–L)** are plotted as a function of age in each ZT. Pearson's correlation coefficient (*r*), regression lines with 95% confidence intervals and *p*-values are shown when a significant linear relation is observed.

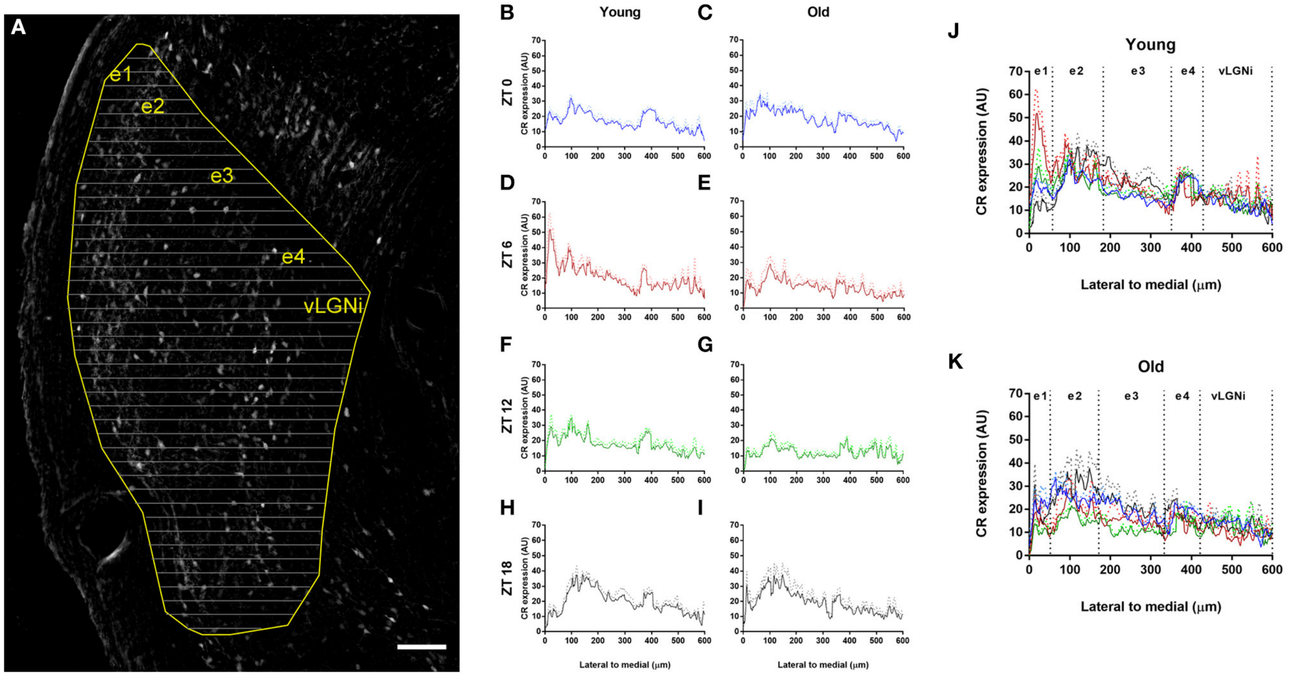

FIGURE 6 | Spatial distribution of CR staining in the vLGN. **(A)** Photomicrograph of the vLGN digitally processed for background subtraction. The vLGN borders are drawn (yellow) and equally spaced lines (gray) in the lateral to medial axis are overlaid to plot profiles of pixel intensity variations in arbitrary units (AU). Scale bar = 100 µm. **(B–I)** CR staining levels through the lateral to medial axis in the young and old animals at t ZTs 0 (blue), 6 (red), 12 (green), and 18 (black). **(J,K)** Every ZT plot overlaid for the young and old animals. Relative CR predominance distinguishes five zones, namely, e1, e2, e3, e4, and vLGNi domains. Data are plotted as mean gray values with standard error for each group.

pattern of reduced CR expression in the dark phase occurs in the ventral and dorsal subdivisions of the medial geniculate body and in the granular cell layer, but not in the polymorphic layer, of the dentate gyrus (Campos et al., 2015a,b). It is also noteworthy that, contrary to what we found for CR, no daily rhythms were detected for the CaBP calbindin D-28k (CB) in the adult rat IGL (Arvanitogiannis et al., 2000). Therefore, it is conceivable that CB and CR characterize distinct neuronal subpopulations in the IGL as occurs in the rat arcuate nucleus and in the human temporal cortex (del Río and DeFelipe, 1996; Foo et al., 2014).

Although daily rhythms of CR expression might reflect important intracellular mechanisms of calcium buffering and signaling, we showed here that it progressively declines with age in the rat non-image forming thalamus. In fact, middle-aged and old animals were completely absent of daily variations in the CR+ cell number of every nucleus. To the best of our knowledge, only one other study addressed the question of whether daily-rhythms of CaBP expression could be a hallmark of cellular aging. In this study, no daily or age-related changes in the density of CB immunopositive neurons were observed in the SCN of the primate, *Microcebus murinus* (Cayetanot et al., 2007). Here, we highlight time of the day as an important methodological consideration for CaBP cell number estimation as two independent studies carried out at isolated ZTs, for instance, one at ZT 12 and other at ZT18, could report either age-related neuronal loss or no alterations whatsoever.

Treating age as a continuous variable, we observed age-related reduction in CR+ neurons in all three nuclei at the ZT 12. At ZT 6, we found such alterations only in IGL and vLGNe. No changes were found in any nucleus at the other ZTs. On comparing with the age categories dataset, such neuronal loss seems to occur at different rates. At the ZT 6 we can detect changes in CR+ neurons of vLGNe in middle-aged rats whereas in the other nuclei at ZT 6 and in every nucleus at ZT 12, the cell numbers were altered only in the old animals. Considering the total neuronal number of these regions remains stable during aging (Fiuza et al., 2017), our findings here are likely due to loss in the capacity of neurons to express CR rather than death of CR+ neuronal population with aging. Such findings add up to a number of reports regarding age-related reductions in CR+ neurons in the hippocampus (Villa et al., 1994), inferior colliculus (Ouda et al., 2012), striatum (Bae et al., 2015), and somatosensory cortex (Ahn et al., 2017) of rodent brains, as well as in the temporal and auditory regions of the human cerebral cortex (Bu et al., 2003). Age-related pathologies also result in decreased number of CR+ neuronal population, as observed in the olfactory cortex of transgenic AβPP/PS1 mice (Saiz-Sanchez et al., 2012) and in the pyriform cortex of patients with Alzheimer's disease (Saiz-Sanchez et al., 2015). In some scenarios, these alterations might be due to a specific reduction of CR expression rather than cell death as we observed here. For instance, the number of CR+ large striatal interneurons, but not the absolute number of these cells, is decreased in Huntington's disease (Massouh et al., 2008). Notwithstanding, in the rat dorsomedial and ventromedial hypothalamic nuclei the percentage of CR+ neurons increases during aging (Vishnyakova et al., 2020). This reinforces the usefulness in understanding CR, or any CaBP, expression as regional markers of cellular changes in normal aging and in the progression of age-related diseases.

Through our analysis of spatial distribution, we observed a predominance of CR staining into the lateral-most and medial-most portions of the vLGNe, with a low density CR zone between these regions, at all ZTs. In the vLGNi, however, we distinguished no specific pattern of CR distribution. That was the case even in the old animals, suggesting that the age-related cell loss we observed is not restricted at a particular subset of spatially-located neurons, except perhaps in the e1 subdivision at ZT 6. We show that CR fairly delimits the vLGNe since sublaminae-specific markers reveal four hidden laminae, all containing GABAergic cells, in a lateral to medial organization (Sabbagh et al., 2020). It is noteworthy that in the vLGNe, but not in the IGL, retinal terminals are segregated into non-overlapping eye domains (Monavarfeshani et al., 2017). Such retinal projections to these nuclei arise from non-image forming RGCs, such as the M1 intrinsically photosensitive and Cdh3-GFP RGCs (Hattar et al., 2006; Osterhout et al., 2011). The lateral-most regions of the vLGNe, which we relate with CR delimited e1, presents retinal terminals from on–off direction-selective RGCs (Monavarfeshani et al., 2017). Also, rods and cones seem to participate in the IGL/vLGN activation since light-induced FOS immunoreactivity is reduced in these nuclei of mice lacking these photoreceptors, a response even more dampened in the aged animals (Lupi et al., 2012). Considering CR+ neurons in the IGL/vLGN may be targets from CR expressing RGCs (Arai et al., 1992), further works are necessary to establish whether a coincident loss of CR expression denotes age-related effects on topographically organized channels of visuomotor and circadian processing.

Unbiased stereological methods for quantitative neuroanatomy greatly enriched the knowledge of how aging affects the nervous system by directing a region-specific approach to detect age-related alterations in the cellular composition of the brain. As many studies focus in total protein quantification to address age-related changes, we highlight the informative feature to quantify cell numbers for an integrative approach. For instance, in here and in a few previous reports, if any, the CR+ cell bodies were found in the rodent dLGN (Arai et al., 1992; Evangelio et al., 2018). However, in comparison with IGL and vLGN, the mouse dLGN presents similar CR levels detected by Western blot and even higher expression of its associated Calb 2 mRNA (Sabbagh et al., 2018). While mRNA levels are not necessarily correlated with protein amounts (Maier et al., 2009), such findings might be due to the presence of CR in axon terminals at the dLGN as it occurs in the macaque prefrontal cortex (Melchitzky et al., 2005). Thus, mRNA and total protein expression approaches could benefit from the understanding if potential changes in molecule amount are accompanied by shifts in the cellular phenotype.

DATA AVAILABILITY STATEMENT

The raw data supporting the conclusions of this article will be made available by the authors, without undue reservation.

ETHICS STATEMENT

The animal study was reviewed and approved by Comissão de ética no uso de animais (CEUA/UFRN).

AUTHOR CONTRIBUTIONS

FF, RE, and JC designed the study and wrote the paper receiving inputs from all the authors. FF, AA, DC, LB, and JC carried out histological procedures. FF, JQ, and RL performed image analysis and prepared figures. All authors contributed to the article and approved the submitted version.

FUNDING

This work was supported by the Brazilian funding agencies, Conselho Nacional de Desenvolvimento Científico e Tecnológico (CNPQ), and Coordenação de Aperfeiçoamento de Pessoal de Ensino Superior (CAPES).

ACKNOWLEDGMENTS

We thank Profs. Carlos Avendaño and Francisco Clascá from the Universidad Autonoma de Madrid-Spain for aiding in the stereological and microscopy analyses.

REFERENCES

Adler, P., Chiang, C. K., Mayne, J., Ning, Z., Zhang, X., Xu, B., et al. (2020). Aging disrupts the circadian patterns of protein expression in the murine hippocampus. *Front Aging Neurosci.* 11:368. doi: 10.3389/fnagi.2019.00368

Ahn, J. H., Hong, S., Park, J. H., Kim, I. H., Cho, J. H., Lee, T. K., et al. (2017). Immunoreactivities of calbindin-D28k, calretinin and parvalbumin in the somatosensory cortex of rodents during normal aging. *Mol. Med. Rep.* 16, 7191–7198. doi: 10.3892/mmr.2017.7573

Alzheimer's Association Calcium Hypothesis Workgroup. (2017). Calcium hypothesis of Alzheimer's disease and brain aging: a framework for integrating new evidence into a comprehensive theory of pathogenesis. *Alzheimers Dement.* 13, 178–82.e17. doi: 10.1016/j.jalz.2016.12.006

Arai, M., Arai, R., Kani, K., and Jacobowitz, D. M. (1992). Immunohistochemical localization of calretinin in the rat lateral geniculate nucleus and its retino-geniculate projection. *Brain Res.* 596, 215–222. doi: 10.1016/0006-8993(92)91550-X

Arvanitogiannis, A., Robinson, B., Beaulé, C., and Amir, S. (2000). Calbindin-D28k immunoreactivity in the suprachiasmatic nucleus and the circadian response to constant light in the rat. *Neuroscience* 99, 397–401. doi: 10.1016/S0306-4522(00)00327-4

Bae, E. J., Chen, B. H., Shin, B. N., Cho, J. H., Kim, I. H., Park, J. H., et al. (2015). Comparison of immunoreactivities of calbindin-D28k, calretinin and parvalbumin in the striatum between young, adult and aged mice, rats and gerbils. *Neurochem. Res.* 40, 864–872. doi: 10.1007/s11064-015-1537-x

Bañuelos, C., LaSarge, C. L., McQuail, J. A., Hartman, J. J., Gilbert, R. J., Ormerod, B. K., et al. (2013). Age-related changes in rostral basal forebrain cholinergic and GABAergic projection neurons: relationship with spatial impairment. *Neurobiol. Aging* 34, 845–862. doi: 10.1016/j.neurobiolaging.2012.06.013

Bishop, D. P., Cole, N., Zhang, T., Doble, P. A., and Hare, D. J. (2018). A guide to integrating immunohistochemistry and chemical imaging. *Chem. Soc. Rev.* 47, 3770–3787. doi: 10.1039/C7CS00610A

Bu, J., Sathyendra, V., Nagykery, N., and Geula, C. (2003). Age-related changes in calbindin-D28k, calretinin, and parvalbumin-immunoreactive neurons in the human cerebral cortex. *Exp. Neurol.* 182, 220–231. doi: 10.1016/S0014-4886(03)00094-3

Campos, L. M. G., Cruz-Rizzolo, R. J., and Pinato, L. (2015a). The primate seahorse rhythm. *Brain Res.* 1613, 81–91. doi: 10.1016/j.brainres.2015.03.054

Campos, L. M. G., Osório, E. C., Santos, G. L., da, S., Nogueira, M. I., Cruz-Rizzolo, R. J., et al. (2015b). Temporal changes in calcium-binding proteins in the medial geniculate nucleus of the monkey Sapajusapella. *J. Chem. Neuroanat.* 68, 45–54. doi: 10.1016/j.jchemneu.2015.07.005

Cavalcante, J. S., Britto, L. R. G., Toledo, C. A. B., Nascimento, E. S., Lima, R. R. M., Pontes, A. L. B., et al. (2008). Calcium-binding proteins in the circadian centers of the common marmoset (*Callithrix jacchus*) and the rock cavy (*Kerodon rupestris*) brains. *Brain Res. Bull.* 76, 354–360. doi: 10.1016/j.brainresbull.2008.02.028

Cayetanot, F., Bentivoglio, M., and Aujard, F. (2005). Arginine-vasopressin and vasointestinal polypeptide rhythms in the suprachiasmatic nucleus of the mouse lemur reveal aging-related alterations of circadian pacemaker neurons in a non-human primate. *Eur. J. Neurosci.* 22, 902–910. doi: 10.1111/j.1460-9568.2005.04268.x

Cayetanot, F., Deprez, J., and Aujard, F. (2007). Calbindin D28K protein cells in a primate suprachiasmatic nucleus: localization, daily rhythm and age-related changes. *Eur. J. Neurosci.* 26, 2025–2032. doi: 10.1111/j.1460-9568.2007.05826.x

Chengetanai, S., Bhagwandin, A., Bertelsen, M. F., Hård, T., Hof, P. R., Spocter, M. A., et al. (2020). The brain of the African wild dog. IV. The visual system. *J. Comp. Neurol.* 528, 3262–84. doi: 10.1002/cne.25000

Dávila, J. C., Guirado, S., and Puelles, L. (2000). Expression of calcium-binding proteins in the diencephalon of the lizard *Psammodromus algirus. J. Comp. Neurol.* 427, 67–92. doi: 10.1002/1096-9861(20001106)427:1<67::AID-CNE5>3.0.CO;2-2

del Río, M. R., and DeFelipe, J. (1996). Colocalization of calbindin D-28k, calretinin, and GABA immunoreactivities in neurons of the human temporal cortex. *J. Comp. Neurol.* 369, 472–482. doi: 10.1002/(SICI)1096-9861(19960603)369:3<472::AID-CNE11>3.0.CO;2-K

Engelberth, R. C. G. J., Pontes, A. L. B., de, Fiuza, F. P., Silva, K. D., de, A., Resende, N. da, S., et al. (2013). Changes in the suprachiasmatic nucleus during aging: implications for biological rhythms. *Psychol. Neurosci.* 6, 287–297. doi: 10.3922/j.psns.2013.3.07

Evangelio, M., García-Amado, M., and Clascá, F. (2018). Thalamocortical projection neuron and interneuron numbers in the visual thalamic nuclei of the adult C57BL/6 mouse. *Front. Neuroanat.* 12:27. doi: 10.3389/fnana.2018.00027

Fairless, R., Williams, S. K., and Diem, R. (2019). Calcium-binding proteins as determinants of central nervous system neuronal vulnerability to disease. *Int. J. Mol. Sci.* 20:2146. doi: 10.3390/ijms20092146

Fiuza, F. P., Aquino, A. C. Q., Câmara, D. A., Cavalcanti, J. R. L. P., Nascimento Júnior, E. S., Lima, R. H., et al. (2017). Region-specific glial hyperplasia and neuronal stability of rat lateral geniculate nucleus during aging. *Exp. Gerontol.* 100, 91–99. doi: 10.1016/j.exger.2017.11.001

Fiuza, F. P., Silva, K. D. A., Pessoa, R. A., Pontes, A. L. B., Cavalcanti, R. L. P., Pires, R. S., et al. (2016). Age-related changes in neurochemical components and retinal projections of rat intergeniculate leaflet. *Age* 38:4. doi: 10.1007/s11357-015-9867-9

Flatt, T., and Partridge, L. (2018). Horizons in the evolution of aging. *BMC Biol.* 16:93. doi: 10.1186/s12915-018-0562-z

Foo, K. S., Hellysaz, A., and Broberger, C. (2014). Expression and colocalization patterns of calbindin-D28k, calretinin and parvalbumin in the rat hypothalamic arcuate nucleus. *J. Chem. Neuroanat.* 61–62, 20–32. doi: 10.1016/j.jchemneu.2014.06.008

Fox, M. A., and Guido, W. (2011). Shedding light on class-specific wiring: development of intrinsically photosensitive retinal ganglion cell circuitry. *Mol. Neurobiol.* 44, 321–329. doi: 10.1007/s12035-011-8199-8

García-Amado, M., and Prensa, L. (2021). Neurons expressing parvalbumin and calretinin in the human amygdaloid complex: a quantitative and qualitative analysis in every nucleus and nuclear subdivision. *Neuroscience* 452, 153–168. doi: 10.1016/j.neuroscience.2020.11.001

Gundersen, H. J., Jensen, E. B., Kiêu, K., and Nielsen, J., null (1999). The efficiency of systematic sampling in stereology–reconsidered. *J. Microsc.* 193, 199–211. doi: 10.1046/j.1365-2818.1999.00457.x

Harrington, M. E. (1997). The ventral lateral geniculate nucleus and the intergeniculate leaflet: interrelated structures in the visual and circadian systems. *Neurosci. Biobehav. Rev.* 21, 705–727. doi: 10.1016/S0149-7634(96)00019-X

Hattar, S., Kumar, M., Park, A., Tong, P., Tung, J., Yau, K. W., et al. (2006). Central projections of melanopsin-expressing retinal ganglion cells in the mouse. *J. Comp. Neurol.* 497, 326–349. doi: 10.1002/cne.20970

Jagota, A., and Kalyani, D. (2008). Daily serotonin rhythms in rat brain during postnatal development and aging. *Biogerontology* 9, 229–234. doi: 10.1007/s10522-008-9132-z

Jeon, M. H., and Jeon, C. J. (1998). Immunocytochemical localization of calretinin containing neurons in retina from rabbit, cat, and dog. *Neurosci. Res.* 32, 75–84. doi: 10.1016/S0168-0102(98)00070-4

Khachaturian, Z. S. (1994). Calcium hypothesis of Alzheimer's disease and brain aging. *Ann. N. Y. Acad. Sci.* 747, 1–11. doi: 10.1111/j.1749-6632.1994.tb44398.x

Kondratova, A. A., and Kondratov, R. V. (2012). Circadian clock and pathology of the ageing brain. *Nat. Rev. Neurosci.* 13, 325–335. doi: 10.1038/nrn3208

Lamerand, S., Shahidehpour, R., Ayala, I., Gefen, T., Mesulam, M. M., Bigio, E., et al. (2020). Calbindin-D28K, parvalbumin, and calretinin in young and aged human locus coeruleus. *Neurobiol. Aging* 94, 243–249. doi: 10.1016/j.neurobiolaging.2020.06.006

Landfield, P. W. (1987). 'Increased calcium-current' hypothesis of brain aging. *Neurobiol. Aging* 8, 346–347. doi: 10.1016/0197-4580(87)90074-1

Langel, J., Ikeno, T., Yan, L., Nunez, A. A., and Smale, L. (2018). Distributions of GABAergic and glutamatergic neurons in the brains of a diurnal and nocturnal rodent. *Brain Res.* 1700, 152–159. doi: 10.1016/j.brainres.2018.08.019

Lee, C. H., Hwang, I. K., Choi, J. H., Yoo, K. Y., Park, O. K., Huh, S. O., et al. (2010a). Age-dependent changes in calretinin immunoreactivity and its protein level in the gerbil hippocampus. *Neurochem. Res.* 35, 122–129. doi: 10.1007/s11064-009-0037-2

Lee, E. S., Lee, J. Y., and Jeon, C. J. (2010b). Types and density of calretinin-containing retinal ganglion cells in mouse. *Neurosci. Res.* 66, 141–150. doi: 10.1016/j.neures.2009.10.008

Lee, S. C. S., Weltzien, F., Madigan, M. C., Martin, P. R., and Grünert, U. (2016). Identification of AII amacrine, displaced amacrine, and bistratified ganglion cell types in human retina with antibodies against calretinin. *J. Comp. Neurol.* 524, 39–53. doi: 10.1002/cne.23821

Long, J. M., Mouton, P. R., Jucker, M., and Ingram, D. K. (1999). What counts in brain aging? Design-based stereological analysis of cell number. *J. Gerontol. A Biol. Sci. Med. Sci.* 54, B407–B417. doi: 10.1093/gerona/54.10.B407

López-Otín, C., Blasco, M. A., Partridge, L., Serrano, M., and Kroemer, G. (2013). The hallmarks of aging. *Cell* 153, 1194–1217. doi: 10.1016/j.cell.2013.05.039

Lucas, R. J., Peirson, S. N., Berson, D. M., Brown, T. M., Cooper, H. M., Czeisler, C. A., et al. (2014). Measuring and using light in the melanopsin age. *Trends Neurosci.* 37, 1–9. doi: 10.1016/j.tins.2013.10.004

Lukas, W., and Jones, K. A. (1994). Cortical neurons containing calretinin are selectively resistant to calcium overload and excitotoxicity *in vitro*. *Neuroscience* 61, 307–316. doi: 10.1016/0306-4522(94)90233-X

Lupi, D., Semo, M., and Foster, R. G. (2012). Impact of age and retinal degeneration on the light input to circadian brain structures. *Neurobiol. Aging* 33, 383–392. doi: 10.1016/j.neurobiolaging.2010.03.006

Maier, T., Güell, M., and Serrano, L. (2009). Correlation of mRNA and protein in complex biological samples. *FEBS Lett.* 583, 3966–3973. doi: 10.1016/j.febslet.2009.10.036

Massouh, M., Wallman, M. J., Pourcher, E., and Parent, A. (2008). The fate of the large striatal interneurons expressing calretinin in Huntington's disease. *Neurosci. Res.* 62, 216–224. doi: 10.1016/j.neures.2008.08.007

Matute, C., and Streit, P. (1985). Selective retrograde labeling with D-[3H]-aspartate in afferents to the mammalian superior colliculus. *J. Comp. Neurol.* 241, 34–49. doi: 10.1002/cne.902410104

Melchitzky, D. S., Eggan, S. M., and Lewis, D. A. (2005). Synaptic targets of calretinin-containing axon terminals in macaque monkey prefrontal cortex. *Neuroscience* 130, 185–195. doi: 10.1016/j.neuroscience.2004.08.046

Míguez, J. M., Recio, J., Sánchez-Barceló, E., and Aldegunde, M. (1998). Changes with age in daytime and nighttime contents of melatonin, indoleamines, and catecholamines in the pineal gland: a comparative study in rat and Syrian hamster. *J. Pineal Res.* 25, 106–115. doi: 10.1111/j.1600-079X.1998.tb00547.x

Monavarfeshani, A., Sabbagh, U., and Fox, M. A. (2017). Not a one-trick pony: Diverse connectivity and functions of the rodent lateral geniculate complex. *Vis. Neurosci.* 34, E012. doi: 10.1017/S0952523817000098

Moore, R. Y. (2016). Calretinin neurons in the rat suprachiasmatic nucleus. *J. Biol. Rhythms* 31, 406–410. doi: 10.1177/0748730416654024

Moore, R. Y., and Speh, J. C. (1993). GABA is the principal neurotransmitter of the circadian system. *Neurosci. Lett.* 150, 112–116. doi: 10.1016/0304-3940(93)90120-A

Morin, L. P. (2013). Neuroanatomy of the extended circadian rhythm system. *Exp. Neurol.* 243, 4–20. doi: 10.1016/j.expneurol.2012.06.026

Morin, L. P., and Studholme, K. M. (2014). Retinofugal projections in the mouse. *J. Comp. Neurol.* 522, 3733–3753. doi: 10.1002/cne.23635

Münkle, M. C., Waldvogel, H. J., and Faull, R. L. (2000). The distribution of calbindin, calretinin and parvalbumin immunoreactivity in the human thalamus. *J. Chem. Neuroanat.* 19, 155–173. doi: 10.1016/S0891-0618(00)00060-0

Osterhout, J. A., Josten, N., Yamada, J., Pan, F., Wu, S., Nguyen, P. L., et al. (2011). Cadherin-6 mediates axon-target matching in a non-image-forming visual circuit. *Neuron* 71, 632–639. doi: 10.1016/j.neuron.2011.07.006

Ouda, L., Burianova, J., and Syka, J. (2012). Age-related changes in calbindin and calretinin immunoreactivity in the central auditory system of the rat. *Exp. Gerontol.* 47, 497–506. doi: 10.1016/j.exger.2012.04.003

Pal, I., Paltati, C. R. B., Kaur, C., Shubhi, S., Kumar, P., Jacob, T. G., et al. (2019). Morphological and neurochemical changes in GABAergic neurons of the aging human inferior colliculus. *Hear. Res.* 377, 318–329. doi: 10.1016/j.heares.2019.02.005

Paxinos, G., and Watson, C. (2014). *The Rat Brain in Stereotaxic Coordinates, 7th Edn*. London: Elsevier Academic Press.

Pike, C. J., and Cotman, C. W. (1995). Calretinin-immunoreactive neurons are resistant to beta-amyloid toxicity *in vitro*. *Brain Res.* 671, 293–298. doi: 10.1016/0006-8993(94)01354-K

Pillay, S., Bhagwandin, A., Bertelsen, M. F., Patzke, N., Engler, G., Engel, A. K., et al. (2020). The diencephalon of two carnivore species: the feliform banded mongoose and the caniform domestic ferret. *J. Comp. Neurol.* doi: 10.1002/cne.25036

Sabbagh, U., Govindaiah, G., Somaiya, R. D., Ha, R. V., Wei, J. C., Guido, W., et al. (2020). Diverse GABAergic neurons organize into subtype-specific sublaminae in the ventral lateral geniculate nucleus. *J. Neurochem.* 00, 1–19. doi: 10.1111/jnc.15101

Sabbagh, U., Monavarfeshani, A., Su, K., Zabet-Moghadam, M., Cole, J., Carnival, E., et al. (2018). Distribution and development of molecularly distinct perineuronal nets in visual thalamus. *J. Neurochem.* 147, 626–646. doi: 10.1111/jnc.14614

Saiz-Sanchez, D., De la Rosa-Prieto, C., Ubeda-Banon, I., and Martinez-Marcos, A. (2015). Interneurons, tau and amyloid-β in the piriform cortex in Alzheimer's disease. *Brain Struct. Funct.* 220, 2011–2025. doi: 10.1007/s00429-014-0771-3

Saiz-Sanchez, D., Ubeda-Bañon, I., De la Rosa-Prieto, C., and Martinez-Marcos, A. (2012). Differential expression of interneuron populations and correlation with amyloid-β deposition in the olfactory cortex of an AβPP/PS1 transgenic mouse model of Alzheimer's disease. *J. Alzheimers Dis.* 31, 113–129. doi: 10.3233/JAD-2012-111889

Schurmans, S., Schiffmann, S. N., Gurden, H., Lemaire, M., Lipp, H. P., Schwam, V., et al. (1997). Impaired long-term potentiation induction in dentate gyrus of calretinin-deficient mice. *PNAS* 94, 10415–10420. doi: 10.1073/pnas.94.19.10415

Sondereker, K. B., Stabio, M. E., and Renna, J. M. (2020). Crosstalk: the diversity of melanopsin ganglion cell types has begun to challenge the canonical divide between image-forming and non-image-forming vision. *J. Compa. Neurol.* 528, 2044–2067. doi: 10.1002/cne.24873

Tremblay, R., Lee, S., and Rudy, B. (2016). GABAergic interneurons in the neocortex: from cellular properties to circuits. *Neuron* 91, 260–292. doi: 10.1016/j.neuron.2016.06.033

Villa, A., Podini, P., Panzeri, M. C., Racchetti, G., and Meldolesi, J. (1994). Cytosolic Ca^{2+} binding proteins during rat brain ageing: loss of calbindin and calretinin in the hippocampus, with no change in the cerebellum. *Eur. J. Neurosci.* 6, 1491–1499. doi: 10.1111/j.1460-9568.1994.tb01010.x

Vishnyakova, P. A., Moiseev, K. Y., Spirichev, A. A., Emanuilov, A. I., Nozdrachev, A. D., and Masliukov, P. M. (2020). Expression of calbindin and calretinin in the dorsomedial and ventromedial hypothalamic nuclei during aging. *Anat. Rec.* 1–11. doi: 10.1002/ar.24536

von Bartheld, C. S., von, Bahney, J., and Herculano-Houzel, S. (2016). The search for true numbers of neurons and glial cells in the human brain: a review of 150 years of cell counting. *J. Comp. Neurol.* 524, 3865–3895. doi: 10.1002/cne.24040

West, M. J., Slomianka, L., and Gundersen, H. J. (1991). Unbiased stereological estimation of the total number of neurons in thesubdivisions of the rat hippocampus using the optical fractionator. *Anat. Rec.* 231, 482–497. doi: 10.1002/ar.1092310411

Yan, F. F., Hou, F., Lu, H., Yang, J., Chen, L., Wu, Y., et al. (2020). Aging affects gain and internal noise in the visual system. *Sci. Rep.* 10:6768. doi: 10.1038/s41598-020-63053-0

Conflict of Interest: The authors declare that the research was conducted in the absence of any commercial or financial relationships that could be construed as a potential conflict of interest.

frontiers
in Aging Neuroscience

ORIGINAL RESEARCH
published: 09 March 2021
doi: 10.3389/fnagi.2021.629214

Persistent Dark Cones in Oligocone Trichromacy Revealed by Multimodal Adaptive Optics Ophthalmoscopy

Joanne Li[1†], Tao Liu[1†], Oliver J. Flynn[1], Amy Turriff[1], Zhuolin Liu[2], Ehsan Ullah[1], Jianfei Liu[1], Alfredo Dubra[3], Mary A. Johnson[4], Brian P. Brooks[1], Robert B. Hufnagel[1], Daniel X. Hammer[2], Laryssa A. Huryn[1], Brett G. Jeffrey[1] and Johnny Tam[1*]

[1] National Eye Institute, National Institutes of Health, Bethesda, MD, United States, [2] Center for Devices and Radiological Health, U.S. Food and Drug Administration, Silver Spring, MD, United States, [3] Department of Ophthalmology, Stanford University, Palo Alto, CA, Unites States, [4] Ophthalmology and Visual Sciences, University of Maryland School of Medicine, Baltimore, MD, United States

Dark cone photoreceptors, defined as those with diminished or absent reflectivity when observed with adaptive optics (AO) ophthalmoscopy, are increasingly reported in retinal disorders. However, their structural and functional impact remain unclear. Here, we report a 3-year longitudinal study on a patient with oligocone trichromacy (OT) who presented with persistent, widespread dark cones within and near the macula. Diminished electroretinogram (ERG) cone but normal ERG rod responses together with normal color vision confirmed the OT diagnosis. In addition, the patient had normal to near normal visual acuity and retinal sensitivity. Occasional dark gaps in the photoreceptor layer were observed on optical coherence tomography, in agreement with reflectance AO scanning light ophthalmoscopy, which revealed that over 50% of the cones in the fovea were dark, increasing to 74% at 10° eccentricity. In addition, the cone density was 78% lower than normal histologic value at the fovea, and 20–40% lower at eccentricities of 5–15°. Interestingly, color vision testing was near normal at locations where cones were predominantly dark. These findings illustrate how a retina with predominant dark cones that persist over at least 3 years can support near normal central retinal function. Furthermore, this study adds to the growing evidence that cones can continue to survive under non-ideal conditions.

Keywords: adaptive optics, scanning laser ophthalmoscopy, optical coherence tomography, dark cones, visual function, color vision, oligocone trichromacy, pde6h

Edited by:
Ann E. Elsner,
Indiana University, United States

Reviewed by:
Adam M. Dubis,
University College London, United Kingdom
Amani Fawzi,
Northwestern Medicine, United States
Jason Charng,
Lions Eye Institute, Australia

Correspondence:
Johnny Tam
johnny@nih.gov

† These authors share first authorship

Received: *13 November 2020*
Accepted: *09 February 2021*
Published: *09 March 2021*

Citation:
Li J, Liu T, Flynn OJ, Turriff A, Liu Z, Ullah E, Liu J, Dubra A, Johnson MA, Brooks BP, Hufnagel RB, Hammer DX, Huryn LA, Jeffrey BG and Tam J (2021) Persistent Dark Cones in Oligocone Trichromacy Revealed by Multimodal Adaptive Optics Ophthalmoscopy. Front. Aging Neurosci. 13:629214. doi: 10.3389/fnagi.2021.629214

INTRODUCTION

Adaptive optics (AO) ophthalmoscopy has become increasingly used to assess cone photoreceptor structure and function in human subjects. In the normal photoreceptor mosaic, the reflectivity of individual cones is highly variable both spatially and temporally (Pallikaris et al., 2003). This reflectance signal is thought to arise from natural variations in the way light interacts with cones, including the capture, waveguiding, and backscattering of light (Roorda and Williams, 2002). However, in disease, structural and functional changes can impact the reflectivity of cones, resulting in what has been previously referred to as "dark cones." Multimodal AO ophthalmoscopy can show cones through different contrast mechanisms simultaneously. Recently, non-confocal split detection revealed that cones with diminished or seemingly absent reflectivity in retinal disorders such as achromatopsia (Georgiou et al., 2020) can have intact inner segments even though they appear dark. However, the clinical implications and functional consequence of having dark cones remain unclear for numerous retinal diseases.

In 1973, van Lith described a patient with a phenotype characterized by a normal fundus exam, reduced visual acuity (VA), normal or near normal color vision, normal scotopic ERG amplitudes but a much reduced photopic ERG (van Lith, 1973). He proposed the term oligocone trichromacy (OT) based on a theory of reduced cone numbers with trichromatism (van Lith, 1973), which was later confirmed in the foveal region of three OT patients using a flood illuminated AO ophthalmoscope (Michaelides et al., 2011). Here, we expand upon this earlier report by longitudinally characterizing persistent, widespread dark cones observed within and near the macula using multimodal AO scanning light ophthalmoscopy (AO-SLO) and AO optical coherence tomography (AO-OCT), alongside detailed analysis of retinal function in a patient with OT (**Figure 1**).

PATIENTS AND METHODS

Study Design

The subject was a 55-year-old female born in South India to consanguineous parents, who reported a history of mildly decreased VA since childhood, minimal photophobia, and reduced contrast sensitivity. She had a history of anemia, hypertension, and chronic renal disease secondary to congenital renal hypoplasia for which she underwent successful kidney transplant. The participant provided written, informed consent. Although not a clinical trial, this research is registered on clinicaltrials.gov (Identifiers: NCT02617966, NCT01878032, and NCT02317328). National Institutes of Health Institutional Review Board (IRB)/Ethics Committee approval was obtained, and this study adhered to the tenets of the Declaration of Helsinki.

A 3-year longitudinal study with comprehensive ophthalmic examination was performed, including VA assessment, anterior segment, and dilated fundus examinations, along with AO imaging.

Genetic Testing

DNA was extracted from whole blood of the proband for genetic testing. Initial quality control and quantification of DNA was done at the Ophthalmic Genomics Laboratory, NEI, whereas for whole exome sequencing, DNA was processed at the NIH Intramural Sequencing Center (NISC). Library preparation was done by using Roche's NimbleGen SeqCap EZ Version 3.0 + UTR kit. Sequencing was carried out on Illumina HiSeq platform to generate 100 bp paired-end reads. Raw data were processed by using a standard in-house bioinformatics pipeline. Briefly, reads were aligned to the hg19 reference genome by using the burrows wheeler aligner and duplicates were marked with the Picard tool. Small InDels and single nucleotide variants (SNVs) were called using GATK and annotated by Variant Effect Predictor (VEP 92). By using maximum allele frequency 0.01, coding and splice variants were prioritized and then further analyzed for pathogenicity and correlation with the patient's phenotype.

Measurements of Retinal Function

Mesopic retinal sensitivity was measured following pupil dilation using a fundus guided perimeter (MP1, Navis Software version 1.7.6, Nidek Technologies, Padua, Italy) as previously described (Cukras et al., 2018). Briefly, retinal sensitivity was measured across 68 foci covering a 20° field centered on the fovea (Humphrey 10-2 pattern). At each locus, retinal sensitivity was measured for a 0.43° white stimulus (Goldmann size III) presented for 200 ms against a mesopic background (1.27 cd/m^2).

Monocular color discrimination thresholds were measured along 8 axes spaced 45° apart in CIE 1976 $L^*u^*v^*$ space measured using a low vision version of the Cambridge Color Test (LvCCT) (Simunovic et al., 1998) implemented on a ViSaGe System (Cambridge Research Systems Ltd., Rochester, United Kingdom) (Zein et al., 2014). Mean color discrimination thresholds were calculated from five separate measurements along each axis at each eccentricity. The range for normal color discrimination thresholds were determined from 22 healthy volunteers. Achromatic area (AA: units = 10^6 u^*v^{*2}), defined by the area inside the polygon formed by the 8 chromatic discrimination thresholds was measured for foveal fixation and for two retinal eccentricities (5° and 10° along the vertical meridian from the superior retina). Color vision was also assessed with the updated Hardy-Rand-Rittler color plates (Bailey et al., 2004) and Nagel anomaloscope.

Full field ERGs (ffERGs) were recorded in accordance with the 2008 version of the International Society for Clinical Electrophysiology of Vision (ISCEV) standard (Marmor et al., 2009) as described in detail previously (Knickelbein et al., 2020). Briefly, the patient was dark-adapted for 30 min prior to the start of the ERG testing. ffERGs were then recorded from bipolar Burian-Allen contact lens electrodes (Hansen Ophthalmic Laboratories, Iowa City, IA) using a commercial electrophysiology system (LKC, Gaithersburg, MD). An Ag/AgCl electrode placed on the forehead served as ground.

Retinal Imaging

Eyes were dilated with 2.5% phenylephrine hydrochloride and 1% tropicamide prior to retinal imaging, which included color fundus photography (Topcon, Tokyo, Japan), fundus autofluorescence (Topcon, Tokyo, Japan), optical coherence tomography (OCT, Spectralis HRA + OCT; Heidelberg Engineering, Heidelberg, Germany), and multimodal AO ophthalmoscopy.

AO retinal imaging was performed using a previously described custom instrument (Dubra and Sulai, 2011; Scoles et al., 2014) that incorporated AO-SLO [confocal reflectance (Dubra and Sulai, 2011) and non-confocal split detection (Scoles et al., 2014)] and AO-OCT [based on spectral domain OCT (Liu Z. et al., 2018)], allowing the capture of co-registered images. The system used 790 nm light (Broadlighter S-790-G-I-15-M, Superlum, Ireland) for the AO-SLO and 1080 nm light (EXS210007-01, Exalos, Switzerland) for the AO-OCT.

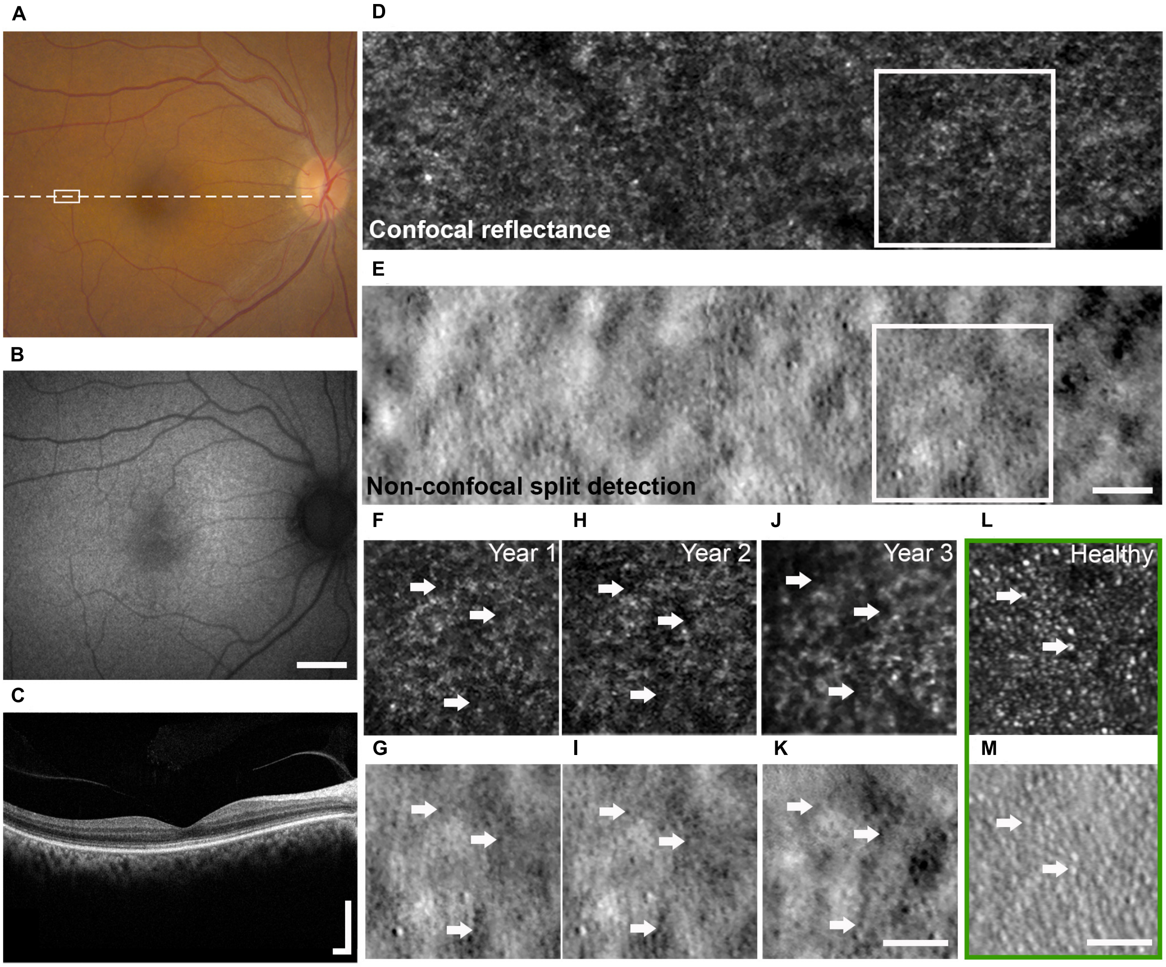

FIGURE 1 | Multimodal clinical and AO imaging of a patient with OT. Color fundus photo **(A)** and fundus autofluorescence **(B)** of the right eye at baseline visit demonstrating mottled RPE with corresponding granular changes. **(C)** OCT of the macula (dashed line in **A**) showed irregularity of the IS/OS band. See **Figure 5** for additional detail. Spatially and temporally co-registered multimodal AO-SLO from year 2 at white rectangle marked in **(A)** revealed the presence of dark cones with diminished cone reflectivity (**D**, confocal reflectance image) associated with intact cone photoreceptor inner segments (**E**, non-confocal split detection image). See **Supplementary Figure 2** for AO images from a healthy eye for comparison. Longitudinal confocal reflectance **(F,H,J)** along with co-registered non-confocal split detection **(G,I,K)** images from the region enclosed by white boxes in **(D,E)** revealed that these dark cones persisted over a period of 3 years, and the same dark cones (e.g., arrows) seen in year 1 **(F,G)** can be tracked through year 3 **(J,K)**. AO confocal reflectance and split detection images from an age-matched healthy eye at a similar retinal location (green box) show normal-appearing cones with reflective outer segments (**L**, e.g., arrows) and their corresponding inner segments (**M**, e.g., arrows). Scale bars: **(A,B)** 2 mm, **(C)** 400 μm horizontal and vertical, **(D–M)** 50 μm.

Combined, the light levels of all sources measured at the cornea were below the maximum permissible exposure limits set by the American National Standards Institute standard Z136.1-2014. During image acquisition, the subject was asked to look at a fixation target and to blink naturally. Imaging was performed at the macula and at additional locations extending to approximately 15° in the temporal direction at the initial and subsequent visits.

Cone Photoreceptor and Outer Retinal Length Measurements

Eye motion in AO-SLO images acquired at overlapping areas was corrected (Dubra and Harvey, 2010) after acquisition using one of the simultaneously acquired channels. Motion-corrected averaged AO images were assembled into a larger montage based on retinal features in areas of overlap. Longitudinal imaging datasets were manually overlaid and registered to non-AO retinal images. Retinal locations from both eyes at the fovea and at 5°, 10°, and 15° eccentricities in the temporal direction across the 3-year follow up period were compared, and analysis of cone photoreceptors was performed at these locations unless poor AO image quality did not permit the analysis to be done. At each location, cone identification was performed on non-confocal split detection images using custom-designed software (Liu J. et al., 2017, 2018), and cone spacing was measured based on the density recovery profile method (Ratnam et al., 2013). Dark cones were manually identified based on the transfer of cone locations determined in the split detection images onto the co-registered confocal reflectance images, and any detected cones that lacked reflective cores based on the confocal reflectance images were categorized as dark cones. At each eccentricity, cone spacing measurements were compared to previously published normative data, and the percentage of dark cones relative to all cones within a region was calculated.

Outer retinal length, defined as the distance between the inner segment (IS)/outer segment (OS) and retinal pigment epithelium (RPE) bands in OCT images, was measured using both commercial OCT and the custom AO-OCT at the same retinal locations where cone measurements were acquired. Commercial OCT was acquired with the B-scan oriented in both the temporal-nasal and the superior-inferior directions across the eye, and AO-OCT in the superior-inferior direction. Measurements on both types of OCT images in the superior-inferior direction were performed on individual A-scans after smoothing with a moving average filter in the lateral direction (kernel size: 6 pixels) and a Gaussian filter in the axial direction (window size: 5 pixels). Measurements were then averaged across all available A-scans within each B-scan.

RESULTS

At the time of initial evaluation, the best corrected VA of the participant was 20/32 in each eye with myopic correction. The participant had no nystagmus and her anterior segment examination was only positive for age-appropriate nuclear sclerotic and cortical cataracts. On dilated fundoscopy, she was noted to have mottled appearing RPE (**Figure 1A**), a few small drusenoid deposits, a healthy optic nerve, and a normal periphery. Fundus autofluorescence revealed granular hypo-autofluorescence in the posterior pole and OCT of the macula showed mild irregularity of the IS/OS junction (**Figures 1B,C**). Close examination of the IS/OS band in OCT suggested the presence of occasional dark gaps, which could not be explained by directionality changes due to focal elevations of the photoreceptor layer (Roorda and Williams, 2002). Over the 3-year longitudinal follow up, there were no significant clinical changes, although her cataract did progress without visual significance.

Cone-mediated photopic ERGs were unrecordable, while rod mediated scotopic dim flash (DA0.01) responses were within the normal range (RE = 175 µV; LE = 170 µV; lower limit of normal = 167 µV) (**Figure 2A**). The scotopic bright flash (DA3) ERG responses which are mediated by both rods and cones were reduced 20% below the lower limit of normal. DA3 ERGs recorded to paired flashes with reduced interstimulus intervals (<20 s) were not markedly reduced, ruling out bradyopsia. Mesopic retinal sensitivity was within the normal range ($\geq$16 dB) for 61 of the 68 loci. The remaining loci were near normal (14 dB, $N = 6$; 12 dB, $N = 1$) (**Supplementary Figure 1**). The participant had good color vision, making no errors on the Hardy-Rand-Rittler color plates and matching over a narrow range (32–38) on

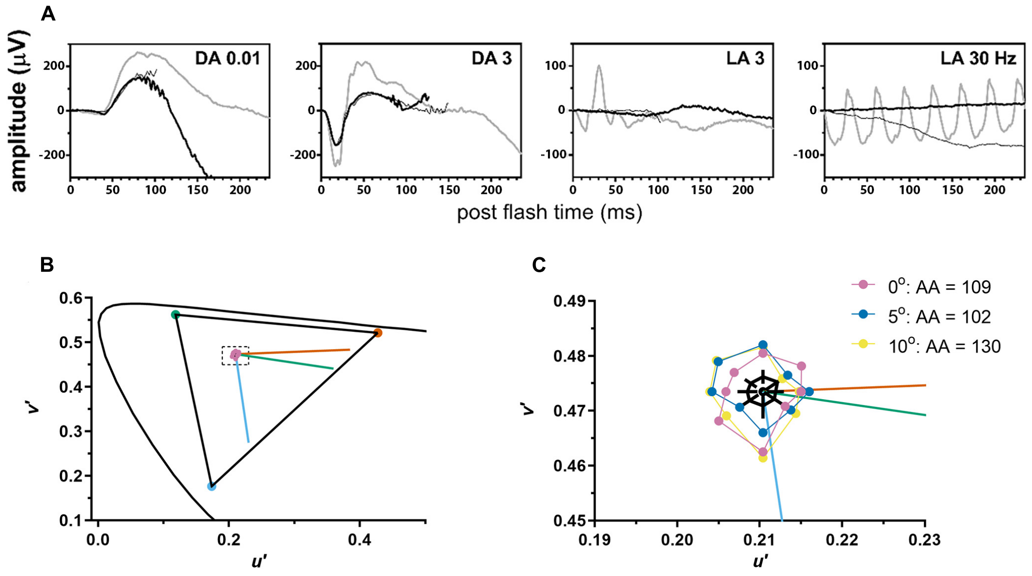

FIGURE 2 | The patient demonstrated normal to near normal retinal function. **(A)** ffERG testing highlighted unrecordable photopic responses (LA, light adapted) with normal scotopic rod-mediated responses to the dim (DA0.01) flash (DA, dark adapted). Gray waveforms: age-matched healthy control; black waveforms: each eye of the patient. **(B)** Color discrimination thresholds (purple circles) were close to the white point (center of dashed rectangle) and indistinguishable from healthy volunteers on this graph. Curved line shows CIE 1976 L*u*v* space. Triangle shows the maximum gamut that could be produced by the monitor. Vermillion, green, and blue lines indicate protan, deutan, and tritan confusion lines, respectively. **(C)** A magnified view of the area inside the dashed rectangle from **(B)**. Mean color discrimination thresholds are plotted for foveal fixation (purple) and for two retinal eccentricities [5° (blue) and 10° (yellow) along the vertical meridian from the superior retina]. For each eccentricity, achromatic area (AA) for the subject with OT was slightly above the upper limit of normal. Black polygon shows mean achromatic area for healthy volunteers and black lines indicate 95% confidence intervals at each of the 8 axes.

the Nagel anomaloscope. Achromatic area measured with LvCCT was slightly above the upper limit of normal (70). Additionally, achromatic area varied little with eccentricity, ranging from 109 for foveal fixation to 102 at 5° eccentricity and increasing slightly to 130 at 10° eccentricity (**Figures 2B,C**). Together, the fundus appearance and the functional measurements confirmed the OT phenotype.

Whole exome sequence analysis prioritized 123 SNVs and small InDels comprised of rare exonic or splice site variants. One heterozygous truncating variant NM 006205.3:c.35C > G (p.Ser12Ter) was identified in *PDE6H*, previously reported as disease-associated in homozygosity (Kohl et al., 2012; Pedurupillay et al., 2016). However, a second deleterious allele was not found. Visualization of *PDE6H* sequence reads on Integrative Genomics Viewer (IGV) did not indicate copy number of structural variations. No other deleterious variants were detected in genes associated with cone dystrophy.

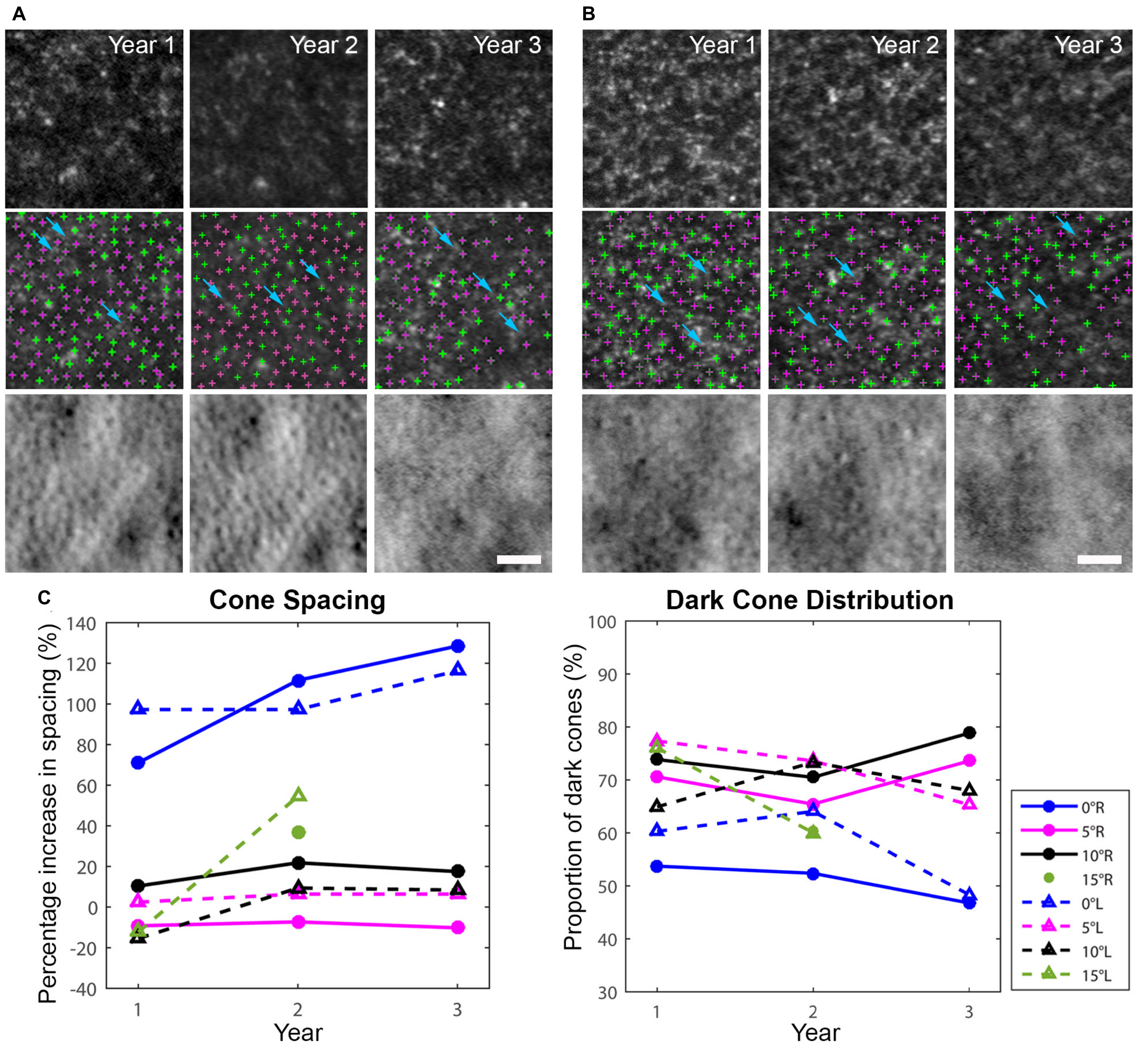

FIGURE 3 | Longitudinal AO imaging of both eyes in eccentric locations (**A:** right eye, **B:** left eye) with measurements of cone spacing and dark cone distribution. Cone spacing was measured based on the density recovery profile method. **(A,B)** Dark cones in both eyes with diminished reflectivity at 5^{o} eccentricity across three years (top row: confocal reflectance images, middle row: confocal reflectance images with identified cones overlaid: green: normally reflective cones, magenta: dark cones), bottom row: non-confocal split detection images). A decrease in image quality was observed in year 3 mostly due to cataract progression. Examples of rods surrounding the dark cones are identified by blue arrows in **(A,B)**. Scale bars: **(A,B)** 25 μm. **(C)** Increased cone spacing was observed when compared to normative data, with the largest increase observed at the fovea (blue lines), and a large population of dark cones was found at all eccentricities. R denotes right eye, L denotes left eye.

AO-SLO imaging revealed widespread dark cones intermixed with normally reflective cones in all areas imaged during the entire longitudinal study, and the high-resolution images provided by AO-SLO allowed the same dark cones to be tracked longitudinally (**Figures 1D–K**, **3A,B**). These dark cones can be readily identified by examining the co-registered confocal reflectance and non-confocal split detection AO-SLO images, which reveal the cone outer segment reflectivity and cone inner segment structure, respectively (Scoles et al., 2014). In a healthy eye, most of the cones are reflective (**Figures 1L,M** and **Supplementary Figure 2**). In contrast, in the patient with OT, there are numerous cones with diminished reflectivity (**Figures 1F,H,J**) that still retain their inner segment structure (**Figures 1G,I,K**), giving rise to the appearance of dark cones. Dark cones were most prevalent at eccentric locations, ranging from 51% at the fovea to 74% at an eccentricity of 10^o (**Figure 3**). Cone spacing measurement was performed based on identifiable cones in non-confocal split detection images (**Figures 3A,B**, third row; Ratnam et al., 2013). When compared to normative histological data (Curcio et al., 1990), the greatest increases in cone spacing were observed at the fovea, with either slight or no progression (i.e., increase in cone spacing) observed at eccentric locations over 3 years (**Figure 3C**). The large population of foveal dark cones were difficult to appreciate solely based on confocal reflectance images due to the lack of surrounding rods (**Figure 4A** left, **Figure 4C** left), but were readily visible in the matching non-confocal split detection images (**Figure 4A** right, **Figure 4C** right). In comparison, a much larger number of reflective foveal cones can be observed in a healthy eye (**Figures 4E,F**). Besides the presence of dark cones, lower than normal cone density was also observed across the retina. The highest cone density was at the fovea: 43,359 cells/mm^2, within the range of expected for OT (Michaelides et al., 2011) and noticeably lower than previously reported normal value [normal histologic value (Curcio et al., 1990): 199,200 cells/mm^2, range: 98,200–324,100 cells/mm^2]. Cone densities at 5–15° eccentricities were 20–40% lower than the normative values and decreased slightly over time. At the final AO imaging visit, the cone density was measured to be around 12,498 cells/mm^2 at 5° eccentricity [normal value (mean ± SD): 14,900 ± 800 cells/mm^2 (Song et al., 2011)], 5,802 cells/mm^2 at 10° eccentricity [normal value: 9,000 ± 900 cells/mm^2 (Song et al., 2011)], and 3,661 cells/mm^2 at 15° eccentricity [normal value: 8,290 ± 2,600 cells/mm^2 (Curcio et al., 1990; Song et al., 2011)].

There were intermittent gaps in the IS/OS band that were detectable using commercial OCT in the patient with OT (**Supplementary Figure 3**). These gaps were distributed throughout the macula and were more pronounced at eccentric locations, regardless of the meridian. There were very few gaps present in the healthy eye (**Supplementary Figure 3C**) with normally reflective cones (**Supplementary Figure 2**). Although the lack of sampling and optical resolution prevented the visualization of individual cone photoreceptors in commercial OCT images (**Figure 5A**), similar intermittent bands which increased with eccentricity were observed using AO-OCT (**Figures 5B–D**), corroborating our claim that the intermittent gaps in the IS/OS band could be associated with the presence of dark cones in the retina. These gaps are especially noticeable when compared to AO-OCT of an age-matched healthy eye at similar retinal locations (**Figures 5E–G**). Outer retinal length derived from AO-OCT images was found to range from 43.3 ± 7.0 μm at the fovea to 43.2 ± 6.7 μm at 10° in the right eye, and 42.9 ± 6.7 μm at the fovea to 46.2 ± 8.7 μm at 10° in the left eye. These were in agreement with co-registered commercial OCT images, which measured 40.9 ± 5.2 μm at the fovea to 41.4 ± 4.4 μm at 10° in the right eye, and 41.4 ± 5.9 μm at the fovea to

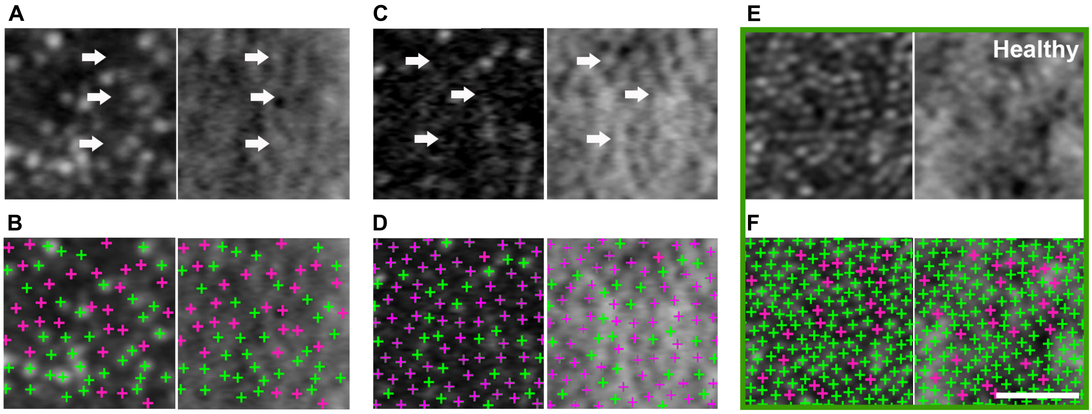

FIGURE 4 | Large population of foveal dark cones observed in both eyes (**A,B**: right eye, **C,D**: left eye). Co-registered AO confocal reflectance (**A–D**: left) and non-confocal split detection (**A–D**: right) images illustrating the presence of dark cones at the fovea, which possess intact inner segments (**A,C** right: arrows) but with diminished reflectivity (**A,C** left: arrows). Multimodal AO imaging confirms that the dark areas seen in confocal reflectance (**A,C** left: arrows) are mostly due to the presence of dark cones, which are more difficult to discern in the fovea using only a single modality (i.e., **A,C** left only) due to the lack of surrounding rods (i.e., the rods in **Figure 3A,B** make it easier to recognize dark cones). Detected cones are identified in both confocal reflectance (**B,D**: left) and non-confocal split detection (**B,D**: right) to show the differences between normally reflective cones (green crosses) and dark cones (magenta crosses). Example foveal images from an age-matched healthy eye are shown in green box, in which normally reflective cones and higher cone density can be observed **(E,F)**. Scale bar: 20 μm.

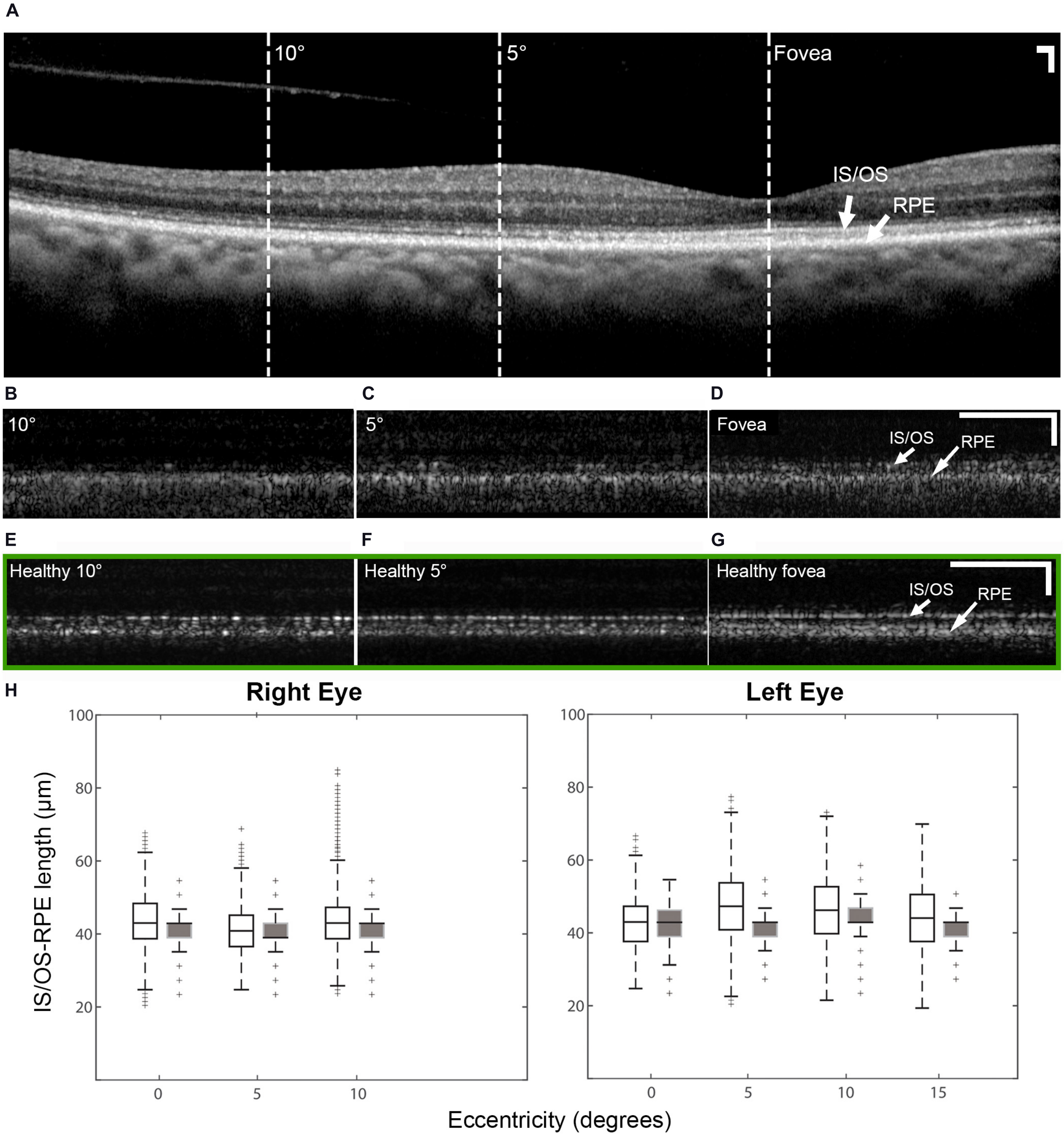

FIGURE 5 | OCT of the patient right eye with outer retinal length (distance between IS/OS band and RPE) measurements and AO-OCT of a healthy right eye. **(A)** Commercial OCT of the patient acquired with the B-scan oriented in the temporal-nasal direction across the eye. Dashed lines indicate areas at which AO-OCT scans were acquired, with the B-scans oriented in the superior-inferior direction across the eye and co-registered using simultaneously acquired multimodal AO-SLO data. AO-OCT of the patient **(B–D)** revealed dark gaps in the IS/OS band, which were more pronounced at eccentric locations **(B,C)**. These dark gaps were much less apparent in an age-matched healthy eye at similar retinal locations (green box **E–G**) Scale bars: **(A–G)** 100 μm horizontal and vertical. **(H)** Box plots showing the lengths measured on AO-OCT (unfilled boxes) and commercial OCT (filled boxes) of the patient with OT. The measurements from AO-OCT were in general agreement with those from commercial OCT.

43.2 ± 4.7 μm at 10° in the left eye (**Figure 5H**). These values were similar to measurements from both a normal subject (Liu Z. et al., 2016) and a previously reported patient with OT (Michaelides et al., 2011).

DISCUSSION

In this study we have investigated the possible relationship between partial loss of cone function and partial loss of cone structure in a patient with OT. The widespread presence of dark cones in OT is reminiscent of achromatopsia (Georgiou et al., 2020), especially in non-foveal regions in which dark cones can be readily identified due to the presence of surrounding reflective rods (**Figures 1D**, **3**). Color vision testing confirmed near-normal color vision at multiple eccentricities despite the large population of dark cones (**Figure 2B**). The preservation of some function in a retina with a majority of dark cones is consistent with reports of both non-reflective and dysflective cones, a special case of dark cones with normal function (Bruce et al., 2015; Tu et al., 2017).

PDE6H (MIM 601190) is associated with autosomal recessive congenital cone dystrophy (MIM 610024) (Kohl et al., 2012; Pedurupillay et al., 2016). While a second allele was not identified, it is conceivable that this case of OT is caused by a non-coding variant altering expression of *PDE6H*, or a variant in another congenital cone dystrophy gene acting in a digenic manner, as reported in patients with achromatopsia (Burkard et al., 2018). More recently, the advent of whole genome sequencing along with RNA-seq has been very helpful in identification of a second pathogenic allele in genes causing achromatopsia, mostly deep intronic variants causing aberrant splice events (Burkard et al., 2018; Weisschuh et al., 2020). Alternative, a previously unknown gene or transcript could harbor pathogenic variation underlying this presentation.

In both eyes, there was a decrease in foveal cone density and a 104% larger than normal cone spacing, which are consistent with a VA of 20/32 (Ratnam et al., 2013). These findings confirm an earlier report of foveal cone disruption in OT using a flood illuminated AO ophthalmoscope (Michaelides et al., 2011). With the additional information provided by multimodal AO ophthalmoscopy (Dubra and Sulai, 2011; Scoles et al., 2014; Liu Z. et al., 2018), we show that most of the observed dark areas in the foveal cone mosaic are due to foveal dark cones as indicated in **Figure 4**, which can be difficult to recognize solely based on AO confocal reflectance images since there are no surrounding reflective rods to provide context. In addition, we show that dark cones were also present beyond the foveal region with larger population in eccentric locations (**Figure 3**). Spatially and temporally co-registered AO-SLO imaging confirmed that the dark cones surrounded by reflective rods (e.g., blue arrows in **Figures 3A,B**) seen in confocal reflectance did indeed contain intact inner segments, with a small population of cones that remained normally reflective. Further comparison of co-registered retinal regions that had both AO images and microperimetry measurements revealed that areas with reduced retinal sensitivity also had increased cone spacing (**Supplementary Figures 4B,C**), which was consistent with a previous publication that showed the same inverse correlation between increased cone spacing and decreased retinal sensitivity as assessed by microperimetry (Foote et al., 2019). However, there was one location with normal retinal sensitivity (20 dB) and slightly decreased cone spacing (supernormal: 10% decrease), that also had a particularly high percentage of dark cones (82%, **Supplementary Figure 4D**). This example suggests that some of the dark cones may still contribute to retinal sensitivity. Taken together with the functional results, the data suggest that a retina with widespread stable dark cones may not have a sufficient number of functional cones to produce a global ERG photopic response, but can still provide normal to near normal color vision and retinal sensitivity from either the few remaining normally reflective cones (fewer than 50%, **Figures 3A,B**, **4**), or from the population of dark cones, or both. Despite the large population of dark cones, both commercial and AO-OCT imaging show that although the IS/OS band appeared to be disrupted (especially at eccentric locations; **Supplementary Figure 3**), outer retinal length measurements were similar to those from a healthy subject (**Figure 5**; Liu Z. et al., 2016). Additional measurements including more targeted testing would be required to evaluate the functional status of individual dark cones with regard to both sensitivity and color perception and to determine if the dark cones observed in OT are different than dark or dysflective cones observed in other situations (Sincich et al., 2009; Godara et al., 2012; Bruce et al., 2015; Cooper et al., 2017; Schmidt et al., 2019).

We show that the high-resolution images from multimodal AO ophthalmoscopy can identify the presence of dark cones in different retinal locations, which alongside clinical functional measurements help to shed light onto a situation in which cones may lose some, but not all aspects of their structure and function. In addition, the findings in this study further reveal the resiliency of cones. The absent ERG photopic response from this patient suggests that there was not sufficient numbers of cGMP gated ion channels that were closed in response to a light flash. Despite this, dark cones survived and persisted over a period of years and even in the presence of a large population of dark cones, the patient demonstrated normal visual acuity including normal color vision throughout the years. Importantly, this study adds to the growing evidence that cones can survive in harsh environment even with altered structure and function due to the disease (Elsner et al., 2020). We demonstrate the importance of including dark cones in quantitative cone metrics at the fovea and elsewhere for assessing variation in cell density in diseases to avoid potentially undercounting remaining cones. The combination of approaches to characterize the structure and function of cones may be useful for evaluating dark cones in OT and other disorders in which they have been described, illustrating the possibility that retinas with a majority of dark cones can retain much of their overall function.

DATA AVAILABILITY STATEMENT

The datasets presented in this article are not readily available because: the data are not publicly available due to their containing information that could compromise the privacy of research participants. Requests to access the datasets should be directed to JLi, johnny@nih.gov.

ETHICS STATEMENT

The studies involving human participants were reviewed and approved by the National Institutes of Health Institutional Review Board. The patients/participants provided their written informed consent to participate in this study.

AUTHOR CONTRIBUTIONS

JLi contributed to acquisition, analysis and interpretation of data, and drafting the manuscript. TL and EU contributed to acquisition, analysis and interpretation of data, and drafting the manuscript. JLiu contributed to interpretation of data and cone analysis software development. OF contributed to acquisition, analysis, and interpretation of data. AT contributed to acquisition and interpretation of data. ZL and BB contributed to interpretation of data. AD contributed to AO-SLO instrument and DeMotion image registration software development. MJ contributed to patient referral and interpretation of data. RH, LH, BJ, and JT contributed to concept and study design, acquisition, analysis and interpretation of data, and drafting the manuscript. ZL and DH contributed to custom AO-OCT instrument and software development. All authors participated in critical revision of the manuscript for important intellectual content.

FUNDING

This work was supported by the Intramural Research Program of the National Institutes of Health (NIH), National Eye Institute (NEI), as well as by NEI/NIH award nos. R01EY025231, U01EY025477, R01EY028287, and P30EY026877, and by the Research to Prevent Blindness. The content was solely the responsibility of the authors and does not necessarily represent the official views of the National Institutes of Health. The mention of commercial products, their sources, or their use in connection with material reported herein is not to be construed as either an actual or implied endorsement of such products by the U.S. Department of Health and Human Services.

ACKNOWLEDGMENTS

We would like to thank H. Jung, D. Cunningham, and G. Babilonia-Ayukawa for assistance with study procedures.

SUPPLEMENTARY MATERIAL

The Supplementary Material for this article can be found online at: https://www.frontiersin.org/articles/10.3389/fnagi.2021.629214/full#supplementary-material

REFERENCES

Bailey, J. E., Neitz, M., Tait, D. M., and Neitz, J. A. Y. (2004). Evaluation of an updated HRR color vision test. *Vis. Neurosci.* 21, 431–436. doi: 10.1017/S0952523804213463

Bruce, K. S., Harmening, W. M., Langston, B. R., Tuten, W. S., Roorda, A., and Sincich, L. C. (2015). Normal perceptual sensitivity arising from weakly reflective cone photoreceptors. *Invest. Ophthalmol. Vis. Sci.* 56, 4431–4438. doi: 10.1167/iovs.15-16547

Burkard, M., Kohl, S., Krätzig, T., Tanimoto, N., Brennenstuhl, C., Bausch, A. E., et al. (2018). Accessory heterozygous mutations in cone photoreceptor CNGA3 exacerbate CNG channel–associated retinopathy. *J. Clin. Invest.* 128, 5663–5675. doi: 10.1172/JCI96098

Cooper, R. F., Tuten, W. S., Dubra, A., Brainard, D. H., and Morgan, J. I. W. (2017). Non-invasive assessment of human cone photoreceptor function. *Biomed. Opt. Express* 8, 5098–5112. doi: 10.1364/BOE.8.005098

Cukras, C., Wiley, H. E., Jeffrey, B. G., Sen, H. N., Turriff, A., Zeng, Y., et al. (2018). Retinal AAV8-RS1 gene therapy for X-linked retinoschisis: initial findings from a Phase I/IIa trial by intravitreal delivery. *Mol. Ther.* 26, 2282–2294. doi: 10.1016/j.ymthe.2018.05.025

Curcio, C. A., Sloan, K. R., Kalina, R. E., and Hendrickson, A. E. (1990). Human photoreceptor topography. *J. Comp. Neurol.* 292, 497–523. doi: 10.1002/cne.902920402

Dubra, A., and Harvey, Z. (2010). *Registration of 2D Images from Fast Scanning Ophthalmic Instruments*. (Heidelberg: Springer), 60–71.

Dubra, A., and Sulai, Y. (2011). Reflective afocal broadband adaptive optics scanning ophthalmoscope. *Biomed. Opt. Express* 2, 1757–1768. doi: 10.1364/BOE.2.001757

Elsner, A. E., Papay, J. A., Johnston, K. D., Sawides, L., de Castro, A., King, B. J., et al. (2020). Cones in ageing and harsh environments: the neural economy hypothesis. *Ophthalmic Physiol. Opt.* 40, 88–116. doi: 10.1111/opo.12670

Foote, K. G., De la Huerta, I., Gustafson, K., Baldwin, A., Zayit-Soudry, S., Rinella, N., et al. (2019). Cone spacing correlates with retinal thickness and microperimetry in patients with inherited retinal degenerations. *Invest. Ophthalmol. Vis. Sci.* 60, 1234–1243. doi: 10.1167/iovs.18-25688

Georgiou, M., Singh, N., Kane, T., Robson, A. G., Kalitzeos, A., Hirji, N., et al. (2020). Photoreceptor structure in GNAT2-associated achromatopsia. *Invest. Ophthalmol. Vis. Sci.* 61:40. doi: 10.1167/iovs.61.3.40

Godara, P., Cooper, R. F., Sergouniotis, P. I., Diederichs, M. A., Streb, M. R., Genead, M. A., et al. (2012). Assessing retinal structure in complete congenital stationary night blindness and Oguchi disease. *Am. J. Ophthalmol.* 154, 987–1001.e1. doi: 10.1016/j.ajo.2012.06.003

Knickelbein, J. E., Jeffrey, B. G., Wei, M. M., Cheng, S. K., Kesav, N., Vitale, S., et al. (2020). Reproducibility of full-field electroretinogram measurements in birdshot chorioretinopathy patients: an intra- and inter-visit analysis. *Ocul. Immunol. Inflamm.* 1–6. doi: 10.1080/09273948.2019.1697824

Kohl, S., Coppieters, F., Meire, F., Schaich, S., Roosing, S., Brennenstuhl, C., et al. (2012). A nonsense mutation in PDE6H causes autosomal-recessive incomplete achromatopsia. *Am. J. Hum. Genet.* 91, 527–532. doi: 10.1016/j.ajhg.2012.07.006

Liu, J., Jung, H., Dubra, A., and Tam, J. (2017). Automated photoreceptor cell identification on nonconfocal adaptive optics images using multiscale circular voting. *Invest. Ophthalmol. Vis. Sci.* 58, 4477–4489. doi: 10.1167/iovs.16-21003

Liu, J., Jung, H., Dubra, A., and Tam, J. (2018). Cone photoreceptor cell segmentation and diameter measurement on adaptive optics images using circularly constrained active contour model. *Invest. Ophthalmol. Vis. Sci.* 59, 4639–4652. doi: 10.1167/iovs.18-24734

Liu, Z., Kocaoglu, O. P., and Miller, D. T. (2016). 3D imaging of retinal pigment epithelial cells in the living human retina. *Invest. Ophthalmol. Vis. Sci.* 57, OCT533–OCT543. doi: 10.1167/iovs.16-19106

Liu, Z., Tam, J., Saeedi, O., and Hammer, D. X. (2018). Trans-retinal cellular imaging with multimodal adaptive optics. *Biomed. Opt. Express* 9, 4246–4262. doi: 10.1364/BOE.9.004246

Marmor, M. F., Fulton, A. B., Holder, G. E., Miyake, Y., Brigell, M., and Bach, M. (2009). ISCEV Standard for full-field clinical electroretinography (2008 update). *Doc. Ophthalmol.* 118, 69–77. doi: 10.1007/s10633-008-9155-4

Michaelides, M., Rha, J., Dees, E. W., Baraas, R. C., Wagner-Schuman, M. L., Mollon, J. D., et al. (2011). Integrity of the cone photoreceptor mosaic in oligocone trichromacy. *Invest. Ophthalmol. Vis. Sci.* 52, 4757–4764. doi: 10.1167/iovs.10-6659

Pallikaris, A., Williams, D. R., and Hofer, H. (2003). The reflectance of single cones in the living human eye. *Invest. Ophthalmol. Vis. Sci.* 44, 4580–4592. doi: 10.1167/iovs.03-0094

Pedurupillay, C. R. J., Landsend, E. C. S., Vigeland, M. D., Ansar, M., Frengen, E., Misceo, D., et al. (2016). Segregation of incomplete achromatopsia and alopecia due to PDE6H and LPAR6 variants in a consanguineous family from pakistan. *Genes* 7:41.

Ratnam, K., Carroll, J., Porco, T. C., Duncan, J. L., and Roorda, A. (2013). Relationship between foveal cone structure and clinical measures of visual function in patients with inherited retinal degenerations. *Invest. Ophthalmol. Vis. Sci.* 54, 5836–5847. doi: 10.1167/iovs.13-12557

Roorda, A., and Williams, D. R. (2002). Optical fiber properties of individual human cones. *J. Vis.* 2:4. doi: 10.1167/2.5.4

Schmidt, B. P., Boehm, A. E., Tuten, W. S., and Roorda, A. (2019). Spatial summation of individual cones in human color vision. *PLoS One* 14:e0211397. doi: 10.1371/journal.pone.0211397

Scoles, D., Sulai, Y. N., Langlo, C. S., Fishman, G. A., Curcio, C. A., Carroll, J., et al. (2014). In vivo imaging of human cone photoreceptor inner segments. *Invest. Ophthalmol. Vis. Sci.* 55, 4244–4251. doi: 10.1167/iovs.14-14542

Simunovic, M. P., Votruba, M., Regan, B. C., and Mollon, J. D. (1998). Colour discrimination ellipses in patients with dominant optic atrophy. *Vision Res.* 38, 3413–3419. doi: 10.1016/S0042-6989(98)00094-7

Sincich, L. C., Zhang, Y., Tiruveedhula, P., Horton, J. C., and Roorda, A. (2009). Resolving single cone inputs to visual receptive fields. *Nat. Neurosci.* 12, 967–969. doi: 10.1038/nn.2352

Song, H., Chui, T. Y. P., Zhong, Z., Elsner, A. E., and Burns, S. A. (2011). Variation of cone photoreceptor packing density with retinal eccentricity and age. *Invest. Ophthalmol. Vis. Sci.* 52, 7376–7384. doi: 10.1167/iovs.11-7199

Tu, J. H., Foote, K. G., Lujan, B. J., Ratnam, K., Qin, J., Gorin, M. B., et al. (2017). Dysflective cones: visual function and cone reflectivity in long-term follow-up of acute bilateral foveolitis. *Am. J. Ophthalmol. Case Rep.* 7, 14–19. doi: 10.1016/j.ajoc.2017.04.001

van Lith, G. H. M. (1973). "General cone dysfunction without Achromatopsia," in *Xth I.S.C.E.R.G. Symposium. Documenta Ophthalmologica Proceedings Series*, ed. J. T. Pearlman (Dordrecht: Springer), 175–180.

Weisschuh, N., Sturm, M., Baumann, B., Audo, I., Ayuso, C., Bocquet, B., et al. (2020). Deep-intronic variants in CNGB3 cause achromatopsia by pseudoexon activation. *Hum. Mutat.* 41, 255–264. doi: 10.1002/humu.23920

Zein, W. M., Jeffrey, B. G., Wiley, H. E., Turriff, A. E., Tumminia, S. J., Tao, W., et al. (2014). CNGB3-achromatopsia clinical trial with CNTF: diminished rod pathway responses with no evidence of improvement in cone function. *Invest. Ophthalmol. Vis. Sci.* 55, 6301–6308. doi: 10.1167/iovs.14-14860

Conflict of Interest: ZL has a patent on adaptive optics-optical coherence tomography technology and stand to benefit financially from any commercialization of the technology.

The remaining authors declare that the research was conducted in the absence of any commercial or financial relationships that could be construed as a potential conflict of interest.

frontiers
in Aging Neuroscience

ORIGINAL RESEARCH
published: 09 September 2021
doi: 10.3389/fnagi.2021.732287

The Relationship Between Perifoveal L-Cone Isolating Visual Acuity and Cone Photoreceptor Spacing—Understanding the Transition Between Healthy Aging and Early AMD

Rigmor C. Baraas*†, Åshild Horjen, Stuart J. Gilson and Hilde R. Pedersen†

Faculty of Health and Social Sciences, National Centre for Optics, Vision and Eye Care, University of South-Eastern Norway, Kongsberg, Norway

Background: Age-related macular degeneration (AMD) is a multifactorial degenerative disorder that can lead to irreversible loss of visual function, with aging being the prime risk factor. However, knowledge about the transition between healthy aging and early AMD is limited. We aimed to examine the relationship between psychophysical measures of perifoveal L-cone acuity and cone photoreceptor structure in healthy aging and early AMD.

Methods and Results: Thirty-nine healthy participants, 10 with early AMD and 29 healthy controls were included in the study. Multimodal high-resolution retinal images were obtained with adaptive-optics scanning-light ophthalmoscopy (AOSLO), optical-coherence tomography (OCT), and color fundus photographs. At 5 degrees retinal eccentricity, perifoveal L-cone isolating letter acuity was measured with psychophysics, cone inner segment and outer segment lengths were measured using OCT, while cone density, spacing, and mosaic regularity were measured using AOSLO. The Nyquist sampling limit of cone mosaic (N_C) was calculated for each participant. Both L-cone acuity and photoreceptor inner segment length declined with age, but there was no association between cone density nor outer segment length and age. A multiple regression showed that 56% of the variation in log L-cone acuity was accounted for by N_C when age was taken into account. Six AMD participants with low risk of progression were well within confidence limits, while two with medium-to-severe risk of progression were outliers. The observable difference in cone structure between healthy aging and early AMD was a significant shortening of cone outer segments.

Conclusion: The results underscore the resilience of cone structure with age, with perifoveal functional changes preceding detectable changes in the cone photoreceptor mosaic. L-cone acuity is a sensitive measure for assessing age-related decline in this region. The transition between healthy aging of cone structures and changes in cone structures secondary to early AMD relates to outer segment shortening.

Keywords: age-related macular degeneration, isolated L-cone acuity, cone density, aging, outer segment length, inner segment length, cone spacing

Edited by:
Ann E. Elsner,
Indiana University, United States

Reviewed by:
Adam M. Dubis,
University College London,
United Kingdom
Henri Leinonen,
University of California, Irvine,
United States

Correspondence:
Rigmor C. Baraas
rigmor.baraas@usn.no

†These authors have contributed equally to this work and share first authorship

Received: *28 June 2021*
Accepted: *11 August 2021*
Published: *09 September 2021*

Citation:
Baraas RC, Horjen Å, Gilson SJ and Pedersen HR (2021) The Relationship Between Perifoveal L-Cone Isolating Visual Acuity and Cone Photoreceptor Spacing—Understanding the Transition Between Healthy Aging and Early AMD. Front. Aging Neurosci. 13:732287. doi: 10.3389/fnagi.2021.732287

INTRODUCTION

Age-related macular degeneration (AMD) is a multifactorial, chronic disease that progresses through early, intermediate, and late stages (Wong et al., 2014; NICE guideline [NG82], 2018). AMD has a very long asymptomatic phase, typically spanning more than a decade, before the disease produces symptomatic visual loss. The earliest recognizable lesion in humans *in vivo* is the deposition of drusen between the retinal pigment epithelium (RPE) and Bruch's membrane (Mullins et al., 2000; Pedersen et al., 2018), but symptomatic visual loss may not occur before photoreceptors start to degenerate. Rods appear to be more vulnerable to aging than cones, and their function and structure degenerates earlier in AMD (Schuman et al., 2009). Cone inner segments (IS) and outer segments (OS) shorten as AMD progresses (Johnson et al., 2003), with cone IS shortening being associated with shrinking (Litts et al., 2015a) and translocation of mitochondria (Litts et al., 2015b). The neural economy hypothesis (Elsner et al., 2020) argues that cones can survive for longer because of this shortening and/or because of less photopigment allowing for a more economical configuration.

The resilience of the cones (Curcio et al., 1993) is a factor that limits our understanding of the transition between healthy retinal cone function in aging and early AMD (Curcio et al., 2020). This lack of understanding is compounded by most studies being cross-sectional in design, where the small effect size expected for a given individual is likely to be dwarfed by inter-individual variability. For example, individual differences in cone density are large, even in young, healthy eyes (Li and Roorda, 2007; Dees et al., 2011; Song et al., 2011; Zhang et al., 2015; Elsner et al., 2017; Pedersen et al., 2019). Refractive errors, such as myopia affect cone distribution (Chui et al., 2008; Wang et al., 2019) and are associated with myopic macular degeneration (Fricke et al., 2018). Another problem is the frequency of comorbidities in the elderly (e.g., Hoogendijk et al., 2016), which can affect retinal health and function in both controls and AMD participants alike. Cones, however, appear to be resilient in healthy retinal aging—any possible senescent loss of cone photoreceptors is too small to be distinguishable from the large inter-individual differences in cone density (Curcio et al., 1993; Dees et al., 2011; Song et al., 2011; Chui et al., 2012; Land et al., 2014). There is one report of shortening of cone outer and inner segments in healthy aging (Elsner et al., 2020), as well as a reported decline in mitochondrial membrane potential and cellular energy in cone IS (Eells, 2019). In parallel, it is well known that there is a senescent decline, that begins in young adulthood, in spatio-chromatic contrast sensitivity (Dees et al., 2015) and other measures of chromatic sensitivity (Knoblauch et al., 2001; Shinomori et al., 2016). Furthermore, L-cone isolating (spatio-chromatic) acuity has been reported to correlate with cone density (Baraas et al., 2017). As such, L-cone isolating acuity could reveal subtle functional changes in aging, while any corresponding loss of cones would remain difficult to quantify. Together, these findings indicate that functional changes precede structural changes in cones in healthy retinal aging, but both factors have never been assessed in the same individual nor in both healthy aging and early AMD. We hypothesized that measures of L-cone isolating acuity would depend on an individual's cone density and deteriorate with increasing age but precede observable changes in cone density. Furthermore, because of the reported shortening of cone OS/IS in AMD (Johnson et al., 2003), the functional deterioration would be more pronounced in early AMD.

We examined the association between spatio-chromatic acuity, cone density, cone spacing, and age in the same individuals, who had either healthy eyes and retinas, or retinas with signs of early AMD. Healthy controls from young adulthood to old age were included to show the baseline senescent functional decline, and how early-AMD functional loss cannot be explained by this decline alone. The retina was imaged with optical-coherence tomography (OCT) and adaptive-optics scanning-light ophthalmoscopy (AOSLO) to assess both cone outer and inner segment length and cone density. We chose to isolate L-cone function, as L cones are typically more abundant than M cones in the retina of Caucasians (Hagen et al., 2019), and L-cone acuity (but not M-cone acuity) has been reported to correlate with cone density in healthy young adults (Baraas et al., 2017). L cones also have the type of mitochondrial activity associated with IS shortening observed in AMD (Litts et al., 2015a,b), and are the cones that appear to survive the longest in advanced AMD (Curcio et al., 1996). L-cone function is also less affected by age-related changes in the crystalline lens (Dees et al., 2015). Measurements were obtained at 5 degrees eccentricity, where inter-individual variability is less of an issue (Dees et al., 2011; Song et al., 2011; Zhang et al., 2015). This would also circumvent factors that may make the fovea less sensitive to functional changes, such as the redundancy of cones in the foveal center (Dees et al., 2011; Bensinger et al., 2019), and that the central foveal cones are somewhat protected by Müller glia cells and macular pigment (Curcio et al., 2020).

MATERIALS AND METHODS

Participants and Baseline Measurements

In total, 39 males and females, all Caucasian background, were included in this cross-sectional study. Ten individuals (aged 61–78 years), exhibiting signs of early AMD as classified by NICE NG82 (2018), were included in the early AMD group. Twenty-nine were included in the healthy control group (aged 15–70 years). The broad age range in the control group was necessary to measure the expected baseline senescent decline in spatio-chromatic acuity (Dees et al., 2015); to observe that spatio-chromatic acuity correlates with cone density (Baraas et al., 2017) across the large inter-individual variation in cone density (Dees et al., 2011; Song et al., 2011; Zhang et al., 2015; Elsner et al., 2017); and that cone density was expected to be minimally affected by age (Curcio et al., 1993; Dees et al., 2011; Song et al., 2011; Chui et al., 2012; Land et al., 2014).

All participants were healthy with no known ocular pathology (other than AMD for those in the AMD group), and no former intraocular or refractive surgery and/or systemic diseases. All had corrected-to-normal logMAR visual acuity (early AMD group: −0.14 to 0.3; control group: −0.20 to 0.0, TestChart

2000, Thomson Software Solutions, London, United Kingdom). Ocular pathology was assessed with slit-lamp biomicroscopy, fovea-centered digital 45-degrees color fundus photographs (Topcon TRC-NW6S non-mydriatic fundus camera, Topcon Corp., Tokyo, Japan) and high-resolution OCT (Heidelberg Spectralis OCT2, Heidelberg Engineering GmbH, Germany). Grading of small hard drusen was performed as described previously (Pedersen et al., 2018). Axial length, corneal curvature, anterior chamber depth, and central corneal thickness were measured with the IOLMaster 700 (Carl Zeiss Meditec AG, Jena, Germany). All had normal color vision except one (5503) who had a known deutan deficiency, as screened with the Ishihara (24 pl. ed., Kanehara Trading INC, Tokyo, Japan, printed 2005) and the Hardy-Rand-Rittler 4th edition (Richmond Products, Albuquerque, NM) tests. All tests were performed following standard procedures. The initial assessment took about one hour for each participant.

Ethics Statement

The study was approved by the Regional Committee for Medical Research Ethics for the Southern Norway Regional Health Authority and was carried out in accordance with the principles in the Declaration of Helsinki. Informed consent was obtained from all the participants included in the study after full explanation of the study procedures.

OCT Imaging

High-resolution OCT images were acquired with the Heidelberg Spectralis OCT2 (30 × 5 degrees volume; 49 horizontal B-scans; 1536 A-scans per B-scan; 20 frames averaged). The registered and averaged OCT images were scaled for each participant's individual retinal magnification ratio using the Gullstrand four-surface schematic eye model (Wang et al., 2019). The retinal layers were segmented using a semi-automatic active contour method, as described previously (Pedersen et al., 2020). After segmenting the inner boundary of the inner limiting membrane (ILM), successive layers were then segmented at the center of the external limiting membrane (ELM), ellipsoid zone (EZ), and interdigitation zone (IZ), and the posterior boundary of the RPE-Bruch's Membrane (RPE-BrM) band. The foveal center was defined as the section with maximum outer segment length (EZ to IZ) and minimum foveal thickness (ILM to RPE-BrM) within the foveal pit. The B-scan that passed through the defined foveal center was used for analysis. Retinal thickness, outer segment (OS) and inner segment (IS) length measures were extracted over a 0.5 degree region centered on 5 degrees eccentricity (for details see **Figures 1B,C**).

Adaptive Optics Scanning Light Ophthalmoscope Imaging

High-resolution confocal images were acquired with the Kongsberg AOSLO instrument using the 790-nm light channel (Pedersen et al., 2018). The participant's pupil was dilated, and accommodation suspended by instillation of cyclopentolate 1% (those aged < 30 years) or Tropicamide 0.5% eye drops prior to imaging. A dental impression on a bite bar stabilized the head and provided stable pupil positioning during imaging. The macular region was imaged from 0–6 degrees eccentricity along the horizontal meridian. Images were acquired simultaneously using 1 × 1 degree fields of view and were processed according to previously published methods (Li and Roorda, 2007; Dubra and Harvey, 2010; Cooper et al., 2016). The registered and averaged AOSLO images were scaled for each participant's retinal magnification ratio in the same way as the OCT images. The processed images were stitched together into a mosaic aligned to the corresponding infrared en-face image acquired simultaneously with the OCT B-scans (Pedersen et al., 2019). The foveal center was identified anatomically on images as described previously (Pedersen et al., 2019). Individual cones were identified via a semi-automatic algorithm (Li and Roorda, 2007; Garrioch et al., 2012). Manual cone selections were made when some were too dim to be detected automatically, based on the assumption that foveal cones are packed into a nearly hexagonal mosaic, using the non-confocal (split detector) images to disambiguate cones from rods. After manual editing, inter- and intra-cell statistics were obtained from the Voronoi tessellation of these cells including, notably, the mean number of neighbors and the mean inter-cell distance (ICD). ICD was used to calculate the Nyquist sampling limit of the cone photoreceptor mosaic (N_c), where $N_c = \frac{\sqrt{3}}{2} \times ICD$. Cone density was estimated over six 50 × 50 μm sampling windows at 5 degrees temporal eccentricity. The percentage of 5-, 6-, or 7-sided Voronoi cell neighbors was calculated to characterize the regularity of the photoreceptor mosaic.

Perifoveal L-Cone Isolating Single Letter Visual Acuity

Eight in the AMD group (aged 61–78) and fourteen of the healthy controls (aged 24–70 years) also performed the psychophysical tests (L-cone acuity). L-cone isolated spatial acuity was measured with a tumbling Sloan E letter of 23% increment cone contrast as described elsewhere (Baraas et al., 2017). Briefly, the background was always 10 cd/m^2 with chromaticity metameric to CIE illuminant D65 and the CIE (x, y, Y)-coordinate of the L-cone isolating Sloan E stimulus at 23% was (0.385, 0.316, 11.5). The stimuli were displayed on a calibrated 22-inch CRT monitor (ViewSonic P227f, ViewSonic Corporation, Walnut, CA, United States). The participants were placed comfortably in a chin- and forehead-rest and viewed the display monocularly, with their preferred eye, using appropriate refractive correction for the given viewing distance of 229.2 cm. The experiment was carried out in an otherwise darkened room. Prior to each experiment, the participants were dark adapted for 3 min, then light adapted for 1 min by viewing a neutral gray screen with the same color and luminance as the background of the stimuli. A four-alternative forced-choice procedure was implemented, and the size of the Sloan E was altered using an adaptive procedure (Kontsevich and Tyler, 1999; Prins and Kingdom, 2018), and analyzed as described previously (Baraas et al., 2017). The participant's task was to maintain fixation on a black cross that appeared at the side of the display, while the Sloan E was presented at 5 degrees temporal eccentricity for 250 ms. The

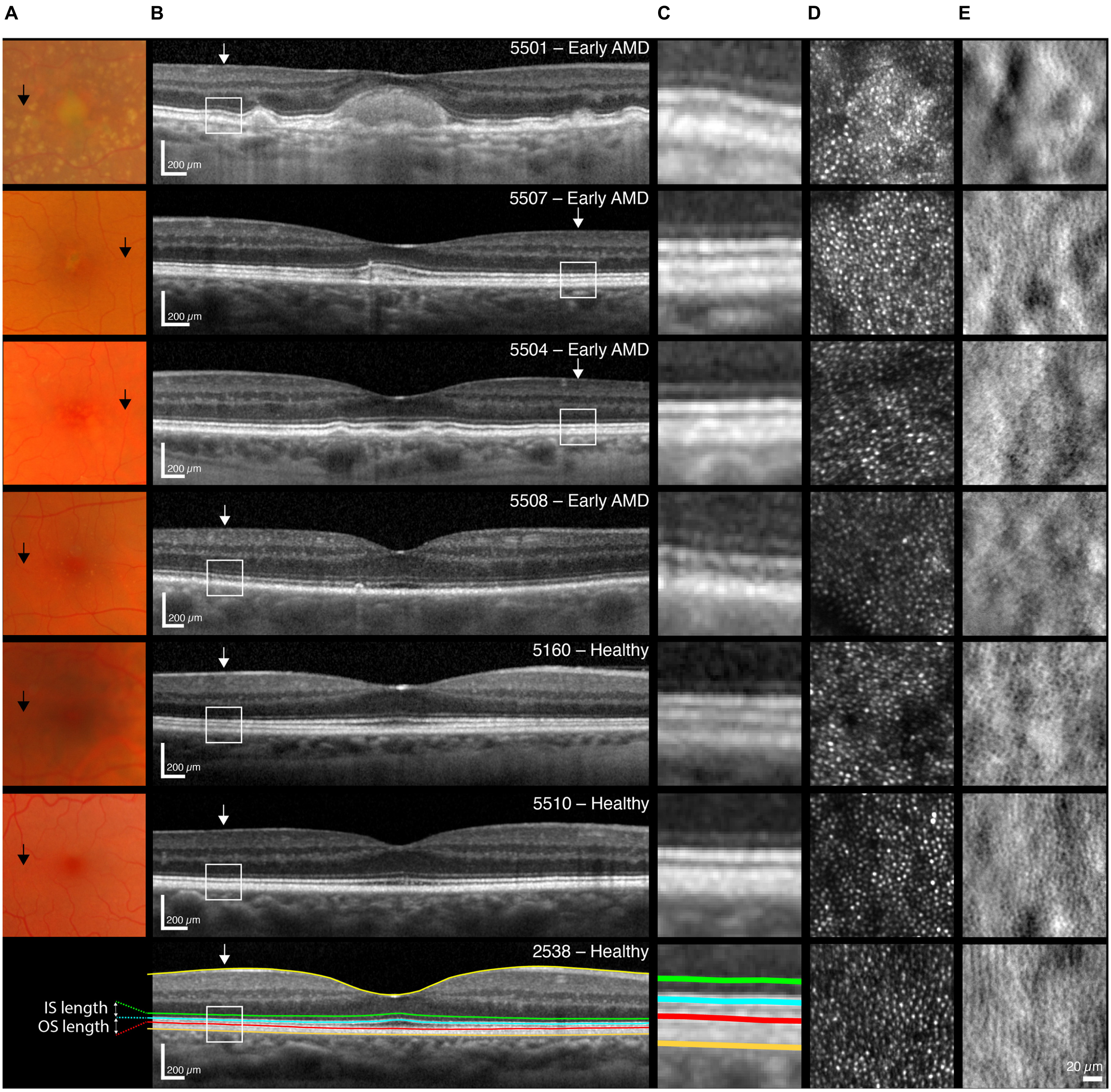

FIGURE 1 | Multimodal images of one participant with early AMD and high-risk of progression (5501, top row), followed by one with medium risk (5507) and two with low-risk (5504, 5508); as well as three normal controls [5160 (68 years), 5510 (65 years), 2538 (35 years)]. **(A)** Color fundus photos of the central 14 degree of the macula. Black arrows indicate 5 degree temporal eccentricity. **(B)** Horizontal SD-OCT scan through the foveal center of the central ±7 degree including an illustration of the segmented inner limiting membrane (ILM, yellow line), the external limiting membrane (ELM, green line), the inner/outer segment junction also referred to as the inner segment ellipsoid zone (EZ, blue line), the cone outer segment tips also referred to as the interdigitation zone (IZ, red line) and the retinal pigment epithelium—Bruch's membrane layer (RPE-BrM, orange line). The inner segment (distance from ELM to EZ) and outer segment (distance from EZ to IZ) lengths were extracted and used for analyses. White arrows indicate 5 degree temporal eccentricity. Scale bars = 200 μm. **(C)** A magnification of a one-degree area centered at 5 degree eccentricity, delineated by white boxes in B. Images from 5501 had visible drusen in this area and showed marked thickening in the RPE layer. None of the other participants with early AMD showed any apparent retinal changes within this area. **(D)** Raw confocal and **(E)** split-detection images showing reflection from cone outer segments and multiple-scatter image of cone inner segments at 5 degree eccentricity (temporal). Images are 150 × 150 μm or approximately 0.52 × 0.52 degree, scale bar = 20 μm.

participant indicated whether the Sloan E was oriented up, down, left, or right by pushing the corresponding response button. Failure to maintain fixation was automatically detected by the software and the trial re-tested with a different orientation of the Sloan E. Fixation was verified with an eye tracker, which monitored direction of gaze 120 times per second (ASL Eye

Tracking System Model 5000, Applied Science Laboratories, Bedford, MA, United States).

Data Analysis

All data analyses were performed with the statistical software R, version 4.0.5 (R Core Team, 2021). Mean, standard deviation, median, range, and Z-scores were calculated for descriptive analysis.

Welch's 2-sample *t*-test (adjusts degrees of freedom to account for variance differences between the samples) were used for comparisons between participants with early AMD and healthy controls, as the data approached a normal distribution (as assessed by QQ-plots, Shapiro-Wilk test, and histograms). The homogeneity of the variances across groups was assessed using the F-test. Correlations were assessed using Pearson (r) coefficients. Multiple linear regressions were performed to assess the relationship between log N_c and L-cone logMAR at 5 degrees eccentricity with age as a covariate. Significance level was set at 0.05. For retinas exhibiting signs of early AMD, cones at 5 degrees eccentricity were semi-automatically identified twice, 6 weeks apart, by one experienced grader (author HRP). The intraclass correlation coefficient (ICC) were calculated for 50 pairs of perifoveal cone density measurements using the **irr** package (version 0.84.1) in R.

RESULTS

Clinical Characteristics

Tables 1, **2** show the clinical characteristics of all AMD participants and healthy controls, respectively. Presence of drusen and their size and texture were assessed within 2 disk diameters of fovea. Of those with AMD, three had metamorphopsia (5500, 5501, and 5503) when assessed with Amsler chart. None had lens nuclear opacity more than NO 2 according to LOCS III (Chylack et al., 1993). None had cortical or posterior subcapsular opacities. All the AMD participants had early AMD, 6 with low risk and 4 with medium-to-high risk of progression according to NICE NG82. The grading encompasses the observed changes in the fovea in these participants (see **Supplementary Material** for OCT B-scans with a more detailed description than that provided in **Table 1**). A qualitative assessment of the fundus and OCT images showed no apparent retinal changes around 5 degrees eccentricity in any of the AMD participants, except participant 5501 who had small and medium drusen in this area (see **Figure 1**, top row). Five of the AMD participants had a disrupted inner segment ellipsoid zone (EZ) (also called inner/outer segmented junction) over one or more drusen at other macular locations. Those with AMD were 61 years or older, whereas eight healthy controls were 50 years or older. None of the controls had metamorphopsia when tested with Amsler chart, nor any gradable lens opacities. None of the healthy controls had any sign of retinal diseases, although eight had 1–3 small hard drusen which are normal age-related changes. One participant with a known color deficiency (5503) failed both pseudoisochromatic plate tests, while the others—in both the AMD and the control group—made 2 or fewer errors, as would be expected of normal trichromats. All participants demonstrated stable central fixation on both OCT and AOSLO.

IS/OS Thickness Measures From OCT Imaging

Figures 1A,B shows fundus images and horizontal SD-OCT scan through the foveal center of the central ±7 degrees for four representative participants with early AMD and three age-matched healthy controls. OCT images with sufficient quality for analysis were obtained from 10 with AMD and 29 healthy controls. There was a significant correlation between age and photoreceptor inner segment length, but not between age and

TABLE 1 | Clinical characteristics of the 10 participants with early AMD presenting age, sex, eye tested, spherical equivalent refractive error (SER), ocular axial length (AL), logMAR visual acuity, frequency of drusen, drusen size and type, the presence of disrupted ellipsoid zone (EZ), pigmentary changes, and clinical classification of AMD according to NICE NG 82 (NICE guideline [NG82], 2018).

ID	Age	Sex	Eye tested	SER	AL	VA	# of drusen	Size*	Type	Disrupted EZ	Pigment changes	OS length	IS length	Classification
5508	61	M	OD	−1.25	26.33	−0.14	15–20	S–M	Hard	Yes	No	21.11	29.01	Early: low risk
5506	72	M	OS	+1.00	23.34	−0.10	20–25	S–M	Both	Yes	No	24.46	27.07	Early: low risk
5503[§]	77	M	OD	+0.10	23.64	0.10	10–15	S–M	Hard	No	No	24.35	24.09	Early: low risk
5502	78	F	OD	+1.41	23.52	0.16	5–10	S–M	Both	No	No	24.98	24.81	Early: low risk
5204	71	F	OS	−0.13	24.24	−0.10	5–10	M	Soft	No	No	22.73	19.35	Early: low risk
5504	61	M	OS	−1.53	24.41	−0.10	15–20	M	Both	No	No	20.85	28.12	Early: low risk
5505	67	F	OS	−4.50	26.05	0.10	25–30	S–L	Both	Yes	No	22.25	23.70	Early: medium risk
5500[§]	66	M	OS	−1.13	24.49	0.10	5–10	S–M	Soft	Yes	Yes	19.75	25.91	Early: medium risk
5507	68	F	OS	+3.00	21.29	0.02	5–10	M	Soft	No	Yes	22.29	27.29	Early: medium risk
5501[§]	77	M	OD	+3.32	23.13	0.30	55–60	M–L	Both	Yes	Yes	21.41	23.51	Early: high risk
Mean (SD)	**70 (6)**			**0.03 (2.32)**	**24.04 (1.45)**	**0.03 (0.14)**						**22.42 (1.73)**	**25.29 (2.83)**	

Participants are sorted according to AMD severity (rightmost column).

**S, Small drusen ≤63 μm; M, medium drusen >63 μm and ≤125 μm; L, large drusen >125 μm.*

[§] *Metamorphopsia when tested with Amsler chart. Mean (SD) are in bold.*

TABLE 2 | As **Table 1** but for the 29 normal controls.

ID	Age	Sex	Eye tested	SER	AL	VA	# of drusen	Size*	Type	OS length	IS length	Classification
5181	15	F	OS	+1.67	22.44	−0.10	0			22.09	28.61	No changes
5188	15	F	OD	+0.83	23.98	−0.10	0			22.27	30.97	No changes
5159	16	F	OS	+5.18	20.63	0.02	0			17.47	29.23	No changes
5170	20	M	OD	+0.38	24.07	−0.16	0			23.76	27.78	No changes
5171	20	M	OD	−2.70	24.98	−0.20	0			24.06	27.69	No changes
5007	21	F	OS	−2.50	25.10	0.00	2	S	Hard	24.23	26.27	Normal changes
5166	21	F	OD	−2.05	24.76	−0.14	0			21.79	28.30	No changes
5169	21	F	OD	+0.19	23.53	−0.14	0			21.04	30.62	No changes
5176	21	F	OD	+0.12	22.67	−0.22	0			25.55	31.55	No changes
8323	22	F	OD	−2.70	24.95	−0.10	0			23.46	26.37	No changes
8340	24	F	OD	+0.17	22.86	−0.06	0			30.89	29.08	No changes
4017	28	M	OS	+0.88	24.01	−0.10	1			23.22	25.16	No changes
5194	33	F	OS	+1.21	22.90	−0.10	0			25.25	27.98	No changes
5197	34	F	OD	+0.45	24.03	−0.10	1	S	Hard	23.48	27.15	Normal changes
2538	35	M	OD	−4.25	24.20	−0.18	0			23.95	26.35	No changes
5165	35	F	OD	+0.12	21.63	0.00	0			24.56	26.89	No changes
4078	37	F	OD	−3.50	23.36	−0.18	0			23.88	30.31	No changes
4064	45	M	OD	+0.75	23.70	−0.10	1	S	Hard	22.46	30.33	Normal changes
4571	47	F	OS	+1.38	22.14	−0.20	0			26.64	26.69	No changes
5196	48	F	OD	−0.08	23.32	−0.10	3	S	Hard	27.87	22.75	Normal aging changes
4027	49	F	OD	+0.10	24.13	−0.10	1	S	Hard	23.21	24.84	Normal aging changes
5205	50	M	OD	−1.68	24.55	−0.08	0			27.08	27.97	No changes
5156	53	F	OD	+1.21	22.20	0.00	2	S	Hard	22.27	25.14	Normal changes
5163	56	M	OD	+0.13	23.45	−0.08	0			28.66	26.04	No changes
4049	60	M	OD	−0.63	24.26	−0.08	0			23.39	25.23	No changes
5510	65	F	OD	0.50	22.59	−0.10	2	S	Hard	26.67	25.51	Normal changes
5160	68	M	OD	−0.50	23.98	−0.08	1	S	Hard	21.69	24.60	Normal changes
5509	69	F	OS	2.25	22.89	−0.20	0			27.02	26.36	No changes
5185	70	M	OD	0.75	23.80	−0.10	0			24.89	28.70	No changes
Mean (SD)	**38 (18)**			**−0.08 (1.90)**	**23.49 (1.06)**	**−0.11 (0.06)**				**24.23 (2.65)**	**27.40 (2.15)**	

None of the normal controls had disrupted ellipsoide zone (EZ) or any pigmentary changes related to clinical classification of AMD according to NICE NG 82. Participants are sorted according to age. Mean (SD) are in bold.

photoreceptor outer segment length at 5 degrees eccentricity [for healthy controls only $r = -0.51$ (95% CI: −0.74 to −0.18), $p = 0.005$ and $r = 0.34$ (−0.03 to 0.63), $p = 0.071$, respectively, $n = 29$; for all $r = -0.57$ (−0.75 to −0.31), $p = 0.0002$ and $r = 0.043$ (−0.50 to 0.12), $p = 0.79$, respectively, $n = 39$). There was a significant difference in OS length at 5 degrees eccentricity between early AMD and healthy controls aged 50 years and older [−2.8 (−5.08 to −0.49) μm, $t_{(11.9)} = -2.65$, $p = 0.0213$]. There was no significant difference in IS length between early AMD and healthy controls aged 50 years and older [−0.90 (−3.12 to 1.30) μm, $t_{(13.9)} = -0.88$, $p = 0.39$].

Cone Density and Spacing From AOSLO Cone Photoreceptor Imaging

Figures 1D,E shows multimodal AOSLO images of cones at 5 degrees temporal eccentricity for four representative participants with early AMD and three healthy controls (two of whom were age-matched with the AMD group). AOSLO images with sufficient quality for analysis were obtained from 9 with AMD and 28 healthy controls. The mean ± SD (full range) difference in perifoveal cone counts for the AMD data set was 130 ± 719 (−1,278 to 1,797) cones/mm^2, and excellent intra-grader repeatability was observed, ICC (95% CI) 0.967 (0.942–0.981). **Table 3**, right part, shows the participants' cone density and inter-cone distance (ICD) measurements at 5 degrees temporal eccentricity. Cone spacing is also presented as Nyquist sampling limit (N$_c$) based on ICD. There was no correlation between age and cone density [for healthy controls only $r = -0.16$ (95% CI. −0.50 to 0.23), $p = 0.43$, $n = 28$; for all $r = -0.21$ (−0.50 to 0.12), $p = 0.21$, $n = 37$]. There was no difference in cone density between the groups [−1,312 (−3,289 to 656) cones/mm^2, $t_{(13.1)} = -1.43$, $p = 0.17$], with all participants with AMD (12,829–20,473 cones/mm^2) having cone density within the normal range (12,248–22,163 cones/mm^2) at 5 degrees eccentricity. In terms of cone mosaic regularity, the mean ± SD percentage of cells with six neighbors was 48.6 ± 4.6% and 53.1 ± 5.8%, for the AMD group

TABLE 3 | Results from perifoveal L-cone isolated Sloan-E letter acuity measured, cone photoreceptor imaging, inter-cone distance (ICD), and Nyquist sampling limit (N_c) at 5 degree eccentricity.

ID	Age	L-cone Sloan-E (logMAR)	Linear cone density (cones/mm^2)	ICD (µm)	N_c (arcmin)
5508	61	0.67	15,142	9.02	1.45
5506	72	0.72	18,066	8.23	1.51
5503	77	0.71	20,473	7.77	1.43
5502	78	0.84	NA	NA	NA
5204	71	0.75	14,828	9.03	1.62
5504	61	0.66	15,180	8.98	1.56
5505	67	0.87	14,215	9.24	1.48
5500	66	NA	12,829	9.73	1.67
5507	68	NA	18,293	8.18	1.70
5501	77	0.90	17,243	8.41	1.58
Mean (SD)	69.8 (6.3)	0.77 (0.09)	16,252 (2,412)	8.73 (0.62)	1.56 (0.10)
8340	24	0.62	17,387	8.35	1.60
4017	28	0.59	18,498	8.11	1.46
5194	33	0.67	16,138	8.69	1.66
2538	35	0.69	16,056	8.70	1.51
5165	35	0.71	18,718	8.06	1.63
4078	37	0.51	20,228	7.79	1.41
4064	45	0.54	20,179	7.78	1.40
4571	47	0.65	16,489	8.58	1.70
4027	49	0.67	14,484	9.18	1.64
5163	56	0.70	20,239	7.72	1.42
4049	60	0.72	16,505	8.60	1.52
5510	65	0.76	19,711	7.86	1.55
5160	68	0.65	18,613	8.08	1.44
5509	69	NA	16,841	8.54	1.51
5185	70	0.74	16,326	8.64	1.56
Mean (SD)	48.1 (15.8)	0.66 (0.07)	17,761 (1,824)	8.31 (0.43)	1.53 (0.10)

AMD participants (top 10 rows) are sorted according to AMD severity (see ***Table 1****), whereas healthy controls (bottom 15 rows) are sorted according to age.*

and control group, respectively, while the mean percentage of cells with five-, six-, or seven-neighbors was 94.9 ± 2.0% and 96.9 ± 1.9%. The AMD group had significantly lower percentage of cones with 6 neighbors and 5–7 neighbors than the healthy controls at 5 degrees eccentricity [−6.5 (−8.4 to −0.5)%, $t_{(17)} = -2.39$, $p = 0.029$ and −2.0 (−3.6 to 0.4)%, $t_{(12.9)} = -2.72$, $p = 0.0176$, respectively].

Perifoveal L-Cone Isolating Single Letter Acuity From Psychophysics

Figure 2A shows an illustration of the Sloan-E stimulus used for measuring L-cone isolating acuity at 5 degrees eccentricity. **Table 3**, middle part, shows the results from measures of perifoveal L-cone isolating Sloan-E acuity for those who performed the test, 8 with early AMD and 14 healthy controls. One elderly healthy control and two with AMD did not complete the experiment because of problems with handling the response box. The participant with a deutan color deficiency (5503) was included, because their deficiency mainly affects the M-cone photopigment, not L-cone. **Figure 2B** shows L-cone acuity as a function of age for these 22 participants. L-cone acuity was poorer with increasing age [$r = 0.679$ (95% CI: 0.36–0.86), $p = 0.0005$, $n = 22$]. There was a significant difference between healthy controls aged under- and over-50 years [$t_{(11.6)} = 2.93$, $p = 0.013$], with the older age group having poorer L-cone acuity (mean ± SD 0.716 ± 0.04) than the younger age group (0.628 ± 0.07). Perifoveal L-cone acuity did not correlate with axial length or spherical refractive error, neither for AMD nor for healthy controls. The difference in perifoveal L-cone acuity between all eight participants with AMD and healthy controls aged 50 years and older was not significant [0.05 (−0.03 to 0.13), $t_{(10.6)} = 1.33$, $p = 0.21$]. Nevertheless, the two participants who had the most severe form of early AMD (5501, 5505) had poorer L-cone acuity than that expected from age alone, with values outside the 95% confidence interval of the regression line (**Figure 2B**).

Relationship Between L-Cone logMAR, log N_c, and Age

Figure 3A show a linear relationship between perifoveal log L-cone visual acuity and log cone Nyquist sampling limit (N_c). The data for the healthy controls are best explained by fitting two regression lines, one each for those aged younger or older than 50 years, respectively [$R^2 = 0.72$, $F_{(2,11)} = 17.33$, $p = 0.0004$]. The acuities of those with early AMD and low risk of progression overlap with the healthy controls. However, the two with early AMD and medium-to-high risk of progression (5501, 5505) had considerably poorer L-cone acuity than that expected based on their N_c. Because L-cone logMAR is associated with N_c as well as with age, a multiple regression was performed to assess if perifoveal log L-cone acuity could be predicted from log N_c with age as a covariate, both for the healthy controls alone and for controls together with early AMD participants. A significant regression was found with log N_c predicting L-cone acuity both for the healthy controls [$R^2 = 0.57$, $F_{(2,11)} = 7.171$, $p = 0.01$, $n = 14$] and for controls and early AMD [$R^2 = 0.56$, $F_{(2,18)} = 11.48$, $p = 0.0006$, $n = 22$] when taking age into account. A linear model in which group (control vs. AMD) was included as a separate factor did not fit the data better than one in which no group variable was included [Likelihood Ratio Test: $F_{(1,17)} = 0.514$, $p = 0.48$]. The two participants (5501, 5505) who had poorer L-cone acuity than expected from their Nyquist sampling limit and age, when considered separately, appeared as outliers in the diagnostic plots. Fitting the data with these two participants excluded had no effect on the significance tests nor on the interpretation of the results. The predicted regression models based on healthy controls are visualized in **Figure 3B**, which show a parallel shift in N_c-dependent L-cone acuity with healthy aging.

DISCUSSION

We have shown that there is an age-related decline in perifoveal L-cone function, a decline that begins in young adulthood without any observable changes in cone density and spacing, supporting the main hypothesis. The decline in L-cone function

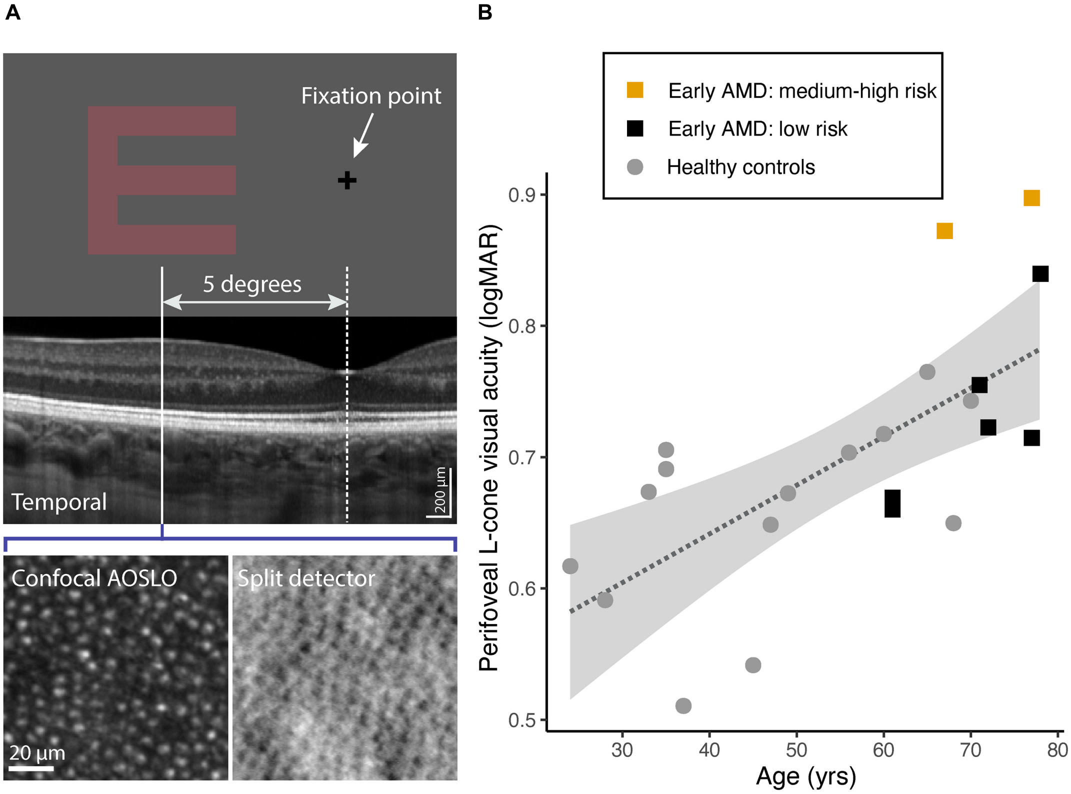

FIGURE 2 | (A) The L-cone isolating Sloan E presented at 5 degree temporal eccentricity. SD-OCT, confocal and spit-detection AOSLO images were analyzed at the corresponding retinal location. **(B)** L-cone logMAR as a function of age: 14 healthy controls (gray filled circles) and 8 participants with early AMD: 6 with low risk of progression (black filled squares) and 2 with medium or high risk of progression (orange filled squares). The dashed line shows the best-fit linear regression to the data. The gray shaded area indicates the 95% confidence intervals for the fitted regression line.

was greater in those with early AMD and preceded any changes in cone density or spacing. This functional decline parallels inner segment shortening in healthy eyes, whilst it parallels inner and outer segment shortening in early AMD. This was the case in those with low or medium risk of progression even in areas without visible changes in RPE/Bruch's membrane. There was no age-related change in photoreceptor OS length in healthy controls, as previously reported (Elsner et al., 2020). In addition, photopigment optical density in OS of perifoveal L and M cones has been reported to increase, not decrease, with age (Renner et al., 2004). As the loss of function in healthy controls cannot be explained by loss of cones or changes of OS length, the most parsimonious explanation is that it is related to IS shortening. Thus, it may be that the combined effect of normal age-related IS shortening and the OS shortening associated with early AMD together explain the significant loss of L-cone function observed in those with early AMD and medium-to-high risk of progression. This indicates that the transition between healthy aging and early AMD appears to be mainly related to structural changes in outer segment length at 5 degrees eccentricity.

There was no age-related change and no difference between early AMD and healthy controls in cone density and spacing at 5 degrees eccentricity. This is consistent with that reported from histology (Curcio et al., 1993, 1996) and *in vivo* imaging (Song et al., 2011; Chui et al., 2012; Land et al., 2014). There are reports of changes in cone density and spacing over small hard drusen in healthy adults (Pedersen et al., 2018), and in more severe forms of early AMD (Land et al., 2014). Here, only mosaic regularity differences indicated structural changes related to cone photoreceptors in early AMD, possibly because the areas assessed had no visible changes in RPE/Bruch's membrane. The observed regularity disruptions in those with early AMD are likely related to rod degeneration as this is known to precede any cone degeneration in AMD (Curcio et al., 1996). When rods die off during healthy aging, the space is filled in by larger rod inner segments leaving the mosaic intact (Curcio et al., 1993).

In a normal human trichromat, L cones are typically twice as numerous as M cones (with S cones making up less than 10% of the total number) and so cone spacing alone would not be expected to fully explain L-cone acuity. Both cone spacing (expressed as Nyquist sampling limit) and age, were significant predictors of log L-cone acuity measured at 5 degrees eccentricity, but cone spacing alone did not correlate with L-cone acuity in early AMD. Note that 5505, who also has an abnormally long axial length and is myopic, has a Nyquist sampling limit that lies roughly in the middle of the distribution (**Figure 3A**, left most orange filled square) but has an L-cone acuity that is still poorer than that expected from her age alone. Healthy controls older

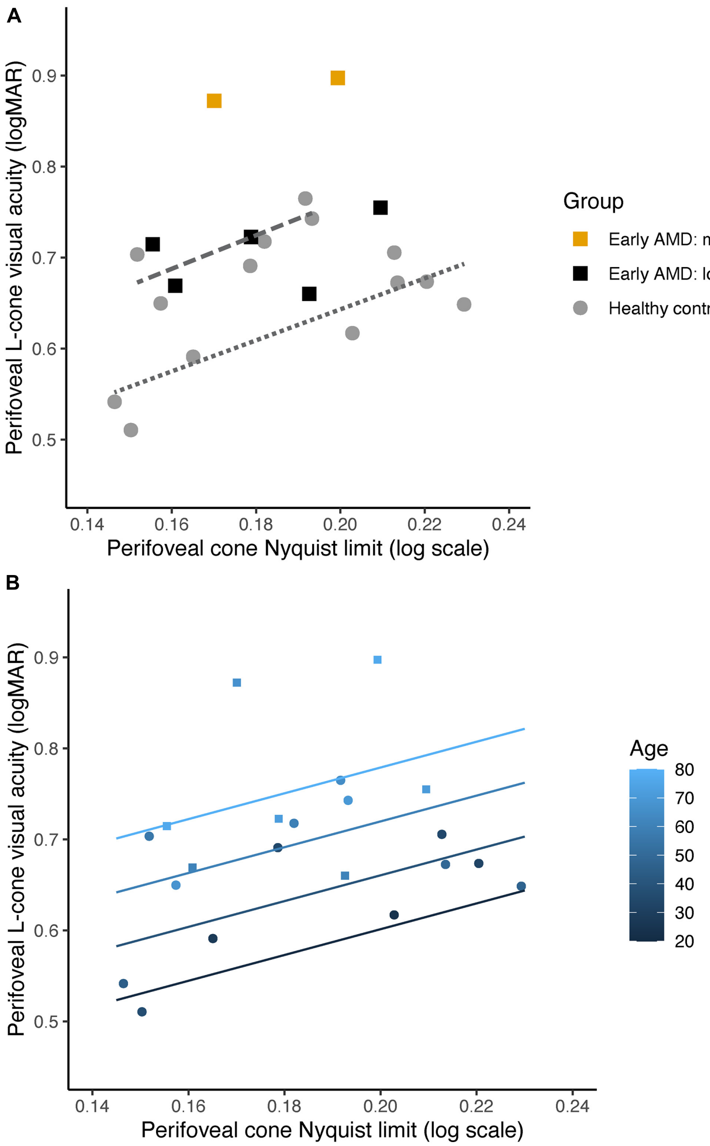

FIGURE 3 | (A) Perifoveal L-cone visual acuity as a function of cone Nyquist sampling limit (N_c) for 14 healthy controls (gray filled circles) and 7 participants with early AMD: 6 with low risk of progression (black filled squares) and 2 with medium or high risk of progression (orange filled squares). Note that data from 5502 is not included in this figure, as we did not obtain AOSLO images of sufficient quality for analysis. Regression lines for log N_c and L-cone acuity for the healthy controls aged 50 years and older (dashed line) and younger than 50 years (dotted line), respectively. **(B)** Predicted regression models for perifoveal L-cone visual acuity as a function of N_c at 20, 40, 60, and 80 years of age for healthy controls (filled circles), color coded from dark blue (youngest) to light blue (oldest). Data for the participants with early AMD are also shown (filled squares).

than 50 have poorer L-cone acuity but retain a Nyquist sampling limit within the same range as those younger than 50. Similarly, the regression models imply (**Figure 3B**) that function, even in healthy aging, deteriorates with age while cone spacing appears to remain stable. Both the observed photoreceptor IS shortening with healthy aging, and OS shortening in AMD without any evidence of age-related changes in number of cones, are in line with the neural economy hypothesis—that cones adapt to survive in "harsh conditions" (Elsner et al., 2020). The photoreceptor IS shortening at 5 degrees eccentricity reported here relates to shortening of both rod and cone inner segments and appears to be a normal aging process, perhaps to uphold some degree of functionality.

Photoreceptor inner segments are rich in mitochondria (Hoang et al., 2002), and mitochondrial function, in general, declines with aging as well as contributing to an increase in the generation of reactive oxygen species (Lopez-Otin et al., 2013). Alterations to the IZ band and IS shortening within 3–4 degrees of eccentricity have previously been reported to be associated with decreased cone function in patients with early AMD (Wu et al., 2013) and with mitochondrial dysfunction (Fritsche et al., 2008). It is reasonable to attribute loss of

L-cone function with decline in mitochondrial function, as mitochondria contribute to IS optical properties (Hoang et al., 2002). However, it cannot be ascertained whether the observed decline in photoreceptor IS length in early AMD can be attributed to normal age-related mitochondrial changes only, before cone OS degenerates in later stages of AMD (Mitamura et al., 2013). Degeneration of cone OS in AMD has been reported to contribute to further shrinking and translocation of mitochondria (Litts et al., 2015a,b). Previous studies have also shown that OS are the first to be affected in both degenerating rods and cones in areas over drusen (Zhang et al., 2014). The results here show that there are observable OS changes in early AMD even in areas where there are no visible changes in the RPE/Bruch's membrane (**Figure 1**). This adds to the body of evidence that AMD is a global retinal phenomenon, not a local one. From OCT images, however, we cannot disentangle the differences between rods and cones, except that the ratio of rods to cones within the perifovea is reported to be 9:1 in younger vs. 6:1 in older adults (Curcio and Allen, 1990).

Strengths and Limitations

A major strength of this study was that it was the first to examine both isolated L-cone functional and photoreceptor structural measures in the same individuals, both in healthy aging and early AMD. Such cross-sectional measures of structure and function may be considered a limitation because they do not have single cell resolution (Duncan and Roorda, 2019), but the robustness of the results indicates that they may have larger clinical utility. Perifoveal L-cone acuity is, potentially, an easy-to-use clinical measure. Our data provides new motivation for investigating sensitive functional measures combined with multimodal imaging to advance the understanding of the transition between healthy aging and early AMD. As seen from OCT images, the differences in OS length and associated vision loss between healthy aging and early AMD in structurally intact parts of the retina may be a very sensitive indicator for risk of progression and potentially a way to monitor treatment success. Measures of isolated L-cone acuity may be particularly useful for measuring cone function, as it is mainly red and green cones that survive without OS in advanced AMD (Curcio et al., 1996).

A limitation of this study was the small number of participants with early AMD and few age-matched controls. The study only included Caucasians, and from an age range that did not include anyone older than 70 (healthy controls) and 78 (early AMD) years old, potentially limiting the generalizability of our results. Despite this limitation, the observed continuous age-related decline in L-cone acuity from young adulthood is the same as that observed for other measures of chromatic sensitivity (Knoblauch et al., 2001; Dees et al., 2015; Shinomori et al., 2016). Furthermore, the inclusion of the more elderly low-risk AMD participants helps to emphasize the differences from those with the more severe form of early AMD.

For the L-cone acuity measures, a technical limitation arose that the response-box buttons were too small for three of the elderly participants, preventing them from reliably providing the correct response within the time limit. For the AOSLO instrument, the eldest participant was unable to maintain a stable tear film, which prevented us from acquiring usable images. A limitation of the OCT imaging was the inability to distinguish rods from cones, in terms of OS and IS lengths, at 5 degrees eccentricity. Additionally, the IZ sometimes appeared diminished and indistinguishable from the reflection from the RPE (see for example 5508 in **Figure 1B**). In these cases, the IZ was segmented at the inner boundary of the RPE reflection, which could overestimate the OS length measurement slightly. Even with this possible over-estimation, OS length in early AMD participants remained shorter than those in controls.

CONCLUSION

We demonstrate that perifoveal L-cone acuity is a sensitive measure for assessing age-related decline in cone function and is more readily detectable than cone photoreceptor mosaic changes. This lends strong support to the neural economy hypothesis (Elsner et al., 2020). The results indicate that the transition between healthy aging of cone structures and changes due to early AMD relates to OS shortening, but more data is needed to understand to what degree OS and IS shortening contribute to the observed decline in L-cone function in early AMD. Vulnerability to loss of cone function secondary to early AMD may very well depend on the cone-richness of the individual's macula. In addition, a healthy lifestyle may delay normal age-related mitochondrial changes in rods and cones (Kaarniranta et al., 2020), delaying the normal age-related shrinking of cone inner segments, preserving cone function for longer.

DATA AVAILABILITY STATEMENT

The original contributions presented in the study are included in the article/**Supplementary Material**, further inquiries can be directed to the corresponding author/s.

ETHICS STATEMENT

The studies involving human participants were reviewed and approved by the Regional Committee for Medical Research Ethics for the Southern Norway Regional Health Authority. Written informed consent to participate in this study was provided by the participants' legal guardian/next of kin.

AUTHOR CONTRIBUTIONS

RB: conceptualization, formal analysis, supervision, funding acquisition, validation, investigation, visualization, methodology, writing—original draft, project administration, and writing—review and editing. ÅH: data acquisition, formal analysis, investigation, and writing—review and editing. SG: software, data curation, formal analysis, investigation, visualization, writing—original draft, and writing—review and editing. HP:

data acquisition and curation, formal analysis, supervision, investigation, visualization, writing—original draft, and writing—review and editing. All authors contributed to the article and approved the submitted version.

FUNDING

The study was funded by the University of South-Eastern Norway and Norwegian Research Council Regional Research Funds: the Oslofjord Fund Grant No. 268696.

ACKNOWLEDGMENTS

We would like to thank K. Knoblauch for his assistance with discussions about analyses.

SUPPLEMENTARY MATERIAL

The Supplementary Material for this article can be found online at: https://www.frontiersin.org/articles/10.3389/fnagi.2021.732287/full#supplementary-material

REFERENCES

Baraas, R. C., Gjelle, J. V., Finstad, E. B., Jacobsen, S. B., and Gilson, S. J. (2017). The relationship between perifoveal achromatic, L- and M-cone acuity and retinal structure as assessed with multimodal high resolution imaging. *Vision. Res.* 132, 45–52. doi: 10.1016/j.visres.2016.06.005

Bensinger, E., Rinella, N., Saud, A., Loumou, P., Ratnam, K., Griffin, S., et al. (2019). Loss of foveal cone structure precedes loss of visual acuity in patients with rod-cone degeneration. *Invest. Ophthalmol. Vis. Sci.* 60, 3187–3196. doi: 10.1167/iovs.18-26245

Chui, T. Y., Song, H., and Burns, S. A. (2008). Individual variations in human cone photoreceptor packing density: variations with refractive error. *Invest. Ophthalmol. Vis. Sci.* 49, 4679–4687. doi: 10.1167/iovs.08-2135

Chui, T. Y., Song, H., Clark, C. A., Papay, J. A., Burns, S. A., and Elsner, A. E. (2012). Cone photoreceptor packing density and the outer nuclear layer thickness in healthy subjects. *Invest. Ophthalmol. Vis. Sci.* 53, 3545–3553. doi: 10.1167/iovs.11-8694

Chylack, L. T. Jr., Wolfe, J. K., Singer, D. M., Leske, M. C., Bullimore, M. A., Bailey, I. L., et al. (1993). The Lens Opacities Classification System III. The Longitudinal Study of Cataract Study Group. *Arch. Ophthalmol.* 111, 831–836.

Cooper, R. F., Wilk, M. A., Tarima, S., and Carroll, J. (2016). Evaluating descriptive metrics of the human cone mosaic. *Invest. Ophthalmol. Vis. Sci.* 57, 2992–3001. doi: 10.1167/iovs.16-19072

Curcio, C. A., and Allen, K. A. (1990). Topography of ganglion cells in human retina. *J. Comp. Neurol.* 300, 5–25. doi: 10.1002/cne.903000103

Curcio, C. A., McGwin, G. Jr., Sadda, S. R., Hu, Z., Clark, M. E., Sloan, K. R., et al. (2020). Functionally validated imaging endpoints in the Alabama study on early age-related macular degeneration 2 (ALSTAR2): design and methods. *BMC Ophthalmol.* 20:196. doi: 10.1186/s12886-020-01467-0

Curcio, C. A., Medeiros, N. E., and Millican, C. L. (1996). Photoreceptor loss in age-related macular degeneration. *Invest. Ophthalmol. Vis. Sci.* 37, 1236–1249.

Curcio, C. A., Millican, C. L., Allen, K. A., and Kalina, R. E. (1993). Aging of the human photoreceptor mosaic: evidence for selective vulnerability of rods in central retina. *Invest. Ophthalmol. Vis. Sci.* 34, 3278–3296.

Dees, E. W., Dubra, A., and Baraas, R. C. (2011). Variability in parafoveal cone mosaic in normal trichromatic individuals. *Biomed. Opt. Express* 2, 1351–1358. doi: 10.1364/BOE.2.001351

Dees, E. W., Gilson, S. J., Neitz, M., and Baraas, R. C. (2015). The influence of L-opsin gene polymorphisms and neural ageing on spatio-chromatic contrast sensitivity in 20-71 year olds. *Vision Res.* 116, 13–24. doi: 10.1016/j.visres.2015.08.015

Dubra, A., and Harvey, Z. (2010). "Registration of 2D images from fast scanning ophthalmic instruments," in *Biomedical Image Registration*, eds B. Fischer, B. M. Dawant, and C. Lorenz (Berlin Heidelberg: Springer), 60–71.

Duncan, J. L., and Roorda, A. (2019). Dysflective cones. *Adv. Exp. Med. Biol.* 1185, 133–137. doi: 10.1007/978-3-030-27378-1_22

Eells, J. T. (2019). Mitochondrial dysfunction in the aging retina. *Biology* 8:31. doi: 10.3390/biology8020031

Elsner, A. E., Chui, T. Y., Feng, L., Song, H. X., Papay, J. A., and Burns, S. A. (2017). Distribution differences of macular cones measured by AOSLO: variation in slope from fovea to periphery more pronounced than differences in total cones. *Vision Res.* 132, 62–68. doi: 10.1016/j.visres.2016.06.015

Elsner, A. E., Papay, J. A., Johnston, K. D., Sawides, L., de Castro, A., King, B. J., et al. (2020). Cones in ageing and harsh environments: the neural economy hypothesis. *Ophthalmic Physiol. Opt.* 40, 88–116. doi: 10.1111/opo.12670

Fricke, T. R., Jong, M., Naidoo, K. S., Sankaridurg, P., Naduvilath, T. J., Ho, S. M., et al. (2018). Global prevalence of visual impairment associated with myopic macular degeneration and temporal trends from 2000 through 2050: systematic review, meta-analysis and modelling. *Br. J. Ophthalmol.* 102, 855–862. doi: 10.1136/bjophthalmol-2017-311266

Fritsche, L. G., Loenhardt, T., Janssen, A., Fisher, S. A., Rivera, A., Keilhauer, C. N., et al. (2008). Age-related macular degeneration is associated with an unstable ARMS2 (LOC387715) mRNA. *Nat. Genet.* 40, 892–896. doi: 10.1038/ng.170

Garrioch, R., Langlo, C., Dubis, A. M., Cooper, R. F., Dubra, A., and Carroll, J. (2012). Repeatability of in vivo parafoveal cone density and spacing measurements. *Optom. Vis. Sci.* 89, 632–643. doi: 10.1097/OPX.0b013e3182540562

Hagen, L. A., Arnegard, S., Kuchenbecker, J. A., Gilson, S. J., Neitz, M., Neitz, J., et al. (2019). The association between L:M cone ratio, cone opsin genes and myopia susceptibility. *Vision Res.* 162, 20–28. doi: 10.1016/j.visres.2019.06.006

Hoang, Q. V., Linsenmeier, R. A., Chung, C. K., and Curcio, C. A. (2002). Photoreceptor inner segments in monkey and human retina: mitochondrial density, optics, and regional variation. *Vis. Neurosci.* 19, 395–407. doi: 10.1017/s0952523802194028

Hoogendijk, E. O., Deeg, D. J., Poppelaars, J., van der Horst, M., Broese van Groenou, M. I., Comijs, H. C., et al. (2016). The Longitudinal Aging Study Amsterdam: cohort update 2016 and major findings. *Eur. J. Epidemiol.* 31, 927–945. doi: 10.1007/s10654-016-0192-0

Johnson, P. T., Lewis, G. P., Talaga, K. C., Brown, M. N., Kappel, P. J., Fisher, S. K., et al. (2003). Drusen-associated degeneration in the retina. *Invest. Ophthalmol. Vis. Sci.* 44, 4481–4488. doi: 10.1167/iovs.03-0436

Kaarniranta, K., Uusitalo, H., Blasiak, J., Felszeghy, S., Kannan, R., Kauppinen, A., et al. (2020). Mechanisms of mitochondrial dysfunction and their impact on age-related macular degeneration. *Prog. Retin. Eye Res.* 79:100858. doi: 10.1016/j.preteyeres.2020.100858

Knoblauch, K., Vital-Durand, F., and Barbur, J. L. (2001). Variation of chromatic sensitivity across the life span. *Vision Res.* 41, 23–36. doi: 10.1016/s0042-6989(00)00205-4

Kontsevich, L. L., and Tyler, C. W. (1999). Bayesian adaptive estimation of psychometric slope and threshold. *Vision Res.* 39, 2729–2737. doi: 10.1016/s0042-6989(98)00285-5

Land, M. E., Cooper, R. F., Young, J., Berg, E., Kitchner, T., Xiang, Q., et al. (2014). Cone structure in subjects with known genetic relative risk for AMD. *Optom. Vis. Sci.* 91, 939–949. doi: 10.1097/OPX.0000000000000323

Li, K. Y., and Roorda, A. (2007). Automated identification of cone photoreceptors in adaptive optics retinal images. *J. Opt. Soc. Am. A Opt. Image Sci. Vis.* 24, 1358–1363.

Litts, K. M., Messinger, J. D., Dellatorre, K., Yannuzzi, L. A., Freund, K. B., and Curcio, C. A. (2015a). Clinicopathological correlation of outer retinal tubulation in age-related macular degeneration. *JAMA Ophthalmol.* 133, 609–612. doi: 10.1001/jamaophthalmol.2015.126

Litts, K. M., Messinger, J. D., Freund, K. B., Zhang, Y., and Curcio, C. A. (2015b). Inner segment remodeling and mitochondrial translocation in cone photoreceptors in age-related macular degeneration with outer retinal tubulation. *Invest. Ophthalmol. Vis. Sci.* 56, 2243–2253. doi: 10.1167/iovs.14-15838

Lopez-Otin, C., Blasco, M. A., Partridge, L., Serrano, M., and Kroemer, G. (2013). The hallmarks of aging. *Cell* 153, 1194–1217. doi: 10.1016/j.cell.2013.05.039

Mitamura, Y., Mitamura-Aizawa, S., Katome, T., Naito, T., Hagiwara, A., Kumagai, K., et al. (2013). Photoreceptor impairment and restoration on optical coherence tomographic image. *J. Ophthalmol.* 2013:518170. doi: 10.1155/2013/518170

Mullins, R. F., Russell, S. R., Anderson, D. H., and Hageman, G. S. (2000). Drusen associated with aging and age-related macular degeneration contain proteins common to extracellular deposits associated with atherosclerosis, elastosis, amyloidosis, and dense deposit disease. *FASEB J.* 14, 835–846.

NICE guideline [NG82]. (2018). *Age-related macular degeneration*. Available online at: https://www.nice.org.uk/guidance/ng82 [accessed May 24, 2021].

Pedersen, H. R., Baraas, R. C., Landsend, E. C. S., Utheim, O. A., Utheim, T. P., Gilson, S. J., et al. (2020). PAX6 genotypic and retinal phenotypic characterization in congenital aniridia. *Invest. Ophthalmol. Vis. Sci.* 61:14. doi: 10.1167/iovs.61.5.14

Pedersen, H. R., Gilson, S. J., Dubra, A., Munch, I. C., Larsen, M., and Baraas, R. C. (2018). Multimodal imaging of small hard retinal drusen in young healthy adults. *Br. J. Ophthalmol.* 102, 146–152. doi: 10.1136/bjophthalmol-2017-310719

Pedersen, H. R., Neitz, M., Gilson, S. J., Landsend, E. C. S., Utheim, O. A., Utheim, T. P., et al. (2019). The cone photoreceptor mosaic in aniridia: within-family phenotype-genotype discordance. *Ophthalmol. Retina* 3, 523–534. doi: 10.1016/j.oret.2019.01.020

Prins, N., and Kingdom, F. A. A. (2018). Applying the model-comparison approach to test specific research hypotheses in psychophysical research using the palamedes toolbox. *Front. Psychol.* 9:1250. doi: 10.3389/fpsyg.2018.01250

R Core Team. (2021). *R: A Language and Environment for Statistical Computing*. Vienna, Austria: R Foundation for Statistical Computing.

Renner, A. B., Knau, H., Neitz, M., Neitz, J., and Werner, J. S. (2004). Photopigment optical density of the human foveola and a paradoxical senescent increase outside the fovea. *Vis. Neurosci.* 21, 827–834. doi: 10.1017/S0952523804216030

Schuman, S. G., Koreishi, A. F., Farsiu, S., Jung, S. H., Izatt, J. A., and Toth, C. A. (2009). Photoreceptor layer thinning over drusen in eyes with age-related macular degeneration imaged in vivo with spectral-domain optical coherence tomography. *Ophthalmology* 116, 488–496.e2. doi: 10.1016/j.ophtha.2008.10.006

Shinomori, K., Panorgias, A., and Werner, J. S. (2016). Discrimination thresholds of normal and anomalous trichromats: model of senescent changes in ocular media density on the Cambridge Colour Test. *J. Opt. Soc. Am. A Opt. Image Sci. Vis.* 33, A65–A76. doi: 10.1364/JOSAA.33.000A65

Song, H., Chui, T. Y., Zhong, Z., Elsner, A. E., and Burns, S. A. (2011). Variation of cone photoreceptor packing density with retinal eccentricity and age. *Invest. Ophthalmol. Vis. Sci.* 52, 7376–7384. doi: 10.1167/iovs.11-7199

Wang, Y., Bensaid, N., Tiruveedhula, P., Ma, J., Ravikumar, S., and Roorda, A. (2019). Human foveal cone photoreceptor topography and its dependence on eye length. *eLife* 8:e47148. doi: 10.7554/eLife.47148

Wong, W. L., Su, X., Li, X., Cheung, C. M., Klein, R., Cheng, C. Y., et al. (2014). Global prevalence of age-related macular degeneration and disease burden projection for 2020 and 2040: a systematic review and meta-analysis. *Lancet Glob. Health* 2, e106–e116. doi: 10.1016/S2214-109X(13)70145-1

Wu, Z., Ayton, L. N., Guymer, R. H., and Luu, C. D. (2013). Relationship between the second reflective band on optical coherence tomography and multifocal electroretinography in age-related macular degeneration. *Invest. Ophthalmol. Vis. Sci.* 54, 2800–2806. doi: 10.1167/iovs.13-11613

Zhang, T., Godara, P., Blanco, E. R., Griffin, R. L., Wang, X., Curcio, C. A., et al. (2015). Variability in human cone topography assessed by adaptive optics scanning laser ophthalmoscopy. *Am. J. Ophthalmol.* 160, 290–300.e1. doi: 10.1016/j.ajo.2015.04.034

Zhang, Y., Wang, X., Rivero, E. B., Clark, M. E., Witherspoon, C. D., Spaide, R. F., et al. (2014). Photoreceptor perturbation around subretinal drusenoid deposits as revealed by adaptive optics scanning laser ophthalmoscopy. *Am. J. Ophthalmol.* 158, 584–596.e1. doi: 10.1016/j.ajo.2014.05.038

Conflict of Interest: The authors declare that the research was conducted in the absence of any commercial or financial relationships that could be construed as a potential conflict of interest.

ORIGINAL RESEARCH
published: 07 October 2021
doi: 10.3389/fnins.2021.729807

Structural and Functional Characteristics of Color Vision Changes in Choroideremia

Jasleen K. Jolly[1,2,3]*, Matthew P. Simunovic[4,5], Adam M. Dubis[6], Amandeep S. Josan[1,2], Anthony G. Robson[7,8], Marco P. Bellini[1], Edward Bloch[6], Odysseas Georgiadis[6], Lyndon da Cruz[6], Holly Bridge[3] and Robert E. MacLaren[1,2]

[1] Nuffield Laboratory of Ophthalmology, Nuffield Department of Clinical Neurosciences, University of Oxford, Oxford, United Kingdom, [2] Oxford Eye Hospital and NIHR Oxford Biomedical Research Centre, Oxford University Hospitals NHS Foundation Trust, Oxford, United Kingdom, [3] Oxford Centre for Functional MRI of the Brain (FMRIB), Wellcome Centre for Integrative Neuroimaging, University of Oxford, Oxford, United Kingdom, [4] Save Sight Institute, Discipline of Ophthalmology, University of Sydney, Sydney, NSW, Australia, [5] Retinal Unit Sydney Eye Hospital, Sydney, NSW, Australia, [6] NIHR Biomedical Resource Centre at Moorfields Eye Hospital and UCL Institute of Ophthalmology, London, United Kingdom, [7] Electrophysiology Department, Moorfields Eye Hospital, London, United Kingdom, [8] University College London Institute of Ophthalmology, London, United Kingdom

OPEN ACCESS

Edited by:
Jan Kremers,
University Hospital Erlangen, Germany

Reviewed by:
Wolf Harmening,
University Hospital Bonn, Germany
Mirella Barboni,
Semmelweis University, Hungary

***Correspondence:**
Jasleen K. Jolly
enquiries@eye.ox.ac.uk

Specialty section:
This article was submitted to Perception Science, a section of the journal Frontiers in Neuroscience

Received: *24 June 2021*
Accepted: *08 September 2021*
Published: *07 October 2021*

Citation:
Jolly JK, Simunovic MP, Dubis AM, Josan AS, Robson AG, Bellini MP, Bloch E, Georgiadis O, da Cruz L, Bridge H and Maclaren RE (2021) Structural and Functional Characteristics of Color Vision Changes in Choroideremia. Front. Neurosci. 15:729807. doi: 10.3389/fnins.2021.729807

Color vision is considered a marker of cone function and its assessment in patients with retinal pathology is complementary to the assessments of spatial vision [best-corrected visual acuity (BCVA)] and contrast detection (perimetry). Rod-cone and chorioretinal dystrophies—such as choroideremia—typically cause alterations to color vision, making its assessment a potential outcome measure in clinical trials. However, clinical evaluation of color vision may be compromised by pathological changes to spatial vision and the visual field. The low vision Cambridge Color Test (lvCCT) was developed specifically to address these latter issues. We used the trivector version of the lvCCT to quantify color discrimination in a cohort of 53 patients with choroideremia. This test enables rapid and precise characterization of color discrimination along protan, deutan, and tritan axes more reliably than the historically preferred test for clinical trials, namely the Farnsworth Munsell 100 Hue test. The lvCCT demonstrates that color vision defects—particularly along the tritan axis—are seen early in choroideremia, and that this occurs independent of changes in visual acuity, pattern electroretinography and ellipsoid zone area on optical coherence tomography (OCT). We argue that the selective loss of tritan color discrimination can be explained by our current understanding of the machinery of color vision and the pathophysiology of choroideremia.

Keywords: color vision, choroideremia, cones, retinal degeneration, ellipsoid zone, pattern electroretinogram, Cambridge color test

INTRODUCTION

The primary retinal neurons for conscious vision are duplex, consisting of two broad types: the rods and the cones (intrinsically photosensitive retinal ganglion cells—ipRGCs—which primarily drive circadian function and the pupillary light reflex are not considered further in this paper). In the healthy retina, rods confer scotopic (nocturnal) function; whilst cones are primarily used for photopic (daylight level) function. Although the cones are present throughout the retina, their high density in the fovea is responsible for high spatial resolution in normal subjects, which is measured clinically by best-corrected visual acuity (BCVA), which in turn provides a functional metric for foveal cones. Spectral discrimination (color vision) is another key function of cone-based vision, and it can be used to monitor cone function in retinal pathology.

The physiological basis of trichromatic color vision is the cone photoreceptor, which has three sub-types: the long- (L-), medium- (M-), and short- (S-)wavelength sensitive cones. These have spectral sensitivities with peaks at around 558 (L-cones), 531 (M-cones), and 419 nm (S-cones) (Dartnall et al., 1983). The signal from any individual cone varies in only one dimension and therefore cannot alone convey information regarding color (univariance). The visual system extracts information about the spectral quality of light by comparing the activity of the three classes of cone, a process that commences in the second-order retinal neurons, the bipolar cells (Solomon and Lennie, 2007; Simunovic, 2016). Early post-receptoral processing is proposed to occur in two molecularly, anatomically and functionally distinct subsystems of color vision (Solomon and Lennie, 2007). The first, phylogenetically ancient subsystem, compares quantal catches from the S-cones to those of the M + L-cones (tritan color discrimination). The S-cone system has poor spatial and temporal resolution, and does not normally contribute significantly to clinical measures of visual acuity (Solomon and Lennie, 2007). The second, more recent sub-system, compares quantal catches from the M- vs. L-cones (red-green color discrimination). Of note, the latter is proposed to have evolved from a mechanism specialized for extracting spatial detail from the visual scene (Mollon, 1999). Thus reductions in visual acuity caused by retinal pathology are often accompanied by acquired red-green color deficiency, whilst acquired tritan deficiency may occur in the presence of normal visual acuity (Simunovic, 2016).

Choroideremia is an X-linked chorioretinal dystrophy with a prevalence of 1 in 50,000 which is caused by mutations in the gene encoding Rab Escort Protein 1 (REP1). Patients with choroideremia have progressive centripetal loss of retinal and choroidal structure and typically have normal visual acuity until their fourth of fifth decade. REP1 is expressed in all retinal cell types, including in cones; however, choroideremia preferentially affects the rods. The differential effects of choroideremia on the rods is believed to reflect their greater dependence (compared to the cones) on normal RPE function, which is compromised early in the disease process (MacDonald et al., 2005, 2009). The rods, in turn, appear to have a role in cone survival through the secretion of trophic factors that have a protective effect on cones. The absence of these factors is thought to be the cause of secondary cone degeneration in rod-cone dystrophies, and this is exemplified by experiments demonstrating that transplantation of normal rods improves cone survival in models of inherited retinal degeneration (Mohand-Said et al., 2000). One key trophic factor has been termed "rod-derived cone viability factor" (RdCVF) (Sahel and Léveillard, 2018), a thioredoxin-like protein which is not produced by defective rods (Narayan et al., 2016). Although other mechanisms have been proposed for bystander cone degeneration, RdCVF appears to be a key player, and has been used in preclinical gene therapy studies to delay secondary cone loss (Byrne et al., 2015).

Anecdotally, choroideremia patients in the Phase I/II trials of sub-retinal gene therapy reported improvements in color saturation following treatment, suggesting that color vision may be a possible biomarker for functional rescue. Although color vision deficiency has not historically been recognized as a feature of choroideremia, it has more recently been demonstrated to result in color vision defects early in the disease course. However, this dyschromatopsia may be difficult to characterize with standard clinical tests (Jolly et al., 2015; Heon et al., 2016), both because of the demands they place on subjects, and because their results cannot be directly related to changes in the machinery of color vision.

Color vision can be examined using a number of different tests: the choice of which depends upon the characteristics of the subject, and the likely mechanism of color vision loss (Dain, 2004). The preferred test of the US Food and Drug Administration (FDA) for the investigation of acquired color vision deficiency in clinical trials is the Farnsworth-Munsell 100 Hue (**Figure 1A**; Farnsworth, 1943), in part as a result of its longstanding use (Seitz et al., 2018). It consists of 85 colored caps divided across four boxes that must be arranged in order by the subject. The colored aperture of each cap subtends about 2 degrees at the recommended viewing distance, and their hues are arranged by the subject so that they appear to form a gradual progression in color. Each subject's performance is quantified using a scoring system, which is based upon the arrangement of the caps. One drawback of the test is the large number of artefacts introduced by the unequal perceptual steps between different caps (Simunovic, 2016). Additionally, there is a high degree of inherent test variability, making reliable quantitative analysis difficult. As a consequence, large alterations are needed between visits to establish genuine change (Kinnear and Sahraie, 2002). The FM 100 Hue is particularly difficult for patients with visual field loss to perform, as the task requires a significant portion of visual search. Although many other color vision tests have been developed, not all are suitable for patients with acquired color vision deficiency (Simunovic, 2016). Fewer still are suited to patients with severely impaired visual acuity or visual field. The low vision Cambridge Color Test (lvCCT) was developed especially to assess patients with acquired color vision deficiency in whom spatial vision, or the visual field, is impaired. Loss of color discrimination in the central visual field is not directly influenced by peripheral visual field loss *per se*, though the latter presents difficulties in the conduct of many tests of color vision—as noted above, and demonstrated in **Figure 1B** (Swanson et al., 1993; Jolly et al., 2015).

The lvCCT is a development of the standard version of the CCT (Regan et al., 1994) (**Figures 1C,D**), which uses a Stilling-type array, that in turn places high(er) demands on spatial vision. The standard CCT has been used to investigate color discrimination ellipses in choroideremia, and has demonstrated evidence of preferential involvement of the tritan system of color vision (Seitz et al., 2018). The standard CCT is demanding and may not be suitable for all clinical trials participants with low vision or visual field loss (Seitz et al., 2018). Additionally, many axes (i.e., ≥8) of color space are typically probed to derive discrimination ellipses (**Figure 1E**), making this approach time-consuming. As an alternative, testing time may be reduced by simply assessing color discrimination along the so-called cardinal axes of color space: the tritan, deutan and protan axes (the so-called "trivector" test approach). The lvCCT (**Figure 1D**) has been used in clinical trials aiming to restore cone function in achromatopsia (Zein et al., 2014; Fischer et al., 2020). It can be used in patients with poor visual acuity and reduced visual fields, making it very useful for patients with retinal and visual pathway pathology (Simunovic et al., 1998; **Figure 1F**).

We aimed to use the lvCCT trivector test to characterize color vision loss in choroideremia, and to test its suitability as a potential outcome measure in clinical trials. Patients with, and without, significant loss of BCVA were tested: in particular, we hypothesized that patients with well-preserved visual acuity may still demonstrate tritan losses in color discrimination and that loss of red-green color discrimination may ensue once visual acuity was sub-normal (see above). Furthermore, we aimed to compare the lvCCT findings with those obtained with the currently preferred test of the US FDA, the FM 100-hue test. Finally, we also aimed to compare color discrimination to other estimates of macular function (electrodiagnostic assessment) and structure [optical coherence tomography (OCT)].

MATERIALS AND METHODS

Patients were examined as part of the screening process to assess eligibility for an ongoing retinal gene therapy trial for choroideremia (NCT02407678). Control participants were recruited from accompanying persons and staff members. Informed consent was obtained and the work adhered to the Declaration of Helsinki. All participants underwent BCVA testing with a Bailey-Lovie style visual acuity chart (Bailey and Lovie, 1976) and color vision testing with the Metropsis System (Cambridge Research Systems, Cambridge, United Kingdom). Individuals with visible media opacities, or likely congenital color vision deficiency (failure at the Ishihara test; $N = 1$) were excluded.

The control group was age-matched to the patients. Patients were divided into two groups for analysis: preserved BCVA (≥80 ETDRS letters) based on population studies defining the upper limit of normal (Brown and Yap, 1995) and reduced BCVA (<80 ETDRS letters) to explore the relationship between BCVA and acquired color vision deficiency in choroideremia (Simunovic, 2016). Examining patients with preserved BCVA permitted investigation of the earliest defects in color vision. Results for protan, deutan, and tritan axes were compared between-groups using one-way ANOVA, following log transformation. Additionally Spearman correlation of color defect and BCVA was conducted.

The full cohort consisted of 21 control participants (mean age 31 years; range 20–46 years), 35 choroideremia patients with BCVA ≥80 letters (equivalent to 0.10 logMAR, mean age 31 years; range 14–55 years), and 18 choroideremia patients with reduced BCVA (mean age 34 years; range 17–71 years). The subset of 30 patients that underwent additional testing had a mean age of 32 years (range 17–55 years), and all had a BCVA of ≥ 80 letters. Summary statistics are shown in **Table 1**.

The trivector lvCCT was used to explore protan, deutan, and tritan color discrimination with the white point of the test set to the chromaticity co-ordinates of CIE D65 ($u' = 0.209$, $v' = 0.488$; CIE (1976) u' v' co-ordinates) and the confusion point set to protan ($u' = 0.678$, $v' = 0.501$), deutan ($u' = -1.217$, $v' = 0.782$) and tritan ($u' = 0.257$, $v' = 0.0$). In this test, 4 discs subtending 4 degrees at a viewing distance of 1.5 m are presented to the subject (see **Figure 1D**). The center of each disc is 4.3 degrees from the center of the screen. Stimuli were presented for a maximum of 20 s to allow participants adequate time to search the display, even in the presence of severe visual field loss. An auditory signal accompanied presentation of the stimulus to alert patients and to draw attention to the screen. In order to negate the possibility of subjects using perceived brightness differences to detect differences in color, the lvCCT employs luminance randomization: i.e., the four discs vary randomly in brightness. One disc—the "test disc"—was varied systematically from the remaining 3 ("background discs") in chromaticity. The subject's task was to determine and then indicate which disc differed from the remaining three in color *via* an attached button box. Thresholds for protan, deutan and tritan axes were established using an interleaved adaptive staircase procedure. Each staircase involved a decrease rate of 50% in hue saturation before the first reversal and a 12.5% decrease after the second reversal (fixed increase rate of 25%). Threshold was calculated as the mean of the final six, of a total of seven, reversals. If the subject was unable to correctly determine the position of the most saturated test disc on five consecutive occasions, testing along that axis was terminated and the threshold set at the maximum saturation. Participants undertook a training run before performing the actual test to familiarize themselves with the task.

A subset of patients underwent both the FM 100 Hue and lvCCT. The FM 100 Hue (DG Color, Wiltshire, United Kingdom) was set at a viewing distance of 50 cm and took place within a lighting cabinet approximating CIE standard illuminant D. Caps were randomized by the examiner prior to testing, and placed back in the tray. The participant was instructed to arrange the caps in a gradual progression in color between the fixed end caps. The order of the caps was recorded using the accompanying custom software to calculate the total error score. The tests were subsequently classified as normal or abnormal based on published values (Kinnear and Sahraie, 2002), and calculated values for the upper 95% confidence limit of normal from the normative data collected above. Normative data for the lvCCT test has been reported by Paramei and Oakley (2014). Additionally, the reported variation across the age ranges represented by our cohort is small. A kappa agreement between tests was calculated.

The same patient subset also underwent ISCEV (International Society for the Clinical Electrophysiology of Vision) pattern electroretinogram (PERG) testing (Bach et al., 2013) with both standard (15 degrees × 12 degrees) and large field (30 degrees × 24 degrees) checkerboard stimuli (Lenassi et al., 2012),

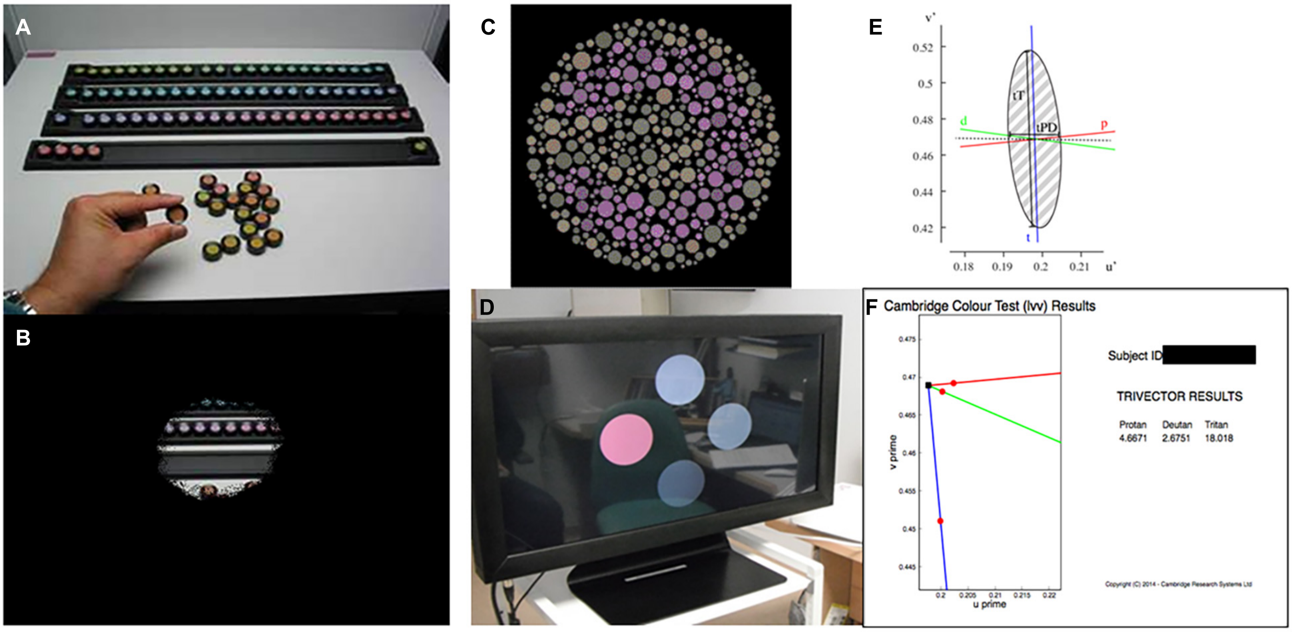

FIGURE 1 | (A) Farnsworth-Munsell 100 Hue color vision test. **(B)** Simulation of visual field loss restricting the view of the test resulting in slow test times. **(C)** Cambridge color test (CCT) target. **(D)** Low vision version of the CCT showing four circles across the screen, providing an easier target for patients with low vision and reduced visual field. **(E)** Example output from full CCT version, producing an ellipse in color vision function in color space. **(F)** Example output from trivector test showing outputs for the protan, deutan, and tritan axes.

TABLE 1 | Summary characteristics of patient groups.

Group	N (eyes)	Age (year)	BCVA (letters)	Protan threshold (×1000 CIE1976 Luv units)	Deutan threshold (× 1000 CIE1976 Luv units)	Tritan threshold (× 1000 CIE1976 Luv units)
Control	21	31 ± 6	91 ± 4.8	3.982 ± 2.353	4.559 ± 3.151	6.725 ± 2.467
Preserved BCVA	35	31 ± 9	86 ± 3.8	13.814 ± 20.334	9.872 ± 10.447	20.813 ± 27.983
Reduced BCVA	18	34 ± 15	72 ± 9.6	17.519 ± 19.946	14.401 ± 18.283	27.602 ± 25.803
Patient subset	30	32 ± 9	83 ± 5.4	3.453 ± 7.455	3.246 ± 6.114	6.673 ± 10.808

All data is presented as mean ± standard deviation.

using the P50 component as an objective measure of suprathreshold cone-driven macular function and N95 as a measure of retinal ganglion cell function. Recordings were obtained using gold foil recording electrodes using a constant check size of 0.8 degrees. Testing was performed using the Espion system (Diagnosys LLC, Lowell, MA). The key features of the PERG are P50 peak time and amplitude as markers of macular dysfunction. Additionally, N95 is indicative of ganglion cell dysfunction.

The color vision results for each axis were treated as Cartesian co-ordinates in CIE (1976) u', v', and a combined vector calculated with $||CV|| = \sqrt{(((protan^2 + deutan^2)/2) + tritan^2)}$, where $||CV||$ is the absolute color vision vector length. Protan and deutan results were averaged to reduce the impact of weighting toward L/M defects. A Spearman regression model examined the relationship between the PERG and the color vision vector combining all axes.

In order to investigate possible structural correlations to color discrimination, a custom program was written in the R programming language (v3.6.3) (R.C. Team, 2017). Spectral domain optical coherence tomography (SD-OCT) images were acquired during screening using the Spectralis OCT volume (Heidelberg Engineering, Heidelberg, Germany). Data were exported as XML files and each OCT b-scan per patient (**Figure 2A**) manually inspected to identify coordinates of the limiting edges of the intact ellipsoid zone (EZ). These coordinates were input into the custom program, resulting in a polygon overlaid on the en-face image (**Figure 2B**) representing the area of the ellipsoid zone across all B-scans in a volume. In difficult cases where the ellipsoid zone termination was unclear, the profile method detailed by Smith et al. (2019) was employed. The relationship between EZ and color vision was examined using Spearman's rank-order correlation coefficients. EZ area was utilized to order avoid the confounding effects of retinal

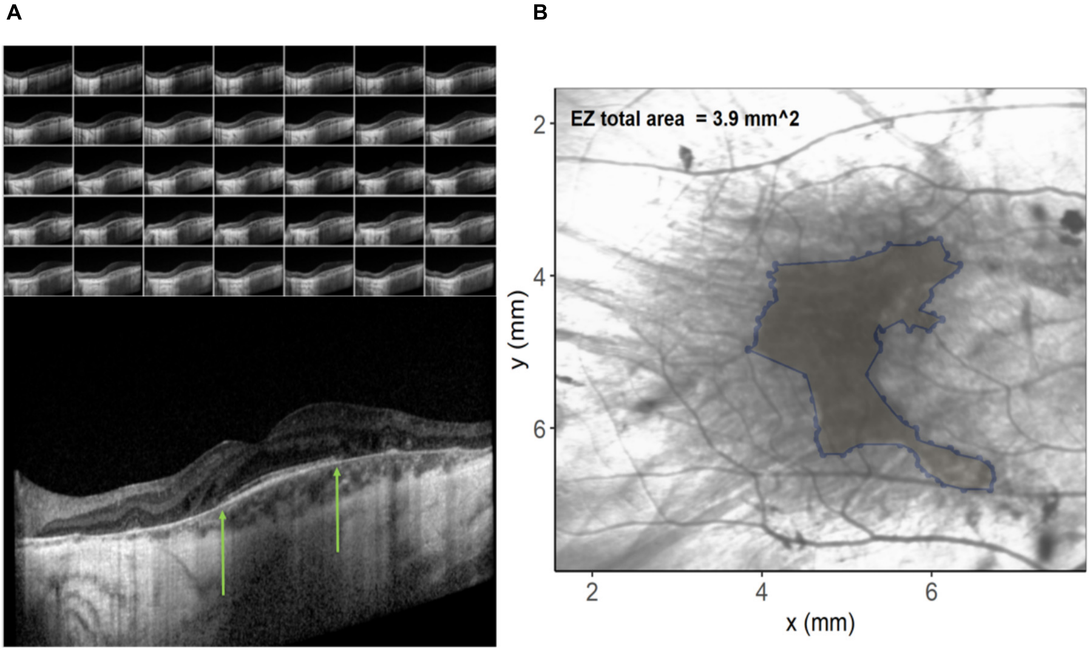

FIGURE 2 | (A) Images on the left show the individual b-scan slices from an optical coherence tomography (OCT) volume with the central slice expanded. The green arrows denote the edges of the ellipsoid zone. These co-ordinates from each of the slices are plotted on the infra-red image on the right **(B)** and connected to create an ellipsoid area across the OCT volume.

remodeling on thickness measurements (Jolly et al., 2020). EZ is a measure of remaining retina.

Groups were compared using a two way ANOVA. Due to unequal variances, *post hoc* analysis was conducted with Games-Howell comparisons. All results are reported for the right eye only. All statistical analyses were conducted in SPSS (version 25.0, IBM Software, New York, NY, United States) or GraphPad Prism 9 (GraphPad Software, San Diego, CA, United States) unless stated otherwise.

RESULTS

Comparison Between Groups Shows Early Tritan Loss

Figure 3 shows the spread of the raw lvCCT color discrimination data, with the highest threshold along the tritan axis in all cohorts as shown by the longest vector lines aligned with the vertical axis. There was greater variation in color discrimination thresholds in the choroideremia patients than the normal controls. Group averages are shown in **Figure 3B**. There was a statistically significant difference between groups, as determined by two-way ANOVA for protan [$F(2, 53) = 9.09$, $P < 0.01$], deutan [$F(2, 53) = 6.44$, $P < 0.01$], and tritan [$F(2, 53) = 19.54$, $P < 0.01$] thresholds. A Games-Howell *post hoc* test revealed that the color discrimination was significantly worse in both the "preserved" and reduced BCVA cohorts compared to the control group for all three color confusion axes ($P \leq 0.05$). However, the two choroideremia cohorts were not significantly different for any of the axes ($P > 0.05$). **Figure 4A** demonstrates the classification of the color defect for each eye with choroideremia and shows that a higher proportion had a tritan defect compared to classification of a red-green defect.

The Spearman correlation co-efficient for BCVA and combined red-green vector length and tritan vector length was -0.59 (-1.1 to -0.12 95% confidence interval) and -0.46 (-0.92 to 0.001 95% confidence interval), respectively. This was significantly for red-green ($P = 0.02$) but not for tritan ($P = 0.05$), consistent with the change in a color defect independent to BCVA (**Figure 4B**).

Comparison With 100 Hue Reveals the Cambridge Color Test Is More Sensitive

The majority of patients demonstrated abnormal results on both tests (**Table 2**). A clear axis of defect on the FM 100 Hue was not evident in any of the eyes (representative test result for the 100 Hue and lvCCT for the same eye shown in **Figure 5**). Out of the 19 eyes classified as abnormal by the lvCCT, 26% were classified as having a clear tritan defect, 11% as having a protan defect, 16% as having a deutan defect and 47% as having a defect along two or more axes. In all instances of the latter, tritan discrimination was affected. The kappa agreement coefficient, $k = 0.3878$ ($P = 0.03$) indicated only fair agreement between the FM 100 Hue and CCT.

No Correlation Between Color Vision and Pattern Electroretinogram

In order to examine suprathreshold macular function objectively, PERG was conducted on the subset that went additional testing

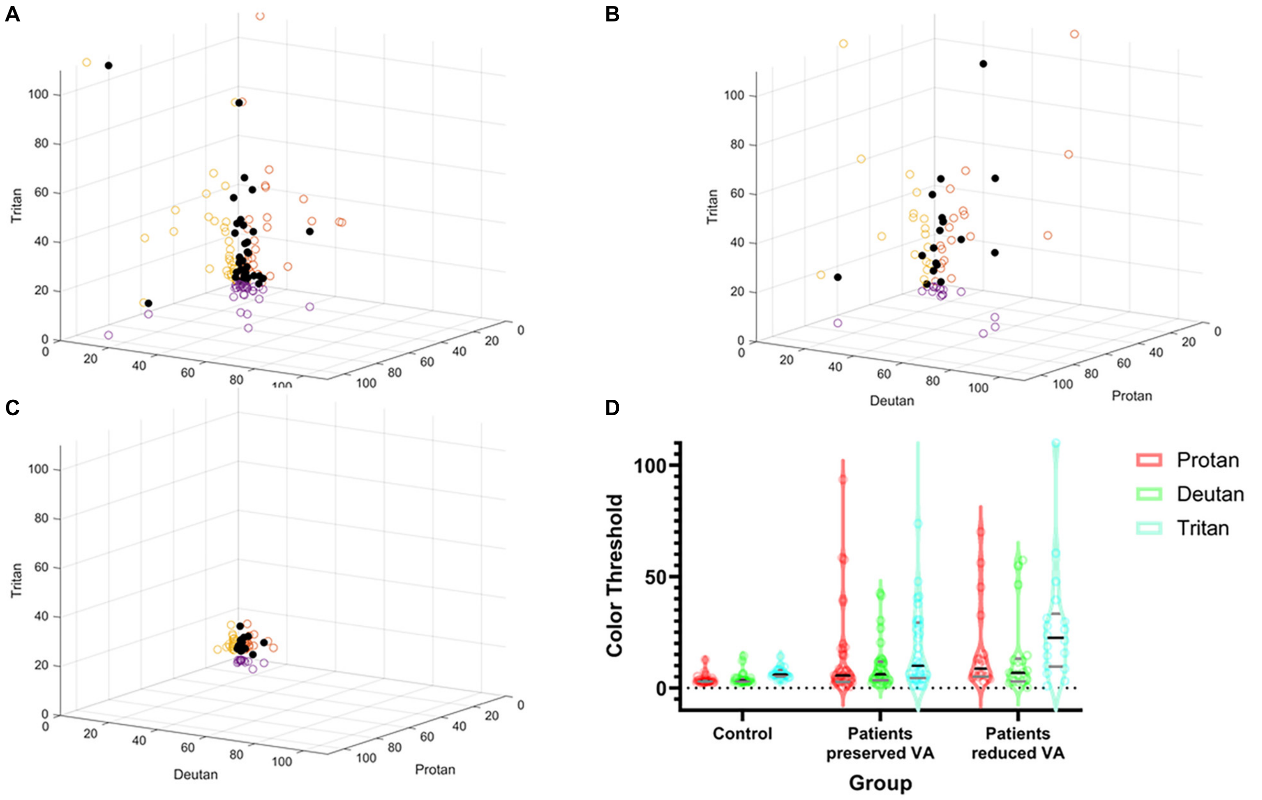

FIGURE 3 | Summary of color discrimination results. Spread of individual data points plotted against protan, deutan, and tritan scores on the X, Y, and Z axes, respectively (black dots). The circles on the axes walls show the corresponding shadows of the results on each axes separately. **(A)** Choroideremia eyes with preserved BCVA. **(B)** Choroideremia eyes with reduced BCVA. **(C)** Control eyes. The higher the number, the greater the degree of the color defect against the corresponding axis. **(D)** Pirate plot of group differences. The outer envelope shows the spread of the raw data with the widest point showing the mean and the black line representing the median. The gray lines represent the interquartile range. Additionally, dots represent each raw data measurement point.

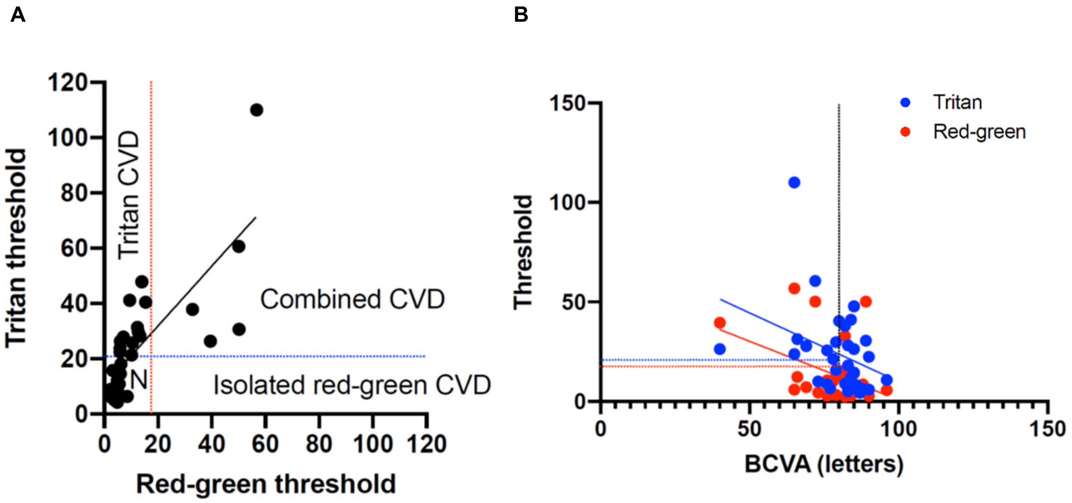

FIGURE 4 | (A) Classification of color vision defects (CVD) measured with the low vision Cambridge Color Test (lvCCT) with the regions of normal color vision, tritan loss, red-green loss, and combined loss labeled. **(B)** Correlation of best-corrected visual acuity (BCVA) with red-green and tritan color defects. The vertical dotted line shows 20/20 visual acuity. The blue and red lines show the upper 95% cutoff of normal for the tritan and red-green loss, respectively.

TABLE 2 | Classification of eyes as normal or abnormal when tested with the 100 Hue and Cambridge Color Test (CCT).

	lvCCT abnormal	lvCCT normal
100 Hue abnormal	17	6
100 Hue normal	2	5

and had preserved BCVA eyes. In response to the standard field PERG stimulus, the P50 and N95 were measurable in 26 out of 30 eyes, with the remaining 4 showing a flatline response. Mean P50 peak time for the cohort was 56.4 ± 12.7 ms with a mean P50 amplitude of 0.77 ± 0.49 μV. The mean amplitudes were subnormal based on local reference ranges (x-x ms and y-y μV, respectively) and the Espion normative database (Lenassi et al., 2012). The N95 amplitude for the cohort was 1.89 ± 1.17 μm, suggesting a preserved N95:P50 ratio, indicating preserved retinal ganglion cell function. The multiple regression model demonstrated no significant relationship between any of the PERG parameters with | | CV| | (R = 0.16, P = 0.90). Coefficients were -0.14 [-7.4 to 7.1], P = 0.96 for P50 peak time, 43.0 [-284.4 to 198.4], P = 0.72 for P50 amplitude, and 32.0 [-65.8 to 129.8], P = 0.50 for N95 amplitude.

Optical Coherence Tomography Ellipsoid Zone Area Does Not Correlate to Color Discrimination

Thirty patients with choroideremia had OCT images from the same day as color vision testing with sufficient quality to enable qualitative delineation of the retinal layers. Measurement of the ellipsoid area was performed using the process described in the methods section. Images on which the ellipsoid zone could not be reliably commented on were excluded from imaging analysis. The color vector was plotted against the ellipsoid area (**Figure 6**) and showed a negative trend. The slope of the regression line indicated a reduction in color vector of -1.15 for each unit reduction in ellipsoid area (95% confidence interval -2.59 to 0.29); the relationship was not statistically significant (P = 0.11). The findings remained non-significant when each color axis was measured separately.

DISCUSSION

This study uses color discrimination, as assessed by the lvCCT, to characterize dyschromatopsia in 53 choroideremia patients, with and without, significant loss of visual acuity. The results were compared to those obtained using more established methods, including the Farnsworth Munsell 100-Hue test and the ISCEV-standard pattern ERG measure of macular function. The lvCCT results were also compared with a spectral-domain OCT measure of macular preservation, with an overall view to assess the potential suitability of color discrimination as an outcome measure in clinical trials.

The lvCCT rapidly characterized color discrimination (mean testing time 5 min) along the cardinal axes of color space. By contrast, the FM 100 Hue took longer to perform (over 30 min) and provided results that could not directly be related to losses of discrimination in either of the two subsystems of color vision (M vs. L-cones, measured *via* protan and deutan axes, and S-cone vs.

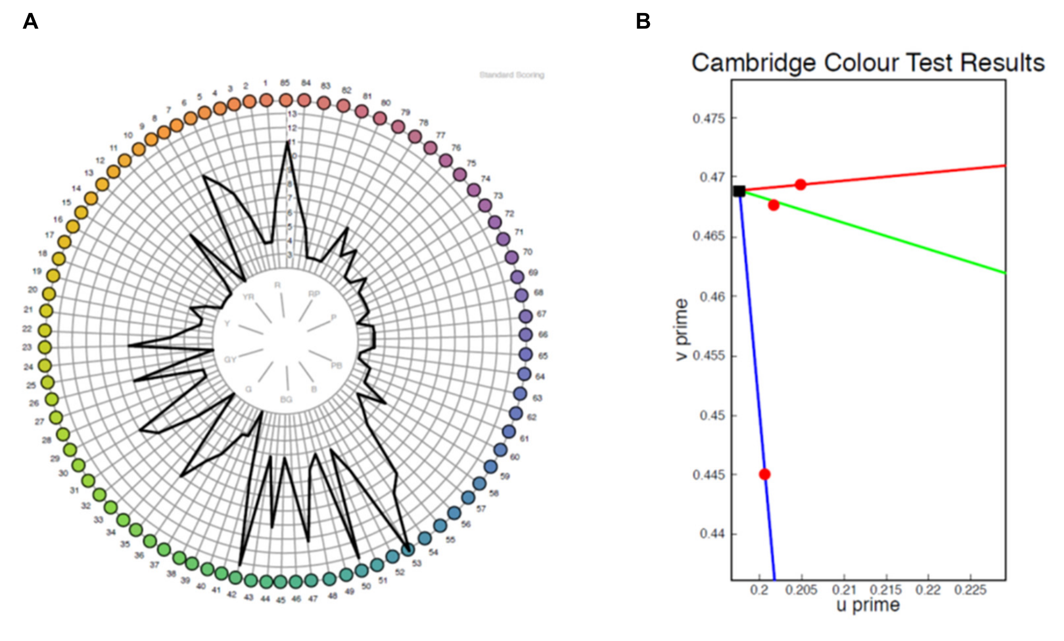

FIGURE 5 | Representative sample of a test result for the same eye from the FM 100 Hue **(A)** and low vision Cambridge Color Test (lvCCT) **(B)**. The FM 100 Hue does not have a clearly definable axis of color loss, whereas the lvCCT results indicate a reduced tritan score (longer vector) but normal protan and deutan scores as shown by the short vectors.

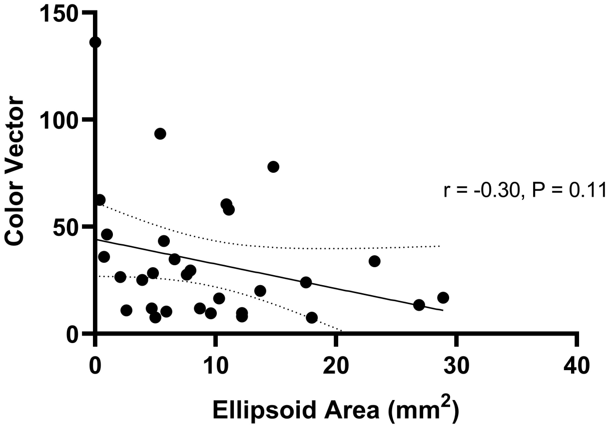

FIGURE 6 | Regression relationship between color vector and ellipsoid area in choroideremia. The color vector represents the degree of color vision loss across the three axes with a higher number representing a greater degree of color loss. The solid line is the regression line and 95% confidence intervals are shown with the dotted lines.

M + L-cone, assessed *via* the tritan axis). Furthermore, the two tests only demonstrated fair agreement.

The majority patients had tritan color defects, which is in keeping with previous reports in rod-cone dystrophies (Swanson et al., 1993; Seitz et al., 2018). The vectors in the S cone direction could be compared to the L and M cone directions due to the use of a normal control group, which allows the use of the color vector | | CV| | to be used as a valid approach. All color spaces include the assumption that just noticeable differences are additive. There are several possibilities that should be considered to account for this finding. Although cataract is a feature of some retinal dystrophies, none of the included patients had significant media opacity: hence absorption by lens pigment cannot account for our observation. It has been previously noted that the S-cones appear to be especially vulnerable to retinal pathology, and there are several hypotheses which have attempted to account for this observation (Mollon, 1982; Simunovic, 2016). Part of the apparent vulnerability of S-cone mediated visual function to pathology appears to arise from adaptational differences between the S-cone mechanism and the M-/L-cone mechanism and biases introduced by testing approaches. Mollon hypothesized that certain tests (e.g., those employing yellow backgrounds) may place the S-cone mechanism at disadvantage through adaptation of post-receptoral mechanisms to one extreme of their operational range. Such a hypothesis cannot be invoked to explain our data, however, as neutral adaptation conditions were used. However, adaptation asymmetries have also been identified for neutral/white backgrounds (Kalloniatis and Harwerth, 1989; Simunovic, 2016; Simunovic et al., 2021). In particular, the S-cone mechanism is more likely to be probed under conditions where it does not display Weber-like adaptation. This may lead to apparent selective pathology through adaptational asymmetry (Kalloniatis and Harwerth, 1989; Simunovic, 2016; Simunovic et al., 2021); this asymmetry may account for at least part of the apparent vulnerability of the S-cones. Another hypothesis—the so-called "vulnerable photoreceptor" hypothesis—supposes that the S-cones are inherently more susceptible to pathological processes. For example, S-cones have been reported to be more susceptible to metabolic damage (Hood and Greenstein, 1988). Furthermore, it has been suggested that S-cones may be preferentially affected by rod-selective pathology. Part of this shared "vulnerability" may be driven by physiological similarities between the rods and the S-cones; for example, S-cones and rods share similarities in distribution which may render them similarly vulnerable to topographically variable pathological processes (Curcio et al., 1991; Hofer et al., 2005). Furthermore, S-cones and rods share similarities in the expression of certain proteins, e.g., carbonic anhydrase (Nork et al., 1990), which may place them under similar pathophysiological stress under certain conditions. Furthermore, both S-cones and rods derive from a common precursor cell, as evidenced by patients with Nr2E3 mutations, who have an increased S-cone complement, but a grossly abnormal rod complement (Sohn et al., 2010). There is an increase in the inflammatory response following rod death which has a greater effect on S-cones compared to L- and M-cones (Di Pierdomenico et al., 2020). Cone cells have access to an alternative Mũller cell-mediated visual cycle, which reduces their reliance on the RPE for chromophore recycling. Mũller cells have a lower association with S-cones compared to other cone types, which may make them more vulnerable RPE degeneration (Lindenau et al., 2019) in choroideremia. In view of the differences between S-cones and other cone types, and simultaneous similarities with rods, it is possible that S-cones may be preferentially affected by primary rod disease, either *via* inflammatory processes or other degenerative processes.

Dyschromatopsia was evident prior to reductions in BCVA in many choroideremia subjects; for this reason, it may prove to be a suitable functional biomarker for very early abnormalities in macular function. In choroideremia, foveal architecture is observed to be disrupted before BCVA loss occurs (typically retinal thickening with blunting of the foveal depression). This in turn suggests that other aspects of visual function may better reflect early macular pathology in choroideremia and therefore highlights the importance of this work (Jacobson et al., 2006). In particular, it has previously been noted that tritan color vision deficiency typically occurs in patients with well-preserved BCVA. It has been argued that this reflects in part the underlying physiology of color processing. In particular, the S-cones comprise only a small proportion of the cone complement (about 4%) and their loss will not affect spatial resolution (BCVA) in the majority of patients. However, the M-/L-cone mechanism has been proposed to be parasitic upon a pathway which initially evolved to extract spatial detail (Mollon, 1999). For this reason, loss of M-/L-cone mediated color discrimination is often seen in patients who have concurrent loss of BCVA (Marré and Pinckers, 1985; Simunovic, 2016).

All patients with choroideremia had an abnormal pattern ERG P50 component, consistent with macular dysfunction, including those with preserved BCVA. However, the severity of the PERG reduction does not correlate with color discrimination at the lvCCT; this is in keeping with previous findings (Falcao-Reis et al., 1991). PERG and psychophysical measures of macular function have been reported to be discordant, and this may reflect the different areas assessed by the two modes of testing (Ciavarella et al., 1997). We have previously demonstrated a relationship between color vision defect with central microperimetry threshold (Jolly et al., 2015). Microperimetry is likely reflective of cone function in the area tested so is probably exploring a more comparable cone population (Simunovic et al., 2016; Han et al., 2018). Different functional measures test different aspects of vision over different regions of the visual field so will not necessarily show good correlation. Additionally, previous work has shown autofluorescence area of preservation and location in relation to the fovea appeared to play a role in explaining color vision losses in choroideremia. This may reflect the fact that more advanced FAF changes correlate to decreased photoreceptor function/visual pigment cycling (Jolly et al., 2015).

The OCT ellipsoid area was utilized as an indirect marker of cone presence, and the direction and extent of association was examined in relation to color discrimination. Although a negative correlation was shown, this was not statistically significant. Ellipsoid area in part reflects the disease stage, it may correlate poorly to color discrimination for two reasons. First, if such changes occur outside of the retinal areas probed by the lvCCT, no correlation would be anticipated. Second, early functional alterations in the cones may be indicated by changes other than complete obliteration of the ellipsoid layer (e.g., fundus autofluorescence).

In summary, tritan defects are seen early in choroideremia, prior to BCVA loss. This finding is generally in keeping with our current understanding of the machinery of color vision, the known adaptational asymmetries in the S- and M-/L-cone subsystems of color vision and the dependence of cones on the rods for survival. We note that several patients who have undergone sub-retinal *AAV2.REP1* gene "replacement" therapy have reported subjective improvements in color saturation following surgery, which has prompted us to explore color discrimination as part of an ongoing Phase 2 trial. Color vision appears to be an early biomarker of macular dysfunction in choroideremia and may be more sensitive than BCVA when used for monitoring gene therapy outcomes. We note that other approaches could be used to explore these subjective reports in color vision. For example, patients with symmetrical vision loss could undergo testing to assess inter-ocular differences in perceived saturation following first-eye surgery. Where this is not possible, exploration of white-points/long term color constancy could be explored. Furthermore, changes in receptoral function could be determined by assessing threshold-vs. intensity functions pre-, and post-surgery, to elucidate changes in the S-, M-, and L-cones as well as the rods. Such testing may also help to identify the site of losses of sensitivity (i.e., $d_{1/2}$, or receptoral vs. d_3, or post-receptoral), as previously outlined (Seiple et al., 1993; Simunovic et al., 2021).

In summary, this study quantifies color vision deficits in patients with choroideremia with both preserved and reduced visual acuity, and reveals a high incidence of S-cone/tritan pathway dysfunction. The lvCCT trivector test provides a rapid means of quantifying color discrimination along the cardinal axes of color space in this patient group. Furthermore, it identifies losses in central macular function in patients prior to the loss of visual acuity or evidence of structural change on OCT. This highlights the potential use of color discrimination as an outcome measure in future clinical trials which target sub-retinal gene therapy to the macula.

DATA AVAILABILITY STATEMENT

The raw data supporting the conclusions of this article will be made available by the authors, without undue reservation.

ETHICS STATEMENT

The studies involving human participants were reviewed and approved by the Health Research Authority 15/LO/1379. The patients/participants provided their written informed consent to participate in this study.

AUTHOR CONTRIBUTIONS

JJ designed the study, collected and analyzed the data, and wrote the manuscript. AR and AJ contributed to the data collection. AJ, MS, and AD contributed to the data analysis. AR, AD, HB, and RM provided input on the test procedures and analysis techniques. MS contributed to the writing of the manuscript. All authors reviewed the manuscript.

FUNDING

This article presents independent research funded by the National Institute for Health Research (NIHR) (Clinical Doctoral Research Fellowship CA-CDRF-2016-02-002 for JJ). This work was also supported by the NIHR Oxford Biomedical Research Centre, NIHR Moorfields and UCL Institute of Ophthalmology Biomedical Research Centre, and funding by the NIHR Efficacy and Mechanism Evaluation programme grant 12/66/35. MS was supported by the Foundation Fighting Blindness CD-CL-0816-0710-SYD. AR was supported by the National Institute for Health Research Biomedical Research Centre at Moorfields Eye Hospital NHS Foundation Trust and UCL Institute of Ophthalmology, London, United Kingdom.

ACKNOWLEDGMENTS

Some of this work formed part of the DPhil thesis for JJ. Thanks to Andy Rider and Andrew Stockman for contributing to the data collection.

REFERENCES

Bach, M., Brigell, M. G., Hawlina, M., Holder, G. E., Johnson, M. A., McCulloch, D. L., et al. (2013). ISCEV standard for clinical pattern electroretinography (PERG): 2012 update. *Doc. Ophthalmol.* 126, 1–7. doi: 10.1007/s10633-012-9353-y

Bailey, I. L., and Lovie, J. E. (1976). New design principles for visual acuity letter charts. *Optom. Vis. Sci.* 53, 740–745. doi: 10.1097/00006324-197611000-00006

Brown, B., and Yap, K. H. (1995). Differences in visual acuity between the eyes: determination of normal limits in a clinical population. *Ophthalmic Physiol. Opt.* 15, 163–169.

Byrne, L. C., Dalkara, D., Luna, G., Fisher, S. K., Clérin, E., Sahel, J. A., et al. (2015). Viral-mediated RdCVF and RdCVFL expression protects cone and rod photoreceptors in retinal degeneration. *J. Clin. Invest.* 125, 105–116. doi: 10.1172/JCI65654

Ciavarella, P., Moretti, G., Falsini, B., and Porciatti, V. (1997). The pattern electroretinogram (PERG) after laser treatment of the peripheral or central retina. *Curr. Eye Res.* 16, 111–115. doi: 10.1076/ceyr.16.2.111.5094

Curcio, C. A., Allen, K. A., Sloan, K. R., Lerea, C. L., Hurley, J. B., Klock, I. B., et al. (1991). Distribution and morphology of human cone photoreceptors stained with anti-blue opsin. *J. Comp. Neurol.* 312, 610–624. doi: 10.1002/cne.903120411

Dain, S. J. (2004). Clinical colour vision tests. *Clin. Exp. Optom.* 87, 276–293. doi: 10.1111/j.1444-0938.2004.tb05057.x

Dartnall, H., Bowmaker, J., and Mollon, J. (1983). Human visual pigments: microspectrophotometric results from the eyes of seven persons. *Proc. R. Soc. Lond. Ser. B. Biol. Sci.* 220, 115–130. doi: 10.1098/rspb.1983.0091

Di Pierdomenico, J., Martínez-Vacas, A., Hernández-Muñoz, D., Gómez-Ramírez, A. M., Valiente-Soriano, F. J., Agudo-Barriuso, M., et al. (2020). Coordinated intervention of microglial and müller cells in light-induced retinal degeneration. *Invest. Ophthalmol. Vis. Sci.* 61:47. doi: 10.1167/iovs.61.3.47

Falcao-Reis, F. M., O'Sullivan, F., Spileers, W., Hogg, C., and Arden, G. B. (1991). Macular colour contrast sensitivity in ocular hypertension and glaucoma: Evidence for two types of defect. *Br. J. Ophthalmol.* 75, 598–602. doi: 10.1136/bjo.75.10.598

Farnsworth, D. (1943). The farnsworth-munsell 100-Hue and Dichotomous tests for color vision. *J. Opt. Soc. Am.* 33, 568–578. doi: 10.1364/JOSA.33.000568

Fischer, M. D., Michalakis, S., Wilhelm, B., Zobor, D., Muehlfriedel, R., Kohl, S., et al. (2020). Safety and vision outcomes of subretinal gene therapy targeting cone photoreceptors in achromatopsia: A nonrandomized controlled trial. *JAMA Ophthalmol.* 138, 643–651. doi: 10.1001/jamaophthalmol.2020.1032

Han, R. C., Gray, J. M., Han, J., Maclaren, R. E., and Jolly, J. K. (2018). Optimisation of dark adaptation time required for mesopic microperimetry. *Br. J. Ophthalmol.* 103, 1092–1098. doi: 10.1136/bjophthalmol-2018-312253

Heon, E., Alabduljalil, T., McGuigan, D. B., Cideciyan, A. V., Li, S., Chen, S., et al. (2016). Visual function and central retinal structure in choroideremia. *Investig. Ophthalmol. Vis. Sci.* 57, OCT377–OCT387. doi: 10.1167/iovs.15-18421

Hofer, H., Carroll, J., Neitz, J., Neitz, M., and Williams, D. R. (2005). Organization of the human trichromatic cone mosaic. *J. Neurosci.* 25, 9669–9679. doi: 10.1523/JNEUROSCI.2414-05.2005

Hood, D. C., and Greenstein, V. C. (1988). Blue (S) cone pathway vulnerability: a test of a fragile receptor hypothesis. *Appl. Opt.* 27, 1025–1029. doi: 10.1364/ao.27.001025

Jacobson, S. G., Cideciyan, A. V., Sumaroka, A., Aleman, T. S., Schwartz, S. B., Windsor, E. A. M., et al. (2006). Remodeling of the human retina in choroideremia: Rab escort protein 1 (REP-1) mutations. *Investig. Ophthalmol. Vis. Sci.* 47, 4113–4120. doi: 10.1167/iovs.06-0424

Jolly, J. K., Groppe, M., Birks, J., Downes, S. M., and MacLaren, R. E. (2015). Functional defects in color vision in patients with choroideremia. *Am. J. Ophthalmol.* 160, 822–831. doi: 10.1016/j.ajo.2015.06.018

Jolly, J. K., Menghini, M., Johal, P. A., Buckley, T. M. W., Bridge, H., and MacLaren, R. E. (2020). Inner retinal thickening affects microperimetry thresholds in the presence of photoreceptor thinning in patients with RPGR retinitis pigmentosa. *Br. J. Ophthalmol.* 2020, 1–6. doi: 10.1136/bjophthalmol-2020-317692

Kalloniatis, M., and Harwerth, R. S. (1989). "Differential Adaptation of Cone Mechanisms Explains the Preferential Loss of Short-Wavelength Cone Sensitivity in Retinal Disease BT - Colour Vision Deficiencies IX: Proceedings of the ninth symposium of the International Research Group on Colour Vision D," in *Colour Vision Deficiencies*, eds B. Drum and G. Verriest (Dordrecht: Springer), 353–364.

Kinnear, P. R., and Sahraie, A. (2002). New farnsworth-munsell 100 hue test norms of normal observers for each year of age 5–22 and for age decades 30–70. *Br. J. Ophthalmol.* 86, 1408–1411.

Lenassi, E., Robson, A. G., Hawlina, M., and Holder, G. E. (2012). The value of two-field pattern electroretinogram in routine clinical electrophysiologic practice. *Retina* 32, 588–599. doi: 10.1097/IAE.0b013e31822059ae

Lindenau, W., Kuhrt, H., Ulbricht, E., Körner, K., Bringmann, A., and Reichenbach, A. (2019). Cone-to-Müller cell ratio in the mammalian retina: A survey of seven mammals with different lifestyle. *Exp. Eye Res.* 181, 38–48. doi: 10.1016/j.exer.2019.01.012

MacDonald, I. M., Chan, C. C., Hiriyanna, K. T., Shen, D., and Fariss, R. (2005). REP–1 Localization in the Eye. *Invest. Ophthalmol. Vis. Sci.* 46:540.

MacDonald, I. M., Russell, L., and Chan, C.-C. (2009). Choroideremia: new findings from ocular pathology and review of recent literature. *Surv. Ophthalmol.* 54, 401–407. doi: 10.1016/j.survophthal.2009.02.008

Marré, M., and Pinckers, A. (1985). Basic phenomena of acquired color vision defects. *Bull. Soc. Belge Ophtalmol.* 215, 17–25.

Mohand-Said, S., Hicks, D., Dreyfus, H., and Sahel, J. A. (2000). Selective transplantation of rods delays cone loss in a retinitis pigmentosa model. *Arch. Ophthalmol.* 118, 807–811. doi: 10.1001/archopht.118.6.807

Mollon, J. D. (1982). A taxonomy of tritanopias. *Doc. Ophthalmol. Proc. Ser.* 33, 87–101.

Mollon, J. D. (1999). Color vision: Opsins and options. *Proc. Natl. Acad. Sci. U. S. A.* 96, 4743–4745. doi: 10.1073/pnas.96.9.4743

Narayan, D. S., Wood, J. P. M., Chidlow, G., and Casson, R. J. (2016). A review of the mechanisms of cone degeneration in retinitis pigmentosa. *Acta Ophthalmol.* 94, 748–754. doi: 10.1111/aos.13141

Nork, T. M., McCormick, S. A., Chao, G. M., and Odom, J. V. (1990). Distribution of carbonic anhydrase among human photoreceptors. *Investig. Ophthalmol. Vis. Sci.* 31, 1451–1458.

Paramei, G. V., and Oakley, B. (2014). Variation of color discrimination across the life span. *J. Opt. Soc. Am. A* 31, 375–384.

R.C. Team (2017). *A language and environment for statistical computing*. Vienna: Austria R Found. Statatical Computing.

Regan, B. C., Reffin, J. P., and Mollon, J. D. (1994). Luminance noise and the rapid determination of discrimination ellipses in colour deficiency. *Vision Res.* 34, 1279–1299. doi: 10.1016/0042-6989(94)90203-8

Sahel, J.-A., and Léveillard, T. (2018). Maintaining cone function in rod-cone dystrophies. *Adv. Exp. Med. Biol.* 1074, 499–509.

Seiple, W. H., Holopigian, K., Greenstein, V. C., and Hood, D. C. (1993). Sites of cone system sensitivity loss in retinitis pigmentosa. *Investig. Ophthalmol. Vis. Sci.* 34, 2638–2645.

Seitz, I. P., Jolly, J. K., Dominik Fischer, M., and Simunovic, M. P. (2018). Colour discrimination ellipses in choroideremia. *Graefe's Arch. Clin. Exp. Ophthalmol.* 256, 665–673. doi: 10.1007/s00417-018-3921-0

Simunovic, M. P. (2016). Acquired color vision deficiency. *Surv. Ophthalmol.* 61, 132–155. doi: 10.1016/j.survophthal.2015.11.004

Simunovic, M. P., Hess, K., Avery, N., and Mammo, Z. (2021). Threshold versus intensity functions in two-colour automated perimetry. *Ophthalmic Physiol. Opt.* 41, 157–164. doi: 10.1111/opo.12743

Simunovic, M. P., Moore, A. T., and MacLaren, R. E. (2016). Selective automated perimetry under photopic, mesopic, and scotopic conditions: Detection mechanisms and testing strategies. *Transl. Vis. Sci. Technol.* 5, 1–13. doi: 10.1167/tvst.5.3.10

Simunovic, M. P., Votruba, M., Regan, B. C., and Mollon, J. D. (1998). Colour discrimination ellipses in patients with dominant optic atrophy. *Vision Res.* 38, 3413–3419. doi: 10.1016/S0042-6989(98)00094-7

Smith, T. B., Parker, M. A., Steinkamp, P. N., Romo, A., Erker, L. R., Lujan, B. J., et al. (2019). Reliability of spectral-domain OCT ellipsoid zone area and shape measurements in retinitis pigmentosa. *Transl. Vis. Sci. Technol.* 8:37. doi: 10.1167/tvst.8.3.37

Sohn, E. H., Chen, F. K., Rubin, G. S., Moore, A. T., Webster, A. R., and MacLaren, R. E. (2010). Macular function assessed by microperimetry in patients with enhanced S-Cone Syndrome. *Ophthalmology* 117, 1199–1206. doi: 10.1016/j.ophtha.2009.10.046

Solomon, S. G., and Lennie, P. (2007). The machinery of colour vision. *Nat. Rev. Neurosci.* 8, 276–286. doi: 10.1038/nrn2094

Swanson, W., Birch, D. G., and Anderson, J. L. (1993). S-cone function in patients with retinitis pigmentosa. *Investig. Ophthalmol. Vis. Sci.* 34, 3045–3055.

Zein, W. M., Jeffrey, B. G., Wiley, H. E., Turriff, A. E., Tumminia, S. J., Tao, W., et al. (2014). CNGB3-achromatopsia clinical trial with CNTF: Diminished rod pathway responses with no evidence of improvement in cone function. *Investig. Ophthalmol. Vis. Sci.* 55, 6301–6308. doi: 10.1167/iovs.14-14860

Author Disclaimer: The views expressed are those of the authors and not necessarily those of the NHS, the NIHR or the Department of Health. The sponsor and funding organization had no role in the design or conduct of this research.

Conflict of Interest: RM is a consultant in retinal gene therapy to Novartis, Gyroscope Therapeutics, and Biogen, but these companies had no input into the work presented.

The remaining authors declare that the research was conducted in the absence of any commercial or financial relationships that could be construed as a potential conflict of interest.

frontiers in Aging Neuroscience

MINI REVIEW
published: 07 December 2021
doi: 10.3389/fnagi.2021.744444

Functionally Assessing the Age-Related Decline in the Detection Rate of Photons by Cone Photoreceptors

*Asma Braham chaouche[1]†, Maryam Rezaei[1]†, Daphné Silvestre[2], Angelo Arleo[3] and Rémy Allard[1]**

[1] School of Optometry, Université de Montréal, Montréal, QC, Canada, [2] Department of Educational and Counselling Psychology, McGill University, Montréal, QC, Canada, [3] INSERM, CNRS, Institut de la Vision, Sorbonne Université, Paris, France

Age-related decline in visual perception is usually attributed to optical factors of the eye and neural factors. However, the detection of light by cones converting light into neural signals is a crucial intermediate processing step of vision. Interestingly, a novel functional approach can evaluate many aspects of the visual system including the detection of photons by cones. This approach was used to investigate the underlying cause of age-related visual decline and found that the detection rate of cones was considerably affected with healthy aging. This functional test enabling to evaluate the detection of photons by cones could be particularly useful to screen for retinal pathologies affecting cones such as age-related macular degeneration. However, the paradigm used to functionally measure the detection of photons was complex as it was evaluating many other properties of the visual system. The aim of the current mini review is to clarify the underlying rationale of functionally evaluating the detection of photons by cones, describe a simpler approach to evaluate it, and review the impact of aging on the detection rate of cones.

Keywords: photoreceptors, cones, photon noise, contrast sensitivity, motion, noise, equivalent input noise, detection of photons

Edited by:
Jessica I. W. Morgan,
University of Pennsylvania,
United States

Reviewed by:
Ramkumar Sabesan,
University of Washington,
United States
Thomas Ach,
University Hospital Bonn, Germany

****Correspondence:***
Rémy Allard
remy.allard@umontreal.ca

† These authors have contributed equally to this work

Received: *20 July 2021*
Accepted: *16 November 2021*
Published: *07 December 2021*

Citation:
Braham chaouche A, Rezaei M, Silvestre D, Arleo A and Allard R (2021) Functionally Assessing the Age-Related Decline in the Detection Rate of Photons by Cone Photoreceptors. Front. Aging Neurosci. 13:744444. doi: 10.3389/fnagi.2021.744444

INTRODUCTION

Age-related macular degeneration (AMD) is a widespread age-related retinal pathology that can severely impair vision by progressively damaging the macula of the retina responsible for central vision. A study on AMD patients found a decline in the ability of retinal photoreceptors to detect light years before the atrophic changes occur (Elsner et al., 2002), which suggests that functional consequences of AMD may be detectable before structural changes (Elsner et al., 2002; Owsley, 2016). Thus, a decline in visual functions could be a useful predictor of vision loss. A functional test sensitive to a decline in the number of photons detected by cones could have a potential prognostic value to aid earlier diagnosis and intervention to slow down the progression of the vision loss.

We recently developed a psychophysical paradigm to evaluate many components of the visual system (Silvestre et al., 2018) including the modulation transfer function of the eye (MTF), the number of photons detected by cones, and different sources of neural noise. This paradigm was used to investigate the impact of healthy aging on various components of the visual system (Silvestre et al., 2019; Braham chaouche et al., 2020), and the results suggest that healthy aging has a considerable impact on the number of photons detected by cones despite standard visual functions like visual acuity and contrast sensitivity being little affected. These results suggest that the number of photons detected by cones could be affected at early stages of some retinal pathologies despite visual acuity and contrast sensitivity being little affected. Thus, this new psychophysical paradigm enabling to assess the number of photons detected by cones could be useful to screen for retinal pathologies.

However, the quantification of the number of photons detected by cones was embedded into a complex psychophysical paradigm developed to evaluate many components of the visual system, which makes the evaluation of only the number of photons detected by cones unnecessarily complex. The first purpose of this mini review is to summarize and clarify how the number of photons detected by cones can be assessed based on two functional measures of contrast sensitivity. The second section reviews the impact of healthy aging on the number of photons detected by cones that was observed using this functional approach.

FUNCTIONALLY MEASURING THE NUMBER OF PHOTONS DETECTED BY CONES

The current section shows how the number of photons detected by cones can be evaluated by measuring contrast sensitivity under two specific visual conditions. The basic rationale is that the number of photons detected by cones varies in time and this variability [referred to as photon noise (Pelli, 1990; Silvestre et al., 2018)] directly depends on the mean number of photons detected. Under some conditions, this variability is limiting contrast sensitivity and its impact can be quantified using a noise paradigm.

Relation Between the Expected Number of Photons Detected and Its Variability

There is a direct relation between the expected number of photons detected by cones and the variability in the number of photons detected. Given that each photon entering the eye has a probability of being detected by a cone, the number of photons detected is stochastic: even when the luminance intensity is constant, the number of photons detected varies with time. This variability is a source of internal noise, named photon noise (Pelli, 1990), that could affect some visual functions like contrast sensitivity. The probability distribution of the number of events follows a Poisson distribution (Hecht et al., 1942; Mueller, 1951), so the variance in the number of photons detected (V) is equal to the expected number of photons detected (N):

$$V = N. \tag{1}$$

Thus, knowing the variability in the number of photons detected by cones indicates the number of photons detected on average.

Impact of Photon Noise on Contrast Sensitivity

If the variation in the number of photons detected by cones (i.e., photon noise) were the only source of internal noise, then contrast sensitivity would be expected to be proportional to the square root of the luminance intensity (Silvestre et al., 2018), which corresponds to the de Vries-Rose law (de Vries, 1943; Rose, 1948). Indeed, since the standard deviation (σ) is equal to the square root of the variance

$$\sigma = \sqrt{V}, \tag{2}$$

then the standard deviation in the number of photons detected in a Poisson distribution is equal to the square root of the expected number of photons detected:

$$\sigma = \sqrt{N}. \tag{3}$$

Given that the number of photons detected by cones is proportional to the retinal luminance intensity (L)

$$N \propto L, \tag{4}$$

then the standard deviation in the number of photons detected is proportional to the square root of the luminance intensity

$$\sigma \propto \sqrt{L}. \tag{5}$$

In contrast units (i.e., relative to the luminance intensity), the standard deviation would be inversely proportional to the square root of the luminance intensity

$$\sigma_{contrast} = \sigma/L, \tag{6}$$

and

$$\sigma_{contrast} \propto 1/\sqrt{L}. \tag{7}$$

Consequently, if the variability in the number of photons detected were the only source of internal noise affecting contrast sensitivity, contrast sensitivity would be proportional to the square root of the luminance intensity (Pelli, 1990; Raghavan, 1995; Silvestre et al., 2018).

The Dominant Source of Noise

Under some visual conditions, the variability in the number of photons detected by cones (i.e., photon noise) is the dominant noise limiting contrast sensitivity. At high luminance intensities, contrast sensitivity is generally independent of luminance intensity (i.e., Weber law; Pelli, 1990; Silvestre et al., 2018), which suggests that it is limited by a source of noise that is independent of luminance intensity (e.g., late noise; Rose, 1948; Pelli, 1990). At low luminance intensities, contrast sensitivity is often proportional to luminance intensity (linear law; Silvestre et al., 2018), which suggests that contrast sensitivity is limited by another source of noise (e.g., early noise). Under some conditions, however, contrast sensitivity is proportional to the square root of the luminance intensity (i.e., de Vries-Rose law), which suggests that contrast sensitivity is limited by the variability in the number of photons detected by cones. For static stimuli, the de Vries-Rose law was observed at relatively high spatial frequencies (**Figure 1**, top right graph) (Silvestre et al., 2018). For dynamic stimuli at low spatial frequencies, the de Vries-Rose law was observed at relatively low temporal frequencies (**Figure 1**, top left graph) (Kelly, 1972). Consequently, under specific conditions, contrast sensitivity would be limited by the variability in the number of photons detected by cones (Pelli, 1990; Allard and Arleo, 2017; Silvestre et al., 2018).

Quantifying the Impact of the Dominant Internal Noise

Interestingly, the impact of the internal noise can be functionally evaluated using a noise paradigm (Pelli, 1981, 1990; Pelli and Farell, 1999) consisting in measuring contrast sensitivity with different levels of visual noise added to the display (**Figure 1**, bottom graph). If the noise added to the display has a weaker impact on contrast sensitivity than the noise within the visual system, then its impact would be negligible (flat asymptote in **Figure 1**, bottom graph). Conversely, if the noise added to the display has a greater impact than the noise within the visual system then it would considerably affect contrast sensitivity (rising asymptote). The external noise level at which the noise starts to considerably affect contrast sensitivity (knee point of the curve in **Figure 1**, bottom graph), the external noise has the same impact on contrast sensitivity as the internal noise. Thus, the impact of the internal noise can be quantified as the level of external noise having the same impact, which is referred to as the equivalent input noise (Pelli, 1981, 1990).

Conveniently, measuring contrast threshold with and without noise (**Figure 1**, second row) is sufficient to derive the equivalent input noise (Pelli and Farell, 1999). Indeed, given that the log-log slope of the two asymptotes is 0 for the flat asymptote and 1 for the rising asymptote (contrast threshold proportional to the noise contrast, bottom graph of **Figure 1**), evaluating the two asymptotes is sufficient to derive the noise level at which they intersect, which corresponds to the equivalent input noise.

Measuring the equivalent input noise under conditions in which contrast sensitivity is limited by photon noise would quantify its impact on contrast sensitivity. In other words, it is possible to quantify the amount of external noise that has the same impact on contrast sensitivity as the variability in the number of photons detected by cones (i.e., photon noise).

However, the impact of an internal noise source on contrast sensitivity does not only depend on the level of the noise, it can also be modulated by a contrast gain preceding this noise source (Lu and Dosher, 2008; Silvestre et al., 2018). Indeed, a contrast gain preceding an internal noise source affects the signal contrast without affecting the noise contrast, which increases the relative impact of the noise.

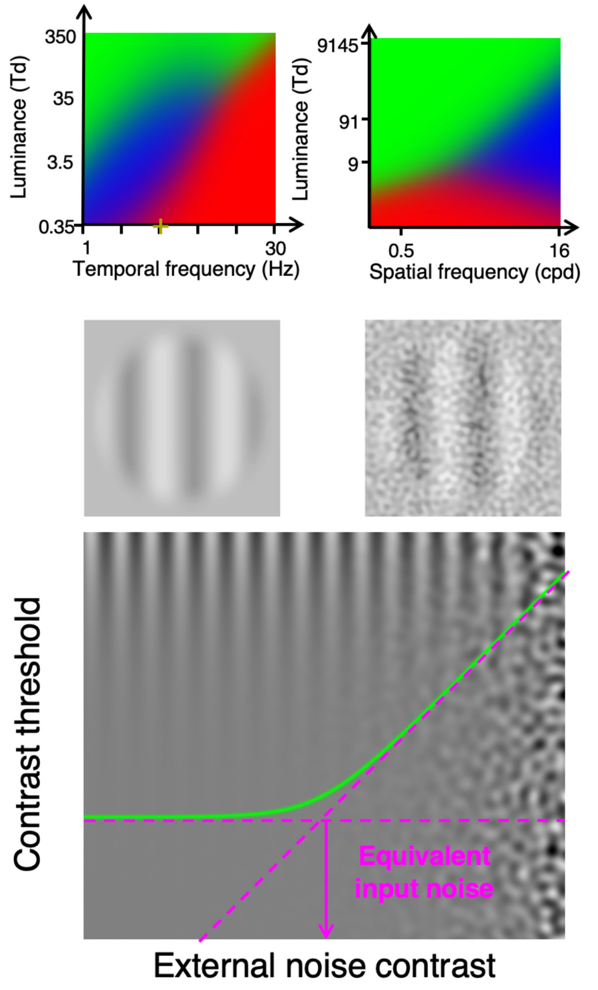

FIGURE 1 | Top row: Dominant noise source identified based on psychophysically measuring contrast sensitivity as a function of luminance intensity. The blue area shows the viewing conditions (luminance intensity and temporal frequency for left graph (Allard and Arleo, 2017), luminance intensity and spatial frequency for right graph (Silvestre et al., 2018) at which the de Vries-Rose law was observed suggesting that the limiting internal noise source is photon noise (variability in the number of photons detected by cones). The green and red areas show conditions in which the Weber law and the linear law were observed, respectively. Second row, stimuli example used to functionally evaluate the detection of light by cones. Bottom graph shows contrast threshold as a function of external noise contrast, which can be used to evaluate the impact of the internal noise (equivalent input noise).

Nonetheless, the detection of light by cones is not preceded by any neural processes, so the only contrast gain preceding the detection of photons by cones is due to optical factors: the MTF of the eye, which reduces the contrast of high spatial frequencies. Thus, if the signal is composed of only low spatial frequencies that are not noticeably affected by the MTF (i.e., retinal image at the same contrast as the stimulus), then the contrast of the signal would not be affected prior to the detection of photons by cones. For static stimuli, contrast sensitivity was found to be limited by the variability in the number of photons detected by cones at high spatial frequencies (top right graph in **Figure 1**).

For moving stimuli composed of low spatial frequencies, contrast sensitivity can be limited by the variability in the number of photons detected by cones at low temporal frequencies and low luminance intensities (top left graph in **Figure 1**). Consequently, by measuring motion contrast sensitivity with and without external noise at a specific spatial frequency, temporal frequency and luminance intensity (e.g., 0.5 cycles per degree, 2 Hz and 10 Td) enables to quantify the variability in the number of photons detected by cones, which is equal to the number of photons detected by cones on average. Thus, the measure of the equivalent input noise under these conditions would directly and only depend on the number of photons detected by cones and should not depend on other processing factors; an observer with a lower detection rate would have a greater equivalent input noise under these viewing conditions.

THE IMPACT OF HEALTHY AGING ON THE DETECTION RATE OF PHOTONS BY CONES

We recently used the psychophysical paradigms developed to evaluate various components of the visual system (Allard and Arleo, 2017; Silvestre et al., 2018) to investigate the effect of healthy aging on various processing components of the visual system. Interestingly, the components that was the most affected with aging was the detection of photons by cones (i.e., photon noise).

In the first study (Silvestre et al., 2019), we investigated the impact healthy aging on spatial contrast sensitivity (i.e., static stimuli) at various spatial frequencies. This study suggested that from 26.5 to 75.9 years old, the detection rate of photons by cones dropped by a factor about 4 (i.e., photon noise increased by a factor of 4, **Figure 2** left graph). In the second study (Braham chaouche et al., 2020), we evaluated the impact of healthy aging on motion contrast sensitivity at various temporal frequencies. This study suggested that from 26.5 to 75.7 years old, the detection rate of photons by cones dropped by a factor about 2.5 (i.e., photon noise increased by a factor of 2.5, **Figure 2** right graph).

A reduction in the number of photons detected by cones does not necessarily imply that cones detected less photons as it could also be the result of less light reaching the retina due to optical factors like the pupil size or cataract development of the lens. However, in these two studies, the age-related declines in the detection rate of photons by cones were not due to age-related miosis (i.e., smaller pupil) because observers were wearing an artificial pupil (2.5 and 3 mm for the two studies, respectively) equating the number of photons entering the eye. Furthermore, the lower photon detection rate cannot be entirely due to cataract development of the lens reducing the number of short-wavelength photons reaching the retina, because a similar age-related effect was observed even when using only high wavelengths that are little affected by cataract development of the lens. Consequently, these two recent studies suggest that the age-related decline in the detection of photons by cones is not explained by a reduced retinal luminance intensity.

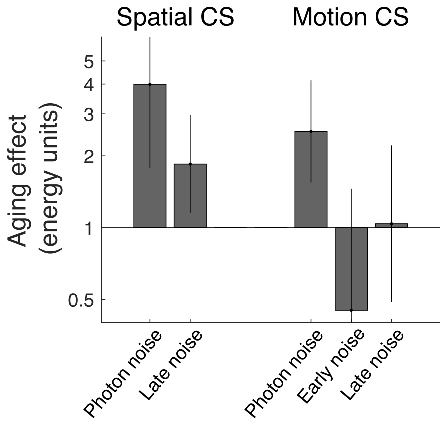

FIGURE 2 | Impact of healthy aging on components of the visual system assessed using a novel noise paradigm for spatial contrast sensitivity (left; Silvestre et al., 2019) and motion contrast sensitivity (right; Braham chaouche et al., 2020). The photon noise represents the variability in the number of photons detected by cones and directly reflects the number of photons detected by cones (i.e., when contrast sensitivity is proportial to the square root of the luminance intensity (de Vries-Rose law). The early noise represents the impact of the dominant noise source for conditions under which contrast sensitivity is proportional to luminance intensity (linear law). The late noise represents the impact of the dominant noise source for conditions under which contrast sensitivity is independent of luminance intensity (Weber's law).

Another ocular factor to consider is intraocular scattering caused by cataract development of the lens, which affects the MTF of the eye by reducing the contrast of high spatial frequencies (Owsley, 2011; Martínez-Roda et al., 2016). In the first study, photon noise was the dominant noise only at high spatial frequencies, so the MTF of the eye had a direct impact on the equivalent input noise. However, the noise paradigm estimated the MTF of the eye, which was subtracted from the equivalent input noise to estimate the photon noise. Thus, the photon noise was theoretically not affected by intraocular scattering affecting high spatial frequencies. Nevertheless, any errors in the estimate of the age-related effect on the MTF would affect the calculated photon noise. In the second study, however, the signal was composed of only low spatial frequencies (0.5 cycles per degree) so the MTF of the eye was expected to have a negligible impact (Watson, 2013). Indeed, an age-related contrast gain reduction due to ocular factors is expected only at high spatial frequencies (Owsley, 2011; Martínez-Roda et al., 2016). Furthermore, any contrast loss due to optical factors would also affect the impact of neural noise, but no significant age-related effect on neural noise was observed (**Figure 2**, right). In other words, an age-effect on the equivalent input noise was observed to moderate luminance intensities (i.e., when photon noise dominated) and not to high luminance intensities (i.e., when late neural noise dominated). Thus, measuring photon noise at low spatial frequencies using motion contrast sensitivity makes the estimate of the photon noise more direct and should be more accurate. To avoid worrying about the MTF of the lens, photon noise should be measured at low spatial frequencies, which is possible using motion contrast sensitivity.

DISCUSSION

The current mini review highlights a new approach to non-invasively evaluate the detection rate of photons by cones. This functional approach enables to address a crucial visual process: the transduction of light into neural signals by cones. By measuring contrast sensitivity with and without external noise in specific conditions in which the variability in the number of photons detected by cones is limiting contrast sensitivity, the number of photons detected by cones can be evaluated. The current review therefore provides a simple functional paradigm to evaluate the efficiency of cones to detect light.

Other traditional techniques are also sensitive to the number of photons detected. For instance, imaging densitometry (e.g., Rushton and Henry, 1968) and subjective color-matching techniques (e.g., Burns et al., 1987) are sensitive to cone photopigments required in the absorption of photons. Such techniques were used to investigate the impact of aging on cone photopigments and the results were consistent with an age-related decline in the number of photons detected by cones (Keunen et al., 1987; Swanson and Fish, 1996). An advantage of the noise paradigm is that measuring the photon noise only requires measuring contrast sensitivity under two specific conditions, which only requires a few minutes without requiring a long light adaptation phase. Further studies are required to compare these techniques directly.

When studying age-related physiological alterations in the retina, it is often relevant to seek for functional correlates to quantify the impact of physiological alterations on visual functions. Typically, visual functions (e.g., visual acuity or contrast sensitivity) are evaluated at high luminance intensities at which performance depends little on luminance intensity. For instance, contrast sensitivity saturates at high luminance intensities (Weber law), which implies that it is independent of the amount of light detected by cones. Consequently, a lower detection rate of light would likely have little impact on contrast sensitivity at high luminance intensities. The fact that all visual functions require the phototransduction of light into neural signals does not imply that a lower detection rate of light would necessarily affect performance. To address the ability of cones to detect photons, a visual function should be evaluated under conditions in which performance critically depends on the number of photons detected by cones. The current mini review shows that it is possible to evaluate the detection of light by cones by measuring contrast sensitivity under two specific visual conditions. This novel approach provides a new way to assess the efficiency of cones to detect light.

Surprisingly, healthy aging was found to have a considerable impact on the detection rate by cones. Some age-related physiological changes at the retinal level could explain the decline in detection rate of photons by cones. One possible age-related alteration is a morphological one: the degeneration of the rods with aging induces a loss of alignment of the cones which lose their support (Curcio et al., 1993; Panda-Jonas et al., 1995) and reduces their detection rate (Cunea and Jeffery, 2007). Another possible change occurring with aging is a molecular one: a high concentration of cGMP (a secondary messenger in phototransduction) inhibits phototransduction and thus cone activation (Angueyra and Rieke, 2013). Further studies are needed to investigate the physiological cause of the age-related decline in the detection of light by cones.

A common symptom in early AMD is the difficulty under dim light conditions, which is consistent with the hypothesis that early AMD affects the detection rate of photons (Elsner et al., 2002) despite standard functions evaluated under clinical conditions are not considerably affected (Owsley, 2016). Consequently, evaluating the detection rate of photons by cones using the functional approach described in the current review could be useful to detect earlier signs of AMD. By enabling an earlier diagnosis, this new tool could prevent the progression of the disease by providing the opportunity to implement therapies at earlier stages of the disease. Further studies are required to investigate if measuring the detection rate of light by cones could be useful to detect early signs of AMD.

AUTHOR CONTRIBUTIONS

AB, MR, and RA co-wrote the mini review. DS and AA proofread the review. All authors contributed to the article and approved the submitted version.

FUNDING

This research was supported by grants from the Fondation des Maladies de l'Oeil, the Réseau de Recherche en Santé de la Vision, and the Fondation Antoine-Turmel to RA and by ANR - Essilor SilverSight Chair ANR-14-CHIN-0001 to AA.

REFERENCES

Allard, R., and Arleo, A. (2017). Photopic motion sensitivity at high temporal frequencies is limited by the dark light of the eye, not quantal noise. *J. Vis.* 17:600. doi: 10.1167/17.10.600

Angueyra, J. M., and Rieke, F. (2013). Origin and effect of phototransduction noise in primate cone photoreceptors. *Nat. Neurosci.* 16, 1692–1700.

Braham chaouche, A., Silvestre, D., Trognon, A., Arleo, A., and Allard, R. (2020). Age-related decline in motion contrast sensitivity due to lower absorption rate of cones and calculation efficiency. *Sci. Rep.* 10:16521. doi: 10.1038/s41598-020-73322-7

Burns, S. A., Elsner, A. E., Lobes, L. A., and Doft, B. H. (1987). A psychophysical technique for measuring cone photopigment bleaching. *Invest. Ophthalmol. Vis. Sci.* 28, 711–717.

Cunea, A., and Jeffery, G. (2007). The ageing photoreceptor. *Vis. Neurosci.* 24, 151–155.

Curcio, C. A., Millican, C. L., Allen, K. A., and Kalina, R. E. (1993). Aging of the human photoreceptor mosaic: evidence for selective vulnerability of rods in central retina. *Invest. Ophthalmol. Vis. Sci.* 34, 3278–3296.

de Vries, H. L. (1943). The quantum character of light and its bearing upon threshold of vision, the differential sensitivity and visual acuity of the eye. *Physica* 10, 553–564.

Elsner, A. E., Burns, S. A., and Weiter, J. J. (2002). Cone photopigment in older subjects: decreased optical density in early age-related macular degeneration. *J. Optic. Soc. Am. A*. 19, 215–222. doi: 10.1364/josaa.19.000215

Hecht, S., Shlaer, S., and Pirenne, M. H. (1942). Energy, quanta and vision. *J. Gen. Physiol.* 1941, 819–840.

Kelly, D. H. (1972). Adaptation effects on spatio-temporal sine-wave thresholds. *Vis. Res.* 12, 89–101.

Keunen, J. E., van Norren, D., and Van Meel, G. J. (1987). Density of foveal cone pigments at older age. *Invest. Ophthalmol. Vis. Sci.* 28, 985–991.

Lu, Z.-L., and Dosher, B. A. (2008). Characterizing observers using external noise and observer models: assessing internal representations with external noise. *Psychol. Rev.* 115, 44–82.

Martínez-Roda, J. A., Vilaseca, M., Ondategui, J. C., Aguirre, M., and Pujol, J. (2016). Effects of aging on optical quality and visual function. *Clin. Exp. Optomet.* 99, 518–525. doi: 10.1111/cxo.12369

Mueller, C. (1951). Frequency of seeing functions for intensity discrimination at various levels of adapting intensity. *J. Gen. Physiol.* 34, 463–474.

Owsley, C. (2011). Aging and vision. *Vis. Res.* 51, 1610–1622. doi: 10.1016/j.visres.2010.10.020

Owsley, C. (2016). Vision and Aging. *Annu. Rev. Vis. Sci.* 2, 255–271. doi: 10.1146/annurev-vision-111815-114550

Panda-Jonas, S., Jonas, J. B., and Jakobczyk-Zmija, M. (1995). Retinal photoreceptor density decreases with age. *Ophthalmology* 102, 1853–1859.

Pelli, D. G. (1981). *The Effects of Visual Noise*. Cambridge: Cambridge University.

Pelli, D. G. (1990). "The quantum efficiency of vision," in *Visual Coding and Efficiency*, ed. C. Blakemore (Cambridge: Cambridge University Press), 3–24.

Pelli, D. G., and Farell, B. (1999). Why use noise? *J. Opt. Soc. Am. A. Opt. Image Sci. Vis.* 16, 647–653.

Raghavan, M. (1995). *Sources of Visual Noise*. Syracuse: Syracuse University.

Rose, A. (1948). The sensitivity performance of the human eye on an absolute scale. *J. Opt. Soc. Am.* 38, 196–208. doi: 10.1364/JOSA.38.000196

Rushton, W. A. H., and Henry, G. H. (1968). Bleaching and regeneration of cone pigments in man. *Vis. Res.* 8, 617–631. doi: 10.1016/0042-6989(68)90040-0

Silvestre, D., Arleo, A., and Allard, R. (2018). Internal noise sources limiting contrast sensitivity. *Sci. Rep.* 8:2596. doi: 10.1038/s41598-018-20619-3

Silvestre, D., Arleo, A., and Allard, R. (2019). Healthy aging impairs photon absorption efficiency of cones. *Invest. Ophthalmol. Vis. Sci.* 60, 544–551. doi: 10.1167/iovs.18-25598

Swanson, W. H., and Fish, G. E. (1996). Age-related changes in the color-match-area effect. *Vis. Res.* 36, 2079–2085. doi: 10.1016/0042-6989(95)00280-4

Watson, A. B. (2013). A formula for the mean human optical modulation transfer function as a function of pupil size. *J. Vis.* 13:18. doi: 10.1167/13.6.18

Conflict of Interest: The authors declare that the research was conducted in the absence of any commercial or financial relationships that could be construed as a potential conflict of interest.

frontiers
in Aging Neuroscience

REVIEW
published: 25 February 2022
doi: 10.3389/fnagi.2022.778404

Variability in Retinal Neuron Populations and Associated Variations in Mass Transport Systems of the Retina in Health and Aging

*Moussa A. Zouache**

John A. Moran Eye Center, Department of Ophthalmology and Visual Sciences, University of Utah, Salt Lake City, UT, United States

Aging is associated with a broad range of visual impairments that can have dramatic consequences on the quality of life of those impacted. These changes are driven by a complex series of alterations affecting interactions between multiple cellular and extracellular elements. The resilience of many of these interactions may be key to minimal loss of visual function in aging; yet many of them remain poorly understood. In this review, we focus on the relation between retinal neurons and their respective mass transport systems. These metabolite delivery systems include the retinal vasculature, which lies within the inner portion of the retina, and the choroidal vasculature located externally to the retinal tissue. A framework for investigation is proposed and applied to identify the structures and processes determining retinal mass transport at the cellular and tissue levels. Spatial variability in the structure of the retina and changes observed in aging are then harnessed to explore the relation between variations in neuron populations and those seen among retinal metabolite delivery systems. Existing data demonstrate that the relation between inner retinal neurons and their mass transport systems is different in nature from that observed between the outer retina and choroid. The most prominent structural changes observed across the eye and in aging are seen in Bruch's membrane, which forms a selective barrier to mass transfers at the interface between the choroidal vasculature and the outer retina.

Keywords: retina, retinal neurons, mass transport, retinal vasculature, Bruch's membrane, choriocapillaris, aging, photoreceptors

Edited by:
Ann E. Elsner,
Indiana University, United States

Reviewed by:
Robert Linsenmeier,
Northwestern University,
United States
Robert Casson,
University of Adelaide, Australia

Correspondence:
Moussa A. Zouache
moussa.zouache@hsc.utah.edu

Specialty section:
This article was submitted to
Cellular and Molecular Mechanisms
of Brain-aging,
a section of the journal
Frontiers in Aging Neuroscience

Received: *16 September 2021*
Accepted: *13 January 2022*
Published: *25 February 2022*

Citation:
Zouache MA (2022) Variability
in Retinal Neuron Populations
and Associated Variations in Mass
Transport Systems of the Retina
in Health and Aging.
Front. Aging Neurosci. 14:778404.
doi: 10.3389/fnagi.2022.778404

INTRODUCTION

Increasing age is associated with a broad range of visual impairments that include loss of spatial contrast sensitivity, decreased light and wavelength sensitivities, deficits in the processing of temporal information and slowing of visual processing speed (Zhang et al., 2008; Owsley, 2011). These changes can have dramatic consequences on the quality of life of those affected (Owsley and Burton, 1991; Owsley et al., 1998); however, they remain poorly understood. Improving our understanding of the mechanisms involved in age-related vision impairments is essential to design strategies to slow or even reverse them. It can also help determine characteristics that may be used to differentiate individuals who "age well" – who suffer minimum or manageable vision loss as they age – to those who do not, and, in doing so, assist in identifying precursors of eye diseases (Owsley, 2011).

Every part of the eye undergoes changes as we age (Owsley, 2011; Grossniklaus et al., 2013). The human eye, like that of other vertebrates, essentially consists of concentric layers of tissue enclosing a fluid-filled chamber (see **Figure 1A**). The primary function of the cornea, iris, and lens located in the anterior part of the eye is to focus and direct light toward the posterior segments, where the retina lies (Zouache et al., 2016b); see **Figure 1B**. It is there that photoreceptor cells perform phototransduction, or the conversion of photons into electrochemical impulses. Signals from the photoreceptors are received and processed by an intricate machinery of neurons and turned into action potentials carried by the axons of approximately one million retinal ganglion cells (see **Figures 1C,D**). These axons run along the inner surface of the retina before converging into the optic nerve, which travels to the brain (Oyster, 1999; Masland, 2012).

While many age-related vision impairments are driven by transmission losses in the optical media of the eye (Hockwin and Ohrloff, 1984; Reim, 1984; Rohen and Lütjen-Drecoll, 1984; Owsley and Burton, 1991; Pierscionek, 1996), cellular and molecular changes occurring within the retina also play an important role (Weale, 1986; Marshall, 1987; Grossniklaus et al., 2013; Campello et al., 2021). Retinal senescence is likely driven by a complex series of changes that affect multiple cellular and extracellular elements that interact with each other (Marshall, 1987). However, our understanding of normal interactions between retinal elements and processes necessary for tissue function and survival is considerably limited. The role that these interactions and their alterations play in retinal aging is therefore not fully appreciated, which considerably restricts our ability to identify strategies to effectively slow or prevent visual changes associated with increasing age.

The purpose of this review is to assess how documented spatial and age-related variations in retinal neuron populations relate to changes observed in the structure and function of the mass transport systems to the retina. Homeostasis, metabolism, and survival of retinal cells rely on the adequate supply of metabolism substrates and clearance of metabolic waste products from the retina. These processes are supported by a dual circulatory system formed by the choroidal and retinal vasculatures (see **Figure 2**). The choroidal vasculature and its microvascular bed, the choriocapillaris, support the metabolic requirement of the outer half of the retina, which is mainly composed of photoreceptors and a monolayer of epithelial cells. The inner part of the retina, which mainly consists of neuronal and glial cells, is sustained by the retinal vasculature (Wong-Riley, 2010).

An underlying hypothesis to this work is that age-related changes in the structure and function of the mass transport systems sustaining the retina correlate with variations in retinal cell populations observed in aging. This would support the idea that the transport of material that is key to healthy cell metabolism is adjusted in aging, so that correlated changes in the retina and its metabolite delivery system are adaptive. Departure from this correlated behavior may then put the eye at a higher risk of vision impairments and disease. The first step in testing this hypothesis is to determine the nature of the relation between retinal neuron populations and mass transport systems in health. The human eye offers an ideal template to explore this relationship. Spatial variations in the structure of the retina and choroid are well-documented and, within an adequate framework, may be harnessed to identify correlated patterns of change. Aging can provide valuable insights into the resilience of correlated behaviors to perturbations occurring over large timescales. Changes in the relation between retinal neurons and their respective metabolite delivery system in aging are therefore also explored.

FRAMEWORK FOR INVESTIGATION

This review investigates biological systems – retinal neurons and their respective metabolite delivery systems – often considered in isolation. An important factor to consider when assessing relations between any biological systems is the characteristic length- and timescales associated with the elements, systems, and processes at play (Lesne, 2013).

Scale and Interactions

Many interactions between retinal cells and the retinal and choroidal vasculatures occur through a movement of molecules. For instance, the movement of oxygen, nutrients, metabolism byproducts, signaling proteins and growth factors between vasculatures and neurons partly determines the metabolism of these cells, their function, and their ability to survive and adapt to changes in their microenvironment. Exchange between neurons and the retinal and choroidal vasculatures may be studied at the scale of cells, tissue or even organs (see **Figure 1**). Phenomena associated with each scale provide different – and sometime overlapping – information on the state of retinal components. For instance, quantum mechanics may be better suited to describe phototransduction (Sia et al., 2014) whereas stochastic kinetics is more appropriate to model chemical kinetics and generate reaction constants (Lecca, 2013). As separate models may be applied to understand and describe processes occurring at different scales, the challenge becomes to integrate them into a framework capable of capturing the interplay between them (Lesne, 2013, 2007; Green and Batterman, 2017).

Advances in molecular techniques have made it possible to explore variations in genome, epigenome, transcriptome, metabolism and immune response in the retina of human donor eyes (Campello et al., 2021). These methods have the potential to provide a resolution sufficient to dissect spatial and temporal changes such as the ones observed in aging up to the level of a cell (Wang S. et al., 2020). Beyond the theoretical and technical issues associated with the processing and analyses of these large datasets (Mattmann, 2013; Leonelli, 2019; Teschendorff, 2019), the characteristic length-scale associated with these methods is too small to extract data pertaining to interactions between cells and extracellular components. For instance, transcription in photoreceptors is partly determined by external stimuli, some of which result from chains of events involving the choroidal vasculature. However, the choroid is far upstream (or downstream) in this chain of event; measuring its effect on photoreceptors may not be possible because of processes involving other retinal components. It is therefore difficult to

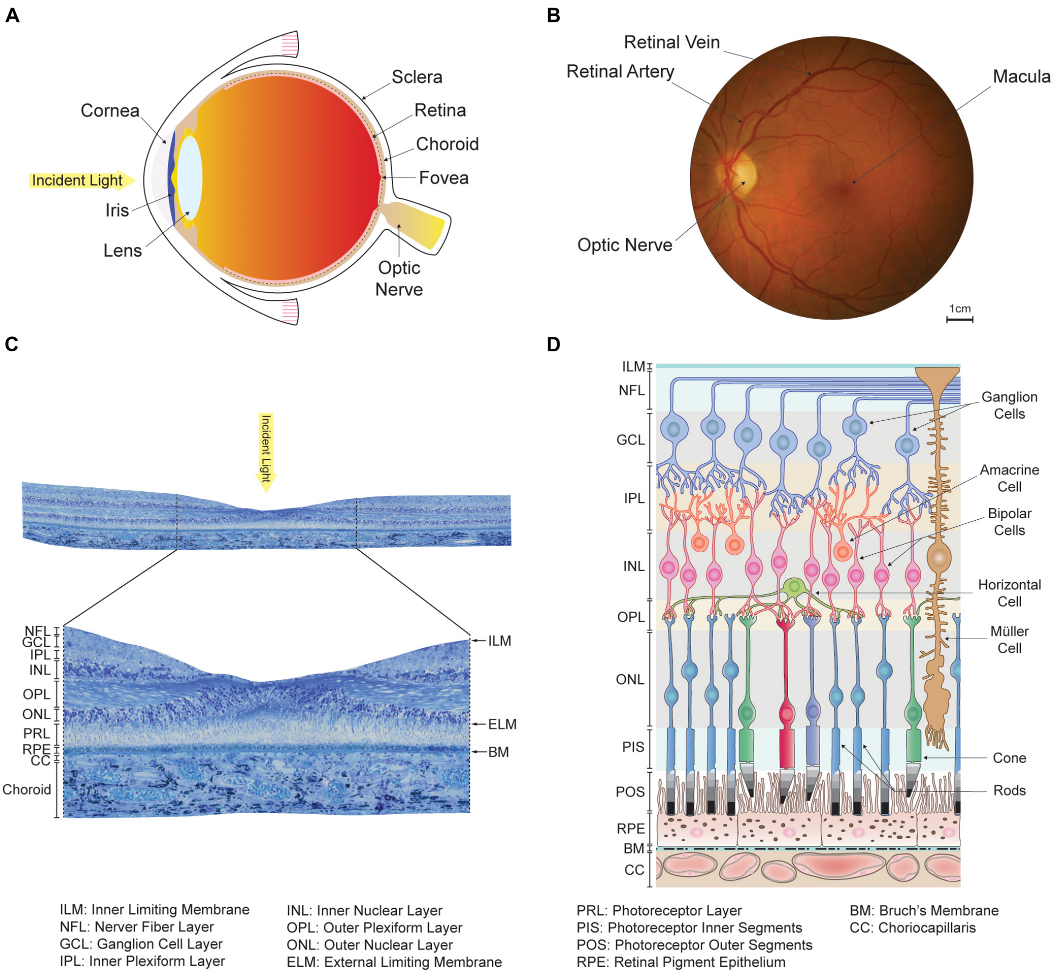

FIGURE 1 | Organization of the human eye and retina. **(A)** Schematic of a human eye. The anterior segments, which include the cornea, iris and lens, direct light toward the retina located in the back of the eye. **(B)** En-face view of the retina captured in a healthy individual using an ophthalmoscope. The optic nerve and large retinal arteries and veins are visible, but the underlying choroidal vasculature is not. The fovea, a region of the retina specialized for high-acuity and color vision, lies at the center of the approximately 5.5 mm wide macula. **(C)** View of a transverse section of the retina taken from a human donor eye in the macula. Histologically, the retina appears as layered tissue formed by retinal neurons, endothelium, and glial cells. **(D)** Schematic of the cellular organization of the retina and choriocapillaris, adapted and modified with permission from Campello et al. (2021). The location of histologically defined retinal layers is indicated. The outer retina consists of the retinal pigment epithelium and photoreceptor outer and inner segments. The inner retina includes horizontal, bipolar, amacrine and ganglion cells, which are all involved in the processing of signals originating from the photoreceptors.

detect the effect of the choroidal vasculature on photoreceptors at this scale. At the other end of the spectrum of length-scales, interactions between retinal neurons and the retinal vasculature are impossible to characterize at the organ level as this scale is too large to consider them as distinct entities.

To ensure that most of the information relevant to interactions between retinal neurons and their respective metabolite delivery systems is captured, this review focuses on structures and processes at the cellular and tissue scales.

From Geometry to Mass Transport

Capturing variations in the structures and processes determining mass exchange at the cellular and tissue levels experimentally is challenging. Our understanding comes mostly from cross-sectional analyses of human donor eyes (Oyster, 1999), which only provide snapshots of variations across the eye and over time. In addition, these analyses are fundamentally limited by the scarcity of human donor eyes in certain age groups. Animal and *in vitro* models have been used to attempt to address this limitation (Conn, 2006); however, the human retina has singular properties that render extrapolation from these systems difficult (Hussain et al., 2010; Kam et al., 2019). In this review, we harness the fact that local mass transport is partly determined by the morphology of cells and the specific geometry of their interface with other tissue components. We can therefore ascertain that variabilities in the structure of the retina provide an indirect way of assessing variations in transport processes. This approach is in some ways imperfect, as structures alone are often insufficient to describe mass transport within any biological system. A good

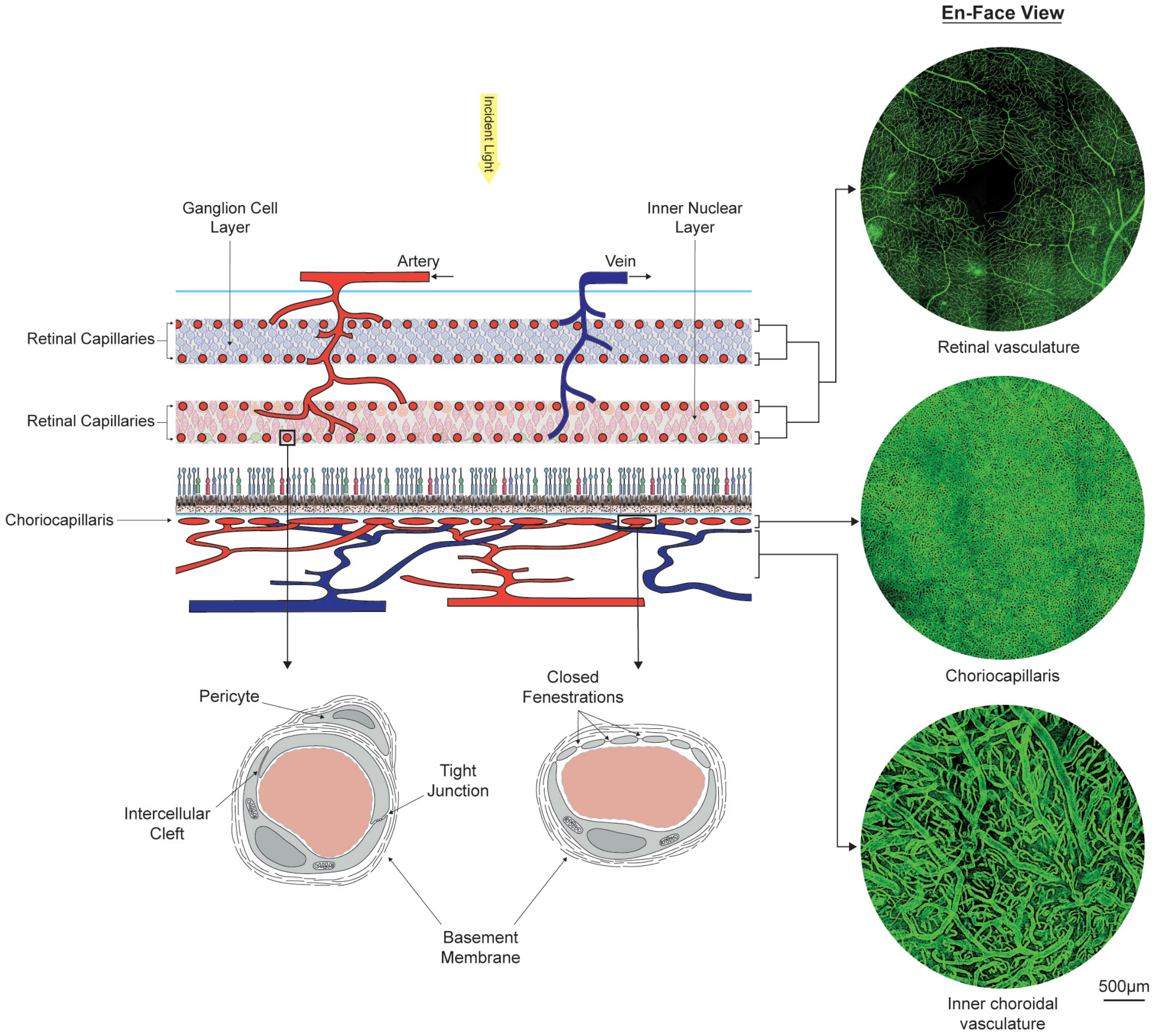

FIGURE 2 | Organization, morphology, and ultrastructure of the dual circulatory systems of the retina formed by the retinal and choroidal vasculatures. The inner two-thirds of the retina is sustained by at least four layers of retinal capillaries, which connect alternating arterial and venous branches. Oxygen and nutrients are supplied to the outer one third of the retina by the choriocapillaris, located externally to the retinal pigment epithelium. En-face visualizations of the retinal and choroidal vasculatures at the fovea were obtained by immunostaining portions of retinas and choroid with Ulex Europaeus Agglutinin and imaging them using confocal microscopy. Stark differences in vascular density between the choriocapillaris and the retinal capillary bed can be observed. Ultrastructural differences are also present. Retinal capillaries form a tightly regulated barrier between blood and tissue. Capillaries from the choriocapillaris present with closed fenestrations, which facilitate the transfer of small and large molecules.

understanding of the fundamental laws governing transport phenomena and how specific structures influence them is necessary to draw any interpretation (Lighthill, 1972). This understanding often comes from experimental and theoretical models developed specifically to study well-defined systems and requires careful considerations centered around basic principles of mass transfers.

Fundamentals of Mass Transfers for Cells and Tissues

Within blood vessels, molecules are transported through a combination of advection and diffusion. Diffusion is the net movement of material along gradients of concentration. Advection is the movement of material due to the motion of a fluid; it is the dominant transport mechanism in blood vessels. Advection is a more efficient mode of transport, and its prominence with respect to diffusion is determined by the balance between pressure gradients along arteries, capillaries and veins that drive blood flow and factors effectively creating a resistance to this flow. Most of this vascular resistance is caused by the diameter of blood vessels and the viscosity of blood (Lighthill, 1972). The Hagen-Poiseuille law, which applies to incompressible uniform viscous fluids flowing through cylindrical tubes (Batchelor, 2000), is commonly used to describe the salient features of the flow associated with the specific geometry of blood vessels (Lighthill, 1972; Pournaras et al., 2008). This approximate law states that blood velocity varies as R^2 and that the blood flow rate varies as $R^2\Delta P/\mu L$, where R and L are the radius and length of the vessel considered, respectively, ΔP is the pressure difference between the entry and exit of the vessel and μ is the viscosity of blood. Blood velocity is minimal within capillaries, where vessel radii are smallest and most of the exchange between plasma and tissue occur.

Molecules contained in plasma may cross blood vessel walls through passive or active transport. Passive transport does not require any input of energy from the cell and instead relies on the tendency of molecules to travel from regions of low concentration to regions of high concentration. The main types of passive transport across cells are diffusion, facilitated diffusion (diffusion mediated by transport proteins embedded in plasma membranes), filtration and osmosis (see **Figure 3**). The transfer of oxygen from blood to tissue relies solely on molecular diffusion, whereas glucose reaches tissue through facilitated diffusion (by way of transporters including GLUTs) (Mantych et al., 1993). Filtration consists of the movement of water and soluble molecules along gradients of hydrostatic pressure. Active transport typically involves a movement of molecules from regions of high concentration to regions of low concentration (thus ensuring that concentration gradients are maintained). It requires energy input from the cell in the form of adenosine triphosphate (ATP) or membrane potential and may also involve moving material through transendothelial channels or vesicles (also called caveolae). Macromolecules including lipids, insulin and albumin typically cross endothelial cells through active transport (Simionescu et al., 2002). Passive transport across microvascular beds has been extensively studied both experimentally and theoretically. Active transport is tightly linked

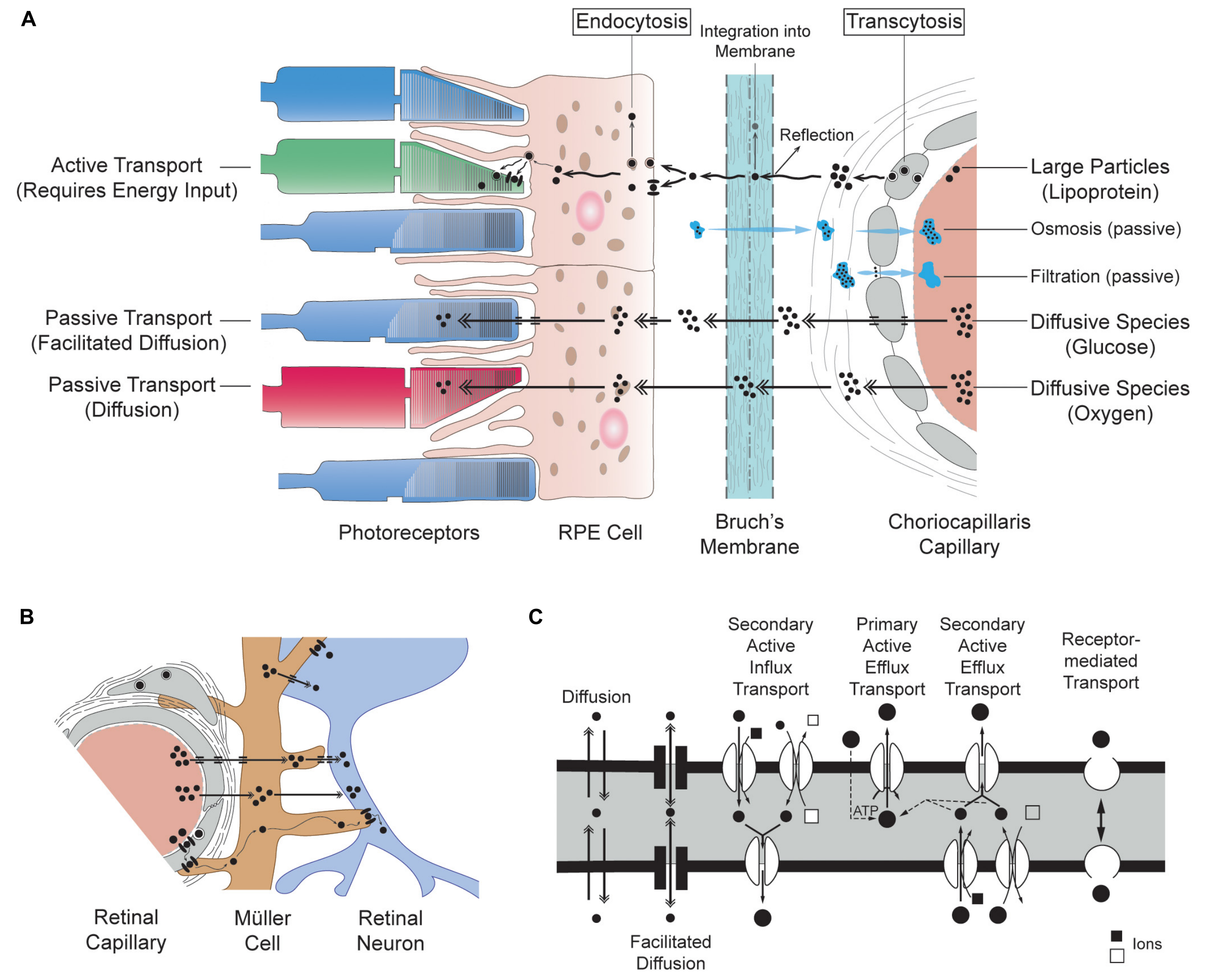

FIGURE 3 | Schematic representation of mass transport systems of the retina. The movement of molecules shown in **(A,B)** is directed from vasculatures to tissue only for simplicity; although, displayed mechanisms are also applicable to the opposite direction. **(A)** Simplified schematic of the transfer of material across choriocapillaris endothelial cells, Bruch's membrane, RPE cells and photoreceptors (not to scale). **(B)** Mass transfers in the inner retina illustrating the symbiotic relationship between retinal endothelial cells, glial cells (here a Müller cell) and retinal neurons. **(C)** Schematic of the mechanisms of transport across cells adapted and modified from Hosoya and Tachikawa (2012). Transport is traditionally classified as passive (diffusion), carrier-mediated (facilitated diffusion, primary active efflux and secondary active influx and efflux) or receptor-mediated. The conventions used to depict mechanisms of transport in **(A,B)** are consistent with **(C)**.

to several interdependent factors including cellular metabolism, microenvironment and external stimuli and is therefore often more complex to model as compared to passive transport. Our understanding of active transport across capillaries relies primarily on classic experimental studies of microvascular permeability to lipid-insoluble endogenous and non-endogenous macromolecules (Simionescu et al., 2002; Sarin, 2010).

The movement of molecules across capillaries is partly determined by the physical characteristics of structures composing them such as the thickness of their basement membranes and the diameter and spatial distribution of inter-endothelial junctions. The molecular composition of the extravascular space, the structure of cells consuming or delivering transported material and their distance from vascular compartments also influence molecular transfers significantly. At a basic tissue scale (~1 mm), the movement of material is generally described using average statistics based on mean squared displacements of molecules. Within this framework, the effect of structures influencing the movement of material – such as the geometry of capillaries and composition of the extravascular space – is described using averaged characteristics, such as diffusivity, permeability and cellular density. These measures translate the underlying small-scale structure of molecules, cells and media across which transfers occur; they may vary in space and time and are often determined experimentally. Within frameworks using averaged statistics (in tissue level models for instance), the transfer of diffusive molecules between the vasculature and tissue is mainly a function of blood flow, the geometry of capillaries, the concentration of a specific compound in blood and its consumption in tissue (which is generally a function of the number of cells consuming this compound per volume of tissue) and the resistance of the capillary wall, extravascular space and cells to diffusion (Keener and Sneyd, 2009; Zouache et al., 2019). The topology of a vascular bed is an important factor to consider when assessing its capacity for tissue perfusion (LaBarbera, 1990; West et al., 1997; Zouache et al., 2016a). Another element often examined is the vascularity – or vascular density – of a vascular bed. This parameter describes the fraction of tissue occupied by blood vessels and is calculated over a closed volume. Variations in vascular density give insights into spatial differences in metabolite supply and tissue energy requirements.

Barriers to Transfers

In the retina, the transfer of metabolism substrates and by-products to and from blood must be adequately controlled and regulated. This is the main function of the blood-retinal barrier (BRB), which involves several cellular and extracellular structures regulating transfers between retinal capillaries and the inner part of the retina (inner BRB, iBRB) and between the choriocapillaris and the outer part of the retina (outer BRB, oBRB) (Cunha-Vaz, 1976). Movement across these barriers is generally described within frameworks that place the cell at the center of all transport processes. While the terminology employed may differ, this cell-centric description is entirely encompassed in the fundamental framework described in Section "Fundamentals of Mass Transfers for Cells and Tissues." Within the cell-centric framework, the exchange of molecules is described in terms of transcellular and paracellular pathways (Pournaras et al., 2008; Nakanishi et al., 2016). The movement of water, small nutrients, ions, and macromolecules across endothelial cells occurs through diffusion, carrier mediated or receptor-mediated transport (see **Figure 3C**), which involve both passive and active types of transport. Most proteins are non-selectively transported across endothelial cells in vesicles (carrier-mediated transport) (Feng et al., 1996; Simionescu et al., 2002; Minshall et al., 2003; Stan, 2005; Mehta and Malik, 2006). The paracellular pathway allows for passive transport across the space separating endothelial cells and is modulated by intercellular adhesion and the structure of intercellular clefts (see **Figure 2**). Tight junctions form size- and charge-selective semipermeable barriers to diffusion (Van Itallie and Anderson, 2004; Campbell and Humphries, 2012; Zihni et al., 2016).

The extracellular structures involved in the regulation of transfers between blood and tissue are the glycocalyx and extracellular matrix. The glycocalyx consists of a coat of macromolecules bound to the apical and luminal plasma membrane of epithelia and endothelial cells (Möckl, 2020). Through its molecular structure it acts as a charge-selective barrier to plasma membranes. It affects oncotic pressure gradients driving capillary filtration (Mehta and Malik, 2006) and may regulate protein diffusion (Freeman et al., 2018). Another important function of the glycocalyx is to attenuate the effect of mechanical forces caused by the flow of blood on endothelial cells and thus to preserve their function (Gouverneur et al., 2006). The extracellular matrix consists of the assembly of many components secreted by surrounding cells. Its composition regulates transport in and out of cells, and therefore influences cellular homeostasis and cell-to-cell signaling (Hubmacher and Apte, 2013).

Experimental Data

Many experimental methods have been applied to characterize retinal and choroidal structures and processes relevant to the study of retinal mass transport systems at the cellular and tissue levels. Investigations using histology rely on a variety of methods to process and image tissue dissected from human eyes. These studies may be limited by tissue availability and the difficulty of phenotyping donor eyes for diseases of the anterior or posterior segments. Variability in times to fixation and processing methods may cause morphological changes that need to be accounted for Tran et al. (2017). Differences in the location and size of the samples analyzed can significantly limit comparisons between studies. Inconsistencies between studies using histology may also be due to the lack of correction for multiple counting of cells on sections and for tissue shrinkage (Curcio et al., 1990; Harman et al., 1997). The absence of consensus on diagnostics and post-processing methods (Garza-Gisholt et al., 2014) can also explain discrepancies between findings. *In vivo* imaging techniques include optical coherence tomography (OCT), optical coherence tomography angiography (OCTA) and adaptive optics (AO). OCT uses low-coherence interferometry to generate cross-sectional images (B-scans) of optical scattering from retinal structures with a longitudinal and lateral spatial resolution of a few micrometers (Huang et al., 1991). By serially recording

B-scans, OCTA captures variations in the intensity and phase of backscattered light due to intrinsic movement within tissue, which comes mainly from erythrocytes in blood vessels (Kashani et al., 2017). OCTA has been used to visualize and quantify the retinal (Coscas et al., 2016; Iafe et al., 2016; Garrity et al., 2017; Lavia et al., 2019) and choroidal (Maruko et al., 2018; Wang et al., 2018; Zheng et al., 2019; Wang E. et al., 2020) vasculatures, including in aging (Spaide, 2016; Wei et al., 2017; Lavia et al., 2019; Zheng et al., 2019) and disease (Laíns et al., 2021). OCT and OCTA provide valuable tissue-level information on the retina; however, the lateral resolution that they offer is not sufficient to image individual cells. AO systems have so far mostly been used in research settings. A large number of groups robustly image and quantify the retina at the cellular and sub-cellular levels using AO, with instrumentation capabilities varying according to applications (Marcos et al., 2017). AO-based systems have been applied to image a variety of neurons including cones (Chui et al., 2008a,b; Song et al., 2011; Zhang et al., 2015), rods (Dubra et al., 2011; Merino et al., 2011; Wells-Gray et al., 2018), and ganglion cells (Liu et al., 2017); subretinal structures such as retinal pigment epithelial cells (Liu et al., 2016) and choriocapillaris (Kurokawa et al., 2017); normal and remodeled retinal vasculature (Chui et al., 2016; Sapoznik et al., 2018); and structures and processes associated with various pathologies of the retina (Langlo et al., 2014; Querques et al., 2014; King et al., 2017; Zhang et al., 2017; Karst et al., 2019; Miller et al., 2019; Hammer et al., 2020). Blood flow in the retinal and choroidal vasculatures has been assessed using several dye dilution techniques such as fluorescent dye angiography and scanning laser ophthalmoscope angiography. Dye dilution techniques rely on the injection of a dye into the general circulation and its visualization as it travels through and across blood vessels (Wei et al., 2018). Extractable information includes structural characteristics of blood vessels and average travel time, which has a dependence on the diffusivity of the dye used (Zouache et al., 2016a).

CELLULAR ORGANIZATION OF THE RETINA

The retina is composed of three classes of cells – neurons, glial cells and epithelial cells – organized in four distinct layers; see **Figure 1C**. Its outermost layer is the retinal pigment epithelium (RPE), which consists of a continuous monolayer of approximately hexagonal pigmented cells. The neural retina lies internally to the RPE and is formed by three nuclear layers enclosing neuronal cell bodies and two plexiform layers of synapses (see **Figure 1D**; Oyster, 1999).

Neuronal Organization

General classifications of retinal neurons are based on morphological and physiological analyses of human tissue. They are consistent with methods based on single-cell RNA sequencing (Liang et al., 2019; Menon et al., 2019; Peng et al., 2019; Orozco et al., 2020; Yan et al., 2020; Yi et al., 2020). The outermost layer of the neural retina is formed by approximately 100 million photoreceptors arranged in a continuous array. Approximately 95% of these cells are rods (Curcio et al., 1990), which use rhodopsin as a pigment and are specialized for vision in dim light. The remaining photoreceptors consist of three types of cones functionally defined by the opsin that they express (Masland, 2012; Hoon et al., 2014). Cones are either sensitive to short-, medium- or long-wavelengths. They are approximately 100 times less sensitive to light than rods and are better adapted for bright-light and high acuity color vision (Hoon et al., 2014). Light is transduced in the outer segments, where photopigments are located; photoreceptor inner segments contain mitochondria, and the outer nuclear layer is made up of photoreceptor nuclei (Oyster, 1999). Photoreceptors synapse onto bipolar and horizontal cells at the outer plexiform layer. The role of these neurons is to modify and edit photoreceptor signals before communicating them to ganglion cells. The retina contains at least twelve types of bipolar cells, each with a unique physiology. Multiple types of bipolar cells are connected to cones; however, only one type is connected to rods (Strettoi et al., 2010; Masland, 2012). Horizontal cells modulate synaptic transmissions between rods and cones and bipolar cells. Widespread synaptic connections emphasize differences in signals between photoreceptor cells by providing inhibitory feedback to rods and cones and possibly bipolar dendrites (Masland, 2012). The streams of information carried by bipolar cells are reorganized at the inner plexiform layer and sampled by ganglion cells under refinement from amacrine cells. The body of ganglion cells along with some displaced amacrine cells form the ganglion cell layer. Ganglion cells integrate the processed signals from bipolar and amacrine cells and convey information to the brain. Approximately 1% (La Morgia et al., 2010) of ganglion cells express the protein melanopsin, which makes them intrinsically photosensitive. With a sensitivity and spatial resolution inferior to those of rods and cones, these cells are mainly involved in non-image-forming vision. They play a key role in contrast detection and modulate many responses to light such as circadian entrainment and the pupillary light reflex (Mure, 2021). The innermost layers of the retina consist of the nerve fiber layer, which contains the axons of the ganglion cells, and the inner limiting membrane, which is composed of terminal expansions of Müller cells extending from the photoreceptor layer (Oyster, 1999).

Glial Cells

The retina contains several types of glial cells that provide structural support to retinal neurons and help maintain retinal homeostasis and retinal integrity (Goldman, 2014; Vecino et al., 2016; Jäkel and Dimou, 2017). Ninety percent of these glial elements are Müller cells. These radially oriented cells extend from the inner limiting membrane to the external limiting membrane, where they form junctions with photoreceptor inner segments (Goldman, 2014; Vecino et al., 2016). Müller cells are not involved in the processing of vision. Their size and number [they are estimated to account for up to 15% of the volume of the retina (Oyster, 1999)], their dense and regular pattern and their close proximity with retinal neurons indicate that they constitute an anatomical and functional intermediary between neurons and compartments with which they exchange molecules (Reichenbach and Robinson, 1995; Bringmann et al., 2006; Vecino et al., 2016). Astrocytes are another type of glial cells present in the human retina. Almost exclusively confined to the innermost retinal layers, their presence and distribution is correlated with that of blood vessels. Astrocyte processes extend to both blood vessels and neurons. Their main functions are to provide enhanced support for degenerating axons and to help maintain the blood-retinal barrier (Vecino et al., 2016).

Retinal Pigment Epithelium

While not involved in the neuronal processing of vision (Strauss, 2005), very few cells of the eye perform as many different functions as the RPE. This monolayer of approximately hexagonal cells separates the retina from the endothelium of the underlying choriocapillaris. The RPE plays a critical role in the normal functioning of photoreceptors by eliminating water from the subretinal space, performing the phagocytosis of photoreceptor outer segment membranes and supplying essential nutrients to the photoreceptors through epithelial transport. In doing so, it impacts on the kinetics of the chemical reactions occurring during the visual cycle significantly (Marmor and Wolfensberger, 1998; Strauss, 2005).

Blood Supply

The retinal vasculature sustains the region of the retina extending approximately from the outer nuclear layer to the inner limiting membrane. The remaining outer retina, which includes the photoreceptor inner and outer segments and the RPE, is supported by the choroidal vasculature (see **Figure 2**). These two vascular systems arise from the ophthalmic artery, which branches into the central retinal artery supplying the retinal vasculature and into the medial and lateral posterior ciliary arteries supplying the choroid (Hayreh, 1962, 1963; Hayreh and Dass, 1962). Neither the retinal nor the choroidal vasculature can compensate for the loss of the other, so that the retina relies on both for survival (Oyster, 1999).

Metabolism of the Retina

The visual system is the highest energy-consuming system of the brain (Niven and Laughlin, 2008). Impaired energy metabolism causes visual deficits (Linsenmeier and Zhang, 2017) and may be to blame in the pathogenesis of degenerative vitreoretinal disorders (Léveillard et al., 2019). Energy necessary for cellular function is transferred in the form of adenosine triphosphate (ATP). This high-energy molecule is produced through glycolysis or oxidative phosphorylation. Glycolysis takes place in the cytosol. It converts glucose into pyruvate, generating two molecules of ATP in the process. Oxidative phosphorylation occurs in the mitochondria and uses pyruvate as a substrate. It requires the presence of oxygen and produces up to 36 molecules of ATP for each molecule of glucose consumed. When oxygen is limited, oxidative phosphorylation is hindered and the pyruvate produced through glycolysis is reduced to lactate (Alberts et al., 2014). As in the brain, retinal neurons use glucose as their main energy substrate and are dependent on the more energetically effective oxidative phosphorylation to generate ATP. They are therefore very sensitive to fluctuations in glucose and oxygen supplies (Erecińska and Silver, 2001; Linsenmeier and Zhang, 2017). ATP supports most neuronal functions, including protein and neurotransmitter syntheses and recycling. Active transport of ions against their electrical and concentration gradients is the largest energy-consuming neuronal functions (Wong-Riley, 2010). In contrast with retinal neurons, glial cells rely mainly on glycolysis for their ATP needs (Winkler et al., 2000).

Photoreceptors have one of the highest metabolic rates of any cell of the human body (Linsenmeier and Braun, 1992; Niven and Laughlin, 2008; Wong-Riley, 2010). Most of the ATP used by photoreceptors is produced through oxidative phosphorylation, which occurs mainly in the mitochondria-rich inner segments. It is there that most of the oxygen diffusing from the choriocapillaris and retinal circulation is consumed. Studies performed on monkeys indicate that oxygen consumption is larger in the perifovea as compared to the fovea (Yu et al., 2005; Birol et al., 2007). Oxygen consumption is also significantly greater in dark-adapted condition than under illumination (Birol et al., 2007). While many aspects of their normal metabolism remain to be fully understood, it is now well established that photoreceptors generate large amounts of lactate in the presence of oxygen through glycolysis (aerobic glycolysis) (Lindsay et al., 2014; Du et al., 2016a; Chinchore et al., 2017). In fact, it has been estimated that between 80 and 90% of glucose molecules used by adult photoreceptors is consumed through aerobic glycolysis alone. This pathway generates intermediates necessary to the formation of large molecules involved in the visual process (Narayan et al., 2017). The large amounts of lactate produced by photoreceptors may also fuel both Müller and RPE cells. Lactate has been shown to suppress glucose consumption in the RPE, with the effect of increasing the amount of the molecule reaching photoreceptors (Kanow et al., 2017). RPE cells are specialized for reductive carboxylation, a type of metabolism that heavily relies on mitochondria (Du et al., 2016b).

DELIVERY SYSTEM TO INNER RETINAL NEURONS

The inner retinal mass transport system supports the metabolism of many retinal neurons including ganglion, bipolar, horizontal and amacrine cells. Highly regulated, it relies on an adequate blood supply to retinal capillaries in different regions of the retina.

Retinal Vasculature

Upon branching from the ophthalmic artery, the central retinal artery travels within the optic nerve and inserts into the retina through the optic nerve head. There, it divides into large superior and inferior branches, which further ramify into dependent branches radiating across the retinal surface (Hayreh, 1962, 1963; Hayreh and Dass, 1962). The basic network topology of the retinal vasculature consists of a tree, where blood may only follow a limited number of anatomical routes determined by the branching pattern of arteries of veins (nodes of the tree). Terminal arteries (arterioles) branch from parent vessels at an approximately right angle (Pournaras et al., 2008). *In vivo* measurements indicate that the relation between blood flow rate and diameter among retinal arteries and veins is consistent with Poiseuille's flows (Riva et al., 1985; Feke et al., 1989); although the velocity profile is flatter rather than parabolic in larger arteries and veins (Zhong et al., 2011). Throughout the retina, larger vessels remain close to the inner limiting membrane. Across most of the retina arteries and veins alternate, so that one vein typically lies between two consecutive arteries (Stokoe and Turner, 1966; Wise et al., 1975); although they tend to be dissociated in the periphery of the retina (Stokoe and Turner, 1966). Capillary beds connect consecutive arterial and venular branches, forming an interconnecting network arranged in a multi-layer pattern, each of them supplying distinct sets of neurons (see **Figure 2**). Retinal veins merge into the central retinal vein, which exit the eye through the optic nerve head and joins the superior ophthalmic vein (Hayreh, 1962, 1963; Hayreh and Dass, 1962).

Retinal Vascular Pattern

Analyses based on histology (Snodderly et al., 1992; Pournaras et al., 2008; Chan et al., 2012; Tan et al., 2012), OCT (Chan et al., 2015), OCTA (Campbell et al., 2017; Muraoka et al., 2018; Hormel et al., 2020) and AO (Kurokawa et al., 2012) indicate that the retinal capillary network is arranged in up to four layers (or plexuses) depending on location. Supplied by the central retinal artery, the superficial vascular plexus consists of a network of arteries, arterioles, capillaries, venules and veins contained primarily within the ganglion cell layer. Intermediate and deep capillary network line the inner and outer sides of the inner nuclear layer, respectively, and support the metabolic requirements of amacrine cells, bipolar cells and horizontal cells. These plexuses are supplied by anastomoses from the superficial vascular network (Snodderly et al., 1992; Provis, 2001) and have a lobular organization. The dense radial peripapillary plexus seen in the proximity of the optic nerve head and part of the macula and posterior pole forms a fourth vascular plexus that sustains the densely packed nerve fiber layer bundles (Michaelson, 1956; Kornzweig et al., 1964; Henkind, 1967; Jia et al., 2014; Campbell et al., 2017). Capillaries composing it are supplied and drained by a small number of arterioles and venules from the superficial vascular plexus and run parallel to axons from the nerve fiber layer (Henkind, 1967; Alterman and Henkind, 1968; Campbell et al., 2017; Muraoka et al., 2018). Close to the fovea, capillary plexuses merge into a single layer of capillaries that delineate a region of the retina deprived of blood vessels, the foveal avascular zone (FAZ) (Campbell et al., 2017; Nesper and Fawzi, 2018).

The nature of the connections between capillary plexuses is a key determinant of blood flow patterns in the retinal vasculature and mass exchange with retinal neurons. Animal experiments indicate that venous drainage may predominantly occur through the deep vascular network (Fouquet et al., 2017). While some controversy remains, evidence suggests that the organization of retinal capillaries is neither serial nor parallel (Hormel et al., 2020). The various retinal vascular plexuses rely on a composite network of horizontal and vertical connections that are yet to be fully characterized (Nesper and Fawzi, 2018).

Structure and Regulation of Blood Flow

The structure of retinal arteries, capillaries and veins is characteristic of a vasculature almost entirely autoregulated for local tissue requirements. The retinal vasculature is deprived of autonomic innervation (Hogan and Feeney, 1963a,b; Laties and Jacobowitz, 1966). Blood flow and local tissue perfusion are adjusted to changes in neuronal activity through myogenic response that involves vasoconstriction and vasodilation in arteries and capillaries (Shepro and Morel, 1993; Haefliger et al., 1994; Lombard, 2006; Peppiatt et al., 2006). Retinal vessels can also adapt blood flow rates to changes in partial pressures of oxygen and carbon dioxide and to variations in the concentration of various molecules essential to retinal metabolism (Pournaras et al., 2008; Aalkjær et al., 2011; Levick, 2018; Yu et al., 2019). Autoregulation is mediated by the endothelium of retinal vessels and by pericytes and smooth muscle cells encompassing them. In contrast with other organs, retinal arteries lack an elastic lamina and the coat of smooth muscle cells enclosing them is more developed. Near the optic disk, this coat comprises five to seven layers of cells. This number decreases to two or three at the equator and to one or two at the periphery (Hogan and Feeney, 1963a; Hogan, 1971). Glial and Müller cells generally lie at the interface between the broad basement membrane enclosing retinal arteries and the adjacent nerve fiber layer. The size and distribution of pericytes surrounding veins is similar to that of smooth muscle cells along arteries (Hogan and Feeney, 1963a; Hogan, 1971). When compared to other tissues, pericytes enclosing retinal capillaries are more numerous and closely spaced (there is approximately a 1:1 ratio between pericytes and endothelial cells). Their basement membrane is adjacent to those of Müller and other glial cells (Hogan and Feeney, 1963b,c; Hogan, 1971).

Components of the Inner Blood-Retinal Barrier

The continuous endothelium of retinal vessels constitutes the main component of the iBRB. Transfers across this selective barrier occur through passive, carrier-mediated or receptor-mediated transports (see **Figure 3**). The wall of retinal capillaries is composed of a single layer of endothelial cells enclosed by intramural pericytes and a basement membrane (see **Figure 2**). A basal lamina separates endothelial cells from pericytes. Passive transport across vessel walls is modulated by the structure and thickness of the basement membrane of capillaries and pericytes, which is thicker than in other organs, and by tight junctions between endothelial cells, which are numerous and extensive (Hogan and Feeney, 1963b; Shakib and Cunha-Vaz, 1966; Hogan, 1971; Frank et al., 1990). The structure of these junctions restricts paracellular transport considerably, so that metabolism substrates and amino acids required for retinal metabolism cross the endothelium predominantly through the transcellular pathway. The permeability of the iBRB to many substrates is known and well-documented (Hosoya and Tachikawa, 2012). Limited evidence suggests that pericytes and smooth muscle cells modulate the molecular permeability of retinal vessels through paracellular transport (Frey et al., 1991). It is unclear if astrocytes and Müller cells impact on the permeability of the iBRB in adults (Vecino et al., 2016). Müller cells may modulate the barrier properties of retinal endothelial cells through the secretion of factors contributing to the formation and maintenance of tight junctions (Tout et al., 1993; Abukawa et al., 2009). In addition, both Müller cells and astrocytes produce many extracellular matrix components including collagens, vitronectin and fibronectin that are likely to impact on mass transfers within the retina (Behzadian et al., 2001).

Tissue-Level Models of Retinal Perfusion

Models linking retinal blood flow and mass exchange to retinal structures or metabolism at the tissue level have mostly been limited to the study of oxygen delivery and consumption. One of the most basic approaches relies on the Krogh cylinder model, which assumes that oxygen is supplied to a cylindrical region surrounding evenly spaced capillaries (Krogh, 1919; Goldman, 2008). This model predicts the concentration of a passively transported molecule in tissue as a function of its consumption (assumed to be constant), its diffusivity and the radius of the cylinder within which it is entirely consumed. While extended to account for a range of complex processes involved in the delivery of oxygen to the inner retina – including facilitated transport (McGuire and Secomb, 2001), tissue metabolism and time-varying concentrations (Friedland, 1978); the Krogh model is not adapted to model supply regions containing multiple capillaries (Wang and Bassingthwaighte, 2001). Alternative approaches, mainly based on Green's function (Secomb et al., 2004; Secomb, 2016), have been developed to model oxygen transport in retinal tissue while accounting for non-uniformities in the retinal vascular network and interactions between capillaries (Causin et al., 2016). While built on general principles, these models require a detailed map of the morphology of the retinal vasculature to generate predictions. These maps may be reconstructed from images of the retina (Fry et al., 2018), or generated randomly by harnessing the regularity and fractal nature of the retinal vascular tree (Causin et al., 2016). Because aspects of the retinal vascular network (such as the pattern of connections between different plexuses) are yet to be fully characterized (see Section "Retinal Vascular Pattern"), methods relying on the fractal nature of the retinal vascular tree are generally only relevant to the description of the salient features of the blood flow.

Oxygenation and metabolism in the retina have been experimentally investigated using oxygen-sensitive electrodes and retinal oximetry (Yu and Cringle, 2001; Linsenmeier and Zhang, 2017). These approaches have been applied to explore the resilience of the retina to perturbations including hypoxia and hyperoxia. The main limitation of these approaches is that measurements are often uncoupled from changes occurring at the level of the retinal vasculature. Data collected mainly from animals are at the basis of several mathematical models of oxygen diffusion across the retina (Haugh et al., 1990; Linsenmeier and Padnick-Silver, 2000; Verticchio Vercellin et al., 2021), some of which include considerations on retinal blood flow (Causin et al., 2016).

DELIVERY SYSTEM TO OUTER RETINAL NEURONS

The metabolite delivery system to the outer retina has three main components: the choriocapillaris, which is the vascular bed of the choroidal vasculature, Bruch's membrane and the RPE. These three intrinsically multifunctional compartments are interdependent and compose the outer blood-retinal barrier (see **Figure 3**).

Choroidal Vasculature

The choroidal vasculature emerges from lateral, medial, superior and long posterior ciliary arteries (PCA) that arise from the ophthalmic artery (Hayreh, 1962). Each of them divides into to 10 to 20 short posterior ciliary arteries, which cross the sclera near the optic nerve (Wybar, 1954; Hayreh, 1962, 1974c; Hogan, 1971; Virdi and Hayreh, 1987) and supply a distinct sector of the choroid (Hayreh, 1974a, 1975). They further divide, each subdivision supplying a smaller segment of the choroid. At the end of this vascular tree, arterioles supply the choriocapillaris, an 8–20 μm thick planar capillary bed extending from the optic nerve to the lateral border of the peripheral retina (the ora serrata) (Zouache et al., 2016a). Functionally, choroidal arteries, arterioles, venules and veins form a segmented vascular tree (Hayreh, 1974a, 1975). The choroid is drained by four vortex veins (one per quadrant), which branch into either the superior or inferior ophthalmic vein (Hayreh, 1990; Oyster, 1999).

The structure of choroidal vessels differs markedly from those forming the retinal vasculature. Smooth muscle cells and pericytes are present along choroidal arteries and veins, respectively; however, their function and subtypes remain poorly characterized in man (Salzman, 1912; Wolter, 1956; Hogan and Feeney, 1961; Hogan, 1971; Condren et al., 2013). Pericytes are the only perivascular cells found in the choriocapillaris. They are horizontally and sparsely distributed, with only 11% of ensheathment observed in adults (compared to 94% in retinal capillaries) (Frank et al., 1990; Chan-Ling et al., 2011). Their function remains unclear (Wolter, 1956; Condren et al., 2013). In contrast with the retinal vasculature, choroidal blood flow sees little to no autoregulation under normal conditions (Bill, 1962; Friedman, 1970; Armaly and Araki, 1975; Bill et al., 1983; Gherezguiher et al., 1991). The presence of extrinsic regulation mediated by sympathetic innervation has been demonstrated in animals including primates (Reiner et al., 2018). This regulation may cause vasoconstriction of arteries and pre-capillary arterioles, which drives the redistribution of arterial blood in the event of an increase in blood pressure (during exercise for instance) (Levick, 2018). Evidence of local regulation of choroidal blood flow mediated through myogenic mechanisms has been found in rabbits (Kiel and Shepherd, 1992; Kiel, 1994; Kiel and van Heuven, 1995).

The Choriocapillaris

The large diameter of choriocapillaris vessels (Hogan, 1971; Olver, 1990; Ramrattan et al., 1994) demonstrates a weaker resistance to blood flow as compared to retinal capillaries. High blood flow – choriocapillaris blood flow is, per unit mass, three to four times higher than that in the kidney (Weiter et al., 1973) – ensures that gradients of concentrations between the choroid and retina remain steep, and therefore that rates of transfers between these two compartments are maintained high. In addition to low resistance to blood flow, the choriocapillaris features many structures facilitating the movement of molecules across its endothelium. Choriocapillaris vessels are composed of a single layer of endothelial cells enclosed by a basement membrane (Missotten, 1962) and are separated by discontinuous tight junctions. Gap junctions are also observed in the plasma membrane of the endothelium (Hogan, 1971; Spitznas and Reale, 1975), generally on the scleral side of the capillaries and between pericytes and endothelial cells (Spitznas and Reale, 1975). As in glomerular capillaries (Satchell and Braet, 2009), blood vessels in the choriocapillaris contain fenestrations (Hogan and Feeney, 1961; Bernstein and Hollenberg, 1965; Hogan, 1971; Torczynski, 1982). These 600 to 800Å pores spanning the width of the endothelium present with a diaphragm covering part of their surface (Missotten, 1962; Garron, 1963; Hogan, 1971; Spitznas and Reale, 1975), and are more frequent on the retinal side of capillaries (Hogan and Feeney, 1961; Bernstein and Hollenberg, 1965; Federman, 1982).

Whereas fenestrations enhance the diffusion of molecules of small to moderate size (typically with a Euler-Einstein radius of 30–40Å or less), they do not allow for the free transport of macromolecules from plasma to the extravascular space as is often assumed (Nakanishi et al., 2016). In fact, the choriocapillaris substantially restricts the passage of large unreactive molecules (Pino and Essner, 1980, 1981; Törnquist et al., 1990; Grebe et al., 2019) and features receptor-mediated types of transport (Bernstein and Hollenberg, 1965; Pino and Essner, 1981; Nakanishi et al., 2016). Choriocapillaris endothelial cells differentially express several transendothelial transport genes including *CAV1* (caveolin), *TSPO* (cholesterol) and *TFRC* (transferring receptor) (Voigt et al., 2019a). One of the genes most strongly differentially expressed by these cells is plasmalemmal vesicle-associated protein (*PLVAP*). The Plvap protein is present in fenestrations, caveolae and transendothelial channels, and therefore plays a key role in the regulation of transendothelial transport (Wisniewska-Kruk et al., 2016; Bosma et al., 2018; Brinks et al., 2021). Our understanding of the mechanisms and dynamics of the transport of specific macromolecules across the choriocapillaris is limited, and mainly comes from examinations of the movement of albumin. This macromolecule was experimentally found to cross choriocapillaris endothelial cells through caveolae-mediated transcytosis, with an estimated travel time of 30 min or less (Nakanishi et al., 2016).

Bruch's Membrane

Molecules reaching the choroidal extravascular space must cross Bruch's membrane, which occupies the space between the choriocapillaris and the RPE, to reach photoreceptor outer segments (see **Figure 3A**). Bruch's membrane forms a selective barrier to the reciprocal transport of molecules between the RPE and choriocapillaris, restricts cellular movement between choroid and retina and physically supports RPE adhesion (Booij et al., 2010). Histologically part of the choroid, Bruch's membrane is 2 to 5 μm thick and is composed of an elastin layer sandwiched by two layers of collagen fibers (the inner and outer collagenous layers). Its inner- and outermost layers are basement membranes to the RPE and choriocapillaris, respectively (Hogan, 1961). The inner and outer collagenous layers are composed of various forms of collagen arranged in a grid-like structure and embedded in a mass of interacting biomolecules. The elastin layer is made up of coarse interlaced linear elastin fibers extending from the optic nerve to the far retinal periphery. The outer basement membrane of Bruch's membrane is composed of several forms of collagen. Because it coincides with the basement membrane of the choriocapillaris, it is discontinuous – it is present close to capillaries of the choriocapillaris but absent in the space separating them (Marmor and Wolfensberger, 1998).

Since Bruch's membrane is acellular, transport across it is passive and entirely determined by its thickness and molecular composition. Gradients of hydrostatic pressure and concentration drive the movement of molecules, which either cross the membrane or bind to it (Marmor and Wolfensberger, 1998; Strauss, 2005). The average diameter of gaps within the elastin layer and its thickness are important determinants of the diffusive properties of Bruch's membrane (Chong et al., 2005). Out of the five layers composing it, the inner collagenous layer has been experimentally found to form the main resistance to fluid movement, and is therefore the principal determinant of Bruch's membrane's hydraulic conductivity (Starita et al., 1997). Controversy exists regarding the maximal size of molecules able to travel across Bruch's membrane. Intravenous injections of protein tracers in animals indicate that particles 64–500 kDa in weight enter Bruch's membrane but do not cross it (Bernstein and Hollenberg, 1965; Pino and Essner, 1981; Pino and Thouron, 1983). However, molecules 40–200 kDA have been shown to cross the membrane *in vitro* (Moore and Clover, 2001). This discrepancy is likely to be caused by the experimental systems used in *in vitro* studies, which may not replicate physiologically realistic gradients of pressure and normal fluid fluxes, and often involve both advective and diffusive transports across the membrane (Hussain et al., 2010).

Retinal Pigment Epithelium

At the level of the RPE, tight junctions connecting adjacent cells ensure that the outer blood-retinal barrier is maintained (Raviola, 1977). The resistance to paracellular transport across the RPE was estimated to be ten times higher than that to transcellular transport in animals (Miller and Steinberg, 1977a,b). Choriocapillaris fenestrations are maintained by growth factors secreted by the RPE that diffuse across Bruch's membrane (Blaauwgeers et al., 1999; Kamba et al., 2006; Kim et al., 2019), highlighting the close relationship between these three components. The expression of *PLVAP* may be induced and regulated by growth factors produced at the level of the RPE including vascular endothelial growth factors (Vegf) (Marneros et al., 2005; Bosma et al., 2018) and pigment epithelium-derived factor (Pedf) (Farnoodian et al., 2018). Vegf exposure has been shown to alter the vascular permeability of endothelial cells

(Bates, 2010), partly by modulating the frequency and structure of their fenestrations (Stan, 2007).

Tissue-Level Models of Exchange Between Choroid and Retina

Tissue-level analyses of the movement of molecules between retina and choriocapillaris, which describe the combination of phenomena occurring at the level of choroidal endothelial cells, Bruch's membrane and the RPE, are scarce. Salient features of the transfer of small passively transported molecules may be inferred from theoretical and experimental analyses of oxygen concentration profiles (Linsenmeier and Zhang, 2017; Yu et al., 2019). These studies indicate that passively transported molecules diffuse along a concentration gradient that is perpendicular to the plane of the choriocapillaris. In the case of oxygen, this gradient is directed toward the outer retina.

Blood enters and leaves the choriocapillaris through a set of arterioles and venules connected to the surface furthest from the retina approximately perpendicularly to the plane of the capillaries. Because of this arrangement, the blood flow is decomposed into contiguous functional vascular segments separated by separation surfaces across which there is no flow (Zouache et al., 2016a). Groups of functional vascular segments are commonly referred to as lobules (Hayreh, 1974b), a term introduced by analogy with liver functional units (Torczynski and Tso, 1976). The pattern of segmentation of the choriocapillaris blood flow is determined by pressure gradients between arteriolar and venular insertions and their relative distribution (Flower et al., 1995; Zouache et al., 2016a). The extraction of diffusive species from the choriocapillaris and the distance across which they diffuse across the retinal tissue is determined by the velocity of blood flowing through the choriocapillaris and by the relative distribution and flow rate of arterioles and venules inserting into its plane. Blood velocities across the choriocapillaris have been experimentally and theoretically shown to be spatially heterogeneous (Flower, 1993; Flower et al., 1995; Zouache et al., 2016a). Mass exchange between choriocapillaris and outer retina (denoted η) is at the level of a functional vascular segment (basic lobule unit) described by the theoretical relation:

$$\eta = \frac{A_0 \mathrm{h}}{\tau Q_a} \Phi$$

where A_0 is the surface area of the lobule, h the local thickness of the choriocapillaris, Q_a is the flow rate in the arteriole feeding the lobule, Φ is the vascular volume fraction of the choriocapillaris (the volume of tissue occupied by capillaries) and $1/\tau$ is a transfer coefficient specific to the compound considered (Zouache et al., 2015, 2016a). This relation may also be expressed as:

$$\eta = \frac{< T >}{\tau}$$

where $< T >$ is the mean travel time of blood between an arteriole and a venule supplying and draining a choriocapillaris lobule, respectively. Both relations are functions of the ratio of arterioles and venules supplying functional vascular segments. Based on experimental data generated in animals, the extraction rate of glucose and oxygen is between less than one percent and five percent per volume of blood (Alm and Bill, 1972; Wang et al., 1997; Linsenmeier and Padnick-Silver, 2000), which yields $\tau \approx 0.2 - 1 \times 10^5 s$. In the case of glucose, this estimate is partly determined by the abundance of GLUT receptors on the plasma membrane of choroidal endothelial cells (Mantych et al., 1993), RPE (Strauss, 2005) and photoreceptor outer segments (Hsu and Molday, 1991).

SPATIAL VARIATIONS IN NEURON POPULATIONS AND INNER AND OUTER RETINAL MASS TRANSPORT SYSTEMS

In this section, we explore the relation between retinal neuron populations and their respective mass transport systems by harnessing spatial variations in the structure of the retina and choroid. This variability evolved as an adaptation to spatial variations in light intensity, contrast and amplitude of visual aberrations across the retina (Walls, 1942; Hughes, 1977). To optimize spatial resolution and sampling of light (Hirsch and Hylton, 1984; Hirsch and Curcio, 1989), the size, density, and tilling geometry of photoreceptors vary across the eye. In addition, as in many vertebrates (Walls, 1937, 1942), the human eye contains a region dedicated to high resolution vision, the *fovea centralis*, which allows for the capture a small part of retinal images only but in great details (Hughes, 1977). Anatomically, the fovea consists of a 1500 μm-wide depression in the retinal tissue caused by the absence of inner retinal layers; see **Figure 1C**. In this region the retina is only 100 μm thick, and is deprived of the inner nuclear, inner plexiform, ganglion cell and nerve fiber layers as well as retinal capillaries (Hogan, 1971). The spatial variation in the human photoreceptor mosaic can also be seen in other cells and structures of the retina and choroid, including ganglion cells and retinal and choroidal vasculatures. The location and classical denomination of retinal regions are described in **Figure 4A**.

Retinal Neurons

Methods based on histology of human donor eyes (Osterberg, 1935; Polyak, 1941; Farber et al., 1985; Curcio et al., 1987, 1990; Jonas et al., 1992) and *in vivo* imaging techniques (Chui et al., 2008a,b; Song et al., 2011; Zhang et al., 2015) have shown that the density of cones is maximal at the fovea (see **Figure 4B**). Its reported peak can vary by several orders of magnitude between individuals, ranging from 49,600 (Dorey et al., 1989) to 238,000 (Ahnelt et al., 1987) cones/mm^2 on average. Inter-individual variability varies with location in the retina (Zhang et al., 2015; Elsner et al., 2017) and may be partly explained by differences in axial length between eyes sampled (Chui et al., 2008a; Legras et al., 2018). The most detailed sampling of the cone mosaic in human donor eyes to date reported a mean peak density of 199,000 cones/mm^2 at the foveal center (Curcio et al., 1987, 1990), which is consistent with measurements made using AO (Zhang et al., 2015). Cone density decreases sharply with distance from the center of the fovea (Osterberg, 1935; Curcio et al., 1987, 1990; Jonas et al., 1992; Chui et al., 2008a; Song et al., 2011; Zhang et al., 2015), and is 40–45% higher in the nasal retina as compared to

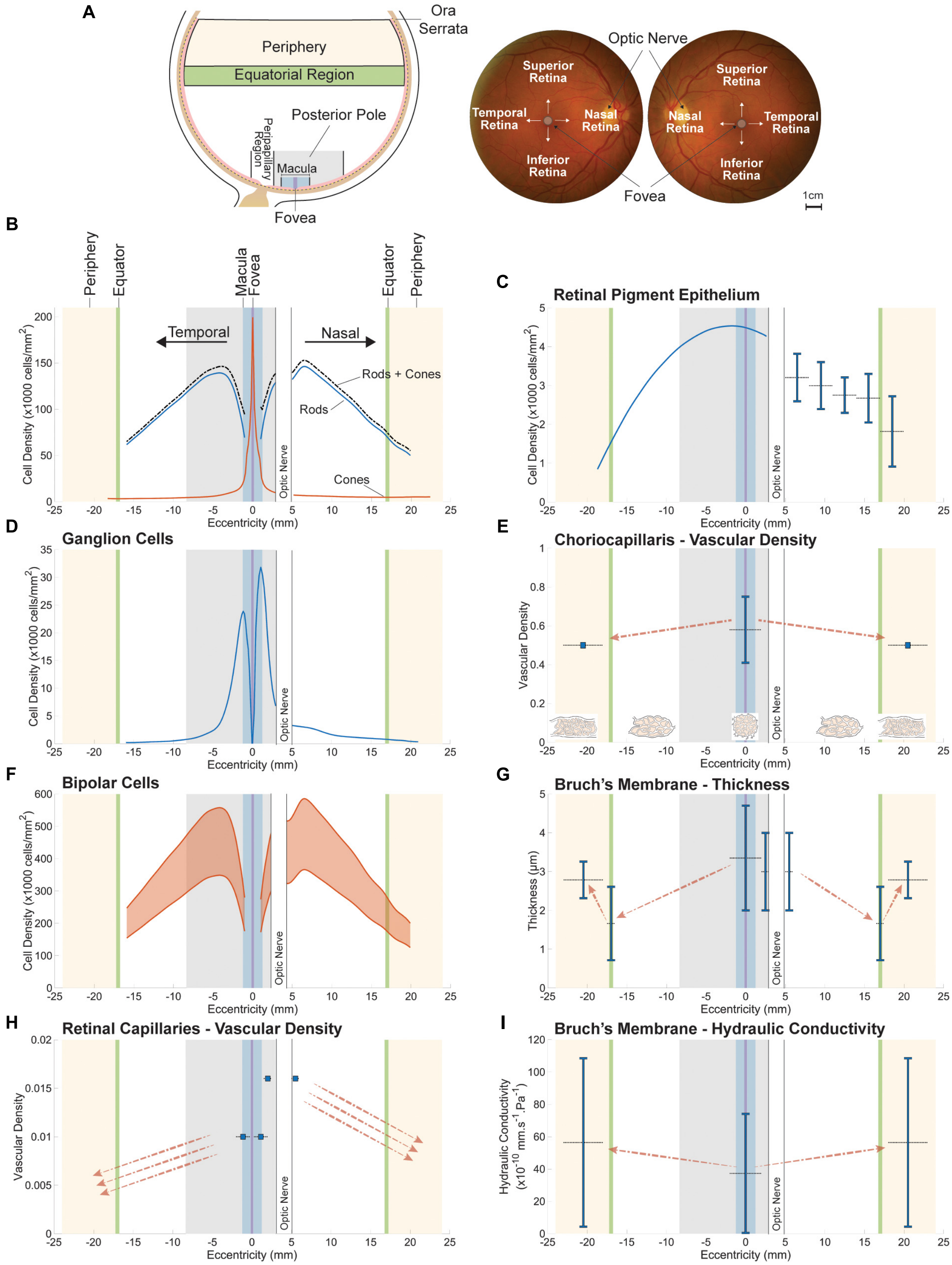

FIGURE 4 | Spatial variations in retinal neuron populations **(B,D,F)** and in the key structures of their respective metabolite delivery systems **(C,E,G–I)**. The approximate location of sampled retinal regions and their associated denomination is described in **(A)**. Terminologies vary between studies; the ones employed here are consistent with the main text. Plotted data were collected from publications listed in **Supplementary Table 1**. All spatial variations are displayed along the nasal-temporal axis as illustrated in **(B)**. Reported values are plotted as vertical line segments (ranges) or single points, and the approximate region they apply to is delineated using horizontal dashed lines. Dashed arrows indicate qualitatively reported trends. The density of bipolar cells **(F)** is plotted as a range inferred from approximate ratios between their density and that of their respective photoreceptor type. The maximal vascular density of retinal capillaries **(H)** appears to overlap with the highest density of bipolar **(F)** and ganglion **(D)** cells. Bruch's membrane is thickest at the fovea **(G)**, where photoreceptor density **(B)** and choriocapillaris vascular density **(E)** are highest.

the temporal region (Curcio et al., 1990). It is also slightly larger in the midperipheral inferior region of the fundus as compared to the superior retina (Osterberg, 1935; Curcio et al., 1990; Jonas et al., 1992). Certain cone subtypes have different distributions, which do not appear to be either random or regular (Curcio et al., 1991; Mollon and Bowmaker, 1992; Roorda and Williams, 1999). Rods are absent from the fovea (Osterberg, 1935; Polyak, 1941; Farber et al., 1985; Curcio et al., 1987, 1990; Jonas et al., 1992). The diameter of the region of the fovea deprived of rods is 0.35 mm on average (Curcio et al., 1990). The density of rods is largest in the nasal region of the retina (Osterberg, 1935; Curcio et al., 1990; Jonas et al., 1992), with a maximal density found in the vicinity of the optic disk (approximately 3–5 mm from the foveal center) (Curcio et al., 1990; Jonas et al., 1992). Peak rod density ranges from 135,000 (Farber et al., 1985) to 176,000 rods/mm^2 (Curcio et al., 1990) in this region. Differences in rod density between individuals can reach 10%, and are much smaller than those observed for cones (Curcio et al., 1990). In addition to their density, the morphology of photoreceptors varies with location in the eye. The diameter of cones increases from approximately 1.6 (Curcio et al., 1990) to 2.23 μm (Scoles et al., 2014) at the center of the fovea to 8–10 μm in the periphery of the retina (Curcio et al., 1990; Jonas et al., 1992; Scoles et al., 2014). The diameter of rods increases from approximately 3 μm in the region with the highest rod density to 5.5 μm in the peripheral retina (Curcio et al., 1990; Jonas et al., 1992).

The ratio between photoreceptors and bipolar cells varies across the eye. At the fovea, bipolar cells are connected on average to one cone and one ganglion cell, thus forming a one-to-one wiring. Multiple connections are observed between bipolar cells and photoreceptors in the region extending from outside the fovea to the peripheral retina, which provides pooling of information over space. Ganglion cells in this region connect to multiple bipolar cells and receive signal originating from distinct photoreceptors (Oyster, 1999). Overall, the density of rod and cone bipolar cells follows the distribution of their respective photoreceptor type. The density of cone bipolar cells is 2.5 to 4 times larger than that of cone photoreceptors whereas rod bipolar cell density is approximately a tenth of that of rods (Martin and Grünert, 1992; Grünert et al., 1994); see **Figure 4F**.

The distribution of horizontal cells has yet to be determined in humans; however, their density has been estimated in monkey retinas. From a minimum of 250 cells/mm^2 at the foveal center, it increases rapidly at the edge of the fovea. It reaches a maximum of approximately 23,000 cells/mm^2 within an annulus of 0.6 mm radius enclosing the fovea (Röhrenbeck et al., 1989). This peak is reached in the region where pedicles of foveal cones are displaced (Tsukamoto et al., 1992). Outside of the fovea, the density of horizontal cells decreases approximately exponentially out to the peripheral retina, in keeping with the distribution of cones (Röhrenbeck et al., 1989; Wässle et al., 1989; Oyster, 1999). In the peripheral retina this density is twenty times smaller than the peak observed close to the fovea (Röhrenbeck et al., 1989).

Absent in the fovea, ganglion cells appear approximately 100–500 μm from the foveal center. Their peak density varies greatly between individuals and ranges from 32,000 to 38,000 cells/mm^2 (Curcio and Allen, 1990), although studies using AO reported lower values (Liu et al., 2017). This maximum is reached within a horizontally oriented elliptical ring located 0.4 to 2.0 mm from the foveal center. Ganglion cell density decreases sharply with distance from the foveal center, reaching approximately 100 cells/mm^2 in the retinal periphery, and does not correlate with cone density (see **Figure 4D**). This pattern of variation is not uniform across the eye. At similar distances from the foveal center, the density of ganglion cells in the nasal retina exceeds that of the temporal region by more than 300%. It is in the superior retina larger than in the inferior region by more than 60% (Curcio and Allen, 1990). The mean peak density of melanopsin-expressing retinal ganglion cells decreases from approximately 20–40 cells/mm^2 at 2 mm from the center of the fovea to 10 cells/mm^2 at about 8 mm eccentricity (Nasir-Ahmad et al., 2019). The topography of amacrine cells has not been mapped in humans. Evidence from monkeys indicates that their distribution, density and coverage varies between subtypes (Dacey, 1990; Wässle et al., 1995). Their density peaks close to the fovea and declines with distance from the foveal center (Dacey, 1990; Rodieck and Marshak, 1992; Wässle et al., 1995).

Differences in the function, distribution and morphology of retinal cells between fovea and peripheral retina are associated with marked differences in gene expression (Peng et al., 2019; Voigt et al., 2019b, 2021; Yan et al., 2020). Using unstructured statistical methods that assessed how close transcription profiles from a large number of cells are, foveal cones were found to form clusters that were distinct from their peripheral counterparts (Voigt et al., 2019b). This method also differentiated between distinct cone subtypes (Lukowski et al., 2019).

Glial Cells

The mean density of Müller cells across the retina in man was estimated to be approximately 11,000 cells/mm^2, a number that is fairly consistent among mammals (Dreher et al., 1992). Information on spatial variations in the density and morphology of these cells is limited. In the monkey retina, the density of Müller cells varies between 6000 cells/mm^2 in the periphery and more than 30,000 cells/mm^2 in the parafoveal region. Müller cells are generally longer in the central retina as compared to the periphery, and the average proximity of neighboring cells increases with distance from the fovea (Distler and Dreher, 1996). The distribution of astrocytes across the monkey retina is uneven. Their concentration, which correlates with the thickness of the nerve fiber layer, is maximal in the proximity of the optic nerve and is particularly low in the perifoveal region. Astrocytes of the nerve fiber layer appear as star-shaped cells in the periphery but seem bipolar close to the optic nerve. The morphology of astrocytes present in the ganglion cell layer is consistent across the retina (Büssow, 1980; Distler et al., 1993).

Retinal Vasculature

There is no evidence of spatial variation in the structure and ultrastructure of blood vessels across the retina (Pournaras et al., 2008). Blood flow to the temporal part of the retina is greater than that to the nasal region (Riva et al., 1985; Feke et al., 1989); it is also greater in the superior quadrant as compared to the inferior retina (Tomita et al., 2020). These differences are likely to be associated with spatial variations in the perfusion of retinal capillary beds across the retina. The arrangement and number of plexuses composing the retinal capillary network varies spatially. The fovea is deprived of retinal capillaries. Close to the FAZ, retinal capillary plexuses merge into a single layer of capillaries (Campbell et al., 2017; Nesper and Fawzi, 2018). The superficial capillary network is present across most of the retina. The intermediate and deep capillary plexuses may be seen in the macula and posterior pole, but merge into one network peripherally (Toussaint et al., 1961; Hogan, 1971; Campbell et al., 2017). The radial peripapillary plexus is observed in the peripapillary region and in part of the macula (Michaelson, 1956; Kornzweig et al., 1964; Henkind, 1967; Jia et al., 2014; Campbell et al., 2017).

The density of retinal vessels is partly determined by the thickness of the portion of the retina that they supply (Michaelson, 1956; Chase, 1982; Buttery et al., 1991; Snodderly et al., 1992). While the combined volume of retinal vessels in the deeper networks remains constant across the eye, the cumulated vascular volume of superficial retinal vessels increases with the thickness of the nerve fiber layer. The fact that this layer contributes more to vascularity than to retinal thickness indicates that the density of retinal vessels is more likely to be determined by local metabolic requirements (and diffusion distances) than by tissue volume (Snodderly et al., 1992). This observation is further strengthened by the fact that the diameter of capillaries is larger in the superficial nerve fiber layer as compared to the inner nuclear layer (Snodderly et al., 1992; Tan et al., 2012). This indicates a smaller resistance to blood flow in this layer and a higher propensity for passive molecular exchange.

Analyses of human donor eyes indicate that the greatest density of retinal capillaries, expressed as a percentage of total retinal volume, is found at the margin of the avascular fovea, where it reaches approximately 1% (Snodderly et al., 1992); see **Figure 4H**. The density of capillaries decreases gradually toward the mid-periphery and periphery of the eye. In these regions the retina is thinner and capillaries are fewer in number (Toussaint et al., 1961; Kornzweig et al., 1964; Hogan, 1971). Histological studies (Snodderly et al., 1992) found that the density of capillaries in the vicinity of the optic nerve is approximately 1.6–1.7% of the volume of the retina and decreases with distance from the optic nerve head. Capillary density extracted from OCTA slabs is generally calculated by dividing the surface area of automatically or manually traced capillaries by the area of the retina sampled. Comparisons between densities extracted from histology and OCTA using perfused human donor eyes (An et al., 2018; Balaratnasingam et al., 2018) and animal eyes (Yu et al., 2021) indicate that OCTA provides a good representation of large retinal vessels but does not visualize all retinal capillaries. Estimates of capillary density obtained from OCTA slabs range from 10 to 60% on average in similar regions of the retina (Coscas et al., 2016; Iafe et al., 2016; Garrity et al., 2017; Lavia et al., 2019). In comparison, histological studies indicate that the percentage of retinal area occupied by capillaries lies between 40 and 55% (Snodderly et al., 1992; An et al., 2018). It increases steeply in the parafovea and reaches a maximum approximately 1.5 mm from the foveal center (Snodderly et al., 1992). OCTA studies have found that the density of the deep capillary network is greater than that of the superficial capillary network (Lavia et al., 2019).

Choroidal Vasculature

The choroidal vasculature displays marked variations in its anatomy and physiology across the eye. The number of arterioles and venules connected to the choriocapillaris per unit of volume is maximal in the submacular region and decreases toward the periphery. The ratio of arteriolar to venular insertions follows a similar pattern, varying from up to 5:1 in the submacular area to 1:4 in the periphery (Amalric, 1983; Fryczkowski et al., 1991; Fryczkowski, 1994). Because of its unconventional morphology and large local variations, quantifying differences in the structure of the choriocapillaris across the eye has proven challenging. Qualitatively, capillaries are narrowest in the posterior pole (Ring and Fujino, 1967; Hogan, 1971; Torczynski, 1982) and become progressively wider in the periphery (Ring and Fujino, 1967; Hogan, 1971). The space between capillaries (called *septa*) follows a similar pattern, varying between about 3 and 18 μm in diameter at the posterior pole (Hogan, 1971) and widening into longer and thinner channel-like structures toward the equator (Salzman, 1912; Wybar, 1954; Hogan, 1971; Torczynski and Tso, 1976); see **Figure 4E**. Septae further elongate and widen toward the periphery and become loose in the region of the ora serrata (Salzman, 1912; Klien, 1966; Yoneya et al., 1983; Fryczkowski et al., 1991). Variations in the diameter of capillaries and septae across the eye are best described by a measure of vascular density. The vascular density of the choriocapillaris has a strong dependence on age. In the macula, it varies between 0.75 and 0.41 over a lifespan (Ramrattan et al., 1994). Measurements unadjusted for age indicate that the density of the choriocapillaris is approximately 0.5 on average in the peripapillary and peripheral regions. It does appear to decline more abruptly in the periphery (Ramrattan et al., 1994; Spraul et al., 1999, 2002); see **Figure 4E**. Choriocapillaris density seems to be independent of extrinsic anatomical features such as the thickness of Bruch's membrane or choroid and correlates with age better than capillary or septae sizes (Ramrattan et al., 1994).

Variations in the anatomy of the choriocapillaris translate important differences in the shape of functional lobules and possibly their mass exchange with the outer retina. These differences are yet to be fully characterized *in vivo*; however, some of them can be inferred from anatomical studies by using existing theoretical frameworks (Zouache et al., 2015, 2016a). Estimates of the average distance (Torczynski and Tso, 1976; Fryczkowski and Sherman, 1988; Olver, 1990) and ratio (Amalric, 1983; Fryczkowski et al., 1991; Fryczkowski, 1994) between arteriolar and venular insertions into the choriocapillaris, of their respective number (Araki, 1976) and variations in vascular density (Ramrattan et al., 1994; Spraul et al., 1999, 2002) indicate that the surface area of lobules is smallest in the submacular area, where their shape is closest to a regular square, pentagon or hexagon. Toward the periphery, the surface of exchange between choriocapillaris and outer retina is larger, and likely to take the shape of an elongated rectangle. Because of a lack of hemodynamic data, it is unclear if differences in the characteristics of functional lobules across the eye are synonymous with spatial variations in transfers between choriocapillaris and outer retina.

Spatial variations in the ultrastructure of choroidal vessels have seldom been examined. Limited data indicate that fenestrations are more frequent in the submacular choriocapillaris as compared to the periphery of the eye (they cover 60.3% of endothelial cell walls in the fovea vs. 36.7% in the periphery) (Federman, 1982).

Bruch's Membrane

The thickness and composition of Bruch's membrane are the main structural factors assessed to characterize its diffusive properties. This thickness appears to be larger in the vicinity of the optic nerve head (Salzman, 1912; Garron, 1963) and in the periphery of the eye (Nakaizumi, 1964; Nakaizumi et al., 1964) as compared to the posterior pole and submacular regions (see **Figure 4G**). The composition of the elastin layer varies across the retina. Qualitatively, it is thicker and occupies a larger portion of Bruch's membrane in the posterior pole (Garron, 1963) and submacular area (Chong et al., 2005) as compared to the peripapillary region; although a large variability is observed between samples. Spatial variations in the porosity of Bruch's membrane were assessed quantitatively by measuring the integrity of this layer, defined as the total length of detectable elastin divided by the length of the portion of membrane considered. This measure is correlated with the thickness of the elastin layer. Elastin integrity is minimal at the fovea (approximately 40%). It is on average 60% higher in the periphery as compared to the subfoveal choroid (Chong et al., 2005). *In vitro* experiments indicate that the hydraulic conductivity of Bruch's membrane is higher in the retinal periphery as compared to the submacular region (Moore et al., 1995); see **Figure 4I**.

Retinal Pigment Epithelium

The density of RPE cells is maximal at the fovea and decreases almost linearly with distance from the foveal center (Ts'o and Friedman, 1968; Streeten, 1969; Young, 1971; Gao and Hollyfield, 1992; Harman et al., 1997; Bhatia et al., 2016; Granger et al., 2018; see **Figure 4C**); although a large variability is observed between subjects. A decrease in the density of RPE cells is associated with an increase in their mean surface area (Ts'o and Friedman, 1968; Granger et al., 2018) and a reduction in the average number of neighbors to each cell (Bhatia et al., 2016). Hexagonal cells are significantly more frequent in the macula than in the peripheral retina (Watzke et al., 1993). The mean cone-to-RPE cell ratio is maximal at the fovea and decreases rapidly starting from 2 mm from the foveal center (Granger et al., 2018).

Conclusion

Most investigations reporting spatial variations among retinal neuron populations, retinal vasculature and choroid have considered these systems in isolation. In part because of this, combining published measurements is not sufficient to capture local differences in retinal and choroidal structures that may indicate a correlated pattern of variation. This "lack of resolution" is exacerbated by variabilities in regions of the retina sampled between studies. Therefore, similarities between the pattern of change in retinal and choroidal structures across the eye can only be described qualitatively.

Past investigations indicate that spatial variations in the structure and physiology of retinal circulatory systems follow those observed among the populations of cells that they support. The density of retinal capillaries (expressed as a function of retinal volume) is maximal close to the optic nerve head, where the concentration of ganglion and bipolar cells is highest. It decreases toward the periphery, where the density of retinal neurons is comparatively reduced. The amplitude of differences in vascular density displayed by the choriocapillaris across the choroid seem almost marginal when compared to those seen among photoreceptors. Variations in the thickness and hydraulic conductivity of Bruch's membrane indicate that this structure forms a greater impediment to mass exchange in the submacular area as compared to the periphery. Therefore, barriers to transport appear to be more selective in regions where the density of photoreceptors is highest.

RELATION BETWEEN NEURONS AND RETINAL MASS TRANSPORT SYSTEMS IN AGING

Aging can provide valuable insights into the relation between retinal neuron populations and mass transport systems, including information about its resilience to perturbations occurring over large timescales. Many structural changes have been observed in the aging retina (see **Figure 5A**). Some reports are conflicting, partly because the effect of aging on retinal cells and structures varies across the eye. Inconsistencies or inaccuracies in the regions of the retina sampled may therefore introduce large variabilities in quantified features, rendering any generalization difficult. In addition, the ability to detect cellular changes or losses caused by aging are limited by large inter-subject variabilities (Gao and Hollyfield, 1992) present at baseline, as seen in Section "Spatial Variations in Neuron Populations and Inner and Outer Retinal Mass Transport Systems," and by differences in the range of ages considered in each study. Finally, it is often difficult to determine if earlier assessments of retinal aging considered samples presenting features that would today be classified as pathological. The definition of many vitreoretinal diseases has evolved considerably over the years, and several phenotypes previously considered as age-related are now known to be associated with degenerative diseases. For instance, changes caused by age-related macular degeneration (AMD) often overlap with those associated with aging prior to the onset of clinical symptoms. However, the existence of genetic associations with AMD (Fritsche et al., 2016) and disease specific phenotypes (Ardeljan and Chan, 2013) indicates that the chain of events associated with the onset and progression of this disease has components that are independent of the aging process.

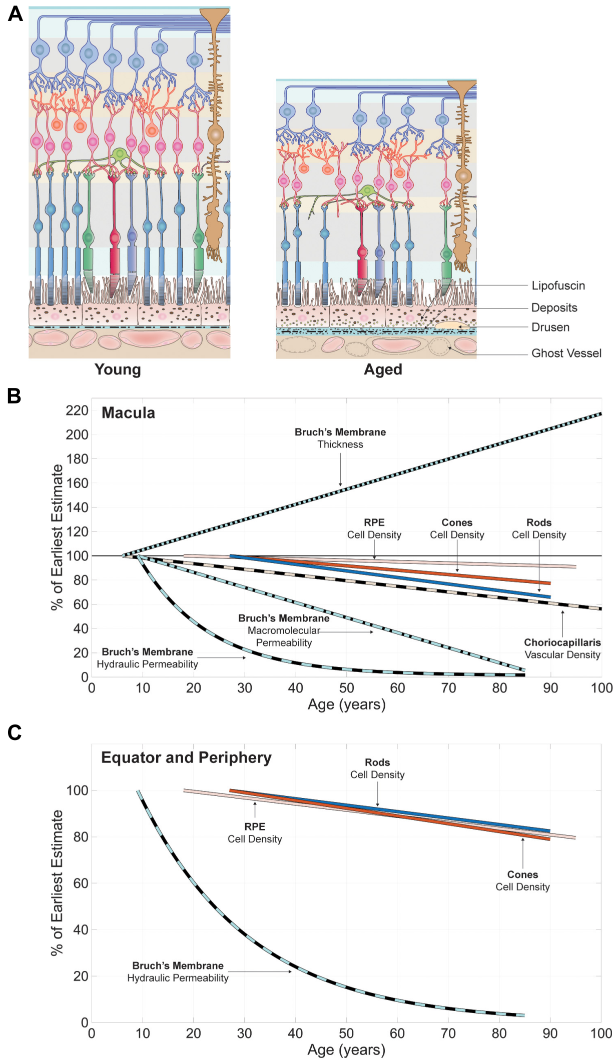

FIGURE 5 | Age-related variations in retinal neuron populations and in the key structures of their respective metabolite delivery systems in the macula and equator and periphery. A schematic of changes affecting the retina and choroid adapted and modified with permission from Campello et al. (2021) is shown in **(A)**. Linear and non-linear regressions were collected from publications listed in **Supplementary Table 2**. The features plotted are normalized by the first value of each regression, which corresponds to the estimate in the youngest eye included in each study. In the macula **(B)**, there can be large inter-individual differences that mask variations in the density of RPE cells and cone photoreceptors with age. With careful elimination of disease and other extraneous variables, some older subjects have significantly lower cone densities than do younger subjects. Aging is associated with an increase in the thickness of Bruch's membrane and a reduction in its hydraulic and macromolecular permeability. The rate of rod loss and the decrease in the vascular density of the choriocapillaris observed with age lie within a similar range. In the equatorial and peripheral region **(C)** loss of cones with age is more pronounced as compared to rods.

Foveal and Macular Regions

Inner Retina

While this is disputed (Oyster, 1999; Harman et al., 2000) due to methodological inconsistencies (Calkins, 2013), cells in the ganglion cell layers may be lost in aging (Gao and Hollyfield, 1992; Curcio and Drucker, 1993). Their density was estimated to decrease by 16% on average between the second and sixth decade (Gao and Hollyfield, 1992). Differences between young and old eyes appear to be more pronounced approximately 3 mm from the foveal center, where losses in mean density reach 25% (Curcio and Drucker, 1993). Data on horizontal, bipolar and amacrine cells are scarce. It is generally assumed that their density remains constant throughout adulthood (Oyster, 1999). Limited data do point to a 21 to 27% decline in bipolar cell density with age over years spanning from the third to the seventh decade (Aggarwal et al., 2007); however, the region of the retina where measurements were made was not specified. Endothelial degeneration (Nag and Wadhwa, 2012) and acellularity of single vessels (Kuwabara et al., 1961), sometimes associated with loss of mural cells, are often seen among retinal capillaries. Acellularity is however not necessarily significative of functional abnormalities or structural changes in adjacent parts of the retina (Kuwabara and Cogan, 1965). A gradual reduction of macular retinal thickness is often observed with age, generally after the fourth decade (Eriksson and Alm, 2009; Karampelas et al., 2013; von Hanno et al., 2017; Ryoo et al., 2018; Zouache et al., 2020; Trinh et al., 2021). The thickness of the ganglion cell, inner plexiform, inner nuclear and outer nuclear layers demonstrate similar rates of decline with age. In contrast, the thickness of the nerve fiber layer does not vary significantly with age (Trinh et al., 2021). *In vivo* methods have found that the vascular density of deep and superficial retinal capillary layers decreases by 0.55–0.86% per decade on average (Wei et al., 2017; Lavia et al., 2019). This variation is associated with a reduction of the mean blood flow velocity among retinal venules (Wei et al., 2017) and a decrease in retinal tissue perfusion (defined as the blood flow supplying the macula divided by the sampled volume of the inner retina) (Lin et al., 2019). The effect of perturbations of the retinal blood flow on metabolism has been investigated experimentally (Linsenmeier and Zhang, 2017; Yu et al., 2019); however, none of these perturbations occurred over a timescale relevant to the aging process.

Outer Retina and Choroid

The amplitude of changes observed in the outer retina and choroid appears larger in magnitude than those documented in the inner retina. Displacement and patchy loss of nuclei in cone outer segments have been observed in the macular retina (Gartner and Henkind, 1981; Dorey et al., 1989; Gao and Hollyfield, 1992). Analyses of human donor eyes suggest that the density of foveal cones decreases with age, although this reduction was not found to be statistically significant (Gao and Hollyfield, 1992; Curcio et al., 1993). Assessments of variations in cone density with age may however be affected by axial length (Park et al., 2013; Wang et al., 2019), undiagnosed retinal pathology and discrepancies in regions sampled (Elsner et al., 2017), which AO-based techniques can control for. Studies using AO have found that older eyes have significantly lower cone densities as compared to younger ones in regions 500 μm to 4 mm (Chui et al., 2012) and 570 to 580 μm (2°eccentricity) (Legras et al., 2018) from the foveal center. Differences in cone density between younger and older subjects are largest near the fovea and decrease with distance from its center (Song et al., 2011; Chui et al., 2012). Loss of rod photoreceptors is observed in the region inferior to the fovea. Starting at the fifth decade, the proportion of rods lost reaches 30% by the ninth decade within an annulus ranging from 0.5 to 3 mm from the foveal center (see **Figure 5B**). Interestingly, this annulus of greatest rod loss lies in a region distinct from the part of the retina displaying the highest rod density. The drop in rod density does not result in reduced rod coverage because the space vacated by lost cells is filled by larger rods (Curcio et al., 1993), thereby maintaining their overall tiling (Oyster, 1999). Loss of RPE at the foveal center (Gao and Hollyfield, 1992) and in the macular and paramacular retina (Ts'o and Friedman, 1968; Dorey et al., 1989) with age have been reported; although this finding has been disputed (Watzke et al., 1993; Harman et al., 1997). Reported variations in cell density may in fact be caused by an increase in the surface area of the retina with age (Harman et al., 1997). An increase in the mean surface area of RPE cells and a reduction of the frequency of hexagonal cells (Watzke et al., 1993; Bhatia et al., 2016) have been observed in aging. These morphological changes are likely to preserve the continuity of the RPE layer, which may be affected by cell loss or changes in retinal area. Some have reported that the ratio between cone and RPE cells lies within a similar range across all age groups (Gao and Hollyfield, 1992). The decrease in retinal thickness with age after the fourth decade (Eriksson and Alm, 2009; Karampelas et al., 2013; von Hanno et al., 2017; Ryoo et al., 2018; Zouache et al., 2020; Trinh et al., 2021) is not attributable to the thickness of the outer plexiform or RPE layers, which do not vary significantly with age (Trinh et al., 2021).

Analyses of OCT volume scans suggest that the total choroidal and mean choroidal luminal areas decrease with age (Nivison-Smith et al., 2020). Choroidal blood flow and volume, measured using laser Doppler flowmetry and expressed in arbitrary units, have been experimentally found to decrease by 7.5 and 8.8% per decade, respectively (Grunwald et al., 1998). Investigations of variations in choroidal blood velocities with age have yielded conflicting results (Grunwald et al., 1998; Straubhaar et al., 2000). The mean cross-sectional diameter of vessels forming the choriocapillaris (equivalent to choriocapillaris thickness) and its vascular density decline by up to 45 and 34% between the first and tenth decade, respectively (Ramrattan et al., 1994). This latter finding may be correlated with the increase in flow deficits observed *in vivo* using OCTA (Zheng et al., 2019). The effect of these changes on the transfer of molecules to the outer retina is unclear. Theoretical considerations suggest that a reduction in choroidal blood flow may result in smaller blood velocities within the choriocapillaris, causing an increase in spatial heterogeneities in mass transfers between this vascular bed and the outer retina (Zouache et al., 2016c). Mathematical models indicate that reduced choriocapillaris thickness causes an increase in resistance to blood flow (Zouache et al., 2015), but is also synonymous with larger passive transfer rates between the choriocapillaris and the outer retina (Zouache et al., 2019). A reduction in vascular density results in a decline in the surface area of the choriocapillaris available for exchange; however, it may also have a positive effect on rates of transfers to the outer retina by causing a local increase in blood velocity. The significance of the observed decline in submacular total choroidal thickness with age (Wakatsuki et al., 2015) is yet to be understood. Increasing age is associated with a thickening of Bruch's membrane by a proportion reaching 135% between the first and tenth decade on average (Ramrattan et al., 1994), a loss of definition of the elastin layer and an accumulation of matrix and non-matrix material rich in lipids within its sublayers (Hogan, 1967; Feeney-Burns and Ellersieck, 1985; Pauleikhoff et al., 1990; Holz et al., 1994; Karwatowski et al., 1995; Johnson et al., 2007). Increased cross-linking of fibers and accumulations of advanced glycation end products (Karwatowski et al., 1995; Handa et al., 1999) are also observed. These structural changes begin early in life (Feeney-Burns and Ellersieck, 1985) and alter the porosity and diffusive properties of the membrane in a molecule-specific manner. The hydraulic conductivity of Bruch's membrane decreases exponentially with age, being halved every 9.5 years on average (Moore et al., 1995). This variation is partly explained by the accumulation of extractable lipids within the membrane (Curcio et al., 2011), which follows a reciprocal pattern (Holz et al., 1994). *In vitro* experiments have demonstrated a 45–65% linear decrease of the transport of amino-acids across Bruch's membrane over a lifespan (Hussain et al., 2002). The diffusional transport of macromolecules (such as dextran) accross the membrane is reduced by 93.5% between the first and ninth decade (Hussain et al., 2010). The maximal size of serum proteins crossing Bruch's membrane is progressively reduced from approximately 200 kDa in the first decade to 100 kDa in the ninth decade, and is associated with a 10-fold reduction in their transport over this time (Moore and Clover, 2001).

Equatorial and Peripheral Regions

At the temporal equator, the density of cones is reduced by 23% on average by the ninth decade (Curcio et al., 1993); see **Figure 5C**. The average rate of decrease of cones and RPE cells is uniform and estimated to be approximately to 16 and 14 cells/mm^2/year, respectively (Gao and Hollyfield, 1992). Some have reported stable rod counts in this region throughout adulthood (Curcio et al., 1993) whereas others observed non-uniform rates of decrease with age (Gao and Hollyfield, 1992). This later study suggested that the variation in the density of rod with age was not linear. Rod loss appeared to be more pronounced between the second and fourth decade than between the fourth and ninth decade. Gao and Hollyfield (1992) found that the ratio of photoreceptor to RPE cells did not vary significantly with age, indicating a parallel loss of these apposed cells. Loss of RPE cells in the far periphery is associated with variations in their typical morphology that are similar to those observed in the macular retina. In contrast, the morphology of RPE cells in the mid-periphery appears to remain stable throughout adulthood (Bhatia et al., 2016). Age-related changes in the structure of Bruch's membrane are not as apparent in the peripheral retina as in the macular region. Changes in non-collagen protein content (Karwatowski et al., 1995) including lipids (Johnson et al., 2007) are not systematically observed. The reduction in hydraulic conductivity is less pronounced as compared to the macula (Moore et al., 1995), and macromolecular diffusion is only reduced by 66% between the first and ninth decade (Hussain et al., 2010).

The extension of dendritic fibers of a subtype of bipolar cells beyond the outer plexiform layer and into the outer nuclear layer has been observed in aged peripheral retinas (Eliasieh et al., 2007). Widespread loss of retinal capillaries with age has been observed in the peripheral retina (Kuwabara et al., 1961; Kuwabara and Cogan, 1965), as well as an increased incidence of vacuole-like structures in capillary basement membranes (Hogan and Feeney, 1963b; Powner et al., 2011); although the significance of this later finding is unclear. The ratio between the density of cells in the ganglion cell layer and that of rods does not vary significantly with age. Similarly to rods, loss of cells within the ganglion cell layer may be more pronounced between the second and fourth decade than between the fourth and ninth decade (Gao and Hollyfield, 1992). This study and others (Curcio et al., 1993) support the idea that ganglion cell losses in the peripheral retina occur at a rate smaller than that seen in the macula, although this has been contested (Harman et al., 2000). Curcio et al. (1993) identified a region of the peripheral retina displaying consistently lower ganglion cell densities in older eyes as compared to younger ones.

Systemic Factors

It is beyond the scope of this review to describe systemic changes associated with aging; however, their effect on retinal mass transport systems should not be overlooked. It has long been known that cardiac output decreases with age while blood pressure increases (Boss and Seegmiller, 1981). Plasma proteome also displays marked variations with age (Lehallier et al., 2019). Serum or plasma proteins influence transport across endothelial cells (by modulating oncotic pressures for instance) (Bhave and Neilson, 2011) and semi-permeable membranes, and are therefore a key determinant of retinal homeostasis. The effect of these changes on retinal and choroidal blood flow is yet to be fully explored. Basic theoretical considerations suggest that a reduction in cardiac output and/or an increase in arterial blood pressure may exacerbate spatial heterogeneities in mass transfers between the choriocapillaris and outer retina (Zouache et al., 2016c). This effect is more pronounced for larger molecules, which have a comparatively longer travel time between blood and tissue. Whether the retinal and choroidal vasculatures have evolved mechanisms to adapt to these changes is unknown.

Conclusion

The effect of aging on the retina is spatially heterogeneous; it is more prominent in the region with the highest energy requirements, the macula, and in the outer retina and choroid as compared to the inner retina. Direct and indirect evidence point to a progressive breakdown of mass transfers between retinal neurons and their respective metabolite delivery systems. However, the contribution of this breakdown to retinal aging and its correlation with cellular alterations and potential loss of function remains to be fully elucidated. The 30% loss in rod density in the macula appears to concord with the 34% decrease in choriocapillaris density observed with age (see **Figure 5B**). However, more work is necessary to understand the relation between these two systems. The largest change in retinal mass transport systems is by far seen in Bruch's membrane. The selectivity of this barrier to transport is dramatically altered in aged eyes, with the transfer of larger molecules and fluids being comparatively more affected. Changes seen in the inner retina appear to be largely independent from those observed among photoreceptors and choroid; however, more work is necessary to confirm this.

CONCLUSION AND PERSPECTIVES

Our ability to fully assess correlations between variations in retinal neuron populations and changes in their respective mass transport systems using published data is limited by the fact that the key components to consider – neurons, vasculatures, extravascular and extracellular elements – have predominantly been studied in isolation. The retina involves many cellular elements that function through *symbiotic* relationships. It is now thought that photoreceptors are at the center of a metabolic landscape involving RPE and Müller cells (Kanow et al., 2017; Viegas and Neuhauss, 2021). These functional units rely on adequate mass exchange between Müller cells and retinal capillaries, and between choriocapillaris, Bruch's membrane and RPE. Investigating these entities as units may yield better insights not only into interaction between retinal cells and mass transport systems, but also into the chain of events driving retinal senescence and vitreoretinal disorders.

Our assessment of the relation between retinal neuron populations and mass transport systems in aging is considerably limited by the lack of models or frameworks developed to differentiate between structural and functional changes caused by aging and those driven by disease. This limitation is more broadly a significant impediment to the study of retinal aging. A large part of our understanding in this regard comes from samples selected based on the absence of phenotypes traditionally associated with vitreoretinal disorders. But many (Zouache et al., 2020; Williams et al., 2021) have shown that defining retinal diseases using phenotype alone is not sufficient. The consequences of genetic mutations driving AMD is for instance often detected late in life; however, their effect on retinal and choroidal structures is likely to begin much earlier. An effective way to address this is to stratify subjects base on genetic susceptibility for disease (Pappas et al., 2021) and to exclude those at high risk from cross-sectional and longitudinal analyses.

Future studies may benefit from considering variations in mass exchange within the retina and their effect at the molecular, cellular and tissue levels. Models developed within frameworks centered around basic physical principles can provide extremely valuable insights into processes driving alterations and help generate hypotheses to be experimentally tested. A benefit of these approaches is the ability to link phenomenon occurring at distinct scales. Biological systems such as the retina are intrinsically multiscale, and cells themselves must integrate several scales to functions (Lecca, 2013). Integrating information from different levels to build a better understanding of the retina is a major challenge; however, it is key to designing effective strategies to slow or even reverse vision losses caused by aging and vitreoretinal disorders.

Laying down a framework capable of assessing the effect of variations in retinal neuron populations and their respective mass transport systems on visual function is incredibly challenging, in part because of the broad range of scales associated with the processes and structure at play. Such a framework is however necessary to determine the nature of the relation between cellular and tissue-level changes and vision. Alterations in the selective permeability of Bruch's membrane restrict the movement of many molecules essential to the visual cycle; however, their effect on visual function is presently impossible to assess directly. Some have proposed that rod visual function is unlikely to be affected by rod losses observed in aging (Oyster, 1999). This would indicate that the relation between photoreceptor loss and visual impairment is not linear. Integrating functional and structural information from multiple scales will be necessary in future studies to understand the full extent of the resilience and adaptability of our visual system.

AUTHOR CONTRIBUTIONS

MAZ performed all literature searches, wrote and revised the review and generated all figures.

FUNDING

This work was in part supported by an Unrestricted Grant from Research to Prevent Blindness, New York, NY, to the Department of Ophthalmology and Visual Sciences, University of Utah.

SUPPLEMENTARY MATERIAL

The Supplementary Material for this article can be found online at: https://www.frontiersin.org/articles/10.3389/fnagi.2022.778404/full#supplementary-material

REFERENCES

Aalkjær, C., Boedtkjer, D., and Matchkov, V. (2011). Vasomotion - what is currently thought? *Acta Physiol.* 202, 253–269. doi: 10.1111/j.1748-1716.2011.02320.x

Abukawa, H., Tomi, M., Kiyokawa, J., Hori, S., Kondo, T., Terasaki, T., et al. (2009). Modulation of retinal capillary endothelial cells by Müller glial cell-derived factors. *Mol. Vis.* 15, 451–457.

Aggarwal, P., Nag, T. C., and Wadhwa, S. (2007). Age-related decrease in rod bipolar cell density of the human retina: an immunohistochemical study. *J. Biosci.* 32, 293–298. doi: 10.1007/s12038-007-0029-9

Ahnelt, P. K., Kolb, H., and Pflug, R. (1987). Identification of a subtype of cone photoreceptor, likely to be blue sensitive, in the human retina. *J. Comp. Neurol.* 255, 18–34. doi: 10.1002/cne.902550103

Alberts, B., Johnson, A., Lewis, J., Raff, M., Roberts, K., and Walter, P. (2014). *Molecular biology of the cell*, 6th Edn. New York, NY: Garland Science, doi: 10.1201/9780203833445

Alm, A., and Bill, A. (1972). The Oxygen Supply to the Retina, II. Effects of High Intraocular Pressure and of Increased Arterial Carbon Dioxide Tension on Uveal and Retinal Blood Flow in Cats. *Acta Physiol. Scand.* 84, 306–319.

Alterman, M., and Henkind, P. (1968). Radial peripapillary capillaries of the retina. II. Possible role in Bjerrum scotoma. *Br. J. Ophthalmol.* 52, 26–31. doi: 10.1136/bjo.52.1.26

Amalric, P. (1983). The Choriocapillaris in the Macular Area: Clinical and Angiographic Study. *Int. Ophthalmol.* 6, 149–153.

An, D., Balaratnasingam, C., Heisler, M., Francke, A., Ju, M., McAllister, I. L., et al. (2018). Quantitative comparisons between optical coherence tomography angiography and matched histology in the human eye. *Exp. Eye Res.* 170, 13–19. doi: 10.1016/j.exer.2018.02.006

Araki, M. (1976). [Observations on the corrosion casts of the choriocapillaries of enzyme-induced glaucomatous eye of rhesus monkey (author's transl)]. *Nihon. Ganka Gakkai Zasshi* 80, 675–683.

Ardeljan, D., and Chan, C.-C. (2013). Aging is not a disease: distinguishing age-related macular degeneration from aging. *Prog. Retin Eye Res.* 37, 68–89. doi: 10.1016/j.preteyeres.2013.07.003

Armaly, M. F., and Araki, M. (1975). Effect of ocular pressure on choroidal circulation in the cat and Rhesus monkey. *Invest. Ophthalmol.* 14, 584–591.

Balaratnasingam, C., An, D., Sakurada, Y., Lee, C. S., Lee, A. Y., McAllister, I. L., et al. (2018). Comparisons Between Histology and Optical Coherence Tomography Angiography of the Periarterial Capillary-Free Zone. *Am. J. Ophthalmol.* 189, 55–64. doi: 10.1016/j.ajo.2018.02.007

Batchelor, G. K. (2000). *An Introduction to Fluid Dynamics (Cambridge Mathematical Library)*. Cambridge: Cambridge University Press.

Bates, D. O. (2010). Vascular endothelial growth factors and vascular permeability. *Cardiovasc. Res.* 87, 262–271. doi: 10.1093/cvr/cvq105

Behzadian, M. A., Wang, X. L., and Windsor, L. J. (2001). TGF-β increases retinal endothelial cell permeability by increasing MMP-9: possible role of glial cells in endothelial barrier function. *Invest. Ophthalmol. Vis. Sci.* 42, 853–859.

Bernstein, M. H., and Hollenberg, M. J. (1965). Fine structure of the choriocappillaris and retinal capillaries. *Invest. Ophthalmol.* 4, 1016–1025.

Bhatia, S. K., Rashid, A., Chrenek, M. A., Zhang, Q., Bruce, B. B., Klein, M., et al. (2016). Analysis of RPE morphometry in human eyes. *Mol. Vis.* 22, 898–916.

Bhave, G., and Neilson, E. G. (2011). Body fluid dynamics: back to the future. *J. Am. Soc. Nephrol.* 22, 2166–2181. doi: 10.1681/ASN.2011080865

Bill, A. (1962). Intraocular pressure and blood flow through the uvea. *Arch. Ophthalmol.* 67, 336–348. doi: 10.1001/archopht.1962.00960020338010

Bill, A., Sperber, G., and Ujiie, K. (1983). Physiology of the choroidal vascular bed. *Int. Ophthalmol.* 6, 101–107. doi: 10.1007/BF00127638

Birol, G., Wang, S., Budzynski, E., Wangsa-Wirawan, N. D., and Linsenmeier, R. A. (2007). Oxygen distribution and consumption in the macaque retina. *Am. J. Physiol. Heart Circ. Physiol.* 293, H1696–H1704. doi: 10.1152/ajpheart.00221.2007

Blaauwgeers, H. G., Holtkamp, G. M., Rutten, H., Witmer, A. N., Koolwijk, P., Partanen, T. A., et al. (1999). Polarized vascular endothelial growth factor secretion by human retinal pigment epithelium and localization of vascular endothelial growth factor receptors on the inner choriocapillaris. Evidence for a trophic paracrine relation. *Am. J. Pathol.* 155, 421–428. doi: 10.1016/S0002-9440(10)65138-3

Booij, J. C., Baas, D. C., Beisekeeva, J., Gorgels, T. G. M. F., and Bergen, A. A. B. (2010). The dynamic nature of Bruch's membrane. *Prog. Retin Eye Res.* 29, 1–18. doi: 10.1016/j.preteyeres.2009.08.003

Bosma, E. K., van Noorden, C. J. F., Schlingemann, R. O., and Klaassen, I. (2018). The role of plasmalemma vesicle-associated protein in pathological breakdown of blood-brain and blood-retinal barriers: potential novel therapeutic target for cerebral edema and diabetic macular edema. *Fluids Barriers CNS* 15:24. doi: 10.1186/s12987-018-0109-2

Boss, G. R., and Seegmiller, J. E. (1981). Age-related physiological changes and their clinical significance. *West J. Med.* 135, 434–440.

Bringmann, A., Pannicke, T., Grosche, J., Francke, M., Wiedemann, P., Skatchkov, S. N., et al. (2006). Müller cells in the healthy and diseased retina. *Prog. Retin. Eye Res.* 25, 397–424. doi: 10.1016/j.preteyeres.2006.05.003

Brinks, J., van Dijk, E. H. C., Klaassen, I., Schlingemann, R. O., Kielbasa, S. M., Emri, E., et al. (2021). Exploring the choroidal vascular labyrinth and its molecular and structural roles in health and disease. *Prog. Retin. Eye Res.* 2021:100994. doi: 10.1016/j.preteyeres.2021.100994

Büssow, H. (1980). The astrocytes in the retina and optic nerve head of mammals: a special glia for the ganglion cell axons. *Cell Tissue Res.* 206, 367–378. doi: 10.1007/BF00237966

Buttery, R. G., Hinrichsen, C. F., Weller, W. L., and Haight, J. R. (1991). How thick should a retina be? A comparative study of mammalian species with and without intraretinal vasculature. *Vision Res.* 31, 169–187. doi: 10.1016/0042-6989(91)90110-q

Calkins, D. J. (2013). Age-related changes in the visual pathways: blame it on the axon. *Invest. Ophthalmol. Vis. Sci.* 54, ORSF37–ORSF41. doi: 10.1167/iovs.13-12784

Campbell, J. P., Zhang, M., Hwang, T. S., Bailey, S. T., Wilson, D. J., Jia, Y., et al. (2017). Detailed Vascular Anatomy of the Human Retina by Projection-Resolved Optical Coherence Tomography Angiography. *Sci. Rep.* 7:42201. doi: 10.1038/srep42201

Campbell, M., and Humphries, P. (2012). The blood-retina barrier: tight junctions and barrier modulation. *Adv. Exp. Med. Biol.* 763, 70–84. doi: 10.1007/978-1-4614-4711-5_3

Campello, L., Singh, N., Advani, J., Mondal, A. K., Corso-Diaz, X., and Swaroop, A. (2021). Aging of the retina: molecular and metabolic turbulences and potential interventions. *Annu. Rev. Vis. Sci.* 2021:114940. doi: 10.1146/annurev-vision-100419-114940

Causin, P., Guidoboni, G., Malgaroli, F., Sacco, R., and Harris, A. (2016). Blood flow mechanics and oxygen transport and delivery in the retinal microcirculation: multiscale mathematical modeling and numerical simulation. *Biomech. Model Mechanobiol.* 15, 525–542. doi: 10.1007/s10237-015-0708-7

Chan, G., Balaratnasingam, C., Xu, J., Mammo, Z., Han, S., Mackenzie, P., et al. (2015). In vivo optical imaging of human retinal capillary networks using speckle variance optical coherence tomography with quantitative clinico-histological correlation. *Microvasc. Res.* 100, 32–39. doi: 10.1016/j.mvr.2015.04.006

Chan, G., Balaratnasingam, C., Yu, P. K., Morgan, W. H., McAllister, I. L., Cringle, S. J., et al. (2012). Quantitative morphometry of perifoveal capillary networks in the human retina. *Invest. Ophthalmol. Vis. Sci.* 53, 5502–5514. doi: 10.1167/iovs.12-10265

Chan-Ling, T., Koina, M. E., McColm, J. R., Dahlstrom, J. E., Bean, E., Adamson, S., et al. (2011). Role of CD44+ stem cells in mural cell formation in the human choroid: evidence of vascular instability due to limited pericyte ensheathment. *Invest. Ophthalmol. Vis. Sci.* 52, 399–410. doi: 10.1167/iovs.10-5403

Chase, J. (1982). The evolution of retinal vascularization in mammals. A comparison of vascular and avascular retinae. *Ophthalmology* 89, 1518–1525. doi: 10.1016/s0161-6420(82)34608-4

Chinchore, Y., Begaj, T., Wu, D., Drokhlyansky, E., and Cepko, C. L. (2017). Glycolytic reliance promotes anabolism in photoreceptors. *Elife* 6:25946. doi: 10.7554/eLife.25946

Chong, N. H. V., Keonin, J., Luthert, P. J., Frennesson, C. I., Weingeist, D. M., Wolf, R. L., et al. (2005). Decreased thickness and integrity of the macular elastic layer of Bruch's membrane correspond to the distribution of lesions associated with age-related macular degeneration. *Am. J. Pathol.* 166, 241–251. doi: 10.1016/S0002-9440(10)62248-1

Chui, T. Y. P., Mo, S., Krawitz, B., Menon, N. R., Choudhury, N., Gan, A., et al. (2016). Human retinal microvascular imaging using adaptive optics scanning light ophthalmoscopy. *Int. J. Retina Vitreous* 2:11. doi: 10.1186/s40942-016-0037-8

Chui, T. Y. P., Song, H., Clark, C. A., Papay, J. A., Burns, S. A., and Elsner, A. E. (2012). Cone photoreceptor packing density and the outer nuclear layer thickness in healthy subjects. *Invest. Ophthalmol. Vis. Sci.* 53, 3545–3553. doi: 10.1167/iovs.11-8694

Chui, T. Y., Song, H., and Burns, S. A. (2008b). Adaptive-optics imaging of human cone photoreceptor distribution. *J. Opt. Soc. Am. A Opt. Image Sci. Vis.* 25, 3021–3029.

Chui, T. Y., Song, H., and Burns, S. A. (2008a). Individual variations in human cone photoreceptor packing density: variations with refractive error. *Invest. Ophthalmol. Vis. Sci.* 49, 4679–4687. doi: 10.1167/iovs.08-2135

Condren, A. B., Kumar, A., Mettu, P., Liang, K. J., Zhao, L., Tsai, J., et al. (2013). Perivascular mural cells of the mouse choroid demonstrate morphological diversity that is correlated to vasoregulatory function. *PLoS One* 8:e53386. doi: 10.1371/journal.pone.0053386

Conn, P. M. (2006). *Handbook of Models for Human Aging*, 1st Edn. Amsterdam: Academic Press.

Coscas, F., Sellam, A., Glacet-Bernard, A., Jung, C., Goudot, M., Miere, A., et al. (2016). Normative data for vascular density in superficial and deep capillary plexuses of healthy adults assessed by optical coherence tomography angiography. *Invest. Ophthalmol. Vis. Sci.* 57, OCT211–OCT223. doi: 10.1167/iovs.15-18793

Cunha-Vaz, J. G. (1976). The blood-retinal barriers. *Doc. Ophthalmol.* 41, 287–327.

Curcio, C. A., Allen, K. A., Sloan, K. R., Lerea, C. L., Hurley, J. B., Klock, I. B., et al. (1991). Distribution and morphology of human cone photoreceptors stained with anti-blue opsin. *J. Comp. Neurol.* 312, 610–624. doi: 10.1002/cne.903120411

Curcio, C. A., and Allen, K. A. (1990). Topography of ganglion cells in human retina. *J. Comp. Neurol.* 300, 5–25. doi: 10.1002/cne.903000103

Curcio, C. A., and Drucker, D. N. (1993). Retinal ganglion cells in Alzheimer's disease and aging. *Ann. Neurol.* 33, 248–257. doi: 10.1002/ana.410330305

Curcio, C. A., Johnson, M., Rudolf, M., and Huang, J.-D. (2011). The oil spill in ageing Bruch membrane. *Br. J. Ophthalmol.* 95, 1638–1645. doi: 10.1136/bjophthalmol-2011-300344

Curcio, C. A., Millican, C. L., Allen, K. A., and Kalina, R. E. (1993). Aging of the human photoreceptor mosaic: evidence for selective vulnerability of rods in central retina. *Invest. Ophthalmol. Vis. Sci.* 34, 3278–3296.

Curcio, C. A., Sloan, K. R., Kalina, R. E., and Hendrickson, A. E. (1990). Human photoreceptor topography. *J. Comp. Neurol.* 292, 497–523. doi: 10.1002/cne.902920402

Curcio, C. A., Sloan, K. R., Packer, O., Hendrickson, A. E., and Kalina, R. E. (1987). Distribution of cones in human and monkey retina: individual variability and radial asymmetry. *Science* 236, 579–582. doi: 10.1126/science.3576186

Dacey, D. M. (1990). The dopaminergic amacrine cell. *J. Comp. Neurol.* 301, 461–489. doi: 10.1002/cne.903010310

Distler, C., and Dreher, Z. (1996). Glia cells of the monkey retina–II. Müller cells. *Vis. Res.* 36, 2381–2394. doi: 10.1016/0042-6989(96)00005-3

Distler, C., Weigel, H., and Hoffmann, K. P. (1993). Glia cells of the monkey retina. I. Astrocytes. *J. Comp. Neurol.* 333, 134–147. doi: 10.1002/cne.903330111

Dorey, C. K., Wu, G., Ebenstein, D., Garsd, A., and Weiter, J. J. (1989). Cell loss in the aging retina. Relationship to lipofuscin accumulation and macular degeneration. *Invest. Ophthalmol. Vis. Sci.* 30, 1691–1699.

Dreher, Z., Robinson, S. R., and Distler, C. (1992). Müller cells in vascular and avascular retinae: a survey of seven mammals. *J. Comp. Neurol.* 323, 59–80. doi: 10.1002/cne.903230106

Du, J., Rountree, A., Cleghorn, W. M., Contreras, L., Lindsay, K. J., Sadilek, M., et al. (2016a). Phototransduction influences metabolic flux and nucleotide metabolism in mouse retina. *J. Biol. Chem.* 291, 4698–4710. doi: 10.1074/jbc.M115.698985

Du, J., Yanagida, A., Knight, K., Engel, A. L., Vo, A. H., Jankowski, C., et al. (2016b). Reductive carboxylation is a major metabolic pathway in the retinal pigment epithelium. *Proc. Natl. Acad. Sci. U S A.* 113, 14710–14715. doi: 10.1073/pnas.1604572113

Dubra, A., Sulai, Y., Norris, J. L., Cooper, R. F., Dubis, A. M., Williams, D. R., et al. (2011). Noninvasive imaging of the human rod photoreceptor mosaic using a confocal adaptive optics scanning ophthalmoscope. *Biomed. Opt. Express* 2, 1864–1876. doi: 10.1364/BOE.2.001864

Eliasieh, K., Liets, L. C., and Chalupa, L. M. (2007). Cellular reorganization in the human retina during normal aging. *Invest. Ophthalmol. Vis. Sci.* 48, 2824–2830. doi: 10.1167/iovs.06-1228

Elsner, A. E., Chui, T. Y. P., Feng, L., Song, H. X., Papay, J. A., and Burns, S. A. (2017). Distribution differences of macular cones measured by AOSLO: Variation in slope from fovea to periphery more pronounced than differences in total cones. *Vis. Res.* 132, 62–68. doi: 10.1016/j.visres.2016.06.015

Erecińska, M., and Silver, I. A. (2001). Tissue oxygen tension and brain sensitivity to hypoxia. *Respir. Physiol.* 128, 263–276. doi: 10.1016/s0034-5687(01)00306-1

Eriksson, U., and Alm, A. (2009). Macular thickness decreases with age in normal eyes: a study on the macular thickness map protocol in the Stratus OCT. *Br. J. Ophthalmol.* 93, 1448–1452. doi: 10.1136/bjo.2007.131094

Farber, D. B., Flannery, J. G., Lolley, R. N., and Bok, D. (1985). Distribution patterns of photoreceptors, protein, and cyclic nucleotides in the human retina. *Invest. Ophthalmol. Vis. Sci.* 26, 1558–1568.

Farnoodian, M., Sorenson, C. M., and Sheibani, N. (2018). PEDF expression affects the oxidative and inflammatory state of choroidal endothelial cells. *Am. J. Physiol. Cell Physiol.* 314, C456–C472. doi: 10.1152/ajpcell.00259.2017

Federman, J. L. (1982). The fenestrations of the choriocapillaris in the presence of choroidal melanoma. *Trans. Am. Ophthalmol. Soc.* 80, 498–516.

Feeney-Burns, L., and Ellersieck, M. R. (1985). Age-related changes in the ultrastructure of Bruch's membrane. *Am. J. Ophthalmol.* 100, 686–697. doi: 10.1016/0002-9394(85)90625-7

Feke, G. T., Tagawa, H., Deupree, D. M., Goger, D. G., Sebag, J., and Weiter, J. J. (1989). Blood flow in the normal human retina. *Invest. Ophthalmol. Vis. Sci.* 30, 58–65.

Feng, D., Nagy, J. A., Hipp, J., Dvorak, H. F., and Dvorak, A. M. (1996). Vesiculo-vacuolar organelles and the regulation of venule permeability to macromolecules by vascular permeability factor, histamine, and serotonin. *J. Exp. Med.* 183, 1981–1986. doi: 10.1084/jem.183.5.1981

Flower, R. W. (1993). Extraction of choriocapillaris hemodynamic data from ICG fluorescence angiograms. *Invest. Ophthalmol. Vis. Sci.* 34, 2720–2729.

Flower, R. W., Fryczkowski, A. W., and McLeod, D. S. (1995). Variability in choriocapillaris blood flow distribution. *Invest. Ophthalmol. Vis. Sci.* 36, 1247–1258.

Fouquet, S., Vacca, O., Sennlaub, F., and Paques, M. (2017). The 3D retinal capillary circulation in pigs reveals a predominant serial organization. *Invest. Ophthalmol. Vis. Sci.* 58, 5754–5763. doi: 10.1167/iovs.17-22097

Frank, R. N., Turczyn, T. J., and Das, A. (1990). Pericyte coverage of retinal and cerebral capillaries. *Invest. Ophthalmol. Vis. Sci.* 31, 999–1007.

Freeman, S. A., Vega, A., Riedl, M., Collins, R. F., Ostrowski, P. P., Woods, E. C., et al. (2018). Transmembrane Pickets Connect Cyto- and Pericellular Skeletons Forming Barriers to Receptor Engagement. *Cell* 172, 305.e–317.e. doi: 10.1016/j.cell.2017.12.023

Frey, A., Meckelein, B., Weiler-Güttler, H., Möckel, B., Flach, R., and Gassen, H. G. (1991). Pericytes of the brain microvasculature express gamma-glutamyl transpeptidase. *Eur. J. Biochem.* 202, 421–429. doi: 10.1111/j.1432-1033.1991.tb16391.x

Friedland, A. B. (1978). A mathematical model of transmural transport of oxygen to the retina. *Bull. Math. Biol.* 40, 823–837.

Friedman, E. (1970). Choroidal blood flow. Pressure-flow relationships. *Arch. Ophthalmol.* 83, 95–99.

Fritsche, L. G., Igl, W., Bailey, J. N. C., Grassmann, F., Sengupta, S., Bragg-Gresham, J. L., et al. (2016). A large genome-wide association study of age-related macular degeneration highlights contributions of rare and common variants. *Nat. Genet.* 48, 134–143. doi: 10.1038/ng.3448

Fry, B. C., Coburn, E. B., Whiteman, S., Harris, A., Siesky, B., and Arciero, J. (2018). Predicting retinal tissue oxygenation using an image-based theoretical model. *Math. Biosci.* 305, 1–9. doi: 10.1016/j.mbs.2018.08.005

Fryczkowski, A. W. (1994). Anatomical and functional choroidal lobuli. *Int. Ophthalmol.* 18, 131–141. doi: 10.1007/BF00915961

Fryczkowski, A. W., and Sherman, M. D. (1988). Scanning electron microscopy of human ocular vascular casts: the submacular choriocapillaris. *Acta Anatomica* 132, 265–269. doi: 10.1159/000146586

Fryczkowski, A. W., Sherman, M. D., and Walker, J. (1991). Observations on the lobular organization of the human choriocapillaris. *Int. Ophthalmol.* 15, 109–120.

Gao, H., and Hollyfield, J. G. (1992). Aging of the human retina. Differential loss of neurons and retinal pigment epithelial cells. *Invest. Ophthalmol. Vis. Sci.* 33, 1–17.

Garrity, S. T., Paques, M., Gaudric, A., Freund, K. B., and Sarraf, D. (2017). Considerations in the understanding of venous outflow in the retinal capillary plexus. *Retina* 37, 1809–1812. doi: 10.1097/IAE.0000000000001784

Garron, L. K. (1963). The Ultrastructure of the Retinal Pigment Epithelium with Observations on the Choriocapillaris and Bruch's Membrane. *Trans. Am. Ophthalmol. Soc.* 61, 545–588.

Gartner, S., and Henkind, P. (1981). Aging and degeneration of the human macula. 1. Outer nuclear layer and photoreceptors. *Br. J. Ophthalmol.* 65, 23–28. doi: 10.1136/bjo.65.1.23

Garza-Gisholt, E., Hemmi, J. M., Hart, N. S., and Collin, S. P. (2014). A comparison of spatial analysis methods for the construction of topographic maps of retinal cell density. *PLoS One* 9:e93485. doi: 10.1371/journal.pone.0093485

Gherezguiher, T., Okubo, H., and Koss, M. (1991). Choroidal and Ciliary Body Blood Flow Analysis: Application of Laser Doppler Flowmetry in Experimental Animals. *Exp. Eye Res.* 53, 151–156.

Goldman, D. (2008). Theoretical models of microvascular oxygen transport to tissue. *Microcirculation* 15, 795–811. doi: 10.1080/10739680801938289

Goldman, D. (2014). Müller glial cell reprogramming and retina regeneration. *Nat. Rev. Neurosci.* 15, 431–442. doi: 10.1038/nrn3723

Gouverneur, M., Berg, B., Nieuwdorp, M., Stroes, E., and Vink, H. (2006). Vasculoprotective properties of the endothelial glycocalyx: effects of fluid shear stress. *J. Intern. Med.* 259, 393–400. doi: 10.1111/j.1365-2796.2006.01625.x

Granger, C. E., Yang, Q., Song, H., Saito, K., Nozato, K., Latchney, L. R., et al. (2018). Human retinal pigment epithelium: in vivo cell morphometry, multispectral autofluorescence, and relationship to cone mosaic. *Invest. Ophthalmol. Vis. Sci.* 59, 5705–5716. doi: 10.1167/iovs.18-24677

Grebe, R., Mughal, I., Bryden, W., McLeod, S., Edwards, M., Hageman, G. S., et al. (2019). Ultrastructural analysis of submacular choriocapillaris and its transport systems in AMD and aged control eyes. *Exp. Eye Res.* 181, 252–262. doi: 10.1016/j.exer.2019.02.018

Green, S., and Batterman, R. (2017). Biology meets physics: Reductionism and multi-scale modeling of morphogenesis. *Stud. Hist. Philos. Biol. Biomed. Sci.* 61, 20–34. doi: 10.1016/j.shpsc.2016.12.003

Grossniklaus, H. E., Nickerson, J. M., Edelhauser, H. F., Bergman, L. A. M. K., and Berglin, L. (2013). Anatomic alterations in aging and age-related diseases of the eye. *Invest. Ophthalmol. Vis. Sci.* 54, ORSF23–ORSF27. doi: 10.1167/iovs.13-12711

Grünert, U., Martin, P. R., and Wässle, H. (1994). Immunocytochemical analysis of bipolar cells in the macaque monkey retina. *J. Comp. Neurol.* 348, 607–627. doi: 10.1002/cne.903480410

Grunwald, J. E., Hariprasad, S. M., and DuPont, J. (1998). Effect of aging on foveolar choroidal circulation. *Arch. Ophthalmol.* 116, 150–154. doi: 10.1001/archopht.116.2.150

Haefliger, I. O., Zschauer, A., and Anderson, D. R. (1994). Relaxation of retinal pericyte contractile tone through the nitric oxide-cyclic guanosine monophosphate pathway. *Invest. Ophthalmol. Vis. Sci.* 35, 991–997.

Hammer, D. X., Agrawal, A., Villanueva, R., Saeedi, O., and Liu, Z. (2020). Label-free adaptive optics imaging of human retinal macrophage distribution and dynamics. *Proc. Natl. Acad. Sci. U S A.* 117, 30661–30669. doi: 10.1073/pnas.2010943117

Handa, J. T., Verzijl, N., Matsunaga, H., Aotaki-Keen, A., Lutty, G. A., te Koppele, J. M., et al. (1999). Increase in the advanced glycation end product pentosidine in Bruch's membrane with age. *Invest. Ophthalmol. Vis. Sci.* 40, 775–779.

Harman, A. M., Fleming, P. A., Hoskins, R. V., and Moore, S. R. (1997). Development and aging of cell topography in the human retinal pigment epithelium. *Invest. Ophthalmol. Vis. Sci.* 38, 2016–2026.

Harman, A., Abrahams, B., Moore, S., and Hoskins, R. (2000). Neuronal density in the human retinal ganglion cell layer from 16-77 years. *Anat. Rec.* 260, 124–131. doi: 10.1002/1097-0185(20001001)260:2<124::AID-AR20<3.0.CO;2-D

Haugh, L. M., Linsenmeier, R. A., and Goldstick, T. K. (1990). Mathematical models of the spatial distribution of retinal oxygen tension and consumption, including changes upon illumination. *Ann. Biomed. Eng.* 18, 19–36. doi: 10.1007/BF02368415

Hayreh, S. S. (1962). The ophthalmic artery: iii. branches. *Br. J. Ophthalmol.* 46, 212–247. doi: 10.1136/bjo.46.4.212

Hayreh, S. S. (1963). Arteries of the orbit in the human being. *Br. J. Surg.* 50, 938–953. doi: 10.1002/bjs.18005022708

Hayreh, S. S. (1974c). The long posterior ciliary arteries. An experimental study. *Albrecht Von Graefes Arch. Klin. Exp. Ophthalmol.* 192, 197–213. doi: 10.1007/BF00416866

Hayreh, S. S. (1974a). Submacular choroidal vascular pattern. Experimental fluorescein fundus angiographic studies. *Albrecht Von Graefes Arch. Klin. Exp. Ophthalmol.* 192, 181–196. doi: 10.1007/BF00416865

Hayreh, S. S. (1974b). The choriocapillaris. *Albrecht Von Graefes Arch. Klin. Exp. Ophthalmol.* 192, 165–179.

Hayreh, S. S. (1975). Segmental nature of the choroidal vasculature. *Br. J. Ophthalmol.* 59, 631–648. doi: 10.1136/bjo.59.11.631

Hayreh, S. S. (1990). In vivo choroidal circulation and its watershed zones. *Eye* 4(Pt 2), 273–289. doi: 10.1038/eye.1990.39

Hayreh, S. S., and Dass, R. (1962). The ophthalmic artery: ii. intra-orbital course. *Br. J. Ophthalmol.* 46, 165–185. doi: 10.1136/bjo.46.3.165

Henkind, P. (1967). Symposium on glaucoma: joint meeting with the National Society for the Prevention of Blindness. New observations on the radial peripapillary capillaries. *Invest. Ophthalmol.* 6, 103–108.

Hirsch, J., and Curcio, C. A. (1989). The spatial resolution capacity of human foveal retina. *Vision Res.* 29, 1095–1101. doi: 10.1016/0042-6989(89)90058-8

Hirsch, J., and Hylton, R. (1984). Quality of the primate photoreceptor lattice and limits of spatial vision. *Vision Res.* 24, 347–355. doi: 10.1016/0042-6989(84)90060-9

Hockwin, O., and Ohrloff, C. (1984). "The eye in the elderly: lens," in *Geriatrics 3*, ed. D. Platt (Berlin: Springer Berlin Heidelberg), 373–424. doi: 10.1007/978-3-642-68976-5_15

Hogan, M. J. (1961). Ultrastructure of the choroid. Its role in the pathogenesis of chorioretinal disease. *Trans. Pac. Coast Otoophthalmol. Soc. Annu. Meet.* 42, 61–87.

Hogan, M. J. (1967). Studies on the human macula. IV. Aging changes in Bruch's Membrane. *Arch. Ophthalmol.* 77:410. doi: 10.1001/archopht.1967.00980020412022

Hogan, M. J. (1971). *Histology of the human eye;: An atlas and textbook*. Philadelphia: Saunders.

Hogan, M. J., and Feeney, A. B. L. (1961). Electron microscopy of the human choroid. III. The blood vessels. *Am. J. Ophthalmol.* 51, 1084/212–1097/225. doi: 10.1016/0002-9394(61)91797-4

Hogan, M. J., and Feeney, L. (1963a). The ultrastructure of the retinal blood vessels. I. The large vessels. *J. Ultrastruct. Res.* 9, 10–28. doi: 10.1016/S0022-5320(63)80033-7

Hogan, M. J., and Feeney, L. (1963b). The ultrastructure of the retinal vessels: II. The small vessels. *J. Ultrastruct. Res.* 9, 29–46. doi: 10.1016/S0022-5320(63)80034-9

Hogan, M. J., and Feeney, L. (1963c). The ultrastructure of the retinal vessels. III. Vascular-glial relationships. *J. Ultrastruct. Res.* 9, 47–64. doi: 10.1016/S0022-5320(63)80035-0

Holz, F. G., Sheraidah, G., Pauleikhoff, D., and Bird, A. C. (1994). Analysis of lipid deposits extracted from human macular and peripheral Bruch's membrane. *Arch. Ophthalmol.* 112, 402–406. doi: 10.1001/archopht.1994.01090150132035

Hoon, M., Okawa, H., Della Santina, L., and Wong, R. O. L. (2014). Functional architecture of the retina: development and disease. *Prog. Retin. Eye Res.* 42, 44–84. doi: 10.1016/j.preteyeres.2014.06.003

Hormel, T. T., Jia, Y., Jian, Y., Hwang, T. S., Bailey, S. T., Pennesi, M. E., et al. (2020). Plexus-specific retinal vascular anatomy and pathologies as seen by projection-resolved optical coherence tomographic angiography. *Prog. Retin. Eye Res.* 2020:100878. doi: 10.1016/j.preteyeres.2020.100878

Hosoya, K., and Tachikawa, M. (2012). The inner blood-retinal barrier: molecular structure and transport biology. *Adv. Exp. Med. Biol.* 763, 85–104. doi: 10.1007/978-1-4614-4711-5_4

Hsu, S. C., and Molday, R. S. (1991). Glycolytic enzymes and a GLUT-1 glucose transporter in the outer segments of rod and cone photoreceptor cells. *J. Biol. Chem.* 266, 21745–21752. doi: 10.1016/S0021-9258(18)54699-8

Huang, D., Swanson, E. A., Lin, C. P., Schuman, J. S., Stinson, W. G., Chang, W., et al. (1991). Optical coherence tomography. *Science* 254, 1178–1181. doi: 10.1126/science.1957169

Hubmacher, D., and Apte, S. S. (2013). The biology of the extracellular matrix: novel insights. *Curr. Opin. Rheumatol.* 25, 65–70. doi: 10.1097/BOR.0b013e32835b137b

Hughes, A. (1977). "The topography of vision in mammals of contrasting life style: comparative optics and retinal organisation," in *The visual system in vertebrates* Handbook of sensory physiology, ed. F. Crescitelli (Berlin: Springer Berlin Heidelberg), 613–756. doi: 10.1007/978-3-642-66468-7_11

Hussain, A. A., Rowe, L., and Marshall, J. (2002). Age-related alterations in the diffusional transport of amino acids across the human Bruch's-choroid complex. *J. Opt. Soc. Am. A Opt. Image Sci. Vis.* 19, 166–172. doi: 10.1364/josaa.19.000166

Hussain, A. A., Starita, C., Hodgetts, A., and Marshall, J. (2010). Macromolecular diffusion characteristics of ageing human Bruch's membrane: implications for age-related macular degeneration (AMD). *Exp. Eye Res.* 90, 703–710. doi: 10.1016/j.exer.2010.02.013

Iafe, N. A., Phasukkijwatana, N., Chen, X., and Sarraf, D. (2016). Retinal Capillary Density and Foveal Avascular Zone Area Are Age-Dependent: Quantitative Analysis Using Optical Coherence Tomography Angiography. *Invest. Ophthalmol. Vis. Sci.* 57, 5780–5787. doi: 10.1167/iovs.16-20045

Jäkel, S., and Dimou, L. (2017). Glial Cells and Their Function in the Adult Brain: A Journey through the History of Their Ablation. *Front. Cell Neurosci.* 11:24. doi: 10.3389/fncel.2017.00024

Jia, Y., Wei, E., Wang, X., Zhang, X., Morrison, J. C., Parikh, M., et al. (2014). Optical coherence tomography angiography of optic disc perfusion in glaucoma. *Ophthalmology* 121, 1322–1332. doi: 10.1016/j.ophtha.2014.01.021

Johnson, M., Dabholkar, A., Huang, J.-D., Presley, J. B., Chimento, M. F., and Curcio, C. A. (2007). Comparison of morphology of human macular and peripheral Bruch's membrane in older eyes. *Curr. Eye Res.* 32, 791–799. doi: 10.1080/02713680701550660

Jonas, J. B., Schneider, U., and Naumann, G. O. (1992). Count and density of human retinal photoreceptors. *Graefes Arch. Clin. Exp. Ophthalmol.* 230, 505–510. doi: 10.1007/BF00181769

Kam, J. H., Weinrich, T. W., Shinhmar, H., Powner, M. B., Roberts, N. W., Aboelnour, A., et al. (2019). Fundamental differences in patterns of retinal ageing between primates and mice. *Sci. Rep.* 9:12574. doi: 10.1038/s41598-019-49121-0

Kamba, T., Tam, B. Y. Y., Hashizume, H., Haskell, A., Sennino, B., Mancuso, M. R., et al. (2006). VEGF-dependent plasticity of fenestrated capillaries in the normal adult microvasculature. *Am. J. Physiol. Heart Circ. Physiol.* 290, H560–H576. doi: 10.1152/ajpheart.00133.2005

Kanow, M. A., Giarmarco, M. M., Jankowski, C. S., Tsantilas, K., Engel, A. L., Du, J., et al. (2017). Biochemical adaptations of the retina and retinal pigment epithelium support a metabolic ecosystem in the vertebrate eye. *Elife* 6:28899. doi: 10.7554/eLife.28899

Karampelas, M., Sim, D. A., Keane, P. A., Papastefanou, V. P., Sadda, S. R., Tufail, A., et al. (2013). Evaluation of retinal pigment epithelium-Bruch's membrane complex thickness in dry age-related macular degeneration using optical coherence tomography. *Br. J. Ophthalmol.* 97, 1256–1261. doi: 10.1136/bjophthalmol-2013-303219

Karst, S. G., Salas, M., Hafner, J., Scholda, C., Vogl, W.-D., Drexler, W., et al. (2019). Three-dimensional analysis of retinal microaneurysms with adaptive optics optical coherence tomography. *Retina* 39, 465–472. doi: 10.1097/IAE.0000000000002037

Karwatowski, W. S., Jeffries, T. E., Duance, V. C., Albon, J., Bailey, A. J., and Easty, D. L. (1995). Preparation of Bruch's membrane and analysis of the age-related changes in the structural collagens. *Br. J. Ophthalmol.* 79, 944–952. doi: 10.1136/bjo.79.10.944

Kashani, A. H., Chen, C.-L., Gahm, J. K., Zheng, F., Richter, G. M., Rosenfeld, P. J., et al. (2017). Optical coherence tomography angiography: A comprehensive review of current methods and clinical applications. *Prog. Retin. Eye Res.* 60, 66–100. doi: 10.1016/j.preteyeres.2017.07.002

Keener, J., and Sneyd, J. (2009). *Mathematical Physiology*, 2nd Edn. New York, NY: Springer.

Kiel, J. W. (1994). Choroidal myogenic autoregulation and intraocular pressure. *Exp. Eye Res.* 58, 529–543. doi: 10.1006/exer.1994.1047

Kiel, J. W., and Shepherd, A. P. (1992). Autoregulation of choroidal blood flow in the rabbit. *Invest. Ophthalmol. Vis. Sci.* 33, 2399–2410.

Kiel, J. W., and van Heuven, W. A. (1995). Ocular perfusion pressure and choroidal blood flow in the rabbit. *Invest. Ophthalmol. Vis. Sci.* 36, 579–585.

Kim, S. A., Kim, S. J., Choi, Y. A., Yoon, H.-J., Kim, A., and Lee, J. (2019). Retinal VEGFA maintains the ultrastructure and function of choriocapillaris by preserving the endothelial PLVAP. *Biochem. Biophys. Res. Commun.* 2019:085. doi: 10.1016/j.bbrc.2019.11.085

King, B. J., Sapoznik, K. A., Elsner, A. E., Gast, T. J., Papay, J. A., Clark, C. A., et al. (2017). SD-OCT and Adaptive Optics Imaging of Outer Retinal Tubulation. *Optom. Vis. Sci.* 94, 411–422. doi: 10.1097/OPX.0000000000001031

Klien, B. A. (1966). Regional and aging characteristics of the normal choriocapillaris in flat preparations. Preliminary remarks. *Am. J. Ophthalmol.* 61, 1191–1197.

Kornzweig, A. L., Eliasoph, I., and Feldstein, M. (1964). Retinal vasculature in the aged. *Bull. N. Y. Acad. Med.* 40, 116–129.

Krogh, A. (1919). The supply of oxygen to the tissues and the regulation of the capillary circulation. *J. Physiol.* 52, 457–474.

Kurokawa, K., Liu, Z., and Miller, D. T. (2017). Adaptive optics optical coherence tomography angiography for morphometric analysis of choriocapillaris [Invited]. *Biomed. Opt. Express* 8:1803. doi: 10.1364/BOE.8.001803

Kurokawa, K., Sasaki, K., Makita, S., Hong, Y.-J., and Yasuno, Y. (2012). Three-dimensional retinal and choroidal capillary imaging by power Doppler optical coherence angiography with adaptive optics. *Opt. Express* 20, 22796–22812. doi: 10.1364/OE.20.022796

Kuwabara, T., and Cogan, D. G. (1965). Retinal vascular patterns. VII. Acellular change. *Invest. Ophthalmol.* 4, 1049–1064.

Kuwabara, T., Carroll, J. M., and Cogan, D. G. (1961). Retinal vascular patterns. III. Age, hypertension, absolute glaucoma, injury. *Arch. Ophthalmol.* 65, 708–716. doi: 10.1001/archopht.1961.01840020710019

La Morgia, C., Ross-Cisneros, F. N., Sadun, A. A., Hannibal, J., Munarini, A., Mantovani, V., et al. (2010). Melanopsin retinal ganglion cells are resistant to neurodegeneration in mitochondrial optic neuropathies. *Brain* 133, 2426–2438. doi: 10.1093/brain/awq155

LaBarbera, M. (1990). Principles of design of fluid transport systems in zoology. *Science* 249, 992–1000.

Laíns, I., Wang, J. C., Cui, Y., Katz, R., Vingopoulos, F., Staurenghi, G., et al. (2021). Retinal applications of swept source optical coherence tomography (OCT) and optical coherence tomography angiography (OCTA). *Prog. Retin. Eye Res.* 84:100951. doi: 10.1016/j.preteyeres.2021.100951

Langlo, C. S., Flatter, J. A., Dubra, A., Wirostko, W. J., and Carroll, J. (2014). A lensing effect of inner retinal cysts on images of the photoreceptor mosaic. *Retina* 34, 421–422. doi: 10.1097/IAE.0b013e3182a2f50c

Laties, A. M., and Jacobowitz, D. (1966). A comparative study of the autonomic innervation of the eye in monkey, cat, and rabbit. *Anat. Rec.* 156, 383–395. doi: 10.1002/ar.1091560403

Lavia, C., Bonnin, S., Maule, M., Erginay, A., Tadayoni, R., and Gaudric, A. (2019). Vessel density of superficial, intermediate, and deep capillary plexuses using optical coherence tomography angiography. *Retina* 39, 247–258. doi: 10.1097/IAE.0000000000002413

Lecca, P. (2013). Stochastic chemical kinetics: A review of the modelling and simulation approaches. *Biophys. Rev.* 5, 323–345. doi: 10.1007/s12551-013-0122-2

Legras, R., Gaudric, A., and Woog, K. (2018). Distribution of cone density, spacing and arrangement in adult healthy retinas with adaptive optics flood illumination. *PLoS One* 13:e0191141. doi: 10.1371/journal.pone.0191141

Lehallier, B., Gate, D., Schaum, N., Nanasi, T., Lee, S. E., Yousef, H., et al. (2019). Undulating changes in human plasma proteome profiles across the lifespan. *Nat. Med.* 25, 1843–1850. doi: 10.1038/s41591-019-0673-2

Leonelli, S. (2019). The challenges of big data biology. *Elife* 8:47381. doi: 10.7554/eLife.47381

Lesne, A. (2007). The discrete versus continuous controversy in physics. *Math. Struct. Comp. Sci.* 17, 185–223. doi: 10.1017/S0960129507005944

Lesne, A. (2013). Multiscale analysis of biological systems. *Acta Biotheor.* 61, 3–19. doi: 10.1007/s10441-013-9170-z

Léveillard, T., Philp, N. J., and Sennlaub, F. (2019). Is Retinal Metabolic Dysfunction at the Center of the Pathogenesis of Age-related Macular Degeneration? *Int. J. Mol. Sci.* 20:ijms20030762. doi: 10.3390/ijms20030762

Levick, J. R. (2018). *Levick's introduction to cardiovascular physiology*, 6th Edn. Florida, FL: CRC Press, doi: 10.1016/C2013-0-06523-1

Liang, Q., Dharmat, R., Owen, L., Shakoor, A., Li, Y., Kim, S., et al. (2019). Single-nuclei RNA-seq on human retinal tissue provides improved transcriptome profiling. *Nat. Commun.* 10:5743. doi: 10.1038/s41467-019-12917-9

Lighthill, M. J. (1972). Physiological fluid dynamics: a survey? *J. Fluid Mech.* 52, 475–497. doi: 10.1017/S0022112072001557

Lin, Y., Jiang, H., Liu, Y., Rosa Gameiro, G., Gregori, G., Dong, C., et al. (2019). Age-Related Alterations in Retinal Tissue Perfusion and Volumetric Vessel Density. *Invest. Ophthalmol. Vis. Sci.* 60, 685–693. doi: 10.1167/iovs.18-25864

Lindsay, K. J., Du, J., Sloat, S. R., Contreras, L., Linton, J. D., Turner, S. J., et al. (2014). Pyruvate kinase and aspartate-glutamate carrier distributions reveal key metabolic links between neurons and glia in retina. *Proc. Natl. Acad. Sci. U S A.* 111, 15579–15584. doi: 10.1073/pnas.1412441111

Linsenmeier, R. A., and Braun, R. D. (1992). Oxygen distribution and consumption in the cat retina during normoxia and hypoxemia. *J. Gen. Physiol.* 99, 177–197.

Linsenmeier, R. A., and Padnick-Silver, L. (2000). Metabolic dependence of photoreceptors on the choroid in the normal and detached retina. *Invest. Ophthalmol. Vis. Sci.* 41, 3117–3123.

Linsenmeier, R. A., and Zhang, H. F. (2017). Retinal oxygen: from animals to humans. *Prog. Retin. Eye Res.* 58, 115–151. doi: 10.1016/j.preteyeres.2017.01.003

Liu, Z., Kocaoglu, O. P., and Miller, D. T. (2016). 3D imaging of retinal pigment epithelial cells in the living human retina. *Invest. Ophthalmol. Vis. Sci.* 57, OCT533–OCT543. doi: 10.1167/iovs.16-19106

Liu, Z., Kurokawa, K., Zhang, F., Lee, J. J., and Miller, D. T. (2017). Imaging and quantifying ganglion cells and other transparent neurons in the living human retina. *Proc. Natl. Acad. Sci. U S A.* 114, 12803–12808. doi: 10.1073/pnas.1711734114

Lombard, J. H. (2006). A novel mechanism for regulation of retinal blood flow by lactate: gap junctions, hypoxia, and pericytes. *Am. J. Physiol.Heart Circulat. Physiol.* 290, H921–H922. doi: 10.1152/ajpheart.01268.2005

Lukowski, S. W., Lo, C. Y., Sharov, A. A., Nguyen, Q., Fang, L., Hung, S. S., et al. (2019). A single-cell transcriptome atlas of the adult human retina. *EMBO J.* 38:e100811. doi: 10.15252/embj.2018100811

Mantych, G. J., Hageman, G. S., and Devaskar, S. U. (1993). Characterization of glucose transporter isoforms in the adult and developing human eye. *Endocrinology* 133, 600–607. doi: 10.1210/endo.133.2.8344201

Marcos, S., Werner, J. S., Burns, S. A., Merigan, W. H., Artal, P., Atchison, D. A., et al. (2017). Vision science and adaptive optics, the state of the field. *Vision Res.* 132, 3–33. doi: 10.1016/j.visres.2017.01.006

Marmor, M. F., and Wolfensberger, T. J. (1998). *The retinal pigment epithelium.* Oxford: Oxford University Press.

Marneros, A. G., Fan, J., Yokoyama, Y., Gerber, H. P., Ferrara, N., Crouch, R. K., et al. (2005). Vascular endothelial growth factor expression in the retinal pigment epithelium is essential for choriocapillaris development and visual function. *Am. J. Pathol.* 167, 1451–1459. doi: 10.1016/S0002-9440(10)61231-X

Marshall, J. (1987). The ageing retina: physiology or pathology. *Eye* 1(Pt 2), 282–295. doi: 10.1038/eye.1987.47

Martin, P. R., and Grünert, U. (1992). Spatial density and immunoreactivity of bipolar cells in the macaque monkey retina. *J. Comp. Neurol.* 323, 269–287. doi: 10.1002/cne.903230210

Maruko, I., Kawano, T., Arakawa, H., Hasegawa, T., and Iida, T. (2018). Visualizing large choroidal blood flow by subtraction of the choriocapillaris projection artifacts in swept source optical coherence tomography angiography in normal eyes. *Sci. Rep.* 8:15694. doi: 10.1038/s41598-018-34102-6

Masland, R. H. (2012). The neuronal organization of the retina. *Neuron* 76, 266–280. doi: 10.1016/j.neuron.2012.10.002

Mattmann, C. A. (2013). Computing: A vision for data science. *Nature* 493, 473–475. doi: 10.1038/493473a

McGuire, B. J., and Secomb, T. W. (2001). A theoretical model for oxygen transport in skeletal muscle under conditions of high oxygen demand. *J. Appl. Physiol.* 91, 2255–2265. doi: 10.1152/jappl.2001.91.5.2255

Mehta, D., and Malik, A. B. (2006). Signaling mechanisms regulating endothelial permeability. *Physiol. Rev.* 86, 279–367. doi: 10.1152/physrev.00012.2005

Menon, M., Mohammadi, S., Davila-Velderrain, J., Goods, B. A., Cadwell, T. D., Xing, Y., et al. (2019). Single-cell transcriptomic atlas of the human retina identifies cell types associated with age-related macular degeneration. *Nat. Commun.* 10:4902. doi: 10.1038/s41467-019-12780-8

Merino, D., Duncan, J. L., Tiruveedhula, P., and Roorda, A. (2011). Observation of cone and rod photoreceptors in normal subjects and patients using a new generation adaptive optics scanning laser ophthalmoscope. *Biomed. Opt. Express* 2, 2189–2201. doi: 10.1364/BOE.2.002189

Michaelson, I. C. (1956). *Retinal Circulation in Man and Animals*. Springfield, IL: C. C. Thomas.

Miller, E. B., Zhang, P., Ching, K., Pugh, E. N., and Burns, M. E. (2019). In vivo imaging reveals transient microglia recruitment and functional recovery of photoreceptor signaling after injury. *Proc. Natl. Acad. Sci. U S A.* 116, 16603–16612. doi: 10.1073/pnas.1903336116

Miller, S. S., and Steinberg, R. H. (1977a). Active transport of ions across frog retinal pigment epithelium. *Exp. Eye Res.* 25, 235–248. doi: 10.1016/0014-4835(77)90090-2

Miller, S. S., and Steinberg, R. H. (1977b). Passive ionic properties of frog retinal pigment epithelium. *J. Membr. Biol.* 36, 337–372. doi: 10.1007/BF01868158

Minshall, R. D., Sessa, W. C., Stan, R. V., Anderson, R. G. W., and Malik, A. B. (2003). Caveolin regulation of endothelial function. *Am. J. Physiol. Lung Cell Mol. Physiol.* 285, L1179–L1183. doi: 10.1152/ajplung.00242.2003

Missotten, L. (1962). Etude des capillaires de la rétine et de la choriocapillaire au microscope électronique. *Ophthalmologica* 144, 1–12.

Möckl, L. (2020). The emerging role of the mammalian glycocalyx in functional membrane organization and immune system regulation. *Front. Cell Dev. Biol.* 8:253. doi: 10.3389/fcell.2020.00253

Mollon, J. D., and Bowmaker, J. K. (1992). The spatial arrangement of cones in the primate fovea. *Nature* 360, 677–679. doi: 10.1038/360677a0

Moore, D. J., and Clover, G. M. (2001). The effect of age on the macromolecular permeability of human Bruch's membrane. *Invest. Ophthalmol. Vis. Sci.* 42, 2970–2975.

Moore, D. J., Hussain, A. A., and Marshall, J. (1995). Age-related variation in the hydraulic conductivity of Bruch's membrane. *Invest. Ophthalmol. Vis. Sci.* 36, 1290–1297.

Muraoka, Y., Uji, A., Ishikura, M., Iida, Y., Ooto, S., and Tsujikawa, A. (2018). Segmentation of the Four-Layered Retinal Vasculature Using High-Resolution Optical Coherence Tomography Angiography Reveals the Microcirculation Unit. *Invest. Ophthalmol. Vis. Sci.* 59, 5847–5853. doi: 10.1167/iovs.18-25301

Mure, L. S. (2021). Intrinsically photosensitive retinal ganglion cells of the human retina. *Front. Neurol.* 12:636330. doi: 10.3389/fneur.2021.636330

Nag, T. C., and Wadhwa, S. (2012). Ultrastructure of the human retina in aging and various pathological states. *Micron* 43, 759–781. doi: 10.1016/j.micron.2012.01.011

Nakaizumi, Y. (1964). The ultrastructure of bruch's membrane. I. Human, Monkey, Rabbit, Guinea Pig, and Rat eyes. *Arch. Ophthalmol.* 72, 380–387. doi: 10.1001/archopht.1964.00970020380016

Nakaizumi, Y., Hogan, M. J., and Feeney, L. (1964). The ultrastructure of bruch's membrane. III. The macular area of the human eye. *Arch. Ophthalmol.* 72, 395–400. doi: 10.1001/archopht.1964.00970020395018

Nakanishi, M., Grebe, R., Bhutto, I. A., Edwards, M., McLeod, D. S., and Lutty, G. A. (2016). Albumen transport to bruch's membrane and RPE by choriocapillaris caveolae. *Invest. Ophthalmol. Vis. Sci.* 57, 2213–2224. doi: 10.1167/iovs.15-17934

Narayan, D. S., Chidlow, G., Wood, J. P., and Casson, R. J. (2017). Glucose metabolism in mammalian photoreceptor inner and outer segments. *Clin. Exp. Ophthalmol.* 45, 730–741. doi: 10.1111/ceo.12952

Nasir-Ahmad, S., Lee, S. C. S., Martin, P. R., and Grünert, U. (2019). Melanopsin-expressing ganglion cells in human retina: Morphology, distribution, and synaptic connections. *J. Comp. Neurol.* 527, 312–327. doi: 10.1002/cne.24176

Nesper, P. L., and Fawzi, A. A. (2018). Human parafoveal capillary vascular anatomy and connectivity revealed by optical coherence tomography angiography. *Invest. Ophthalmol. Vis. Sci.* 59, 3858–3867. doi: 10.1167/iovs.18-24710

Niven, J. E., and Laughlin, S. B. (2008). Energy limitation as a selective pressure on the evolution of sensory systems. *J. Exp. Biol.* 211, 1792–1804. doi: 10.1242/jeb.017574

Nivison-Smith, L., Khandelwal, N., Tong, J., Mahajan, S., Kalloniatis, M., and Agrawal, R. (2020). Normal aging changes in the choroidal angioarchitecture of the macula. *Sci. Rep.* 10:10810. doi: 10.1038/s41598-020-67829-2

Olver, J. M. (1990). Functional anatomy of the choroidal circulation: methyl methacrylate casting of human choroid. *Eye* 4(Pt 2), 262–272. doi: 10.1038/eye.1990.38

Orozco, L. D., Chen, H.-H., Cox, C., Katschke, K. J., Arceo, R., Espiritu, C., et al. (2020). Integration of eQTL and a Single-Cell Atlas in the Human Eye Identifies Causal Genes for Age-Related Macular Degeneration. *Cell Rep.* 30, 1246.e–1259.e. doi: 10.1016/j.celrep.2019.12.082

Osterberg, G. A. (1935). Topography of the layer of rods and cones in the human retina. *Acta Ophthalmol.* 31, 1–97.

Owsley, C. (2011). Aging and vision. *Vision Res.* 51, 1610–1622. doi: 10.1016/j.visres.2010.10.020

Owsley, C., and Burton, K. B. (1991). "Aging and spatial contrast sensitivity: underlying mechanisms and implications for everyday life," in *The changing visual system*, eds P. Bagnoli and W. Hodos (Boston, MA: Springer US), 119–136. doi: 10.1007/978-1-4615-3390-0_9

Owsley, C., Ball, K., McGwin, G., Sloane, M. E., Roenker, D. L., White, M. F., et al. (1998). Visual processing impairment and risk of motor vehicle crash among older adults. *JAMA* 279, 1083–1088. doi: 10.1001/jama.279.14.1083

Oyster, C. W. (1999). *The Human Eye: Structure and Function*. Sunderland, MA: Sinauer Associates.

Pappas, C. M., Zouache, M. A., Matthews, S., Faust, C. D., Hageman, J. L., Williams, B. L., et al. (2021). Protective chromosome 1q32 haplotypes mitigate risk for age-related macular degeneration associated with the CFH-CFHR5 and ARMS2/HTRA1 loci. *Hum. Genomics* 15:60. doi: 10.1186/s40246-021-00359-8

Park, S. P., Chung, J. K., Greenstein, V., Tsang, S. H., and Chang, S. (2013). A study of factors affecting the human cone photoreceptor density measured by adaptive optics scanning laser ophthalmoscope. *Exp. Eye Res.* 108, 1–9. doi: 10.1016/j.exer.2012.12.011

Pauleikhoff, D., Harper, C. A., Marshall, J., and Bird, A. C. (1990). Aging changes in Bruch's membrane. A histochemical and morphologic study. *Ophthalmology* 97, 171–178.

Peng, Y.-R., Shekhar, K., Yan, W., Herrmann, D., Sappington, A., Bryman, G. S., et al. (2019). Molecular classification and comparative taxonomics of foveal and peripheral cells in primate retina. *Cell* 176, 1222.e–1237.e. doi: 10.1016/j.cell.2019.01.004

Peppiatt, C. M., Howarth, C., Mobbs, P., and Attwell, D. (2006). Bidirectional control of CNS capillary diameter by pericytes. *Nature* 443, 700–704. doi: 10.1038/nature05193

Pierscionek, B. K. (1996). Aging changes in the optical elements of the eye. *J. Biomed. Opt.* 1, 147–156. doi: 10.1117/12.230729

Pino, R. M., and Essner, E. (1980). Structure and permeability to ferritin of the choriocapillary endothelium of the rat eye. *Cell Tissue Res.* 208, 21–27. doi: 10.1007/BF00234169

Pino, R. M., and Essner, E. (1981). Permeability of rat choriocapillaris to hemeproteins. Restriction of tracers by a fenestrated endothelium. *J. Histochem. Cytochem.* 29, 281–290. doi: 10.1177/29.2.7252121

Pino, R. M., and Thouron, C. L. (1983). Vascular permeability in the rat eye to endogenous albumin and immunoglobulin G (IgG) examined by immunohistochemical methods. *J. Histochem. Cytochem.* 31, 411–416. doi: 10.1177/31.3.6827079

Polyak, S. L. (1941). *The Retina*. Chicago: University of Chicago.

Pournaras, C. J., Rungger-Brändle, E., Riva, C. E., Hardarson, S. H., and Stefansson, E. (2008). Regulation of retinal blood flow in health and disease. *Prog. Retin. Eye Res.* 27, 284–330. doi: 10.1016/j.preteyeres.2008.02.002

Powner, M. B., Scott, A., Zhu, M., Munro, P. M. G., Foss, A. J. E., Hageman, G. S., et al. (2011). Basement membrane changes in capillaries of the ageing human retina. *Br. J. Ophthalmol.* 95, 1316–1322. doi: 10.1136/bjo.2011.204222

Provis, J. M. (2001). Development of the primate retinal vasculature. *Prog. Retin. Eye Res.* 20, 799–821. doi: 10.1016/s1350-9462(01)00012-x

Querques, G., Kamami-Levy, C., Blanco-Garavito, R., Georges, A., Pedinielli, A., Capuano, V., et al. (2014). Appearance of medium-large drusen and reticular pseudodrusen on adaptive optics in age-related macular degeneration. *Br. J. Ophthalmol.* 98, 1522–1527. doi: 10.1136/bjophthalmol-2014-305455

Ramrattan, R. S., van der Schaft, T. L., Mooy, C. M., de Bruijn, W. C., Mulder, P. G., and de Jong, P. T. (1994). Morphometric analysis of Bruch's membrane, the choriocapillaris, and the choroid in aging. *Invest. Ophthalmol. Vis. Sci.* 35, 2857–2864.

Raviola, G. (1977). The structural basis of the blood-ocular barriers. *Exp. Eye Res.* 25(Suppl.), 27–63. doi: 10.1016/s0014-4835(77)80009-2

Reichenbach, A., and Robinson, S. R. (1995). Phylogenetic constraints on retinal organisation and development. *Prog. Retin. Eye Res.* 15, 139–171. doi: 10.1016/1350-9462(95)00008-9

Reim, M. (1984). "The eye in the aging patient: cornea," in *Geriatrics 3*, ed. D. Platt (Berlin: Springer Berlin Heidelberg), 310–325. doi: 10.1007/978-3-642-68976-5_12

Reiner, A., Fitzgerald, M. E. C., Del Mar, N., and Li, C. (2018). Neural control of choroidal blood flow. *Prog. Retin. Eye Res.* 64, 96–130. doi: 10.1016/j.preteyeres.2017.12.001

Ring, H. G., and Fujino, T. (1967). Observations on the anatomy and pathology of the choroidal vasculature. *Arch. Ophthalmol.* 78, 431–444. doi: 10.1001/archopht.1967.00980030433005

Riva, C. E., Grunwald, J. E., Sinclair, S. H., and Petrig, B. L. (1985). Blood velocity and volumetric flow rate in human retinal vessels. *Invest. Ophthalmol. Vis. Sci.* 26, 1124–1132.

Rodieck, R. W., and Marshak, D. W. (1992). Spatial density and distribution of choline acetyltransferase immunoreactive cells in human, macaque, and baboon retinas. *J. Comp. Neurol.* 321, 46–64. doi: 10.1002/cne.903210106

Rohen, J. W., and Lütjen-Drecoll, E. (1984). "Age-Related Changes in the Anterior Segment of the Eye," in *Geriatrics 3*, ed. D. Platt (Berlin: Springer), 326–351. doi: 10.1007/978-3-642-68976-5_13

Röhrenbeck, J., Wässle, H., and Boycott, B. B. (1989). Horizontal Cells in the Monkey Retina: Immunocytochemical staining with antibodies against calcium binding proteins. *Eur. J. Neurosci.* 1, 407–420. doi: 10.1111/j.1460-9568.1989.tb00349.x

Roorda, A., and Williams, D. R. (1999). The arrangement of the three cone classes in the living human eye. *Nature* 397, 520–522. doi: 10.1038/17383

Ryoo, N.-K., Ahn, S. J., Park, K. H., Ahn, J., Seo, J., Han, J. W., et al. (2018). Thickness of retina and choroid in the elderly population and its association with Complement Factor H polymorphism: KLoSHA Eye study. *PLoS One* 13:e0209276. doi: 10.1371/journal.pone.0209276

Salzman, M. (1912). *The Anatomy and Histology of the Human Eyeball in the Normal State, Its Development and Senescence*. Trans. E. V. L. Brown. Chicago: The University of Chicago Press.

Sapoznik, K. A., Luo, T., de Castro, A., Sawides, L., Warner, R. L., and Burns, S. A. (2018). Enhanced retinal vasculature imaging with a rapidly configurable aperture. *Biomed. Opt. Express* 9, 1323–1333. doi: 10.1364/BOE.9.001323

Sarin, H. (2010). Physiologic upper limits of pore size of different blood capillary types and another perspective on the dual pore theory of microvascular permeability. *J. Angiogenes Res.* 2:14. doi: 10.1186/2040-2384-2-14

Satchell, S. C., and Braet, F. (2009). Glomerular endothelial cell fenestrations: an integral component of the glomerular filtration barrier. *Am. J. Physiol. Renal Physiol.* 296, F947–F956. doi: 10.1152/ajprenal.90601.2008

Scoles, D., Sulai, Y. N., Langlo, C. S., Fishman, G. A., Curcio, C. A., Carroll, J., et al. (2014). In vivo imaging of human cone photoreceptor inner segments. *Invest. Ophthalmol. Vis. Sci.* 55, 4244–4251. doi: 10.1167/iovs.14-14542

Secomb, T. W. (2016). A Green's function method for simulation of time-dependent solute transport and reaction in realistic microvascular geometries. *Math. Med. Biol.* 33, 475–494. doi: 10.1093/imammb/dqv031

Secomb, T. W., Hsu, R., Park, E. Y. H., and Dewhirst, M. W. (2004). Green's function methods for analysis of oxygen delivery to tissue by microvascular networks. *Ann. Biomed. Eng.* 32, 1519–1529. doi: 10.1114/b:abme.0000049036.08817.44

Shakib, M., and Cunha-Vaz, J. G. (1966). Studies on the permeability of the blood-retinal barrier. IV. Junctional complexes of the retinal vessels and their role in the permeability of the blood-retinal barrier. *Exp. Eye Res.* 5, 229–234. doi: 10.1016/s0014-4835(66)80011-8

Shepro, D., and Morel, N. M. (1993). Pericyte physiology. *FASEB J.* 7, 1031–1038. doi: 10.1096/fasebj.7.11.8370472

Sia, P. I., Luiten, A. N., Stace, T. M., Wood, J. P., and Casson, R. J. (2014). Quantum biology of the retina. *Clin. Exp. Ophthalmol.* 42, 582–589. doi: 10.1111/ceo.12373

Simionescu, M., Gafencu, A., and Antohe, F. (2002). Transcytosis of plasma macromolecules in endothelial cells: a cell biological survey. *Microsc. Res. Tech.* 57, 269–288. doi: 10.1002/jemt.10086

Snodderly, D. M., Weinhaus, R. S., and Choi, J. C. (1992). Neural-vascular relationships in central retina of macaque monkeys (Macaca fascicularis). *J. Neurosci.* 12, 1169–1193.

Song, H., Chui, T. Y. P., Zhong, Z., Elsner, A. E., and Burns, S. A. (2011). Variation of cone photoreceptor packing density with retinal eccentricity and age. *Invest. Ophthalmol. Vis. Sci.* 52, 7376–7384. doi: 10.1167/iovs.11-7199

Spaide, R. F. (2016). Choriocapillaris flow features follow a power law distribution: implications for characterization and mechanisms of disease progression. *Am. J. Ophthalmol.* 170, 58–67. doi: 10.1016/j.ajo.2016.07.023

Spitznas, M., and Reale, E. (1975). Fracture faces of fenestrations and junctions of endothelial cells in human choroidal vessels. *Int. Ophthalmol.* 14, 98–107.

Spraul, C. W., Lang, G. E., Grossniklaus, H. E., and Lang, G. K. (1999). Histologic and morphometric analysis of the choroid, Bruch's membrane, and retinal pigment epithelium in postmortem eyes with age-related macular degeneration and histologic examination of surgically excised choroidal neovascular membranes. *Surv. Ophthalmol.* 44(Suppl. 1), S10–S32.

Spraul, C. W., Lang, G. E., Lang, G. K., and Grossniklaus, H. E. (2002). Morphometric changes of the choriocapillaris and the choroidal vasculature in eyes with advanced glaucomatous changes. *Vision Res.* 42, 923–932. doi: 10.1016/s0042-6989(02)00022-6

Stan, R. V. (2005). Structure of caveolae. *Biochim. Biophys. Acta* 1746, 334–348. doi: 10.1016/j.bbamcr.2005.08.008

Stan, R. V. (2007). Endothelial stomatal and fenestral diaphragms in normal vessels and angiogenesis. *J. Cell Mol. Med.* 11, 621–643. doi: 10.1111/j.1582-4934.2007.00075.x

Starita, C., Hussain, A. A., Patmore, A., and Marshall, J. (1997). Localization of the site of major resistance to fluid transport in Bruch's membrane. *Invest. Ophthalmol. Vis. Sci.* 38, 762–767.

Stokoe, N. L., and Turner, R. W. (1966). Normal retinal vascular pattern. Arteriovenous ratio as a measure of arterial calibre. *Br. J. Ophthalmol.* 50, 21–40. doi: 10.1136/bjo.50.1.21

Straubhaar, M., Orgül, S., Gugleta, K., Schötzau, A., Erb, C., and Flammer, J. (2000). Choroidal laser Doppler flowmetry in healthy subjects. *Arch. Ophthalmol.* 118, 211–215. doi: 10.1001/archopht.118.2.211

Strauss, O. (2005). The retinal pigment epithelium in visual function. *Physiol. Rev.* 85, 845–881. doi: 10.1152/physrev.00021.2004

Streeten, B. W. (1969). Development of the human retinal pigment epithelium and the posterior segment. *Arch. Ophthalmol.* 81, 383–394. doi: 10.1001/archopht.1969.00990010385017

Strettoi, E., Novelli, E., Mazzoni, F., Barone, I., and Damiani, D. (2010). Complexity of retinal cone bipolar cells. *Prog. Retin. Eye Res.* 29, 272–283. doi: 10.1016/j.preteyeres.2010.03.005

Tan, P. E. Z., Yu, P. K., Balaratnasingam, C., Cringle, S. J., Morgan, W. H., McAllister, I. L., et al. (2012). Quantitative confocal imaging of the retinal microvasculature in the human retina. *Invest. Ophthalmol. Vis. Sci.* 53, 5728–5736. doi: 10.1167/iovs.12-10017

Teschendorff, A. E. (2019). Avoiding common pitfalls in machine learning omic data science. *Nat. Mater.* 18, 422–427. doi: 10.1038/s41563-018-0241-z

Tomita, R., Iwase, T., Ueno, Y., Goto, K., Yamamoto, K., Ra, E., et al. (2020). Differences in blood flow between superior and inferior retinal hemispheres. *Invest. Ophthalmol. Vis. Sci.* 61:27. doi: 10.1167/iovs.61.5.27

Torczynski, E. (1982). "Choroid and Suprachoroid," in *Ocular anatomy, embryology, and teratology*, ed. F. A. Jakobiec (Philadelphia: Harper & Row).

Torczynski, E., and Tso, M. O. (1976). The architecture of the choriocapillaris at the posterior pole. *Am. J. Ophthalmol.* 81, 428–440. doi: 10.1016/0002-9394(76)90298-1

Törnquist, P., Alm, A., and Bill, A. (1990). Permeability of ocular vessels and transport across the blood-retinal-barrier. *Eye* 4(Pt 2), 303–309. doi: 10.1038/eye.1990.41

Toussaint, D., Kuwabara, T., and Cogan, D. G. (1961). Retinal vascular patterns. II. Human retinal vessels studied in three dimensions. *Arch. Ophthalmol.* 65, 575–581. doi: 10.1001/archopht.1961.01840020577022

Tout, S., Chan-Ling, T., Holländer, H., and Stone, J. (1993). The role of Müller cells in the formation of the blood-retinal barrier. *Neuroscience* 55, 291–301. doi: 10.1016/0306-4522(93)90473-s

Tran, H., Jan, N.-J., Hu, D., Voorhees, A., Schuman, J. S., Smith, M. A., et al. (2017). Formalin fixation and cryosectioning cause only minimal changes in shape or size of ocular tissues. *Sci. Rep.* 7:12065. doi: 10.1038/s41598-017-12006-1

Trinh, M., Khou, V., Zangerl, B., Kalloniatis, M., and Nivison-Smith, L. (2021). Modelling normal age-related changes in individual retinal layers using location-specific OCT analysis. *Sci. Rep.* 11:558. doi: 10.1038/s41598-020-79424-6

Ts'o, M. O., and Friedman, E. (1968). The retinal pigment epithelium. 3. Growth and development. *Arch. Ophthalmol.* 80, 214–216. doi: 10.1001/archopht.1968.00980050216012

Tsukamoto, Y., Masarachia, P., Schein, S. J., and Sterling, P. (1992). Gap junctions between the pedicles of macaque foveal cones. *Vision Res.* 32, 1809–1815. doi: 10.1016/0042-6989(92)90042-h

Van Itallie, C. M., and Anderson, J. M. (2004). The molecular physiology of tight junction pores. *Physiology* 19, 331–338. doi: 10.1152/physiol.00027.2004

Vecino, E., Rodriguez, F. D., Ruzafa, N., Pereiro, X., and Sharma, S. C. (2016). Glia-neuron interactions in the mammalian retina. *Prog. Retin. Eye Res.* 51, 1–40. doi: 10.1016/j.preteyeres.2015.06.003

Verticchio Vercellin, A. C., Harris, A., Chiaravalli, G., Sacco, R., Siesky, B., Ciulla, T., et al. (2021). Physics-based modeling of Age-related Macular Degeneration-A theoretical approach to quantify retinal and choroidal contributions to macular oxygenation. *Math. Biosci.* 339:108650. doi: 10.1016/j.mbs.2021.108650

Viegas, F. O., and Neuhauss, S. C. F. (2021). A metabolic landscape for maintaining retina integrity and function. *Front. Mol. Neurosci.* 14:656000. doi: 10.3389/fnmol.2021.656000

Virdi, P. S., and Hayreh, S. S. (1987). Anterior segment ischemia after recession of various recti. An experimental study. *Ophthalmology* 94, 1258–1271.

Voigt, A. P., Mulfaul, K., Mullin, N. K., Flamme-Wiese, M. J., Giacalone, J. C., Stone, E. M., et al. (2019a). Single-cell transcriptomics of the human retinal pigment epithelium and choroid in health and macular degeneration. *Proc. Natl. Acad. Sci. U S A.* 116, 24100–24107. doi: 10.1073/pnas.1914143116

Voigt, A. P., Mullin, N. K., Whitmore, S. S., DeLuca, A. P., Burnight, E. R., Liu, X., et al. (2021). Human photoreceptor cells from different macular subregions have distinct transcriptional profiles. *Hum. Mol. Genet.* 2021:ddab140. doi: 10.1093/hmg/ddab140

Voigt, A. P., Whitmore, S. S., Flamme-Wiese, M. J., Riker, M. J., Wiley, L. A., Tucker, B. A., et al. (2019b). Molecular characterization of foveal versus peripheral human retina by single-cell RNA sequencing. *Exp. Eye Res.* 184, 234–242. doi: 10.1016/j.exer.2019.05.001

von Hanno, T., Lade, A. C., Mathiesen, E. B., Peto, T., Njølstad, I., and Bertelsen, G. (2017). Macular thickness in healthy eyes of adults (N = 4508) and relation to sex, age and refraction: the Tromsø Eye Study (2007-2008). *Acta Ophthalmol.* 95, 262–269. doi: 10.1111/aos.13337

Wakatsuki, Y., Shinojima, A., Kawamura, A., and Yuzawa, M. (2015). Correlation of Aging and Segmental Choroidal Thickness Measurement using Swept Source Optical Coherence Tomography in Healthy Eyes. *PLoS One* 10:e0144156. doi: 10.1371/journal.pone.0144156

Walls, G. L. (1937). Significance of the foveal depression. *Arch. Ophthalmol.* 18, 912–919. doi: 10.1001/archopht.1937.00850120046005

Walls, G. L. (1942). *The vertebrate eye and its adaptive radiation*. Michigan, USA: The Cranbrook Press.

Wang, C. Y., and Bassingthwaighte, J. B. (2001). Capillary supply regions. *Math. Biosci.* 173, 103–114. doi: 10.1016/s0025-5564(01)00074-8

Wang, E., Zhao, X., Yang, J., and Chen, Y. (2020). Visualization of deep choroidal vasculatures and measurement of choroidal vascular density: a swept-source optical coherence tomography angiography approach. *BMC Ophthalmol.* 20:321. doi: 10.1186/s12886-020-01591-x

Wang, J. C., Laíns, I., Silverman, R. F., Sobrin, L., Vavvas, D. G., Miller, J. W., et al. (2018). Visualization of Choriocapillaris and Choroidal Vasculature in Healthy Eyes With En Face Swept-Source Optical Coherence Tomography Versus Angiography. *Transl. Vis. Sci. Technol.* 7:25. doi: 10.1167/tvst.7.6.25

Wang, L., Kondo, M., and Bill, A. (1997). Glucose metabolism in cat outer retina. Effects of light and hyperoxia. *Invest. Ophthalmol. Vis. Sci.* 38, 48–55.

Wang, S., Zheng, Y., Li, Q., He, X., Ren, R., Zhang, W., et al. (2020). Deciphering primate retinal aging at single-cell resolution. *Protein Cell* 12, 889–898. doi: 10.1007/s13238-020-00791-x

Wang, Y., Bensaid, N., Tiruveedhula, P., Ma, J., Ravikumar, S., and Roorda, A. (2019). Human foveal cone photoreceptor topography and its dependence on eye length. *Elife* 8:47148. doi: 10.7554/eLife.47148

Wässle, H., Boycott, B. B., and Röhrenbeck, J. (1989). Horizontal Cells in the Monkey Retina: Cone connections and dendritic network. *Eur. J. Neurosci.* 1, 421–435. doi: 10.1111/j.1460-9568.1989.tb00350.x

Wässle, H., Grünert, U., Chun, M. H., and Boycott, B. B. (1995). The rod pathway of the macaque monkey retina: identification of AII-amacrine cells with antibodies against calretinin. *J. Comp. Neurol.* 361, 537–551. doi: 10.1002/cne.903610315

Watzke, R. C., Soldevilla, J. D., and Trune, D. R. (1993). Morphometric analysis of human retinal pigment epithelium: correlation with age and location. *Curr. Eye Res.* 12, 133–142. doi: 10.3109/02713689308999481

Weale, R. A. (1986). Chapter 2 Retinal senescence. *Prog. Retin. Res.* 5, 53–73. doi: 10.1016/0278-4327(86)90005-2

Wei, X., Balne, P. K., Meissner, K. E., Barathi, V. A., Schmetterer, L., and Agrawal, R. (2018). Assessment of flow dynamics in retinal and choroidal microcirculation. *Surv. Ophthalmol.* 63, 646–664. doi: 10.1016/j.survophthal.2018.03.003

Wei, Y., Jiang, H., Shi, Y., Qu, D., Gregori, G., Zheng, F., et al. (2017). Age-Related Alterations in the Retinal Microvasculature, Microcirculation, and Microstructure. *Invest. Ophthalmol. Vis. Sci.* 58, 3804–3817. doi: 10.1167/iovs.17-21460

Weiter, J. J., Schachar, R. A., and Ernest, J. T. (1973). Control of intraocular blood flow. I. Intraocular pressure. *Invest. Ophthalmol.* 12, 327–331.

Wells-Gray, E. M., Choi, S. S., Zawadzki, R. J., Finn, S. C., Greiner, C., Werner, J. S., et al. (2018). Volumetric imaging of rod and cone photoreceptor structure with a combined adaptive optics-optical coherence tomography-scanning laser ophthalmoscope. *J. Biomed. Opt.* 23, 1–15. doi: 10.1117/1.JBO.23.3.036003

West, G. B., Brown, J. H., and Enquist, B. J. (1997). A general model for the origin of allometric scaling laws in biology. *Science* 276, 122–126. doi: 10.1126/science.276.5309.122

Williams, B. L., Seager, N. A., Gardiner, J. D., Pappas, C. M., Cronin, M. C., Amat di San Filippo, C., et al. (2021). Chromosome 10q26-driven age-related macular degeneration is associated with reduced levels of HTRA1 in human retinal pigment epithelium. *Proc. Natl. Acad. Sci. U S A.* 118, 2103617118. doi: 10.1073/pnas.2103617118

Winkler, B. S., Arnold, M. J., Brassell, M. A., and Puro, D. G. (2000). Energy metabolism in human retinal Müller cells. *Invest. Ophthalmol. Vis. Sci.* 41, 3183–3190.

Wise, G. N., Dollery, C. T., and Henkind, P. (1975). *The Retinal Circulation*. New York, NY: Harper and Row.

Wisniewska-Kruk, J., van der Wijk, A.-E., van Veen, H. A., Gorgels, T. G. M. F., Vogels, I. M. C., Versteeg, D., et al. (2016). Plasmalemma Vesicle-Associated Protein Has a Key Role in Blood-Retinal Barrier Loss. *Am. J. Pathol.* 186, 1044–1054. doi: 10.1016/j.ajpath.2015.11.019

Wolter, J. R. (1956). The pericytes of the choroid of the human eye. *Am. J. Ophthalmol.* 41, 990–995. doi: 10.1016/0002-9394(56)91048-0

Wong-Riley, M. T. T. (2010). Energy metabolism of the visual system. *Eye Brain* 2, 99–116. doi: 10.2147/EB.S9078

Wybar, K. C. (1954). Vascular anatomy of the choroid in relation to selective localization of ocular disease. *Br. J. Ophthalmol.* 38, 513–527. doi: 10.1136/bjo.38.9.513

Yan, W., Peng, Y.-R., van Zyl, T., Regev, A., Shekhar, K., Juric, D., et al. (2020). Cell atlas of the human fovea and peripheral retina. *Sci. Rep.* 10:9802. doi: 10.1038/s41598-020-66092-9

Yi, W., Lu, Y., Zhong, S., Zhang, M., Sun, L., Dong, H., et al. (2020). A single-cell transcriptome atlas of the aging human and macaque retina. *Natl. Sci. Rev.* 2020:nwaa179. doi: 10.1093/nsr/nwaa179

Yoneya, S., Tso, M. O., and Shimizu, K. (1983). Patterns of the choriocapillaris. A method to study the choroidal vasculature of the enucleated human eye. *Int. Ophthalmol.* 6, 95–99.

Young, R. W. (1971). The renewal of rod and cone outer segments in the rhesus monkey. *J. Cell Biol.* 49, 303–318. doi: 10.1083/jcb.49.2.303

Yu, D. Y., and Cringle, S. J. (2001). Oxygen distribution and consumption within the retina in vascularised and avascular retinas and in animal models of retinal disease. *Prog. Retin. Eye Res.* 20, 175–208. doi: 10.1016/S1350-9462(00)00027-6

Yu, D.-Y., Cringle, S. J., and Su, E.-N. (2005). Intraretinal oxygen distribution in the monkey retina and the response to systemic hyperoxia. *Invest. Ophthalmol. Vis. Sci.* 46, 4728–4733. doi: 10.1167/iovs.05-0694

Yu, D.-Y., Cringle, S. J., Yu, P. K., Balaratnasingam, C., Mehnert, A., Sarunic, M. V., et al. (2019). Retinal capillary perfusion: Spatial and temporal heterogeneity. *Prog. Retin. Eye Res.* 70, 23–54. doi: 10.1016/j.preteyeres.2019.01.001

Yu, P. K., Mehnert, A., Athwal, A., Sarunic, M. V., and Yu, D.-Y. (2021). Use of the retinal vascular histology to validate an optical coherence tomography angiography technique. *Transl. Vis. Sci. Technol.* 10:29. doi: 10.1167/tvst.10.1.29

Zhang, C., Hua, T., Li, G., Tang, C., and Zhou, P. (2008). *Visual function declines during normal aging*. Berlin: ResearchGate.

Zhang, T., Godara, P., Blanco, E. R., Griffin, R. L., Wang, X., Curcio, C. A., et al. (2015). Variability in human cone topography assessed by adaptive optics scanning laser ophthalmoscopy. *Am. J. Ophthalmol.* 160, 290.e–300.e. doi: 10.1016/j.ajo.2015.04.034

Zhang, Y., Wang, X., Godara, P., Zhang, T., Clark, M. E., Witherspoon, C. D., et al. (2017). Dynamism of dot subretinal drusenoid deposits in age-related macular degeneration demonstrated with adaptive optics imaging. *Retina* 2017, 1504. doi: 10.1097/IAE.0000000000001504

Zheng, F., Zhang, Q., Shi, Y., Russell, J. F., Motulsky, E. H., Banta, J. T., et al. (2019). Age-Dependent Changes in the Macular Choriocapillaris of Normal

Eyes Imaged with Swept-Source OCT Angiography. *Am. J. Ophthalmol.* 200, 110–122. doi: 10.1016/j.ajo.2018.12.025

Zhong, Z., Song, H., Chui, T. Y. P., Petrig, B. L., and Burns, S. A. (2011). Noninvasive measurements and analysis of blood velocity profiles in human retinal vessels. *Invest. Ophthalmol. Vis. Sci.* 52, 4151–4157. doi: 10.1167/iovs.10-6940

Zihni, C., Mills, C., Matter, K., and Balda, M. S. (2016). Tight junctions: from simple barriers to multifunctional molecular gates. *Nat. Rev. Mol. Cell Biol.* 17, 564–580. doi: 10.1038/nrm.2016.80

Zouache, M, Eames, I., Klettner, C. A., and Luthert, P. J. (2016c). Computational analysis of the impact of a reduction of the blood flow in large choroidal arteries on the function of the choriocapillaris. *Invest. Ophthalmol. Vis. Sci.* 57, 4628–4628.

Zouache, M. A., Bennion, A., Hageman, J. L., Pappas, C., Richards, B. T., and Hageman, G. S. (2020). Macular retinal thickness differs markedly in age-related macular degeneration driven by risk polymorphisms on chromosomes 1 and 10. *Sci. Rep.* 10:21093. doi: 10.1038/s41598-020-78059-x

Zouache, M. A., Eames, I., and Luthert, P. J. (2015). Blood flow in the choriocapillaris. *J. Fluid Mech.* 774, 37–66. doi: 10.1017/jfm.2015.243

Zouache, M. A., Eames, I., and Samsudin, A. (2016b). Allometry and scaling of the intraocular pressure and aqueous humour flow rate in vertebrate eyes. *PLoS One* 11:e0151490. doi: 10.1371/journal.pone.0151490

Zouache, M. A., Eames, I., Klettner, C. A., and Luthert, P. J. (2019). Flow and passive transport in planar multipolar flows. *J. Fluid Mech.* 858, 184–227. doi: 10.1017/jfm.2018.771

Zouache, M. A., Eames, I., Klettner, C. A., and Luthert, P. J. (2016a). Form, shape and function: segmented blood flow in the choriocapillaris. *Sci. Rep.* 6:35754. doi: 10.1038/srep35754

Conflict of Interest: The author declares that the research was conducted in the absence of any commercial or financial relationships that could be construed as a potential conflict of interest.

frontiers in Medicine

ORIGINAL RESEARCH
published: 17 March 2022
doi: 10.3389/fmed.2022.826643

Cone Photoreceptors in Diabetic Patients

Ann E. Elsner, Brittany R. Walker, Robert N. Gilbert, Vamsi Parimi, Joel A. Papay, Thomas J. Gast and Stephen A. Burns*

School of Optometry, Indiana University, Bloomington, IN, United States

Purpose: Cones in diabetic patients are at risk due to metabolic and vascular changes. By imaging retinal vessel modeling at high magnification, we reduced its impact on cone distribution measurements. The retinal vessel images and retinal thickness measurements provided information about cone microenvironment.

Methods: We compared cone data in 10 diabetic subjects (28–78 yr) to our published norms from 36 younger and 10 older controls. All subjects were consented and tested in a manner approved by the Indiana University Institutional Review Board, which adhered to the Declaration of Helsinki. Custom adaptive optics scanning laser ophthalmoscopy (AOSLO) was used to image cones and retinal microcirculation. We counted cones in a montage of foveal and temporal retina, using four non-contiguous samples within 0.9–7 deg that were selected for best visibility of cones and least pathology. The data were fit with a two parameter exponential model: ln(cone density) = a * microns eccentricity + b. These results were compared to retinal thickness measurements from SDOCT.

Results: Diabetic cone maps were more variable than in controls and included patches, or unusually bright and dark cones, centrally and more peripherally. Model parameters and total cones within the central 14 deg of the macula differed across diabetic patients. Total cones fell into two groups: similar to normal for 5 vs. less than normal for 2 of 2 younger diabetic subjects and 3 older subjects, low but not outside the confidence limits. Diabetic subjects had all retinal vascular remodeling to varying degrees: microaneurysms; capillary thickening, thinning, or bends; and vessel elongation including capillary loops, tangles, and collaterals. Yet SD-OCT showed that no diabetic subject had a Total Retinal Thickness in any quadrant that fell outside the confidence limits for controls.

Conclusions: AOSLO images pinpointed widespread retinal vascular remodeling in all diabetic eyes, but the SDOCT showed no increased retinal thickness. Cone reflectivity changes were found in all diabetic patients, but significantly low cone density in only some. These results are consistent with early changes to neural, glial, or vascular components of the retinal without significant retinal thickening due to exudation.

Keywords: cones, diabetic patients, macula, risk to photoreceptors, vascular changes, fovea, cone distribution

Edited by:
Ravirajsinh Jadeja,
Augusta University, United States

Reviewed by:
Syed A. H. Zaidi,
Augusta University, United States
Fabio Scarinci,
GB Bietti Foundation (IRCCS), Italy
Erica Woertz,
Medical College of Wisconsin,
United States

***Correspondence:**
Ann E. Elsner
aeelsner@indiana.edu

Specialty section:
This article was submitted to
Ophthalmology,
a section of the journal
Frontiers in Medicine

Received: *01 December 2021*
Accepted: *31 January 2022*
Published: *17 March 2022*

Citation:
Elsner AE, Walker BR, Gilbert RN, Parimi V, Papay JA, Gast TJ and Burns SA (2022) Cone Photoreceptors in Diabetic Patients. Front. Med. 9:826643. doi: 10.3389/fmed.2022.826643

INTRODUCTION

Photoreceptors are the potential victims of the harsh environment found in the diabetic retina (1). Due to their high rate of metabolism, photoreceptors not only can be reduced in number via apoptotic death in altered glucose models (2), but photoreceptors and outer retina have been reported to undergo a variety of changes and can be considered as potential culprits in diabetic retinopathy and diabetic macular edema (3, 4).

Visual function abnormalities in diabetic patients have long been documented by a wide variety of methods, including those that depend heavily upon cones or cone pathways such as color vision and multifocal electroretinography (5, 6). Foveal color vision deficits in diabetic patients are consistent with a combination of early lens changes that decrease the light focused on the retina, particularly for short wavelengths (5, 7), and failure of the foveal cones to properly guide light despite the lack of clinical evidence of macular edema (5). Both of these factors can decrease the capture of quanta, which then can decrease sensitivity, and also decrease the contrast and alter the spectra at the retina, which can lead to poorer performance on a wide variety of visual function tasks. With imaging, dark patches of cones can be spatially correlated with defects in the deeper fundus layers seen on OCT (8). Further there is neuronal damage that includes additional retinal neurons (9–12). In diabetic patients without clinically significant macular edema, there is not evidence of cones so shortened or photopigment so dilute that spectral sensitivity is altered for L- and M- cones, i.e., those that contribute substantially to foveal vision and visual acuity. Thus, while decreased color vision, particularly for short wavelengths, and poor contrast interfere with tasks of daily living in diabetic patients, biomarkers for detection and management require sensitive or specific information.

Cones underlie visual acuity, fine color vision, and fine spatial discriminations that require dense packing. Cones are irreplaceable and in humans form complex neural connections, leading to extensive signal processing in the retina. Living human cones can be individually mapped by increasing the magnification of the retinal image, using scanning to improve the contrast of the retinal image, and correcting the flawed optics of the eye with adaptive optics, in an adaptive optics scanning laser ophthalmoscope (AOSLO), with differences in techniques among laboratories (13, 14). While the number of human cones is set before birth, cones are known migrate to during the first 5 yr of life to densely pack a normal fovea (15), and become less densely packed with aging (16–18). The young fovea has a higher cone density along the horizontal meridian than the vertical one, similar to a visual streak. There are large individual differences among subjects found by several laboratories, particularly at the fovea, previously reviewed (14, 18, 19). In older subjects the horizontal vertical asymmetry is not always preserved (17). While the density of cones decreases monotonically from fovea to periphery in the healthy eye, the large interindividual differences in cone density distribution across the retina must be modeled with at least two parameters, such as overall numbers of cones and the slope of the decrease from the fovea outward (19). That is, one individual does not have a constant proportion more cones across all retinal locations than another; instead cone density at 2 and 7 deg is uncorrelated across individuals. Instead, there is a strong negative correlation between cone density at 2 deg and the ratio of cone density at 7 and 2 deg, expected because when cones migrate from the periphery to the center, then there are fewer in the periphery.

In diabetic patients without proliferative diabetic retinopathy or clinically significant macular edema, there is clear evidence of relatively intact foveal cones in humans that is provided by SD-OCT B-scans (20). However, on a finer scale, what are the potential changes to living cones and the microenvironment? Using AOSLO in the same subjects, we find that there is remodeling of retinal vasculature (20, 21). Extensive vessel remodeling occurs in some patients that is earlier than expected by clinical classification, and in some cases accompanied by numerous hard exudates or cysts too small to be seen without adaptive optics. Microaneurysms, cysts, and hard exudates smaller than the resolution of instrumentation found in the clinic, and even in the OCT images, are routinely visualized in our diabetic subjects. This both indicates a metabolic challenge to the cones, and also can make accurate quantification difficult when imaging through the overlying retinal pathology.

Despite the surprising ability of cones to survive and guide light in atrophy (18, 22) creating and maintaining high cone density in the fovea and a smooth distribution across the posterior pole may be difficult in a metabolically challenged retina. The migration of cones during early development places foveal cones in the foveal avascular zone, where even in healthy eyes there are few retinal vessels to help support photoreceptor metabolism. Inner retinal thickness is closely related to the proximity to retinal vessels, but there are large individual differences in size and shape (23). The foveal avascular zone is now rapidly and readily measured non-invasively with SD-OCT (3) and OCTA (24), again with individual variations in the size and shape, demonstrating the increased metabolic load in aging and for many diabetic foveas due to capillary closure and dropout. This indicates an even greater challenge for the retina to support foveal cones.

There is evidence that cones do not merely die in response to changes in metabolic support, but instead they can be found in highly irregular distributions. In patients with dry age-related macular degeneration there are patches of cone density at some perifoveal locations that are significantly greater than normative values, while in other locations there is atrophy with few cones (18). It is not yet known if these cones migrated slowly to regions with better metabolic support, the retina became distorted and stretched, or both. The metabolic support to maintain the arrangement of dense cones in the fovea, a visual streak, and a uniform distribution of cones, may be challenged also in diabetic patients. In young Type 1 diabetic subjects measured with AOSLO at 7 deg, eccentric to the fovea or perifovea and limited to a single eccentricity, a significantly lower number of cones is not reported, but there is a lack of the asymmetry of horizontal to vertical cone density that is the basis of the visual streak that is seen for young control subjects (25). Using the imaging device from this study and similar ones that scan to improve the contrast of retinal images is important because of contrast degradation from poor tear film, early cataract, or retinal changes that are common in diabetic eyes. This instrumentation also provided a wide field image so that the measurement locations were assured. It could be the case that the cones did not die off but never attained or could not maintain the asymmetry due to the metabolic challenge of diabetes. As the foveal peak was not measured, the potential for a meaningful proportion of fovea cones being lost was not studied.

Cone measurement results differing in some aspects were found for nearer the fovea (230–460 microns) in a study that used an AO device that lacked scanning to increase contrast and eye positioning other than pupil monitoring (26). The diabetic patients having increased central macular thicknesses indicates that diabetic changes are already measurable. At the locations measured, limited to fixed perifoveal samples, about a 10% decrease in cones is reported. Large individual differences are found, with 3 of 11 diabetic subjects having some values above the control densities. Foveal density values nearest the fovea are less than we find for young control subjects. A follow-on study reports a similar average decrease of cones in diabetic patients but only at a single eccentricity and again with large individual differences (27). To discriminate subjects with no retinopathy vs. controls also requires metrics besides cone density to quantify variability in distribution, i.e., linear dispersion and a heterogeneity packing index. Similarly, a cone heterogeneity packing index, again at only a single eccentricity in the perifoveas of diabetic subjects but with AOSLO, indicates a more disorganized cone distribution with poorer deep capillary plexus flow on OCTA (28). In a separate study using AOSLO and measurements limited to 4.6 deg eccentricity, cone density and spacing are not associated with presence of diabetes or severity of retinopathy other than presence of diabetic macular edema, but variability of cone packing is significantly associated (29). We previously showed striking changes in cone reflectivity in some diabetic eyes, with a variety of sizes of patches of dark cones that make quantification at specific locations challenging (8). Taken together, these previous studies demonstrate the potential for less regular distribution of cones in metabolically challenged eyes. However, the measurements do not clearly address the potential for decrease of cone density because single point measurements cannot be adjusted in position to avoid retinal pathology and therefore may be unable to detect small changes, have wide confidence intervals due to individual variability, suffer in some instruments from positional uncertainty, and most importantly cannot model the two factors needed to specify cone density or total numbers. Thus, a better estimate of number of cones and the resulting metabolic load due to cones is needed, especially since the overall numbers outside the central fovea are much greater despite lower density.

To document retinal health and properties of cones, SD-OCT methods have been used to measure reduction in the length of photoreceptors in diabetes (30) and aging (18), which must be distinguished from diabetes. OCT methods are useful for detecting disruption to the cone distribution and cone pathway distributions including other retinal layers. However, OCT thickness measures do not provide an accurate assessment of all the changes in cones, such as subtle decreases in cone density, since the thickness of the outer nuclear layer has been shown to increase even in the presence of a loss of cones in aging, likely due to neural remodeling and Mueller cell changes that alter the thickness of the outer nuclear layer (17).

Even without structural changes detectable by standard clinical methods such as OCT thickness metrics, patients are not free of structural changes to their retinas. In a recent study (31), we compared the frequency spectra from the FFT of the OCT B-scan of diabetic patients without retinopathy and age-matched controls. These subjects, having no retinopathy detected through clinical examination, also have no significant difference in the values for the total retinal thickness for any quadrant in the ETDRS grid, nor systematic relation with age for the total retinal thickness of any quadrant. There is a trend for the thickness between the retinal pigment epithelial/choroid border to the inner segment/outer segment junction to be thinner in the diabetic subjects, with significantly thinner values at 1 deg temporal and 3 deg nasal to the fovea for diabetic subjects. Despite these structural OCT findings, which are comparable to the healthiest eyes in the previous cones studies, the frequency analysis showed differences in the diabetic eyes vs. controls. In the deeper layers of the fundus, the diabetic patients had relatively higher amplitudes at the spatial frequencies that contained outer retinal features, capillaries, and structures of similar sizes, and less amplitude in several other frequency bands. It is not known whether neuronal or vascular changes led to the shift in frequencies present in the OCT images, but these changes indicate very early changes to diabetic eyes. Similarly, recall that the above length and thickness measurements occur within a microenvironment that we now know has extensive changes early on, compared to the retinal structure expected by clinical classification (20). Therefore, quantifying neuronal changes may provide earlier detection of eyes at risk and improve management of an individual eye or patient, as well as benefit the understanding of neural-vascular coupling, but it should not be assumed that neuronal changes occur prior to any vascular changes.

MATERIALS AND METHODS

Subjects

We compared 10 diabetic subjects (28–78 yr, 54.7 ± 12.8 yr; seven females and 3 males) tested between 2/18 and 5/19 to our published norms for cone density in 36 younger and 10 older controls (16, 17, 19). The 36 younger normal controls were aged 18–34 yr, mean 24.4 ± 3.42 yr (19). The 10 older normal controls (16, 17) were aged 51–65 yr, mean 56.3 ± 3.71 yr. Control subjects had strict limitations on refractive error, since myopic subjects have sufficiently different cone density distributions to obscure the effects of aging or disease (32). Subjects had axial lengths that indicated a lack of high myopia or hyperopia, ranging from 22.0 to 24.1 mm (mean = 23.0 ± 0.660 mm). All subjects were consented and tested in a manner approved by the Indiana University Institutional Review Board, which adhered to the Declaration of Helsinki.

Apparatus and Image Acquisition

Following consenting and pupil dilation, we imaged cones and retinal vasculature using a custom adaptive optics scanning laser ophthalmoscope (AOSLO), similar to previous methods (8, 16–20, 32, 33). Each patient first underwent imaging with an en face and wide field SLO, SD-OCT, and OCT-A (Heidelberg Spectralis II, Heidelberg Engineering, Heidelberg, Germany) to further document retinal status. A dense macular grid was obtained under fixation control for each eye. As previously, the wide field SLO provided a template for the AOSLO imaging. The axial length was quantified using an IOLMaster (Zeiss Meditec, Carlsbad, CA), as previously, to provide correction for sampling and computations of cones. Normative data for SD-OCT were obtained from our previous study of the analysis of retinal thickness from 33 diabetic patients without retinopathy and 33 age-and sex-matched controls, aged 39–77 yr, mean 54.1 ± 9.40 yr (31). These data provided a two-tailed, 95% confidence interval for controls, who did not differ as a group in age from the sample of diabetic subjects evaluated for cone distribution. The SD-OCT and OCT-A images were used to characterize the diabetic patients, along with a dilated fundus examination. Selected clinical characteristics and demographic information is given in **Table 1**. The diabetic patients ranged from two with no background retinopathy through one with proliferative diabetic retinopathy (**Table 1**).

In the custom AOSLO, two imaging beams were simultaneously delivered (769 and 842 nm) with 160 and 110 microwatts at the pupil, respectively, using a supercontinuum laser (NKT Photonics, Birkerod, Denmark). For the present quantification of cones, confocal images with an aperture of 100 microns at the detector (two Airy disks) were analyzed from the data of the optical channel with the 769 nm imaging beam. The illumination was scanned in a raster pattern with a horizontal frequency of 15.1 kHz and a vertical frequency of 29 Hz to produce 1.9° × 1.6° (W × H) retinal images of 780 × 520 pixels. All images shown were acquired at a constant magnification that is practical for these large datasets, but even better resolution of the very narrow foveal cones is also collected at higher magnification (not shown). Each subject's optical aberrations were measured at 20 Hz using a Shack-Hartmann sensor that allowed for correction over a customized size and shape of pupil (34). This optimized the optical correction on an individualized basis and allowed AOSLO imaging in subjects who had pupils less than the full 8 mm or mild lens changes.

Typically 100 frames of video were collected for each image acquisition, using a graphics overlay on the en face SLO image to steer the image capture to the approximate position as the subject looked straight ahead. For all subjects tested that provided normative values for younger and older subjects, the samples formed a "+" shape around the fovea to include not only temporal but also inferior, superior, and nasal meridians to at least 7 deg eccentricity (16, 17). For later subjects (8, 18, 19), an abbreviated protocol was used for most subjects to ensure the highest quality data (**Figure 1**). This shorter session reduced the decrease in contrast found particularly in older subjects due to tear film irregularities increasing over time within an imaging session. The temporal meridian was chosen for emphasis because there are fewer overlying blood vessels to interfere with sampling. Further, individual differences in the peripapillary region that can be large in older subjects were therefore not a factor.

Following imaging of cones, the focus of the AOSLO was set more superficially, and imaging of the retinal vasculature in the foveal and temporal regions of interest was performed using both channels. These data, along with the SLO and OCT imaging, helped document dilated capillaries, small hemorrhages, and microvascular remodeling, needed to guide the sampling of cones away from artifacts. These portions of the protocol for experimental imaging techniques with AO typically required about 40 min for the 90 subjects tested to date, exclusive of ophthalmic exam and detailed results discussions with patients.

Image Analysis

After removing the sinusoidal scanning pattern motion, corrected images were processed by automatically detecting a frame without significant eye motion and then aligning other frames within the 100 frame sequence to the template image using a strip alignment method, as previously described (8, 19). Frames with large eye motions or blinks were automatically rejected by the computations. To improve contrast of summary images for grading, the lucky average images were typically used for cone counting (35). The average data for each sampled location were built into a montage, with about 50% overlap between samples, and additional overlap when acquiring samples left to right vs. right to left. The montage method eliminates the need for precise fixation by the subject to determine locations for sampling, as long as fixation is stable enough for averaging.

To count cones, we used the software developed previously that provided the younger and older normative data (16, 17, 19) and cone counts in diseased retinas (18), with upgrades to display more channels and choices of display contrasts and magnifications (MATLAB, Mathworks Inc, Natick, MA). We sampled temporal retina, ∼0.9 to 7 deg to obtain 4 non-contiguous samples of roughly 100 × 100 microns. Many diabetic datasets contained overlying retinal vascular lesions, but the software allowed selection for best visibility of cones and least pathology, with the eccentricity corrected for axial length. Spacing the samples apart and not oversampling at the fovea provide the best comparison of patient to control data, since the data near the foveal center are the most variable and some subjects have a steeper decrease of cones near the fovea than others (19).

Cone Distribution Model

The data were fit with a 2 parameter exponential model:

$$\ln\left(cone\ density\right) = a * microns\ eccentricity + b \tag{1}$$

where a is a slope parameter that indicates the steepness of decrease in cone density from fovea to periphery and b is an offset parameter. As b is weighted heavily by points outside the fovea in our typical sample of four spaced positions, then b is related to an asymptotic density of cones in the periphery and the overall number of cones within the error of the fits. As previously discussed, the fits of the exponential model yield excellent R^2 values when there are four widely spaced data points, but some subjects have a steeper slope near the fovea than is described by an

TABLE 1 | Age, sex, clinical characteristics, and sample results for the diabetic patients.

Age in yr	Sex	Axial length in mm	DR stage	Features	CRT in microns	R^2	a	b	Total cones in 14 deg
28	M	23.36	Bkgd DR	MA, d/b heme	316	0.908	−0.00066	10.40	175,813
39	F	22.76	Proliferative DR	NVE, peripheral PRP, venous beading	291	0.984	−0.00063	10.43	189,193
50	F	22.69	Bkgd DR	MA, d/b heme	291	0.893	−0.00058	10.77	282,972
56	F	22.17	No Bkgd DR		246	0.873	−0.00039	10.45	263,505
56	M	24.10	Bkgd DR	MA only	261	0.946	−0.00060	10.31	174,847
58	F	23.05	Severe non-proliferative DR	Venous beading, d/b heme	246	0.924	−0.00060	10.37	185,808
59	F	23.84	Bkgd DR	MA, d/b heme	261	0.851	−0.00034	10.28	240,853
61	F	21.99	Bkgd DR	MA only	281	0.791	−0.00068	10.83	265,231
62	F	22.38	No Bkgd DR	RPE lesion	267	0.856	−0.00043	10.54	272,577
78	M	23.28	Bdgd DR	MA only	265	0.767	−0.00062	10.32	172,712

DR stage, diabetic retinopathy stage; CRT, central retinal thickness; R^2, linear fit to exponential model; Bkgd DR, background diabetic retinopathy; MA, microaneurysms; d/b heme, dot blot hemorrhage; NVE, new vessels elsewhere; PRP, pan retinal photocoagulation; RPE, retinal pigment epithelium.

exponential model (19). Further errors occur when there are large variations in the density of cones in association with diseased retinas (18).

Total cones within the central 14 deg of the macular were estimated from parameters a and b, as previously (19). The previous data were normalized for the horizontal:vertical asymmetry in cone density. Given the lack of this asymmetry in several of our older control subjects (17) and potentially in diabetic patients (25), we compared the temporal quadrant cone model without further normalization.

Retinal Thickness From SD-OCT

Vendor supplied software provided the mean and SD for each subject for total retinal thickness of quadrants within a standard ETDRS grid. The center region of interest is a foveal center circle that is 1 mm wide with respect to the emmetropic retina. The inner nasal, superior, temporal, and inferior quadrants cover from 1 to 3 mm. The outer nasal, superior, temporal, and inferior quadrants cover from 3 to 6 mm. The normative data are those previously reported for our institution (31).

Statistical Analysis

The density of cones data were computed with custom software, as described previously (17–19). The fits to the exponential model were performed by using linear regression on the ln(cone density) as described previously (19), and the confidence limits were computed, using Excel and Statview. The total cones modeling was performed in Excel as described previously (19). The Total Retinal Thickness means and standard deviations were computed from SD-OCT, using vendor software on the Spectralis and then compared via ANOVA with SAS and with linear regression with Statview.

RESULTS

Cone Appearance in Diabetic Maculas

Cones could be counted in all subjects. In the young, healthy eye, there is a systematic distribution of cones, which provides an organized sensor array with the highest cone density at the fovea and cone density decreasing sharply with increasing distance from the fovea (**Figure 1**). In the young, normal eye there is a wide variation in the reflectivity of individual cones, but primarily a regular pattern of reflectivity differences of single bright or dark cones. Regions of darker appearing cones beyond a single cone are typically in the shadow of overlying retinal blood vessels. Cones increase in size and center-to-center spacing, on average, with increasing eccentricity (**Figures 1B–G**). Small disruptions in the cone mosaic occur in normal subjects and are intentionally shown (**Figures 1E,F**), along with individual cones that are not uniformly guiding light **Figures 1B,C**). It is typical that disruptions with age are more common (17), but not as extreme as those found in subjects with atrophy (18). Even in control subjects, overlying retinal vessels can shadow cones (**Figure 1F**) and make it more difficult to count them.

While previous cone distribution modeling resulted from sampling regions of interest at fixed locations, we found that in all diabetic subjects there were retinal vascular changes and obscuration from retinal remodeling that required moving the sampled regions of interest to locations that were not at the precise eccentricities of the control data (**Figures 2**, **3**). At some locations, obvious shadowing due to overlying retinal vessels or retinal remodeling prevented sampling. Thus, the amount of displacement of the sampled region of interest was considerably greater in diabetic patients than the minor changes required in sampling the control data. There were scattered low contrast regions, larger than in older controls but smaller than the AOSLO image. Patchiness of the clarity of focal regions in the images of diabetic eyes was not due to variation in image quality related to optical degradation of the anterior segment, as this would alter the clarity of the whole sampled image at once. That is, pupil plane artifacts lead to roughly uniform degradation of contrast in the retinal image of an AOSLO. However, there were also occasional pupil plane artifacts, evidenced by an entire image sample within the montage being of lower contrast, indicating fluctuations in correction by the AO over time, such as with variations in tear film. Thus, although for our control subjects, and most previous studies, sampling was at roughly the same retinal eccentricities along a temporal meridian, for the diabetic subjects we fit the exponential model to each subject's

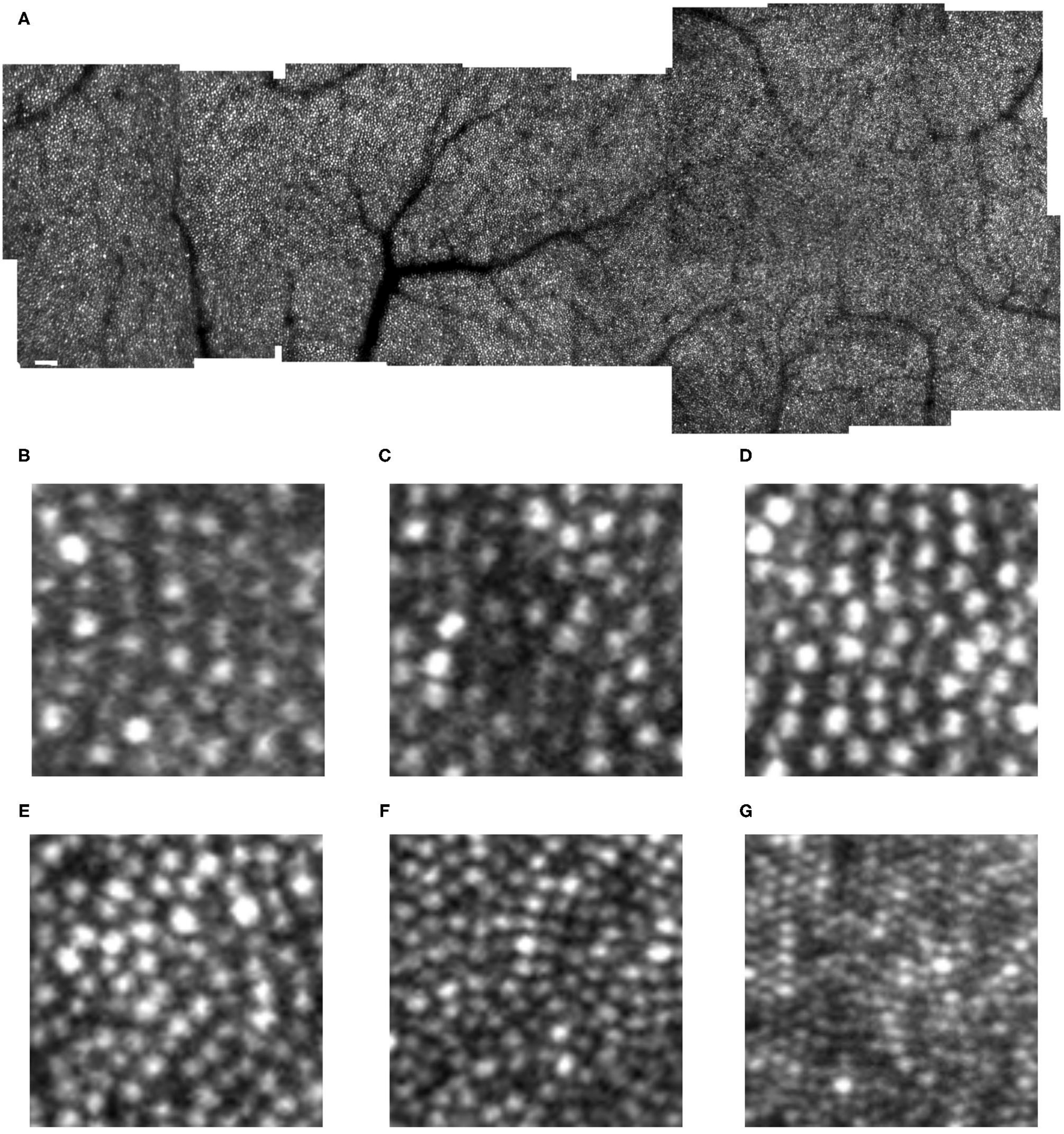

FIGURE 1 | Cone distribution for a 25 yr old female control subject, shown in a montage of individual images **(A)** of the right eye collected with the confocal mode of the AOSLO. The fovea, which is on the right, has the highest cone density. There is smoothly decreasing cone density farther from the fovea, with the temporal meridian shown. Small white scale bar at lower left = 100 microns. **(B–F)** Individual cones shown at increased magnification in regions of 100 × 100 microns with the upper far corner at 8.7 **(B)**, 8.4 **(C)**, 7.0 **(D)**, 4.8 **(E)**, 2.8 **(F)** temporal and 1.1 deg temporal inferior **(G)** deg temporal with respect to the fovea.

data to obtain parameters for cone density as a function of retinal eccentricity.

Diabetic cone maps showed that cones were found distributed over a wide variety of locations, but included bright patches, with unusually bright cones alone or in clusters, and clusters of dark cones as noted previously (**Figures 2**, **3**). These unusually bright or dark cones were not limited to the fovea and perifovea. Similarly, over the entire montaged region there is a qualitative

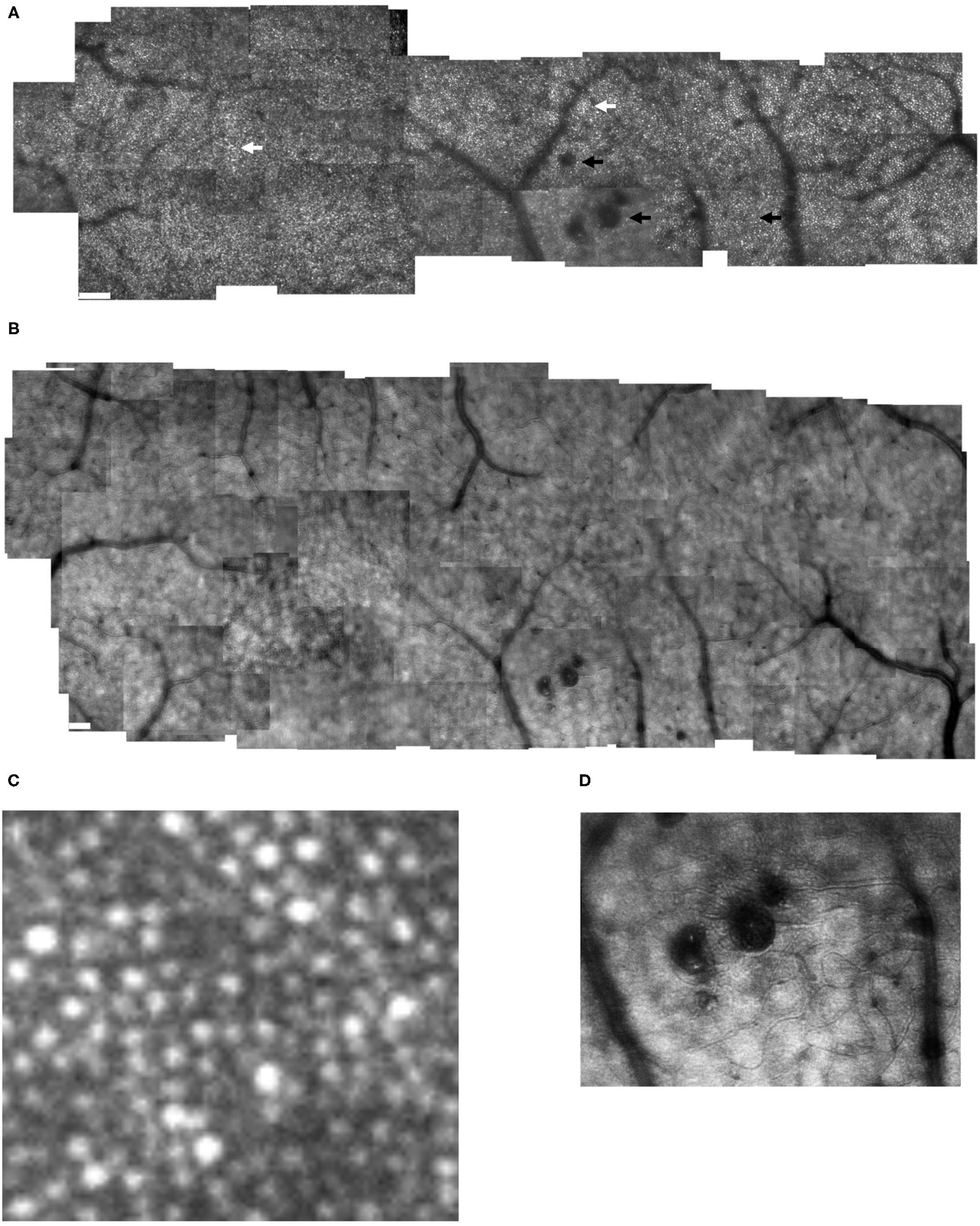

FIGURE 2 | Cone distribution for a 59 yr old female diabetic subject, collected with the confocal mode of the AOSLO **(A)**, shown in a montage of cone images with the foveal region on the left. The retinal microvasculature layer montage **(B)** shows a strong response to ischemia, with numerous retinal vascular changes shadowing *(Continued)*

FIGURE 2 | the cone layer: multiple microaneurysms with vascular remodeling surrounding them, capillary bends or loops, and doubled or collateral vessels, particularly near microaneurysms or complex tangles. The montage of individual images shows that cone density is highest in the fovea, then decreases with increasing eccentricity, with single cones or patches of cones being unusually bright (white arrows), as well as patches of dark cones. There are regions in which the overlying retinal vessel remodeling interferes with measurements of cones, by obscuring them (top black arrow). Sometimes the contrast across an entire individual image sequence of cone images was decreased, either due to the tear film or a decreased the wavefront correction across in a large area of edema (bottom left black arrow). Elsewhere, the contrast is decreased for regions smaller than an entire image, which rules out anterior segment artifact as the sole source of image degradation (bottom right arrow). Small white scale bars at lower left = 100 microns. A magnified region of 100 × 100 microns **(C)** shows patches of bright cones and areas of decreased contrast. An enlargement of the retinal microvascular layer **(D)** shows microaneurysms and extensive vessel remodeling. The cone parameters were a = −0.00034, and b = 10.28, outside of normal limits. RMS fit = 0.851.

disruption to a smooth distribution of cone density, previously noted for the perifoveal region. These two findings indicate that disruption to the cone distribution is not limited to just locations near the foveal avascular zone.

Cone Distribution and Estimate of Total Cones in Diabetic Maculas

As humans differ in both the overall numbers of cones and the steepness of the decline in cone density from fovea to periphery, determining cone loss from a single location can be misleading. The normative data indicate a monotonic decrease in cone density from the fovea to greater eccentricities. High cone densities are more typical in younger subjects, which correspond in some subjects to a steeper decline in cone density with increasing distance from the fovea, so that more peripheral cone densities in the periphery overlap to a greater extent than near the fovea. The decrease in cone density for diabetic subjects also varied across subjects, not just in the overall numbers of cones but also the rate of decline (**Figure 4**). While there was a general decline in cone density from the fovea toward the periphery, some subjects had densities that did not decline monotonically due to local variability.

The exponential model provided excellent fits for both younger and older controls: for the linear fit to the ln density transform for four widely spaced samples, $R^2 = 0.9371 \pm 0.0387$ and 0.959 ± 0.0267, for younger and older, respectively (**Figure 5**). Thus, while the variability for older subjects in cone density is large, the goodness of fit indicates that this is an overall phenomenon and not due to local variability. Inspection of the cone maps on and between samples supports this conclusion (17). The fit to the model was similarly good for some diabetic patients and poorer for others. The R^2 was 0.767–0.984 in diabetic data set. Despite the large proportion of variance accounted for in the diabetic patients, the control data fit the model so well that four of 10 diabetics had $R^2 <$ the 95% confidence limit for younger or older controls, as appropriate. Thus, while the model fit the data sufficiently well to determine whether the diabetic patients had a less peaked foveal slope or fewer overall cones, as compared to age-matched controls, the variability is consistent with a less even distribution of cones in diabetic eyes, as previously reported for small perifoveal regions. The variability is seen when examining the cone maps of diabetic subjects (**Figures 2**, **3**).

The 95% CI's were computed from the exponential model. Parameter b (younger subjects) = 10.7 ± 0.146, with the 95% CI = 10.4–10.9. Parameter a (younger subjects) = −0.000692 ± 0.0000985, with the 95% CI = −0.00050 to −0.000885. Parameter b (older subjects) = 10.7 ± 0.222, with 95% the CI = 10.4–11.3. Parameter a (older subjects) = −0.0008071 ± 0.0000984, with the 95% CI = −0.000582 to −0.00103. For the older subjects, three of 10 subjects had lower values of parameter b than younger subjects, and one of 10 subjects had a lower parameter b than the confidence limits for younger subjects. For parameter a, there was considerable overlap between younger and older subjects, with great variability for older subjects but only one of 10 older subjects falling outside the confidence limits for younger subjects.

Overall cone density was often lower in diabetic patients, as indicated by parameter b compared to the lower 95% confidence limits (**Figure 5**). For the two younger diabetic subjects, parameter b fell below the 95% confidence limit for younger controls. For five of the eight older diabetic subjects, parameter b fell below the 95 % confidence limit for older controls, for a total of seven of 10 diabetic subjects having low values for parameter b. If parameter b is thought as analogous to an asymptote for cone density at the greater eccentricities, then the data can be examined for trends at the greater eccentricities measured, i.e., the cone density that a metabolically challenged retina could support. The fit is consistent with five of the 10 subjects having cone densities at the greater eccentricities that clearly fell below the densities other five (**Figure 4**). Further, there is a range of cone density among the top five subjects with two subjects falling below the other three.

The decline in cone density from the fovea outward was often shallow in diabetic patients, as indicated by parameter a. All diabetic patients had slopes less than the mean for their age group. For the two younger subjects, parameter a was not below the 95% confidence limit. For the older diabetic subjects, three of eight had slopes shallower than the 95% confidence limits for their age group.

Total cones in the central 14 deg of the macula, as estimated from temporal quadrant data, were 238,000 ± 18,300 for younger subjects, with a minimum of 207,000 and a maximum of 272,000 (**Figure 6**). The 95% confidence limits were 203,000 and 274,000. Total cones for the 10 older subjects were 214,000 ± 33,000, resulting in wide confidence intervals: a minimum of 140,000 and a maximum of 289,000. Total cones were lower than the mean of the younger subjects in nine of 10 older subjects, statistically different from chance (Binomial test with 10 df, $p = 0.00977$). However, only two of eight older subjects had total cones less than the lower 95% confidence limit of the younger subjects. There were large individual differences in both younger and older control groups, as expected from the cone density data (16, 17, 19). The coefficient of variation of total cones was significantly greater for older subjects than for younger ones, 0.145 and 0.0767,

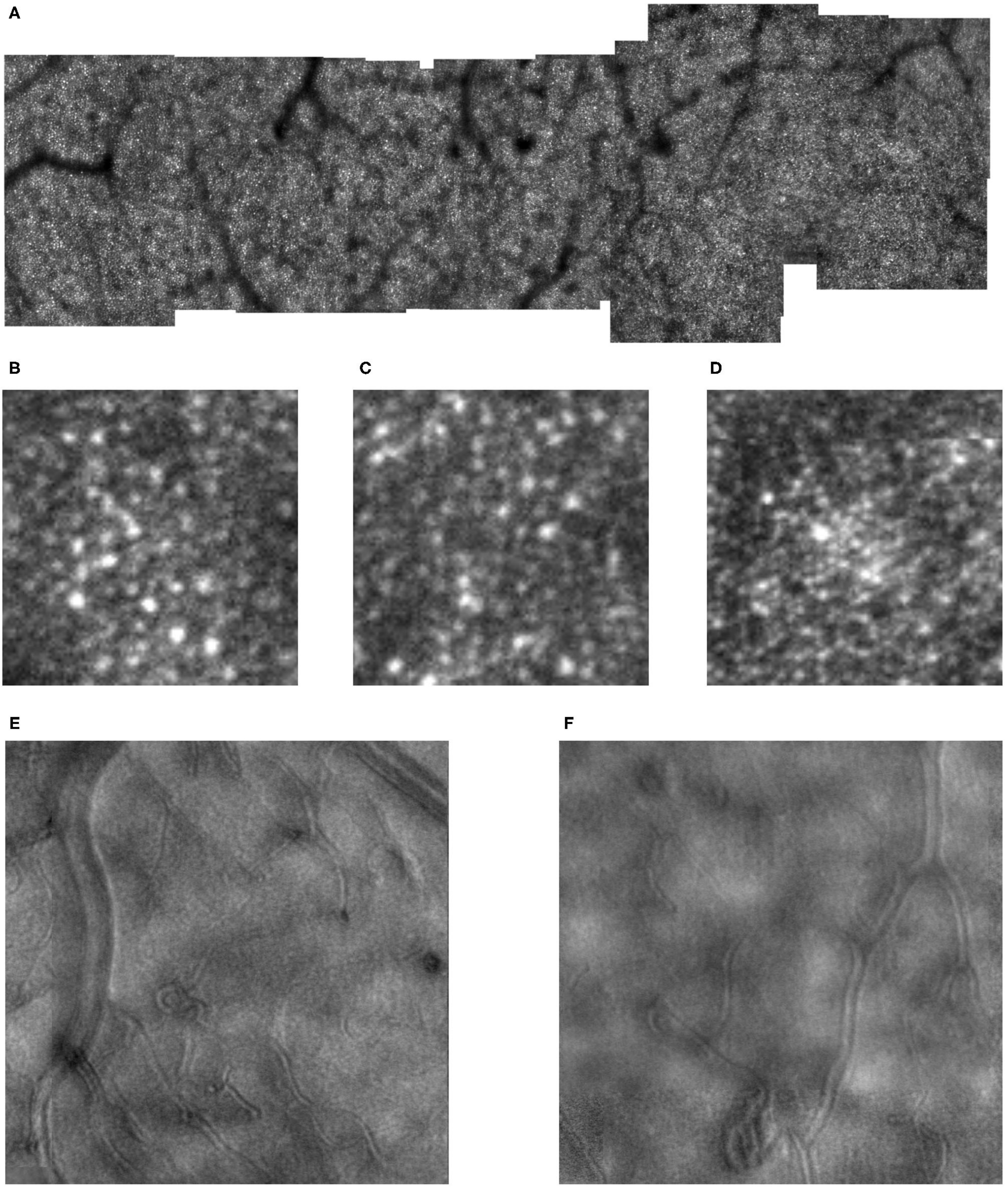

FIGURE 3 | Cone distribution for a 61 yr old female diabetic subject **(A)**, shown in a montage of cone images with the foveal region on the right, with a more moderate response to ischemia than in **Figure 2**. Small white scale bar at lower left = 100 microns. There are microaneurysms, but less frequent capillary bends or loops, and few doubled or collateral vessels or the more complex tangles. **(B–D)** Magnified view of cones, showing the phenomena of both extra bright and dark cones in unusually large numbers in 100 × 100 micron samples of cones, with the upper far corner at 7.6, 5.6, and 1.0 deg temporal with respect to the fovea. **(E,F)** Enlarged views of the retinal microvascular layer, showing 500 × 500 microns samples of microaneurysms, capillary bends, and elongated and collateral vessels, but smaller or less frequent than in **Figure 2**. Cone parameters, were a = −0.00068, and b = 10.83, within normal limits. RMS fit = 0.791.

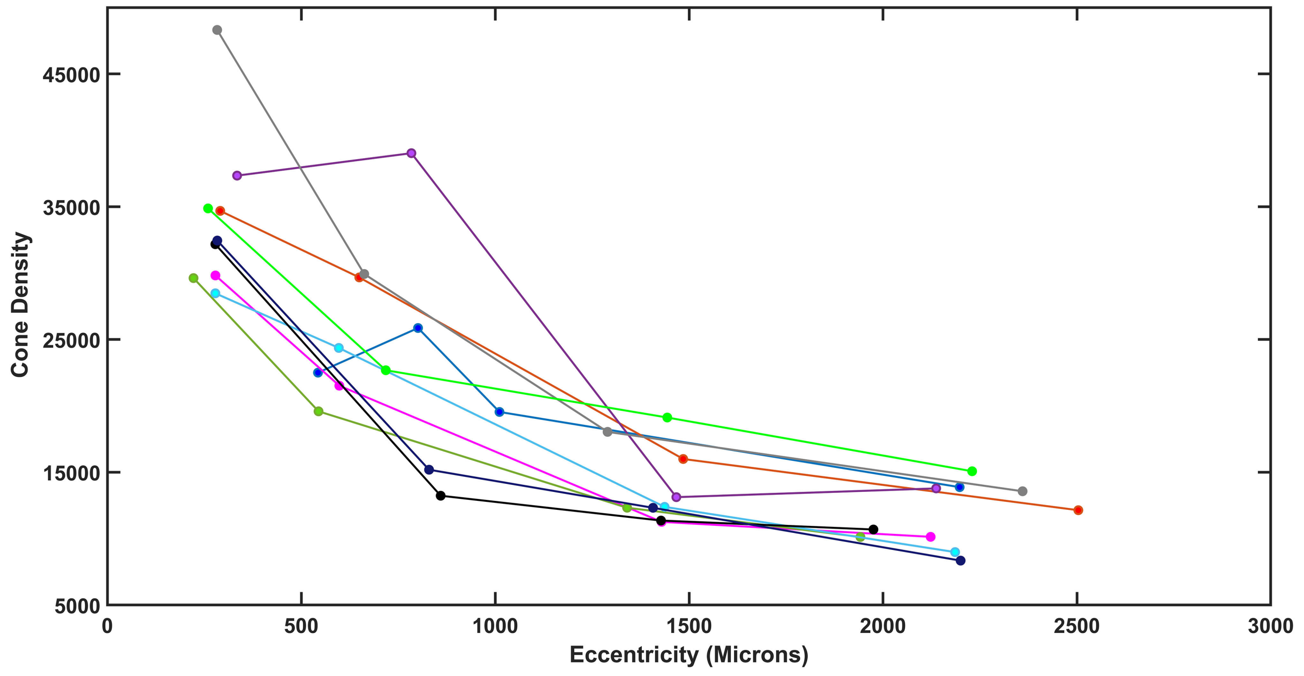

FIGURE 4 | Total density plotted as a function of retinal eccentricity for the diabetic subjects, showing differences among subjects at all eccentricities.

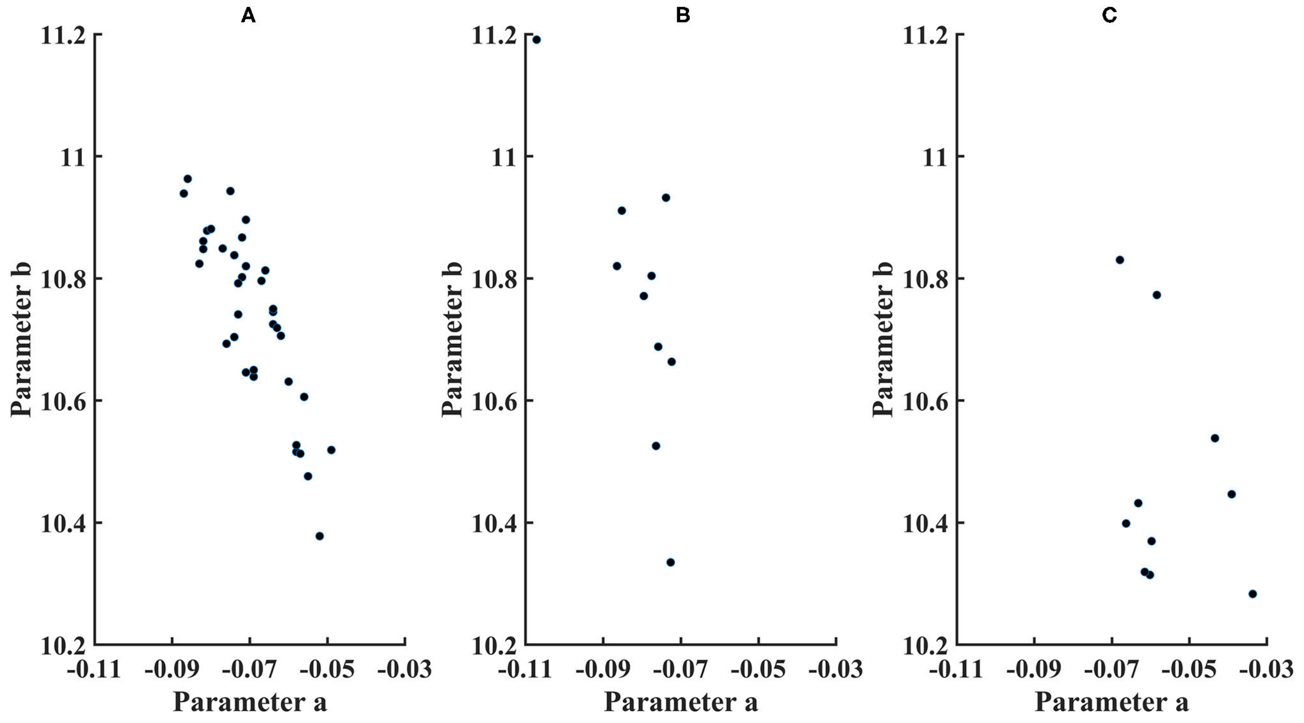

FIGURE 5 | Parameters for cone distribution from the exponential model ln (*cone density*)=*a*microns eccentricity+b*, *with a plotted as a**100. **(A)** younger control subjects, **(B)** older control subjects, and **(C)** diabetic subjects.

respectively, [$F_{(35,9)} = 4.03$, $p < 0.025$]. This finding is based on, and consistent with, the high intra-individual variability of cone density reported previously in the younger subjects based on 10 of the 36 younger subjects and the same older subjects (17) and in 36 younger subjects (19). However, the greater variability of the older subjects may be in part due to a smaller sample size. While

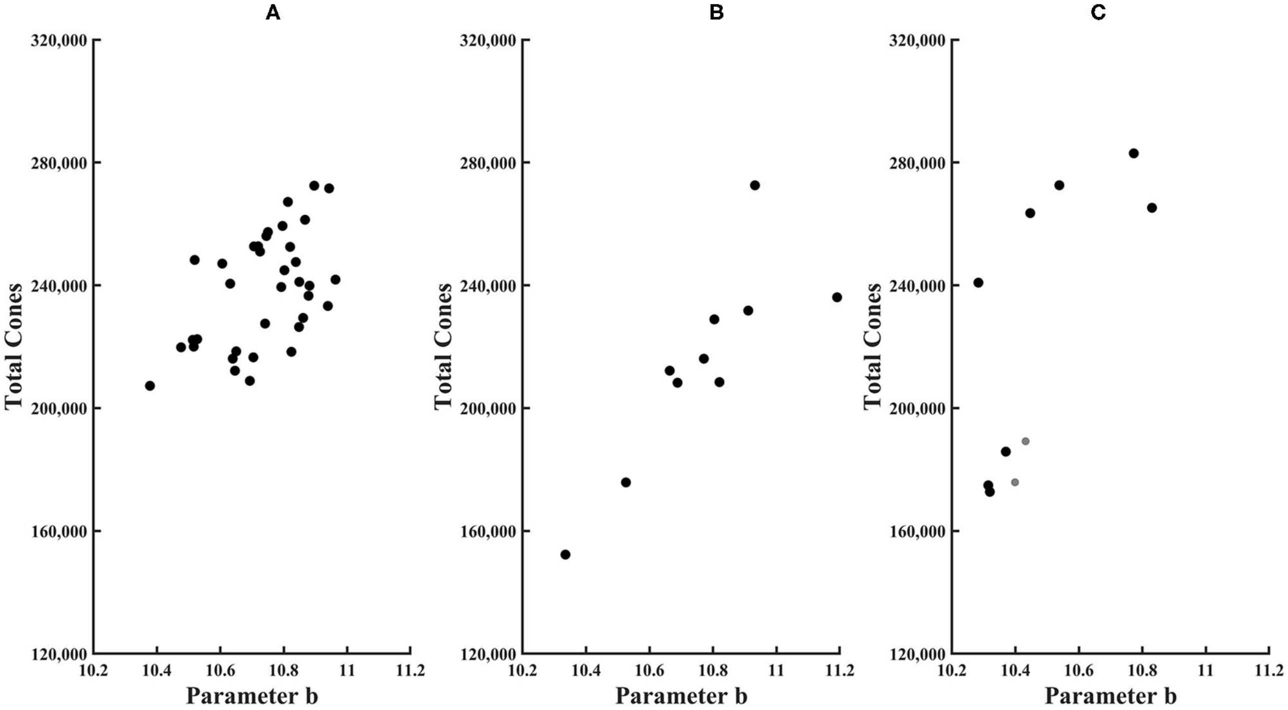

FIGURE 6 | Total cones plotted as a function of parameter b of the exponential model for **(A)** younger control subjects, **(B)** older control subjects, and **(C)** diabetic subjects. Younger subjects have smaller symbols.

the clinical classification of a patient and the total cones were not always consistent, it should be noted that the two subjects with no background diabetic retinopathy had among the highest total cones (**Table 1**).

Total cones were lower in some in diabetic subjects. For both younger diabetic subjects, the total cone values of 176,000 and 189,000 fell below the 95% confidence limit. In three of eight older diabetic subjects, total cones was lower than the mean for older controls. However, given the high variability of older controls, none of the diabetic subjects had total cones either greater than or less than the 95% confidence limits of older subjects. For these diabetic subjects, there was no significant association with age for total cones, parameter a, or parameter b, with R^2 from the linear regression being only 0.026, 0.070, and 0.0020, respectively.

Structural Changes Associated With Cones in Diabetic Maculas

All diabetic subjects had retinal microvascular changes seen on AOSLO, likely in response to ischemia (**Figures 2B,D**, **3E,F**), but to varying amounts. The strongest response to ischemia included multiple microaneurysms with vascular remodeling surrounding them, capillary bends or loops, and doubled or collateral vessels, particularly near microaneurysms or complex tangles.

From the SD-OCT data for the control subjects, the Total Retinal Thickness of the three ETDRS quadrants that corresponded to cone distribution data, Central Macular Thickness, Inner Temporal Thickness, and Outer Temporal Thickness, had 95% confidence limits for the age-similar control subjects of 226–327, 290–370, and 253–322 microns, respectively. For the diabetic subjects, the Total Retinal Thickness for Central Macular Thickness, Inner Temporal Thickness, and Outer Temporal Thickness ranged from 246 to 316, 303 to 355, and 260 to 316 microns, respectively. Despite clear-cut abnormal retinal vasculature on AOSLO in all 10 diabetic subjects, the Total Retinal Thickness values for each subject in each quadrant were within the 95% confidence values, being neither thicker nor thinner than controls (**Figure 7**). For the other ETDRS subfields, again Total Retinal Thickness values for each of the 10 diabetic subjects were within the 95% confidence values, other than a missing Outer Nasal value for one subject (**Figure 8**). However, there was a significant correlation of age with Total Retinal Thickness for most of the subfields, with R = 0.700, 0.705, 0.600, 0,772, 0.390, 0.787, 0.587, 0.627, and 0.293 for the foveal, temporal, outer temporal, nasal, outer nasal, superior, outer superior, inferior, and outer inferior quadrants. Decrease in Total Retinal Thickness per year with age was 1.14, 0.806, 0.688, 0.677, 0.392, 0.677, 0.727, 0.591, and 0.345 microns, respectively. Significance of the association of Total Retinal Thickness with age varied across subfields for the diabetic subjects, with $P < 0.005$ for nasal and superior; $P < 0.02$ for foveal and inner temporal; and $P < 0.05$ for outer temporal, outer superior, and inferior; but only $P < 0.15$ for the outer nasal and $P < 0.7$ for the outer inferior quadrants. These results are consistent with relatively greater loss in Total Retinal Thickness near the fovea. In contrast to our previous results that indicated no change with age, but included only subjects without retinopathy on clinical examination (31), the present subjects had clear cut retinopathy and vascular remodeling. The lack of a measurable decrease in thickness compared with controls in the present study, but yet a significant decline with age in retinal thickness while the values fell within the confidence limits, supported the conclusions that there is a loss of neural, vascular, or glial elements.

Cone Reflectivity and Distribution Compared for Younger, Older, and Diabetic Maculas

The most obvious difference between cone montages for younger (**Figure 1**) and older controls (**Figures 9A,B**) as opposed to diabetic patients (**Figures 2**, **3**) is the lack of shadowing of the cones by overlying remodeled capillaries and microaneurysms in the control subjects. While there is shadowing by overlying retinal vessels, it is less and does not prohibit measurements. Cones in all maculas in this study varied over space in reflectivity and distribution. In all subjects, the central macula has a higher density of cones than more peripherally. However, the decrease in cone density with increasing eccentricity was monotonic in all subjects except two (**Figure 4**), but could be steep or gradual and overall not a large change. Older subjects have more variable cones densities, particularly in the fovea (16, 17), but this may not be obvious from viewing the montages; the two older subjects shown have the highest and the second lowest cones in the control sample. The large variation in cone density across subjects is clear from the wide confidence limits, and model parameters a and b. As previously described, there are not large areas of missing cones in normal older subjects. Although the outer nuclear layer is on average thicker in the older subjects (17), and this layer overlies the outer segments, the return of light to the AOSLO is sufficient to quantify the cones. All subjects have cones of variable reflectivity, i.e., brighter appearing cones and darker appearing cones, but the extremes are typically not contiguous in the older eyes, even in older subjects (**Figures 9A,B**). (In contrast, some diabetic subjects have numerous localized dark cone regions with knife edge borders that take up the space required for multiple cones (**Figures 2**, **3**), as found previously (8). There are cones that appear much brighter than surrounding cones in all eyes, but in diabetic eyes some of these cones appear even brighter and larger than in control eyes.

DISCUSSION

Combining the appearance of cones, parametric data, and the model of total cones, there is evidence that cones undergo changes despite the lack of sufficient structural changes to result in thickened or thinned Total Retinal Thickness. Cones are altered in their ability to interact with light, in that there are patches of both light and dark cones. As the visualization of bright cones is via the light they return to the AOSLO, there is more than one possible interpretation of the bright cones that appear large. There is evidence for a decrease in cone numbers, which would allow cones to expand laterally. Rods were not measured, and if decreased could provide extra expansion space, but bright cones are seen in areas within the foveal avascular zone where rods are normally few in numbers (**Figure 3D**). Alternatively, and not mutually exclusively, cones may be leaking light, i.e., not guiding light back to the instrument is as narrow an angle or through the entire length down to the retinal pigment epithelium. This is consistent with the appearance of dark cones, also, in which leakage of light may lead to failure to guide light back to the instrument. The configuration of the custom AOSLO used here does employ a confocal aperture, but the diameter of the aperture is wide enough to allow for the capture of some multiply scattered light, trading off directionality of signal with signal intensity. Thus, we can image dark cones in the fovea (8). In contrast, an AOSLO can be configured to provide the maximum contrast from cones that do guide light, but this configuration reduces the signal from multiply scattered light or background signal, and makes difficult the detection of dark cones in the fovea due to a lack of rods surrounding the cones to provide contrast (36). The present configuration also allows some light from additional planes to be included in the signal, so that multiply scattered light from deeper or more superficial layers is detected. Thus, the early retinal damage that changes the amplitude of the frequency spectra in OCT, but is not readily pinpointed as visible features (31), can increase the brightness of the image focally. This may contribute to the increased brightness in regions with multiple and contiguous bright cones.

Several aspects of the data indicate damage in and near the fovea, as well as in the periphery. In several subjects, there was a lack of a peak maximum of cone density near the fovea or only a moderately steep decrease of cone density from fovea to periphery. The decrease from central to more peripheral locations was not always monotonic. The greatest decline with age in Total Retinal Thickness was in the fovea, with inner quadrants having more decline with age than the outer ones. While dark cones and the swollen appearing bright cones are not necessarily more numerous in the foveal region, this region is not spared of these changes.

There is evidence that the cone distribution across the retina changes in relation to diabetes, rather than just death of cones. The heterogeneity of cone spacing just outside the foveal avascular zone is a promising metric for neuronal involvement. Increased cone disarray has been shown in three studies, in comparison to controls and related to vascular changes (28) and retinal thickening on OCT (27, 29), but results were mixed with regard to whether cones decrease in numbers or migrate. We found evidence of cone reduction in some eyes on measurements not limited to locations near the fovea avascular zone, and cone distribution changes that are both qualitatively seen on montages and quantified by parameter changes in the exponential model. Further, the cone changes occurred without increases or decreases in retinal thickness on OCT. However, it cannot be determined with the cone changes began prior to any vascular changes, since there was evidence of retinal vascular remodeling in response to ischemia in all diabetic subjects. Cones persist despite clear-cut evidence of an ischemic response. Sufficient numbers of cones survive despite their

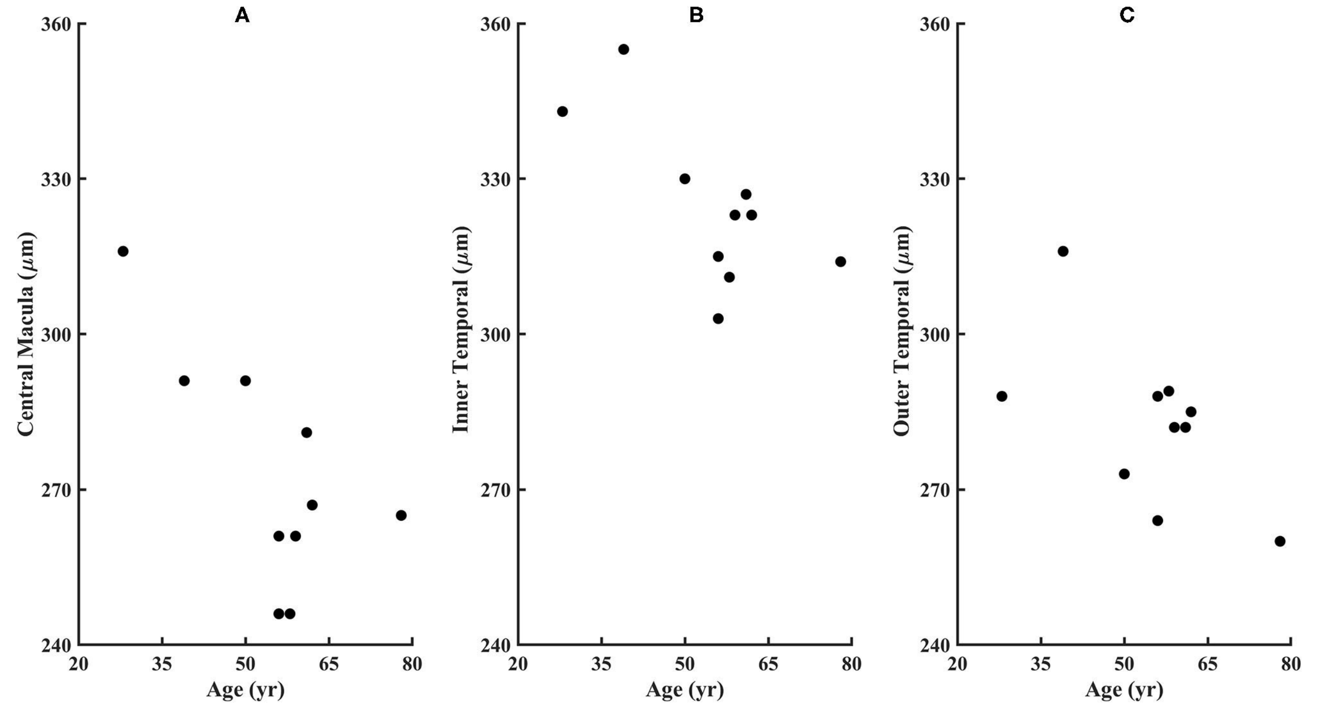

FIGURE 7 | Retinal thicknesses of the diabetic subjects from the ETDRS grid from the SD-OCT for **(A)** Central Macular Thickness, **(B)** Inner Temporal Thickness, and **(C)** Outer Temporal Thickness. No subject fell outside the confidence limits from the age-similar controls, although subject 209 is missing the outer nasal thickness measurement due to fixation error. The Total Retinal Thickness is significantly correlated with age for the diabetic subjects, with $P < 0.02$, 0.02, and 0.05 for the Central Macular Thickness, Inner Temporal Thickness, and Outer Temporal Thickness.

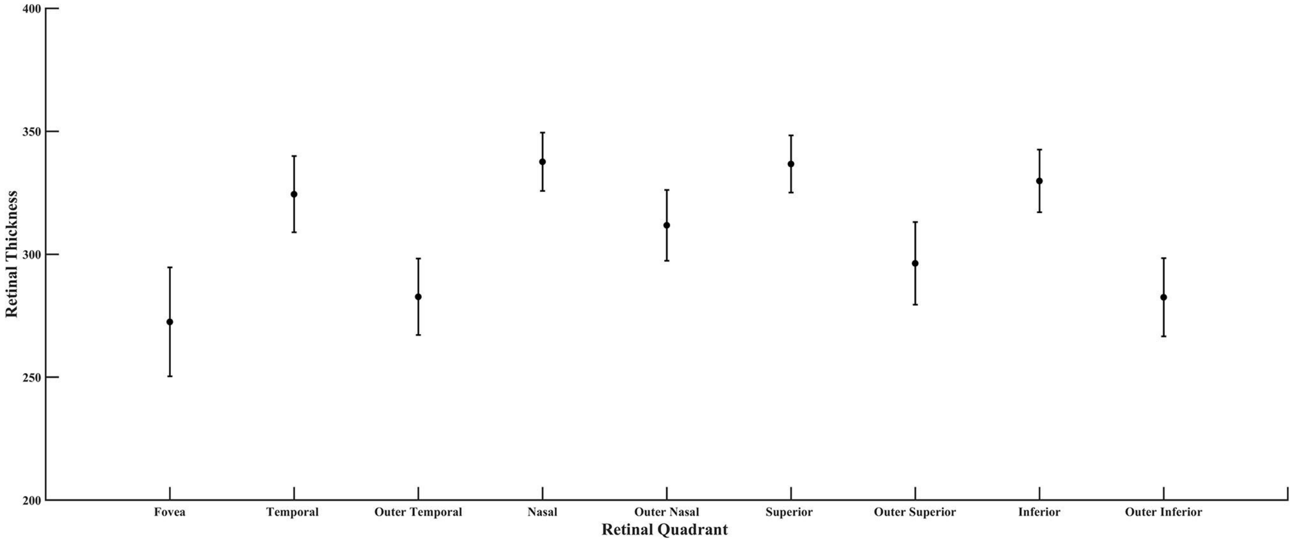

FIGURE 8 | Retinal thickness of the diabetic subjects for all quadrants of the ETDRS grid, plotted as mean and standard deviation.

microenvironment and can provide a metabolic challenge to the diabetic retina.

Our cone measurements are likely to be dominated by M- and L-cones, since there are few S-cones near the fovea and a sparse distribution elsewhere. The decrease of cones found in the two younger diabetic subjects was greater than the numbers of S-cones at the locations measured. From previous visual function data with L- and M-cones in diabetic patients without extensive retinopathy, there is not a great loss of L- and M- cones, as evidenced by color matching in these subjects being accurate

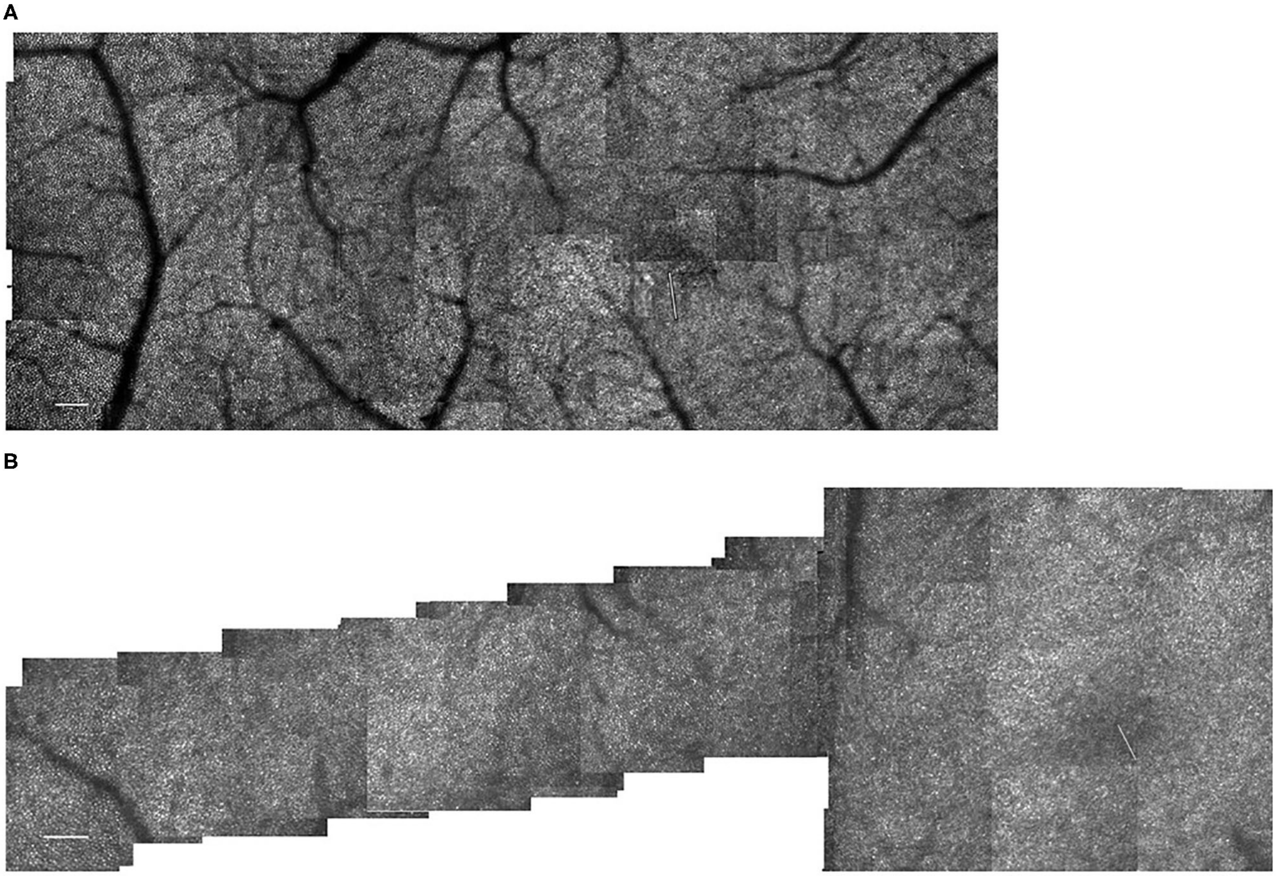

FIGURE 9 | (A) Cone distribution for a 55 yr old female subject from our control population, shown in a montage of cone images with the foveal region on the right. This subject was selected because she had the second lowest cone densities in the sample. Small white scale bar at lower left = 100 microns. White line on the right indicates the foveal center, where the cones are not readily distinguished with this setting on the AOSLO. **(B)** Cone distribution for a 58 yr old male subject from our control population, shown in a montage of cone images with the foveal region on the right. This subject was selected because he had the highest cone densities in the sample. This subject lacks a foveal avascular zone, having readily imaged capillaries through the foveal center. Small white scale bar at lower left = 100 microns. White line on the right indicates the foveal center, where the cones are not readily distinguished with this setting on the AOSLO.

enough to provide quantitative parameters (5). However, changes to S-cones could alter cone distribution somewhat and visual function significantly, but results are mixed (4). Histology findings demonstrate structural changes to only S-cones, which clearly are not impacted by the yellowing of the human lens, yet may not be readily translated to testing with *in vivo* methods. The low numbers of S-cones in the fovea and sparse and irregular distribution elsewhere limit the potential impact of diabetes on foveal acuity, spatial resolution of white or long wavelength stimuli, or contrast sensitivity, as well as functions depending on numbers of cones. Similarly, the sparse distribution of S-cones would make difficult the comparison of small retinal regions, since there might not be S-cones in the sample. Functional tests that require S-cone input specifically and short wavelength light have been used. Conclusions for S-cone pathway damage providing a sensitive metric, or show more damage than occurs for M- or L-cone pathways, require individualized controls for removal of the short wavelength artifact due to pre-retinal filtering properties of the aging and diabetic lens.

Other early neuronal damage is described for the retina, which impacts on cone pathways. The cotton wool spots in diabetes have been shown to have longer term functional consequences, which likely have a negative impact on cone vision (10). Thinning of layers, as measured first with scanning laser polarimetry (9) and then OCT (11), has been shown in diabetic patients, particularly for inner retinal structures such as the retinal ganglion cells and the retinal nerve fiber layer. A carefully selected sample of Type 1 diabetics had a thickened retinal sublayer, the inner nuclear layer, early on in the course of the disease (37). The cone changes that we found occurred without thickness changes to total retinal thickness on OCT, which were reported on an individual patient basis rather than a group. A thickness metric has been shown to be related to cone changes (27, 29) in patients with sufficient pathological changes. Thus, the variability of a thickness metric may mask early vascular changes in diabetic eyes that might proceed or contribute to cone damage. Losses of either neural, glial, or vascular components were measurable without exudation leading to significant retinal thickening. More sensitive measures of retinal vascular changes, such as those provided by AOSLO imaging or OCTA, can help provide a better understanding of neuronal changes and neuronal-vascular coupling, and provide improved biomarkers for the management of diabetic eyes.

DATA AVAILABILITY STATEMENT

The raw data supporting the conclusions of this article will be made available by the authors, without undue reservation.

ETHICS STATEMENT

The studies involving human participants were reviewed and approved by Indiana University Institutional Review Board. The patients/participants provided their written informed consent to participate in this study.

AUTHOR CONTRIBUTIONS

AE supervised the collection of the majority of the normative data, developed the model, guided the image processing tasks, sampled the diabetic data, graded images, analyzed the summary data, prepared statistics, wrote the manuscript, and made or designed the figures. BW collected the majority of the diabetic data on AOSLO and OCT, collected clinical data, analyzed OCT data on the diabetic subjects, maintained and queried the subject database for selection and quantification of subjects, processed AOSLO images, and edited the manuscript. RG processed images and made the AOSLO montages, selected cones montages for quantification, created a database for OCT and AOSLO data, and edited the manuscript. VP graded AOSLO montages, made figures, performed some of the statistics, and edited the manuscript. JP collected the OCT control data and provided summary statistics, assisted with plotting figures, and edited the manuscript. TG performed the examinations to qualify the diabetic patients, help select subjects for inclusion, helped design and performed OCT data collection and analysis, graded and interpreted images, and edited the manuscript. SB built the AOSLO apparatus, wrote the analysis software, helped select diabetic subjects, guided or performed the collection of diabetic and normative data, fine-tuned montaging, and edited the manuscript. All authors contributed to the article and approved the submitted version.

FUNDING

Data collection and preparation of this article was supported by research grants from the National Eye Institute EY007624 to AE and EY024315 to SB.

REFERENCES

1. Antonetti DA, Silva PS, Stitt AW. Current understanding of the molecular and cellular pathology of diabetic retinopathy. *Nat Rev Endocrinol.* (2021) 17:195–206. doi: 10.1038/s41574-020-00451-4
2. Park SH, Park JW, Park SJ, Kim KY, Chung JW, Chun MH, et al. Apoptotic death of photoreceptors in the streptozotocin-induced diabetic rat retina. *Diabetologia.* (2003) 46:1260–8. doi: 10.1007/s00125-003-1177-6
3. Arthur E, Papay JA, Haggerty BP, Clark CA, Elsner AE. Subtle changes in diabetic retinas localised in 3D using OCT. *Ophthalm Physiol Opt.* (2018) 38:477–91. doi: 10.1111/opo.12578
4. Tonade D, Kern TS. Photoreceptor cells and RPE contribute to the development of diabetic retinopathy. *Prog Retin Eye Res.* (2021) 83:100919. doi: 10.1016/j.preteyeres.2020.100919
5. Elsner AE, Burns SA, Lobes LAJr, Doft BH. Cone photopigment bleaching abnormalities in diabetes. *Invest Ophthalmol Vis Sci.* (1987) 28:718–24.
6. Ng JS, Bearse MAJr, Schneck ME, Barez S, Adams AJ. Local diabetic retinopathy prediction by multifocal ERG delays over 3 years. *Invest Ophthalmol Vis Sci.* (2008) 49:51622–8. doi: 10.1167/iovs.07-1157
7. Lutze M, Bresnick GH. Lenses of diabetic patients "yellow" at an accelerated rate similar to older normals. *Invest Ophthalmol Vis Sci.* (1991) 32:194–9.
8. Sawides L, Sapoznik KA, de Castro A, Walker BR, Gast TJ, Elsner AE, et al. Alterations to the foveal cone mosaic of diabetic patients. *Invest Ophthalmol Vis Sci.* (2017) 58:3395–403. doi: 10.1167/iovs.17-21793
9. Lopes de Faria JM, Russ H, Costa VP. (2002). Retinal nerve fibre layer loss in patients with type 1 diabetes mellitus without retinopathy. *Br J Ophthalmol* 86, 725–728. doi: 10.1136/bjo.86.7.725
10. Kozak I, Bartsch DU, Cheng L, Freeman WR. Hyperreflective sign in resolved cotton wool spots using high-resolution optical coherence tomography and optical coherence tomography ophthalmoscopy. *Ophthalmology.* (2007) 114:537–43. doi: 10.1016/j.ophtha.2006.06.054
11. van Dijk HW, Verbraak FD, Kok PH, Garvin MK, Sonka M, Lee K, et al. Decreased retinal ganglion cell layer thickness in patients with type 1 diabetes. *Invest Ophthalmol Vis Sci.* (2010) 51:3660–5. doi: 10.1167/iovs.09-5041
12. Sun JK, Lin MM, Lammer J, Prager S, Sarangi R, Silva PS, et al. Disorganization of the retinal inner layers as a predictor of visual acuity in eyes with center-involved diabetic macular edema. *JAMA Ophthalmol.* (2014) 132:1309–16. doi: 10.1001/jamaophthalmol.2014.2350
13. Marcos S, Werner JS, Burns SA, Merigan WH, Artal P, Atchison DA, et al. Vision science and adaptive optics, the state of the field. *Vision Res.* (2017) 132:3–33. doi: 10.1016/j.visres.2017.01.006
14. Burns SA, Elsner AE, Sapoznik KA, Warner RL, Gast TJ. Adaptive optics imaging of the human retina. *Prog Retin Eye Res.* (2019) 68:1–30. doi: 10.1016/j.preteyeres.2018.08.002
15. Hendrickson AE, Yuodelis C. The morphological development of the human fovea. *Ophthalmology.* (1984) 91:603–12. doi: 10.1016/S0161-6420(84)34247-6
16. Song H, Chui TY, Zhong Z, Elsner AE, Burns SA. Variation of cone photoreceptor packing density with retinal eccentricity and age. *Invest Ophthalmol Vis Sci.* (2011) 52:7376–84. doi: 10.1167/iovs.11-7199
17. Chui TY, Song H, Clark CA, Papay JA, Burns SA, Elsner AE. Cone photoreceptor packing density and the outer nuclear layer thickness in healthy subjects. *Invest Ophthalmol Vis Sci.* (2012) 53:3545–53. doi: 10.1167/iovs.11-8694
18. Elsner AE, Papay JA, Johnston KD, Sawides L, de Castro A, King BJ, et al. Cones in ageing and harsh environments: the neural economy hypothesis. *Ophthalmic Physiol Opt.* (2020) 40:88–116. doi: 10.1111/opo.12670
19. Elsner AE, Chui TY, Feng L, Song HX, Papay JA, Burns SA. Distribution differences of macular cones measured by AOSLO: variation in slope from fovea to periphery more pronounced than differences in total cones. *Vision Res.* (2017) 132:62–8. doi: 10.1016/j.visres.2016.06.015
20. Burns SA, Elsner AE, Chui TY, Vannasdale DAJr, Clark CA, Gast TJ, et al. *In vivo* adaptive optics microvascular imaging in diabetic patients without clinically severe diabetic retinopathy. *Biomed Opt Express.* (2014) 5:961–74. doi: 10.1364/BOE.5.000961
21. Burns SA, Elsner AE, Gast TJ. Imaging the retinal vasculature. *Annu Rev Vis Sci.* (2021) 7:129–53. doi: 10.1146/annurev-vision-093019-113719

22. King BJ, Sapoznik KA, Elsner AE, Gast TJ, Papay JA, Clark CA, et al. SD-OCT and adaptive optics imaging of outer retinal tubulation. *Optom Vis Sci.* (2017) 94:411–22. doi: 10.1097/OPX.0000000000001031
23. Chui TY, VanNasdale DA, Elsner AE, Burns SA. The association between the foveal avascular zone and retinal thickness. *Invest Ophthalmol Vis Sci.* (2014) 55:6870–7. doi: 10.1167/iovs.14-15446
24. Arthur E, Elsner AE, Sapoznik KA, Papay JA, Muller MS, Burns SA. Distances from capillaries to arterioles or venules measured using OCTA and AOSLO. *Invest Ophthalmol Vis Sci.* (2019) 60:1833–44. doi: 10.1167/iovs.18-25294
25. Tan W, Wright T, Rajendran D, Garcia-Sanchez Y, Finkelberg L, Kisilak M, et al. Cone-photoreceptor density in adolescents with type 1 diabetes. *Invest Ophthalmol Vis Sci.* (2015) 56:6339–43. doi: 10.1167/iovs.15-16817
26. Lombardo M, Parravano M, Lombardo G, Varano M, Boccassini B, Stirpe M, et al. Adaptive optics imaging of parafoveal cones in type 1 diabetes. *Retina.* (2014) 34:546–57. doi: 10.1097/IAE.0b013e3182a10850
27. Lombardo M, Parravano M, Serrao S, Ziccardi L, Giannini D, Lombardo G. Investigation of adaptive optics imaging biomarkers for detecting pathological changes of the cone mosaic in patients with type 1 diabetes mellitus. *PLoS ONE.* (2016) 11:e0151380. doi: 10.1371/journal.pone.0151380
28. Nesper PL, Scarinci F, Fawzi AA. Adaptive optics reveals photoreceptor abnormalities in diabetic macular ischemia. *PLoS ONE.* (2017) 12:e0169926. doi: 10.1371/journal.pone.0169926
29. Lammer J, Prager SG, Cheney MC, Ahmed A, Radwan SH, Burns SA, et al. Cone photoreceptor irregularity on adaptive optics scanning laser ophthalmoscopy correlates with severity of diabetic retinopathy and macular edema. *Invest Ophthalmol Vis Sci.* (2016) 57:6624–32. doi: 10.1167/iovs.16-19537
30. Forooghian F, Stetson PF, Meyer SA, Chew EY, Wong WT, Cukras C, et al. Relationship between photoreceptor outer segment length and visual acuity in diabetic macular edema. *Retina.* (2010) 30:63–70. doi: 10.1097/IAE.0b013e3181bd2c5a
31. Papay JA, Elsner AE. Quantifying frequency content in cross-sectional retinal scans of diabetics vs. controls. *PLoS ONE.* (2021) 16:e0253091. doi: 10.1371/journal.pone.0253091
32. Chui TY, Song H, Burns SA. Individual variations in human cone photoreceptor packing density: variations with refractive error. *Invest Ophthalmol Vis Sci.* (2008) 49:4679–87. doi: 10.1167/iovs.08-2135
33. Ferguson RD, Zhong Z, Hammer DX, Mujat M, Patel AH, Deng C, et al. Adaptive optics scanning laser ophthalmoscope with integrated wide-field retinal imaging and tracking. *J Opt Soc Am A Opt Image Sci Vis.* (2010) 27:A265–77. doi: 10.1364/JOSAA.27.00A265
34. de Castro A, Sawides L, Qi X, Burns SA. Adaptive optics retinal imaging with automatic detection of the pupil and its boundary in real time using Shack-Hartmann images. *Appl Opt.* (2017) 56:6748–54. doi: 10.1364/AO.56.006748
35. Huang G, Zhong Z, Zou W, Burns SA. Lucky averaging: quality improvement of adaptive optics scanning laser ophthalmoscope images. *Opt Lett.* (2011) 36:3786–8. doi: 10.1364/OL.36.003786
36. Li J, Liu T, Flynn OJ, Turriff A, Liu Z, Ullah E, et al. Persistent dark cones in oligocone trichromacy revealed by multimodal adaptive optics ophthalmoscopy. *Front Aging Neurosci.* (2021) 13:629214. doi: 10.3389/fnagi.2021.629214
37. Scarinci F, Picconi F, Virgili G, Giorno P, Di Renzo A, Varano M, et al. Single retinal layer evaluation in patients with Type 1dDiabetes with no or early Signs of diabetic retinopathy: The first hint of neurovascular crosstalk damage between neurons and capillaries? *Ophthalmologica.* (2017) 237:223–31. doi: 10.1159/000453551

Conflict of Interest: The authors declare that the research was conducted in the absence of any commercial or financial relationships that could be construed as a potential conflict of interest.

frontiers | Frontiers in Medicine

ORIGINAL RESEARCH
published: 15 April 2022
doi: 10.3389/fmed.2022.846738

Foveal Phase Retardation Correlates With Optically Measured Henle Fiber Layer Thickness

Phillip T. Yuhas[1]*, Marisa L. Ciamacca[1], Keith A. Ramsey[1], Danielle M. Mayne[1], Elizabeth A. Stern-Green[1], Matthew Ohr[2], Aaron Zimmerman[1], Andrew T. E. Hartwick[1] and Dean A. VanNasdale[1]

[1] College of Optometry, The Ohio State University, Columbus, OH, United States, [2] Department of Ophthalmology and Visual Sciences, College of Medicine, The Ohio State University, Columbus, OH, United States

This study quantified and compared phase retardation distribution in the central macula with the thickness of the Henle fiber layer (HFL). A scanning laser polarimeter (SLP) was used to acquire 20° × 40° macular-centered images, either with fixed corneal compensation or with variable corneal compensation, in two cohorts of clinically normal subjects ($N = 36$). Phase retardation maps from SLP imaging were used to generate a macular cross pattern (fixed compensation) or an annulus pattern (variable compensation) centered on the macula. Intensity profiles in the phase retardation maps were produced using annular regions of interest at eccentricities from 0.25° to 3°. Pixel intensity was averaged at each eccentricity, acting as a surrogate for macular phase retardation. Directional OCT images were acquired in the horizontal and vertical meridians in all subjects, allowing visualization of the HFL thickness. HFL thickness was manually segmented in each meridian and averaged. In both cohorts, phase retardation and HFL thickness were highly correlated in the central 3° assessed, providing further evidence that the source of the phase retardation signal in the central macula is dominated by the HFL and that the center of the macula on cross sectional imaging corresponds closely with the center of the macular cross on SLP imaging.

Keywords: Henle fiber layer, scanning laser polarimetry, directional optical coherence tomography, fovea, macula HFL thickness, phase retardation

Edited by:
Ann E. Elsner,
Indiana University, United States

Reviewed by:
Raffaele Nuzzi,
University of Turin, Italy
Hongxin Song,
Capital Medical University, China
Kaitlyn Sapoznik,
University of Houston, United States

***Correspondence:**
Phillip T. Yuhas
yuhas.10@osu.edu

Specialty section:
This article was submitted to
Ophthalmology,
a section of the journal
Frontiers in Medicine

Received: 31 December 2021
Accepted: 23 March 2022
Published: 15 April 2022

Citation:
Yuhas PT, Ciamacca ML, Ramsey KA, Mayne DM, Stern-Green EA, Ohr M, Zimmerman A, Hartwick ATE and VanNasdale DA (2022) Foveal Phase Retardation Correlates With Optically Measured Henle Fiber Layer Thickness. Front. Med. 9:846738.
doi: 10.3389/fmed.2022.846738

INTRODUCTION

The cone photoreceptors in the central macula have important roles in mediating high spatial acuity and color discrimination in the human visual system. The axons of these central photoreceptors can exceed 500 μm in length, which is considerably longer than the axons (∼20 μm) of photoreceptors located at greater eccentricities (1, 2). As another difference, central cone axons are oriented relatively perpendicular to light incident on the retina, and the lateral displacement of their axon terminals produces a foveal pit that is devoid of inner retinal neurons. These bundles of cone axons are the primary contributors to the Henle fiber layer (HFL) present in the macular region of the primate retina.

Using traditional clinical imaging modalities, the HFL is difficult to assess and quantify. Cross-sectional optical coherence tomography (OCT) imaging in its routine use poorly delineates the HFL (3, 4). The HFL appears as an optically indistinct/transparent section of the outer retina and is difficult to differentiate from the outer nuclear layer. As a result, the HFL and the outer nuclear layer are commonly combined and assessed as a single entity in OCT imaging studies (5, 6).

Alternative imaging methods, specifically directional OCT imaging (7), enables improved differentiation and visualization of the Henle fiber layer. By aligning the incident light with the HFL's primary scattering angle, the reflectivity and the optical contrast of the HFL, relative to the outer nuclear layer, is enhanced. Lateral displacement of the imaging beam across the pupil allows visualization of the HFL as a hyper-reflective layer in the OCT cross section. This technique is directionally dependent, as the offset position (nasal vs. temporal; superior vs. inferior) of the beam at the pupil determines the relative emphasis of the HFL appearance on the two sides (distal vs. proximal) of the OCT image (7). Directional OCT imaging provides a visible landmark of the anterior border of the HFL on the side of the offset and the posterior border on the contralateral side of the offset. Combining two images from opposite offset entry positions can be used to quantify the HFL thickness along a common meridian. This technique has been validated and has been shown to be accurate (8) and to be repeatable across imaging sessions and across graders with little variability (9).

Scanning laser polarimetry (SLP) is an additional technique capable of quantifying the HFL based on the birefringent properties of the microtubules contained in the macular cone axons (10). Phase retardation, or meridional differences in index of refraction, is an optical signature of the HFL and can be used to localize the fovea in normal (11) and in diseased eyes (12), track eye position (13, 14), and quantify changes associated with normal aging (15) and with ocular disease (10, 16).

A key feature in SLP imaging of the posterior pole is the macular cross, an interaction between the corneal polarization properties (17) and those of the radially oriented HFL. The polarization properties of the cornea need to be accounted for when analyzing macular birefringence. Early-generation SLP devices were equipped with a fixed corneal compensator. Although this compensator is not ideal in the assessment of the fovea, point-by-point quantification of pixel intensity can be used to measure the amplitude of phase retardation in the macular cross along a circular region of interest at different eccentricities. This characteristic pattern exhibits a maximum phase retardation occurring within the central 3° in normal subjects, with reduced amplitudes associated with normal aging (15) and in patients with non-exudative age-related macular degeneration (16). A variable corneal compensator on newer SLP devices is able to more fully account for corneal birefringence and produces an annular pattern of birefringence around the retina. However, foveal phase retardation measurements made with full corneal compensation are less fully characterized than those made with fixed corneal compensation. Both corneal compensation techniques, fixed and variable, are used in this study.

While it has long been speculated that the foveal phase retardation signal originates from the HFL, a comparison with HFL assessments from alternative imaging techniques could test the validity of this assumed relationship. This study will examine two optical properties associated with the HFL using directional OCT and SLP in order to assess the correlation between the HFL thickness and phase retardation distribution at eccentricities from 0° to 3°, centered on the fovea. It is hypothesized that HFL thickness from directional OCT will correlate closely with the phase retardation distribution from SLP.

METHODS

This cross-sectional study followed the tenets of the Declaration of Helsinki and was approved by the Institutional Review Board in Biomedical Sciences at the Ohio State University. Informed consent was obtained from all subjects before data collection.

Subjects

Two cohorts of healthy subjects were prospectively recruited from the Ohio State University. The first cohort comprised 11 adults (age range 25–54 years, 63% female). The second cohort comprised 25 healthy adults (age range 20–58 years, 52% female). All subjects received a dilated fundus examination within at least 1 year of participation and did not have a previous diagnosis of ocular disease. Spherical equivalent refractive error ranged between +2D and −8D for all participants.

Protocol and Instrumentation

All subjects attended a single study session where images of the retina were acquired using both SLP and OCT. Prior to imaging, subjects underwent pupil dilation either with 1% tropicamide or with a combination of 1% tropicamide and 2.5% phenylephrine to achieve maximal pupil dilation, which is needed to offset the imaging beam appropriately during directional OCT imaging.

Directional Optical Coherence Tomography Imaging and Processing

All study participants sat for directional OCT imaging. Cross sectional OCT images were acquired from both eyes using a Heidelberg Spectralis spectral domain OCT (Heidelberg Engineering, Heidelberg, Germany). Vertical and horizontal 30° cross sectional images centered on the fovea were acquired for each subject. To minimize noise, each cross section used for analysis was the composite average of 100 individual registered b-scans acquired using the Heidelberg TruTrack Active Eye Tracking. Images were acquired at the high-resolution setting, which collects 1,536 a-scans per b-scan. The nominal axial and lateral resolutions are 7 and 14 μm, respectively. During imaging, the compiling average of b-scans is shown while a live image is simultaneously displayed. The live image was used to ensure that the angular orientation of the retina remained constant throughout the collection of the 100 images used for each averaged cross section. Three cross sections were acquired in both the horizontal and vertical meridian, for a total of 6 images. One cross section was acquired by aligning the imaging beam to the optical axis passing through the center of the fovea, resulting in an image where retinal displacement is symmetric about the foveal center. Two additional images were acquired in each the horizontal and vertical meridians by offsetting the entrance of the imaging beam position by 3 mm on either side of the centered foveal optical axis position. Offsetting the entry position along a meridian enables visualization of the Henle fiber layer on the

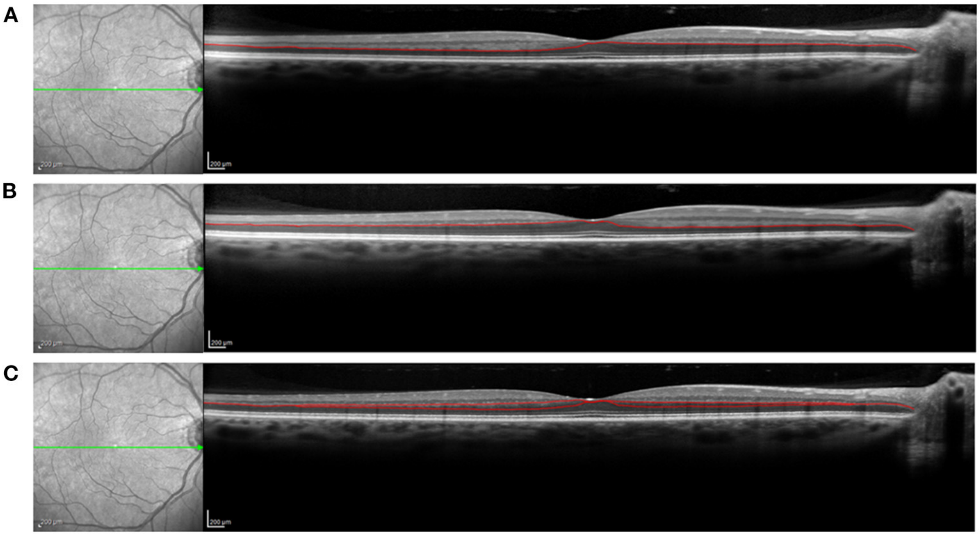

FIGURE 1 | OCT imaging of the Henle fiber layer (HFL). Offset of the entry position of the imaging beam though the pupil results in improved visualization of the HFL. The posterior border of the HFL is more clearly delineated on the distal side of the pupil offset, while the anterior border is more clearly delineated on the proximal side of the pupil offset. **(A)** Nasal offset of the imaging beam through the pupil, resulting in improved visualization of the posterior border of the temporal HFL and anterior border of the nasal HFL with manual segmentation line. **(B)** Temporal offset of the OCT imaging beam through the pupil, resulting in improved visualization of the posterior border of the nasal HFL and anterior border of the temporal HFL with manual segmentation line. **(C)** No offset of OCT imaging beam through the pupil, with poor delineation of the HFL. Segmentation lines from nasal and temporal offsets are included to demonstrate the HFL thickness profile along the horizontal meridian. The green arrows on the en face images represent the meridian of interest.

contralateral side of the offset, and minimizes visualization on the ipsilateral side (**Figures 1A,B**). The six collected images, all centered on the fovea, include a horizontal cross sectional image aligned with the foveal axis, a directional OCT cross section with a right lateral offset in the pupil, a directional OCT image with a left lateral offset in the pupil, a vertical cross sectional image aligned with the foveal axis, a directional OCT image with a superior offset in the pupil, and a directional OCT image with an inferior offset in the pupil.

Images from the right eye with a quality metric >20 dB were kept for analysis. The HFL was manually segmented from the cross sectional OCT images using Adobe Photoshop (Adobe, San Jose, CA). The posterior location of the Henle fiber layer on the distal side of each of the directional OCT images, and the anterior border was segmented on the proximal side. The anterior and posterior boundaries of each aligned directional OCT image were combined to generate the HFL thickness profile along that meridian (**Figure 1C**).

The foveal center was localized using the longest photoreceptor outer segment distance on the OCT cross sectional images in both the horizontal and vertical images. Custom MATLAB programming (Mathworks, Natick, MA) computed the thickness in pixels from the segmented HFL images centered on the foveal position, and Henle fiber layer thickness was measured for each of 4 meridians: temporal, superior, nasal, and inferior (**Figure 2A**). Because there is variability in the HFL thickness in different meridians (8), an average of the four meridians was calculated and used for analysis (**Figure 2B**). HFL thickness was then measured at 0.25° intervals from 0° to 3° eccentricity from the center of the fovea. Axial length was not measured as part of this study, which prevented the correction of lateral magnification. Instead, a conversation factor of 320 microns/degree was used to identify measurement locations on the OCT image. This approach is consistent with previous work that compared between OCT images and SLP images (18).

Scanning Laser Polarimetry Imaging and Processing

All subjects then sat for confocal SLP imaging using a GDx device (Laser Diagnostic Technologies, San Diego, CA). A 20° vertical × 40° horizontal macular-centered image was collected from both eyes of each subject using a raster scanning 780 nm polarized light source on the retina. The GDx instrument used to image the first cohort had a fixed birefringent element with a magnitude of 60 nm (single pass retardance) and a slow axis oriented at 15° nasally downward to compensate for corneal birefringence. Fixed compensation in this instrument does not result in complete corneal compensation, however, and results in a radial macular cross pattern (**Figure 3A**), instead of the annulus pattern expected to occur with full compensation (19). The second cohort was imaged with the same SLP device but utilized variable corneal compensation, which more fully corrects for corneal birefringence than fixed compensation. This approach reduces or eliminates the cross pattern in the macula that is characteristic of fixed compensation and allows for more direct annular assessment of the HFL (**Figure 3B**). Images were kept for analysis if the machine-generated quality score was ≥8, per the recommendation of the manufacturer.

The phase retardation maps of the right eye that include the macular cross (fixed corneal compensation) or annulus

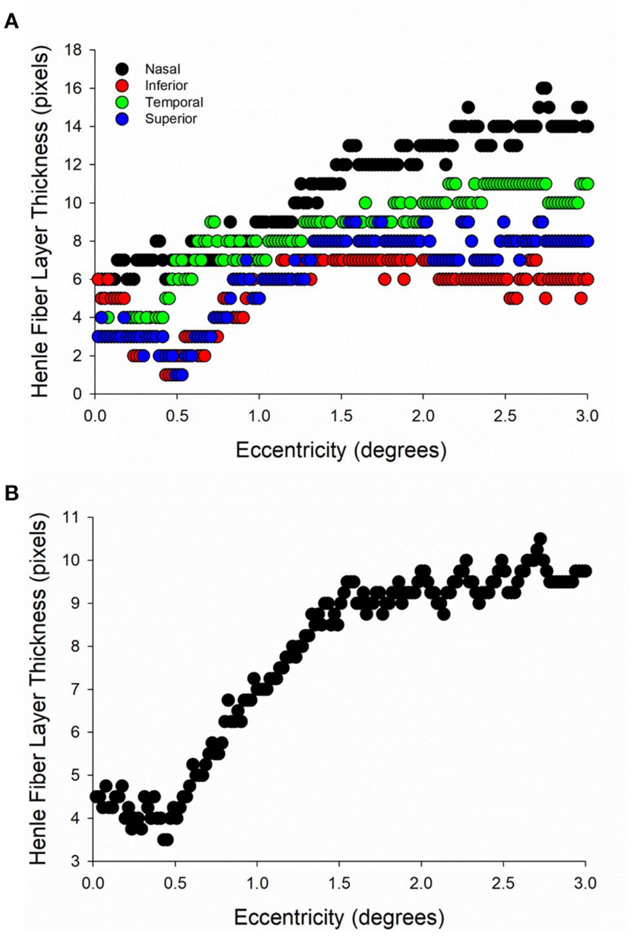

FIGURE 2 | Henle fiber layer (HFL) thickness distribution in a single subject from directional OCT imaging. **(A)** HFL thickness in each of the 4 meridians of interest. **(B)** HFL thickness averaged across the four meridians in the same subject.

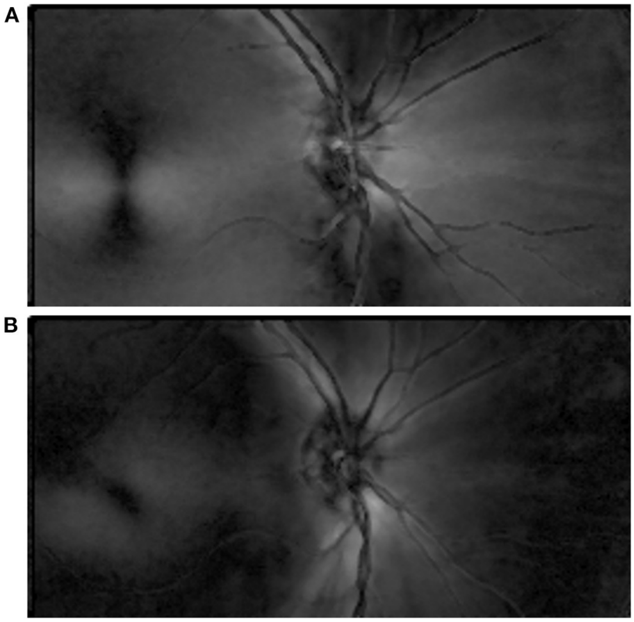

FIGURE 3 | Phase retardation distribution map in 20° × 40° scanning laser polarimetry image. **(A)** An image acquired from a subject in the first cohort included a fixed polarization element that partially compensated for corneal birefringence. Due to incomplete compensation, a characteristic macular cross pattern resulted, centered on the macula. **(B)** An image acquired from a subject in the second cohort included a variable polarization element that more fully accounted for corneal birefringence than a fixed-compensation setting. It manifested an annulus, centered on the macula.

(variable corneal compensation) were exported from the GDx and imported into MATLAB for pixel-intensity analysis. In summary, concentric rings at varying eccentricities from the fovea produced pixel intensity profile curves that exhibit either a sinusoidal pattern at double the frequency of the circular region of interest if imaged with fixed compensation (**Figures 4A,B**) or a linear pattern if imaged with variable compensation. For all images, pixel intensity was then averaged across all points contained within eccentric rings centered on the fovea from 0° to 3° (**Figure 4C**). The average pixel intensity represented the phase retardation signal across each eccentric ring.

Statistical Analysis

All statistical analyses were conducted with SigmaPlot 14.5 (Systat, Palo Alto, CA).

Comparison of Henle Fiber Layer Thickness

The thickness of the HFL across all eccentricities was compared between the first cohort and the second cohort. Since the data were not normally distributed, a Mann-Whitney Rank Sum Test ($\alpha = 0.05$) compared the thickness between the two cohorts.

Comparison of Pixel Intensity Amplitude

The pixel intensity measured by SLP across all eccentricities was compared between the first cohort (fixed corneal compensation) and the second cohort (variable corneal compensation). Since the data were not normally distributed, a Mann-Whitney Rank Sum Test ($\alpha = 0.05$) compared the intensity between the two cohorts.

Comparison of Pixel Intensity Variability

The variability of pixel intensity measurements made with the fixed-compensated SLP (first cohort) was compared to the variability of the pixel intensity measurements made with the variable-compensated SLP (second cohort). For both instruments, the coefficient of variation was measured at each eccentric ring, from 0° to 3° in 0.25° intervals. These values were then averaged for an overall measurement of variability for each cohort. A Mann-Whitney Rank Sum Test ($\alpha = 0.05$) compared the variability between the two cohorts.

Correlation Between Henle Fiber Layer Thickness and Pixel Intensity

For all subjects, the HFL thickness, as measured using directional OCT imaging, and pixel intensity, a representation of the phase retardation signal, as measured with SLP, were

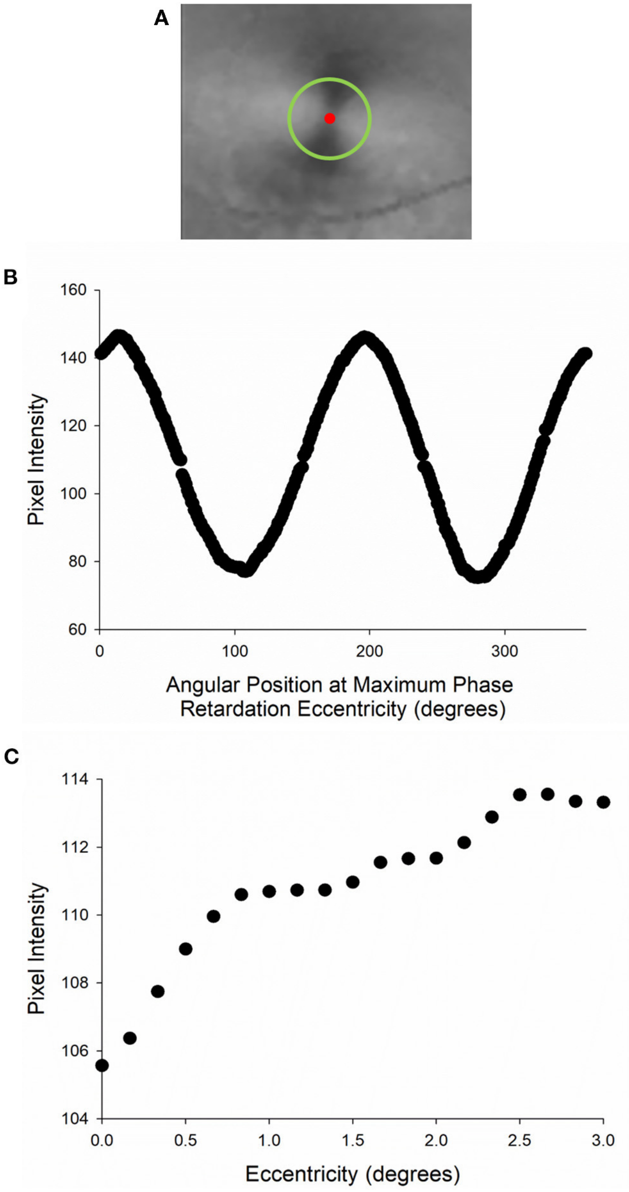

FIGURE 4 | Analysis of phase retardation distribution map. **(A)** Center of macular cross (red circle) with a circular region of interest (green circle). **(B)** Pixel intensity profile along the circular region of interest. **(C)** The amplitude of pixel intensity was used as a relative measure of phase retardation and plotted as a function of eccentricity.

plotted against each other at 0.25° intervals from 0° to 3° eccentricity (**Figure 5**). The correlation coefficients (R) for the association between the HFL thickness and pixel intensity at eccentricities between 0° and 3° in 0.25° increments were determined for each subject. Individual R values were then converted to z-values using Fisher-Z-Transformation. Z-values were then averaged within each cohort and transformed back to R-values to generate a representative R and R^2-values for the cohorts.

RESULTS

Henle Fiber Layer Thickness Measured by Directional Optical Coherence Tomography

Three subjects in the second cohort had at least one image with a quality score ≤20 dB (for representative image, see **Supplementary Figure 1**); these subjects were removed from analysis. For both the first cohort (**Figure 6A**) and for the second cohort (**Figure 6B**), the HFL thickness increased as the retinal eccentricity changed from 0° to 2° before decreasing at greater macular eccentricities. Across all eccentricities, the first cohort (median HFL thickness [25% quartile, 75% quartile] = 11.4 [8.55, 12.0] pixels) had a significantly ($n = 0.015$, Mann-Whitney Rank Sum Test) thicker measured HFL than the second cohort (8.33 [5.35, 8.83] pixels).

Pixel Intensity Measured by Scanning Laser Polarimetry

Signal Pattern and Inter-cohort Differences in Amplitude

All SLP scans had a quality score ≥8 and were therefore analyzed. For both the first cohort (fixed-compensated SLP; **Figure 7A**) and for the second cohort (variable-compensated SLP; **Figure 7B**), pixel intensity increased as the retinal eccentricity increased from 0 to 2 degrees before decreasing at greater retinal eccentricities. Across all eccentricities, pixel intensity generated by the fixed-compensated SLP (median pixel intensity [25% quartile, 75% quartile] = 66.1 [63.5, 67.3]) was significantly ($p < 0.001$, Mann-Whitney Rank Sum Test) higher than that generated by the variable-compensated SLP (46.4 [37.7, 48.5]).

Inter-cohort Variability

The first cohort (fixed-compensated SLP) and the second cohort (variable-compensated SLP) exhibited different magnitudes of variability. In both cohorts, the coefficients of variation near the center of the fovea were relatively large, and those at farther eccentricities were relatively small (**Table 1**). However, across all eccentricities, the first cohort exhibited significantly ($p < 0.001$, Mann-Whitney Rank Sum Test) more variability (median coefficient of variation [25% quartile, 75% quartile] = 31.5 [30.9, 34.1]) than the second cohort (12.4 [11.4, 17.9]).

Correlation Between Pixel Intensity and Henle Fiber Layer Thickness

There was a strong correlation between pixel intensity and HFL thickness in both cohorts. In the first cohort, the average R^2-value was 0.785 (range: 0.031–0.988; **Supplementary Figure 2**). **Figure 8A** contains a representation of this correlation, using mean values for pixel intensity and for HFL thickness at all eccentricities. In the second cohort, the average R^2-value was 0.872 (range: 0.043–0.974; **Supplementary Figure 3**). **Figure 8B** contains a representation of this correlation, using mean values for pixel intensity and for HFL thickness at all eccentricities. Combining subjects from the first and second cohorts, the overall R^2-value was 0.846.

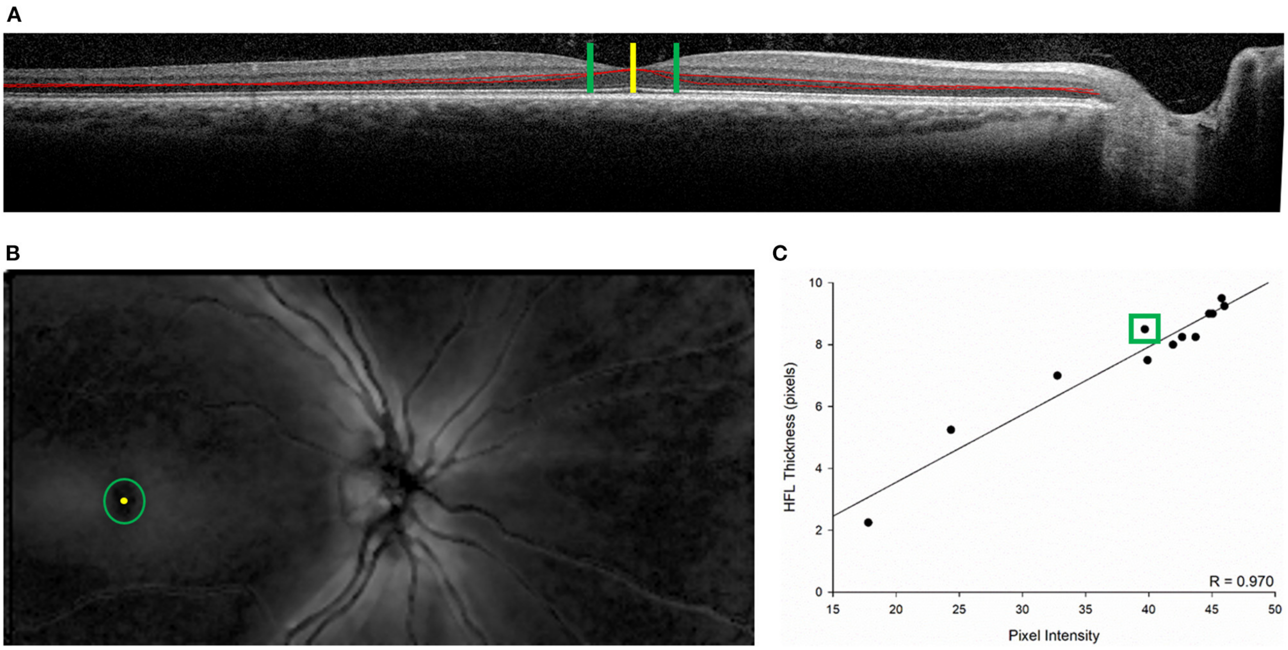

FIGURE 5 | Example of the association between Henle fiber layer (HFL) thickness and phase retardation in an individual subject from the second cohort. **(A)** Directional optical coherence tomography image along the horizontal axis with the HFL outlined in red. The yellow vertical bar represents the center of the fovea. The green vertical bars mark 1° of eccentricity (temporal on the left and nasal on the right) from the center of the fovea. **(B)** Scanning laser polarimetry image of the posterior pole. Bright regions within the image indicate high phase retardation caused by tissue birefringence. The yellow circle marks the center of the fovea. The green ring indicates 1° of eccentricity from the center of the fovea. **(C)** Regression plot showing the association between pixel intensity (a proxy for magnitude of phase retardation) and HFL thickness. The data point in the green box represents (i, y-axis) HFL thickness averaged from the superior, inferior, nasal (right green bar in **A**), and temporal (left green bar in **A**) meridians 1° from the central fovea and (ii, x-axis) phase pixel intensity averaged along an eccentric ring (green ring in **B**) 1° from the central fovea. The other data points represent the other eccentricities measured (0°-3° eccentricity in 0.25° steps from the center of the fovea).

DISCUSSION

This study used two clinically available imaging modalities, OCT and SLP, to establish a correlation between HFL thickness and phase retardation in the central macula. In two healthy cohorts, HFL thickness increased from to foveal center to 2° eccentricity, and then decreased beyond 2°. This result is consistent with previous reports from clinical (8) and from histological (5) studies on normal populations. Foveal pixel intensity—a representation of tissue birefringence, with high pixel intensity indicating high phase retardation—was also measured. Similar to the HFL thickness results, in both cohorts pixel intensity increased from the foveal center to 2° eccentricity, beyond which it receded. There was a strong correlation between HFL thickness and pixel intensity across the central 3° of the macula. The fixed-compensated SLP device (used on the first cohort) manifested more variability in its pixel intensity measurements than the variable-compensated SLP device (used on the second cohort).

Correlation Between Henle Fiber Layer Thickness and Phase Retardation

To the authors' knowledge, this is the first study to report a correlation between HFL thickness and phase retardation amplitude. This finding may be important for several reasons. It has long been assumed that phase retardation in the central macula is the result of the birefringent properties of the HFL (20), but delineation of the HFL boundaries and determination of its thickness are challenging due to its relative optical transparency. Adaptations of existing techniques, such as directional OCT, overcome this constraint and improve optical contrast of the HFL, allowing for improved quantification of its thickness. Here, it is shown that the thickness and phase retardation signals are both minimal centrally, increase proportionally with increasing eccentricity until reaching a maximum, and decline at greater eccentricities. Although this study does not establish causation, the strong correlation between phase retardation distribution and HFL thickness in the central macula provides supporting evidence that the macular phase retardation signal results primarily from the birefringent HFL in healthy, normal subjects.

These results may have considerable clinical implications. The closely matched HFL thickness distribution, centered on the fovea, and phase retardation distribution support previous assumptions that the center of the macular cross corresponds closely with the foveal center, which can be used for foveal localization in *en face* SLP imaging. The correlation between HFL thickness and phase retardation amplitude may also be an optical signature for density or for integrity changes to photoreceptor axons in the central macula. The source of the HFL signal from these two imaging techniques is thought to

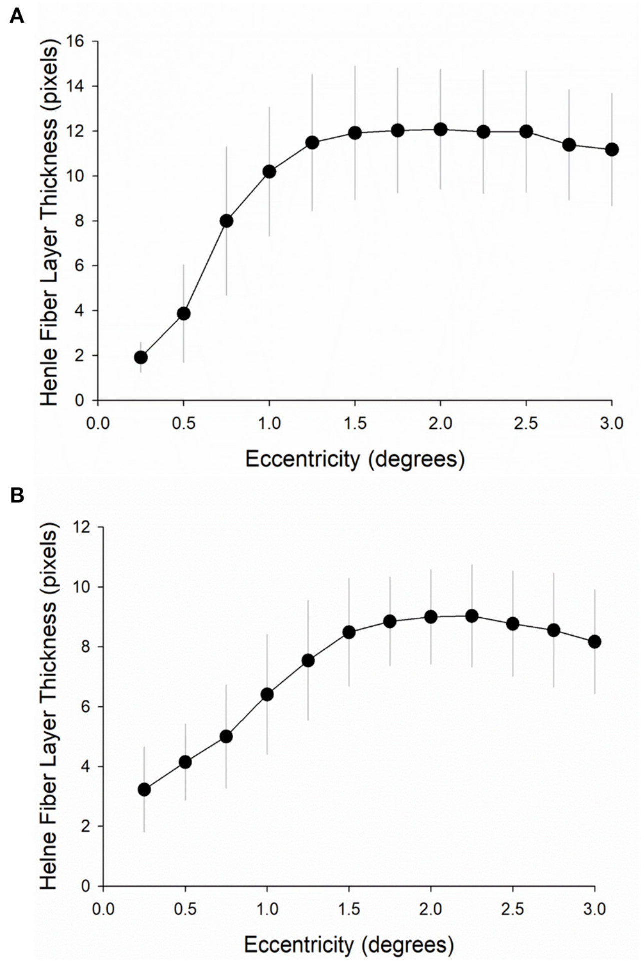

FIGURE 6 | Henle fiber layer thickness at increasing macular eccentricities. Henle fiber layer thickness was measured at 12 different macular eccentricities from 0° to 3° from the foveal center in 0.25° steps **(A)** in the first cohort (n = 11) and **(B)** in the second cohort (n = 22). Error bars are one standard deviation from the mean (circles).

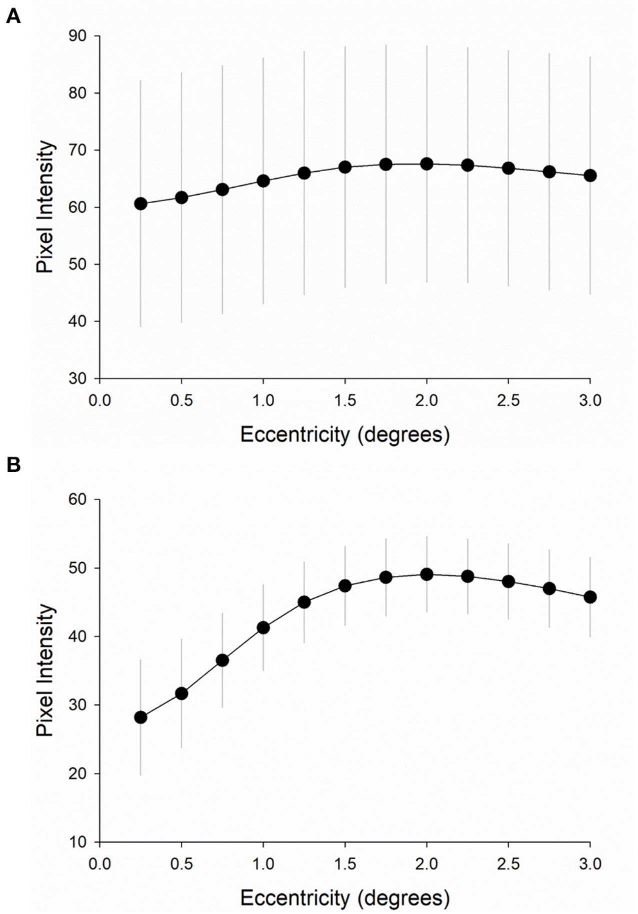

FIGURE 7 | Pixel intensity at increasing macular eccentricities. Pixel intensity was measured at 12 different macular eccentricities (from 0° to 3° from the foveal center in 0.25° steps) **(A)** in the first cohort (fixed-compensation scanning laser polarimetry, n = 11) and **(B)** in the second cohort (variable-compensated scanning laser polarimetry, n = 25). Error bars are one standard deviation from the mean (circles).

occur through different mechanisms. Directional OCT uses the angularly dependent scattering properties of the HFL to measure its thickness, and SLP relies on the birefringent properties of the microtubules in the HFL photoreceptor axons. Although directional OCT can be used to quantify HFL thickness, it likely cannot ascertain the components of and the integrity of structures within the HFL. Seemingly counterintuitive to the reduction in phase retardation in the central macula with normal aging (12), histological studies indicate the HFL thickens with age, while other cell layers simultaneously thin (5). This decrease in phase retardation is consistent with high resolution imaging (21) and with histological studies of photoreceptor density (22), indicating a gradual decrease in cone photoreceptor density associated with normal aging. Although they may seem mutually exclusive, it is possible for the HFL to thicken while foveal phase retardation wanes with age. This paradoxical relationship may represent the diversity of cells found in the HFL. Increased HFL thickness found in histological studies is not thought to be related to changes in cone photoreceptor density, but instead attributable to an increased volume of Muller cells, which are present in response to numerous acute and chronic insults as well as to normal aging stresses (5). While contributing to the increased thickness, Muller cells are not thought to possess the same birefringent properties as the photoreceptor axons in the HFL, and are therefore unlikely to contribute to the phase retardation signal in SLP imaging. The thickening of the HFL with reduced phase retardation may occur as a result of declining photoreceptor density or reduced viability of those photoreceptors, making phase retardation a sensitive marker for subtle aging changes.

Beyond aging, the combined use of retinal layer thickness with phase retardation in birefringent retinal structures shows promise in providing insight into early neurodegenerative

TABLE 1 | Variability of pixel intensity at increasing macular eccentricities.

Eccentricity (degrees)	First cohort ($n = 11$)	Second cohort ($n = 25$)
0.25	35.5	29.8
0.50	35.4	25.0
0.75	34.4	18.8
1.00	33.3	15.2
1.25	32.3	13.1
1.50	31.5	12.1
1.75	30.9	11.6
2.00	30.6	11.2
2.25	30.5	11.1
2.50	30.8	11.4
2.75	31.3	12.0
3.00	31.6	12.6

Values are coefficients of variation. Phase retardation was measured with a scanning laser polarimeter with a fixed corneal compensator in the first cohort and with a variable corneal compensator in the second cohort.

changes in sight-threatening disease. Examples of the sensitivity of polarization sensitive biomarkers is shown in primate models of glaucoma, where a decrease in the phase retardation of the nerve fiber layer (NFL) precedes thickness changes of the NFL on OCT (23). Histological examination of the NFL in these animals demonstrates residual axonal structure, but in a highly degenerated state. This degeneration results in reduced birefringence, even though the degenerated structures initially occupy the same volume in the retina and NFL thickness is not affected by early degenerative changes. Because the phase retardation signal in both the HFL and the NFL is believed to originate from microtubules in cell axons (10, 24), extrapolating from this animal model suggests that retinal layer thickness and phase retardation could be used similarly for early detection of retinal axonal compromise in the central macula. Identification of retinal cell compromise would be useful in instances where loss of axons or axonal integrity of the central cone and HFL could precede retinal layer thickness changes or when OCT changes are seemingly inconsistent with functional loss, such as Alzheimer's disease (25) and traumatic brain injury (26).

Variability in Measurements of the Henle Fiber Layer

Scanning Laser Polarimetry

Two corneal compensation settings within the same device were used to measure phase retardation of the central macula. As a result, the performance of the two settings could be compared. A fixed compensator was used on the first cohort. This setting can only partially compensate for the polarization properties of the cornea when acquiring retinal images. A variable compensator was used on the second cohort. This setting can more fully compensates for the polarization properties of the cornea compared to the fixed-compensation. Although the two cohorts contained healthy subjects with similar demographic characteristics, the images acquired using fixed anterior segment compensation exhibited significantly greater average pixel intensity and significantly more variability across individuals at all eccentricities than the images acquired using the variable anterior segment compensation. These differences were expected and are likely the result of residual uncompensated anterior segment birefringence, which can vary considerably across individuals. The variable compensator used on the second cohort produced an annular phase retardation map centered on the fovea. Although the overall average pixel intensity was lower at all eccentricities, compared to the fix compensator, there was less variability across individuals. Both in the first cohort and in the second cohort, variability was greatest at the center of the macula and then tapered in the periphery. This relatively high variability near the central macula was likely due to the relatively weak phase retardation signal at that location, where the HFL is absent or very thin. These findings suggest that variable-compensated SLP should be the preferred technique over fixed-compensated SLP for clinical care and for research.

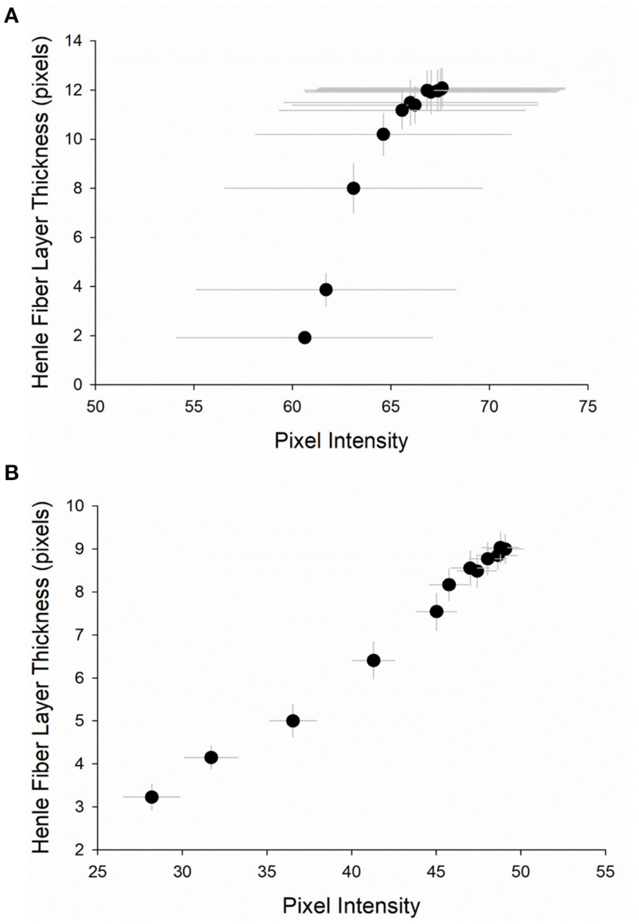

FIGURE 8 | Representation of the relationship between pixel intensity and Henle fiber layer thickness **(A)** in the first cohort ($n = 11$) and **(B)** in the second cohort ($n = 22$). Circles are the mean at each of the 12 eccentricities, from 0° to 3° (0.25° steps) in the central macula. Vertical and horizontal error bars are the standard error of the mean.

Despite the difference in variability between the two corneal compensation settings, both generated foveal phase retardation maps that were strongly associated with HFL thickness, which was measured with directional OCT. This fact strengthens the validity of our results, and it also may make our results more generalizable.

An enhanced corneal-compensator is available for SLP as a software upgrade that optimizes imaging by improving the signal-to-noise ratio compared with the variable compensation, alone. Although there is some evidence that enhanced compensator correlates well to other imaging modalities (27) and may be more sensitive to changes in the NFL than other compensation strategies (28), it was not utilized in the present study. Future work could correlate its performance with HFL thickness.

Directional Optical Coherence Tomography

Even though the HFL thickness profiles of the two groups shared a similar shape, the first cohort exhibited a significantly thicker HFL than the second cohort. Also, there was a wide range of R^2-values in both groups when correlating HFL thickness to pixel intensity. Image quality is a possible cause of the variability between cohorts and of the large range of correlation coefficients. Directional OCT data from three subjects in the second cohort were removed from analysis due to poor image quality metrics. Images from several of the remaining subjects did not cross the threshold for removal from the study but were nevertheless not of ideal quality because the imaging beam of the OCT was not offset enough in the pupil to clearly delineate the HFL from surrounding tissues. Manually segmenting the HFL on a poor-quality OCT images, even those with sufficiently high decibel quality indicators, likely leads to variable thickness measurements, even for well-trained and experienced researchers, because the boarders of the HFL are less defined than in high-quality images.

There are several possible explanations for this difference in subjective image quality. First, the second cohort was larger than the first and contained individuals with small pupils (even after dilation) and deep-set globes. These physical attributes made obtaining high-quality offset OCT images a challenge in some cases. Second, there were different operators of the OCT instrument for the two cohorts, which likely contributed to differences between the two cohorts in how much the imaging beam was offset in the pupil. A third possible explanation is that different individuals segmented the HFL for each cohort. The effect of this variable may be small, however, because previous work has shown manual segmentation of the HFL to be highly repeatable (9).

The development of quality-control software that indicates to the OCT operator when the HFL is of sufficient quality would help eliminate the issue of a poorly delineated HFL in an otherwise high-decibel image. In addition, the creation of software to segment the HFL would likely help mollify the problem of directional OCT being very sensitive to image quality.

Study Limitations

Scanning Laser Polarimetry

A limitation to SLP imaging is that light returning to the system comes from the entire depth of the retina and cannot be axially segmented. While this constraint does not pose a problem for producing a macular cross pattern or a macular annulus pattern in normal individuals, phase retardation changes associated with pathology (29, 30) are difficult to differentiate from overlying or adjacent retina. The combined use of polarized light and cross sectional imaging in polarization sensitive OCT (PS-OCT) can overcome some of these limitations for quantifying HFL phase retardation (31–33), but these systems are expensive, require considerable technical expertise, and are not widely available outside of research institutions.

Directional Optical Coherence Tomography

Although directional OCT can visualize the HFL in cross section, it has limitations that currently curb its clinical utility. First the ability, or lack thereof, to quickly and easily collect HFL thickness measurements in multiple meridians. HFL visualization is ideal when the entry position of the imaging beam is along the retinal axis of interest; therefore, imaging in multiple meridians requires technical skill and at least two images, one from each opposite offset positions, along a common meridian. This constraint limited the measurements made in this study to the horizontal and vertical meridians and forced the use of average thicknesses across these meridians as a representative sample of the central macula.

Second, there is no normative database available for HFL thickness. This study represents an initial step in assessing the fovea for changes that could cause alterations to the integrity of the HFL without necessarily impacting the HFL thickness. The full potential of this approach cannot be realized, however, until normative databases of HFL thickness and phase retardation are established.

CONCLUSION

This study established a strong and positive association between HFL thickness and phase retardation amplitude in the central macula. It also demonstrated that fixed-compensated SLP produces more varied pixel intensity signals than variable-compensated SLP. With future refinements, the combined use of directional OCT and SLP or other polarization-sensitive imaging methods may be able to detect early changes to photoreceptor integrity in the central macula as a harbinger to ocular or to neurological disease.

DATA AVAILABILITY STATEMENT

The raw data supporting the conclusions of this article will be made available by the authors, without undue reservation.

ETHICS STATEMENT

The studies involving human participants were reviewed and approved by the Institutional Review Board in Biomedical

Sciences at the Ohio State University. The patients/participants provided their written informed consent to participate in this study.

AUTHOR CONTRIBUTIONS

PY: study design, data collection, data processing, data analysis, and manuscript writing. MC: study design, data collection, data analysis, and manuscript writing. KR: data collection, data processing, and manuscript writing. DM and ES-G: data collection, data processing, and manuscript review. MO, AZ, and AH: study design and manuscript writing. DV: research question, study design, data processing, data analysis, and manuscript writing. All authors contributed to the article and approved the submitted version.

FUNDING

This study was provided by NEI T35 EY007151, by a Career Development Award from the American Academy of Optometry (DV), and by a Lois Hagelberger Huebner Young Investigator Award from the Ohio Lions Eye Research Foundation (PY). PY also received financial support from NEI L30 EY024749 during the study.

ACKNOWLEDGMENTS

Aspects of this work first appeared in the master's thesis of MC (34). Thank you to Erica Shelton, to Elizabeth Day, and to Kelly Klimo for assistance with data collection and to Catherine McDaniel for help with subject recruitment.

SUPPLEMENTARY MATERIAL

The Supplementary Material for this article can be found online at: https://www.frontiersin.org/articles/10.3389/fmed.2022.846738/full#supplementary-material

REFERENCES

1. Hsu A, Tsukamoto Y, Smith RG, Sterling P. Functional architecture of primate cone and rod axons. *Vision Res.* (1998) 38:2539–49. doi: 10.1016/s0042-6989(97)00370-2
2. Drasdo N, Millican CL, Katholi CR, Curcio CA. The length of Henle fibers in the human retina and a model of ganglion receptive field density in the visual field. *Vision Res.* (2007) 47:2901–11. doi: 10.1016/j.visres.2007.01.007
3. Otani T, Yamaguchi Y, Kishi S. Improved visualization of Henle fiber layer by changing the measurement beam angle on optical coherence tomography. *Retina.* (2011) 31:497–501. doi: 10.1097/IAE.0b013e3181ed8dae
4. Ouyang Y, Walsh AC, Keane PA, Heussen FM, Pappuru RK, Sadda SR. Different phenotypes of the appearance of the outer plexiform layer on optical coherence tomography. *Graefes Arch Clin Exp Ophthalmol.* (2013) 251:2311–7. doi: 10.1007/s00417-013-2308-5
5. Curcio CA, Messinger JD, Sloan KR, Mitra A, McGwin G, Spaide RF. Human chorioretinal layer thicknesses measured in macula-wide, high-resolution histologic sections. *Invest Ophthalmol Vis Sci.* (2011) 52:3943–54. doi: 10.1167/iovs.10-6377
6. Chui TY, Song H, Clark CA, Papay JA, Burns SA, Elsner AE. Cone photoreceptor packing density and the outer nuclear layer thickness in healthy subjects. *Invest Ophthalmol Vis Sci.* (2012) 53:3545–53. doi: 10.1167/iovs.11-8694
7. Lujan BJ, Roorda A, Knighton RW, Carroll J. Revealing Henle's fiber layer using spectral domain optical coherence tomography. *Invest Ophthalmol Vis Sci.* (2011) 52:1486–92. doi: 10.1167/iovs.10-5946
8. Lujan BJ, Roorda A, Croskrey JA, Dubis AM, Cooper RF, Bayabo JK, et al. Directional optical coherence tomography provides accurate outer nuclear layer and Henle fiber layer measurements. *Retina.* (2015) 35:1511–20. doi: 10.1097/IAE.0000000000000527
9. Tong KK, Lujan BJ, Zhou Y, Lin MC. Directional optical coherence tomography reveals reliable outer nuclear layer measurements. *Optom Vis Sci.* (2016) 93:714–9. doi: 10.1097/OPX.0000000000000861
10. Elsner AE, Weber A, Cheney MC, Vannasdale DA. Spatial distribution of macular birefringence associated with the Henle fibers. *Vision Res.* (2008) 48:2578–85. doi: 10.1016/j.visres.2008.04.031
11. VanNasdale DA, Elsner AE, Weber A, Miura M, Haggerty BP. Determination of foveal location using scanning laser polarimetry. *J Vis.* (2009) 9:21–17. doi: 10.1167/9.3.21
12. VanNasdale DA, Elsner AE, Kohne KD, Peabody TD, Malinovsky VE, Haggerty BP, et al. Foveal localization in non-exudative AMD using scanning laser polarimetry. *Optom Vis Sci.* (2012) 89:667–77. doi: 10.1097/OPX.0b013e31824eeb25
13. Gramatikov BI, Zalloum OH, Wu YK, Hunter DG, Guyton DL. Birefringence-based eye fixation monitor with no moving parts. *J Biomed Opt.* (2006) 11:34025. doi: 10.1117/1.2209003
14. Gramatikov BI, Zalloum OH, Wu YK, Hunter DG, Guyton DL. Directional eye fixation sensor using birefringence-based foveal detection. *Appl Opt.* (2007) 46:1809–18. doi: 10.1364/ao.46.001809
15. VanNasdale DA, Elsner AE, Hobbs T, Burns SA. Foveal phase retardation changes associated with normal aging. *Vision Res.* (2011) 51:2263–72. doi: 10.1016/j.visres.2011.08.017
16. VanNasdale DA, Elsner AE, Peabody TD, Kohne KD, Malinovsky VE, Haggerty BP, et al. Henle fiber layer phase retardation changes associated with age-related macular degeneration. *Invest Ophthalmol Vis Sci.* (2014) 56:284–90. doi: 10.1167/iovs.14-14459
17. Knighton RW, Huang XR. Linear birefringence of the central human cornea. *Invest Ophthalmol Vis Sci.* (2002) 43:82–6.
18. VanNasdale DA, Elsner AE, Malinovsky VE, Peabody TD, Kohne KD, Haggerty BP, et al. Polarization variability in age-related macular degeneration. *Optom Vis Sci.* (2018) 95:277–91. doi: 10.1097/OPX.0000000000001197
19. Zhou Q, Weinreb RN. Individualized compensation of anterior segment birefringence during scanning laser polarimetry. *Invest Ophthalmol Vis Sci.* (2002) 43:2221–8.
20. Brink HB, van Blokland GJ. Birefringence of the human foveal area assessed *in vivo* with Mueller-matrix ellipsometry. *J Opt Soc Am A.* (1988) 5:49–57. doi: 10.1364/JOSAA.5.000049
21. Song H, Chui TY, Zhong Z, Elsner AE, Burns SA. Variation of cone photoreceptor packing density with retinal eccentricity and age. *Invest Ophthalmol Vis Sci.* (2011) 52:7376–84. doi: 10.1167/iovs.11-7199
22. Panda-Jonas S, Jonas JB, Jakobczyk-Zmija M. Retinal photoreceptor density decreases with age. *Ophthalmology.* (1995) 102:1853–9. doi: 10.1016/s0161-6420(95)30784-1
23. Fortune B, Burgoyne CF, Cull G, Reynaud J, Wang L. Onset and progression of peripapillary retinal nerve fiber layer (RNFL) retardance changes occur earlier than RNFL thickness changes in experimental glaucoma. *Invest Ophthalmol Vis Sci.* (2013) 54:5653–61. doi: 10.1167/iovs.13-12219

24. Huang XR, Knighton RW. Linear birefringence of the retinal nerve fiber layer measured *in vitro* with a multispectral imaging micropolarimeter. *J Biomed Opt.* (2002) 7:199–204. doi: 10.1117/1.1463050
25. Zhang J, Gao F, Ma Y, Xue T, Shen Y. Identification of early-onset photoreceptor degeneration in transgenic mouse models of Alzheimer's disease. *iScience.* (2021) 24:103327. doi: 10.1016/j.isci.2021.103327
26. Braza ME, Young J, Hammeke TA, Robison SE, Han DP, Warren CC, et al. Assessing photoreceptor structure in patients with traumatic head injury. *BMJ Open Ophthalmol.* (2018) 3:e000104. doi: 10.1136/bmjophth-2017-000104
27. Bertuzzi F, Benatti E, Esempio G, Rulli E, Miglior S. Evaluation of retinal nerve fiber layer thickness measurements for glaucoma detection: GDx ECC versus spectral-domain OCT. *J Glaucoma.* (2014) 23:232–9. doi: 10.1097/IJG.0b013e3182741afc
28. Milano G, Lombardo S, Bossolesi L, Bordin M, Raimondi M, Lanteri S, et al. Gdx-vcc Vs Gdx-ecc In Glaucoma Diagnosis. *Invest Ophthalmol Vis Sci.* (2011) 52:208.
29. Elsner AE, Weber A, Cheney MC, VanNasdale DA, Miura M. Imaging polarimetry in patients with neovascular age-related macular degeneration. *J Opt Soc Am A Opt Image Sci Vis.* (2007) 24:1468–80. doi: 10.1364/josaa.24.001468
30. Weber A, Elsner AE, Miura M, Kompa S, Cheney MC. Relationship between foveal birefringence and visual acuity in neovascular age-related macular degeneration. *Eye.* (2007) 21:353–61. doi: 10.1038/sj.eye.6702203
31. Pircher M, Gotzinger E, Leitgeb R, Sattmann H, Findl O, Hitzenberger C. Imaging of polarization properties of human retina *in vivo* with phase resolved transversal PS-OCT. *Opt Express.* (2004) 12:5940–51. doi: 10.1364/opex.12.005940
32. Pircher M, Gotzinger E, Findl O, Michels S, Geitzenauer W, Leydolt C, et al. Human macula investigated *in vivo* with polarization-sensitive optical coherence tomography. *Invest Ophthalmol Vis Sci.* (2006) 47:5487–94. doi: 10.1167/iovs.05-1589
33. Cense B, Wang Q, Lee S, Zhao L, Elsner AE, Hitzenberger CK, et al. Henle fiber layer phase retardation measured with polarization-sensitive optical coherence tomography. *Biomed Opt Express.* (2013) 4:2296–306. doi: 10.1364/BOE.4.002296
34. Ciamacca ML, VanNasdale DA. *Foveal phase retardation correlation with Henle fiber layer thickness* (OhioLINK Electronic Theses and Dissertations Center). Columbus, OH: The Ohio State University College of Optometry (2017).

Conflict of Interest: The authors declare that the research was conducted in the absence of any commercial or financial relationships that could be construed as a potential conflict of interest.

frontiers | Frontiers in Aging Neuroscience

ORIGINAL RESEARCH
published: 02 May 2022
doi: 10.3389/fnagi.2022.765966

Inverse Problem Reveals Conditions for Characteristic Retinal Degeneration Patterns in Retinitis Pigmentosa Under the Trophic Factor Hypothesis

*Paul A. Roberts**

Baden Lab, Centre for Sensory Neuroscience and Computation, School of Life Sciences, University of Sussex, Brighton, United Kingdom

Retinitis pigmentosa (RP) is the most common inherited retinal dystrophy with a prevalence of about 1 in 4,000, affecting approximately 1.5 million people worldwide. Patients with RP experience progressive visual field loss as the retina degenerates, destroying light-sensitive photoreceptor cells (rods and cones), with rods affected earlier and more severely than cones. Spatio-temporal patterns of retinal degeneration in human RP have been well characterised; however, the mechanism(s) giving rise to these patterns have not been conclusively determined. One such mechanism, which has received a wealth of experimental support, is described by the trophic factor hypothesis. This hypothesis suggests that rods produce a trophic factor necessary for cone survival; the loss of rods depletes this factor, leading to cone degeneration. In this article, we formulate a partial differential equation mathematical model of RP in one spatial dimension, spanning the region between the retinal centre (fovea) and the retinal edge (ora serrata). Using this model we derive and solve an inverse problem, revealing for the first time experimentally testable conditions under which the trophic factor mechanism will qualitatively recapitulate the spatio-temporal patterns of retinal regeneration observed in human RP.

Keywords: partial differential equations, asymptotic analysis, retina, photoreceptors, rod-derived cone viability factor

Edited by:
Adam M. Dubis,
University College London,
United Kingdom

Reviewed by:
Filip Van Den Broeck,
Ghent University, Belgium
Moussa A. Zouache,
The University of Utah, United States
Robert Linsenmeier,
Northwestern University, United States

****Correspondence:***
Paul A. Roberts
p.a.roberts@univ.oxon.org

Specialty section:
This article was submitted to
Neurocognitive Aging and Behavior,
a section of the journal
Frontiers in Aging Neuroscience

Received: *27 August 2021*
Accepted: *21 March 2022*
Published: *02 May 2022*

Citation:
Roberts PA (2022) Inverse Problem Reveals Conditions for Characteristic Retinal Degeneration Patterns in Retinitis Pigmentosa Under the Trophic Factor Hypothesis.
Front. Aging Neurosci. 14:765966.
doi: 10.3389/fnagi.2022.765966

1. INTRODUCTION

The group of inherited retinal diseases known as retinitis pigmentosa (RP) causes the progressive loss of visual function (Hamel, 2006; Hartong et al., 2006). The patterns of visual field loss associated with the human version of this condition have been well characterised (Grover et al., 1998); however, the mechanisms underpinning these patterns have yet to be conclusively determined (Newton and Megaw, 2020). In this article, we use mathematical models to predict the conditions under which a trophic factor mechanism could explain these patterns.

The retina is a tissue layer lining the back of the eye containing light-sensitive cells known as photoreceptors, which come in two varieties: rods and cones (**Figure 1A**). Rods confer monochromatic vision under low-light (scotopic) conditions, while cones confer colour vision under well-lit (photopic) conditions (Oyster, 1999). In RP, rod function and health are typically affected earlier and more severely than those of cones, with cone loss following rod loss. Rods are lost since either they or the neighbouring retinal pigment epithelium express a mutant version of one or both alleles (depending on inheritance mode) of a gene associated with RP (over 80 genes have been identified to date, see Gene Vision and Ge et al., 2015; Haer-Wigman et al., 2017; Birtel et al., 2018; Coussa et al., 2019). It is hypothesised that cones are lost following rods since they depend upon rods either directly or indirectly for their survival (Hamel, 2006; Hartong et al., 2006; Daiger et al., 2007).

A number of mechanisms have been hypothesised to explain secondary cone loss, including trophic factor (TF) depletion (Léveillard et al., 2004; Aït-Ali et al., 2015; Mei et al., 2016), oxygen toxicity (Travis et al., 1991; Valter et al., 1998; Stone et al., 1999), metabolic dysregulation (Punzo et al., 2009, 2012), toxic substances (Ripps, 2002), and microglia (Gupta et al., 2003). While not typically related to spatio-temporal patterns of retinal degeneration in the literature, it is reasonable to infer that these mechanisms play an important role in determining spatio-temporal patterns of retinal degeneration.

Grover et al. (1998) have classified the spatio-temporal patterns of visual field loss in RP patients into three patterns and six sub-patterns (see **Figure 2**). Pattern 1A consists in a restriction of the peripheral visual field, while Pattern 1B also includes a para-/peri-foveal ring scotoma (blind spot); Pattern 2 (A, B and C) involves an initial loss of the superior visual field, winding nasally or temporally into the inferior visual field; lastly, Pattern 3 starts with loss of the mid-peripheral visual field, before spreading into the superior or inferior visual field and winding around the far-periphery. In all cases central vision is the best preserved, though it too is eventually lost (Hamel, 2006; Hartong et al., 2006). Patterns of visual field loss and photoreceptor degeneration (cell loss) are directly related (Escher et al., 2012), loss of the superior visual field corresponding to degeneration of photoreceptors in the inferior retina and *vice versa*, and loss of the temporal visual field corresponding to degeneration of photoreceptors in the nasal retina and *vice versa*.

In this article, we explore the conditions under which the TF mechanism, in isolation, can replicate the patterns of cone degeneration observed *in vivo*. Isolating a mechanism in this way enables us to identify the effects for which it is sufficient to account, avoiding confusion with other mechanistic causes. Understanding the mechanisms of secondary cone degeneration is important since it is the cones that provide high-acuity color vision, and hence their loss, rather than the preceding rod loss, which is the most debilitating. Therefore, by elucidating these mechanisms, we can develop targeted therapies to prevent or delay cone loss, preserving visual function. The TF mechanism has been studied in detail. Rod photoreceptors have been shown to produce a TF called rod-derived cone viability factor (RdCVF), which is necessary for cone survival (Mohand-Saïd et al., 1997, 1998, 2000; Fintz et al., 2003; Léveillard et al., 2004; Yang et al., 2009). RdCVF increases cone glucose uptake, and hence aerobic glycolysis, by binding to the cone transmembrane protein Basigin-1, which consequently binds to the glucose transporter GLUT1 (Aït-Ali et al., 2015). Cones do not produce RdCVF, thus, when rods are lost, RdCVF concentration drops and cone degeneration follows (though it has been suggested that it may ultimately be oxygen toxicity which kills cones; Léveillard and Sahel, 2017).

Thus far, two groups have developed mathematical models operating under the TF hypothesis. Camacho *et al.* have developed a series of (non-spatial) dynamical systems ordinary differential equation models to describe the role of RdCVF in health and RP (Colón Vélez et al., 2003; Camacho et al., 2010, 2014, 2016a,b,c, 2019, 2020, 2021; Camacho and Wirkus, 2013; Wifvat et al., 2021). In Roberts (2022), we developed the first partial differential equation (PDE) models of the TF mechanism in RP, predicting the spatial spread of retinal degeneration. It was found that, assuming all cones are equally susceptible to RdCVF deprivation and that rods degenerate exponentially with a fixed decay rate, the mechanism is unable to replicate *in vivo* patterns of retinal degeneration. Previous modeling studies have also considered the oxygen toxicity (Roberts et al., 2017, 2018 and related Roberts et al., 2016b) and toxic substance (Burns et al., 2002) mechanisms, predicting the spatio-temporal patterns of retinal degeneration they would generate. For a review of these and other mathematical models of the retina in health, development and disease see (Roberts et al., 2016a).

In this study, we extend our work in Roberts (2022) by formulating and solving an inverse problem to determine the spatially heterogeneous cone susceptibility to RdCVF deprivation and rod exponential decay rate profiles that are required to qualitatively recapitulate observed patterns of spatio-temporal degeneration in human RP.

2. MATERIALS AND METHODS

2.1. Model Formulation

We begin by formulating a reaction-diffusion PDE mathematical model (a simplified version of the model presented in Roberts, 2022). Reaction-diffusion PDE models describe the way in which the spatial distribution of cells and chemicals change over time as a result of processes such as movement (diffusion), production, consumption, death, and decay. We pose the model on a spherical geometry to replicate that of the human retina. This geometry is most naturally represented using a spherical polar coordinate system, (r,θ,ϕ), centred in the middle of the vitreous body, where $r \geq 0$ (m) is the distance from the origin, $0 \leq \theta \leq \pi$ (rad) is the polar angle and $0 \leq \phi < 2\pi$ (rad) is the azimuthal angle. To create a more mathematically tractable model, we simplify the geometry by assuming symmetry about the z-axis (directed outward from the origin through the foveal centre), eliminating variation in the azimuthal direction, and effectively depth-average through the retina, assuming that it lies at a single fixed distance, $R > 0$ (m), from the origin at all eccentricities, θ, leveraging the fact that the retinal width is two orders of magnitude smaller than the eye's radius (Oyster, 1999). Thus, we have reduced the coordinate system to (R,θ), where R is a positive constant parameter and $0 \leq \theta \leq \Theta$ is an independent variable, which we bound to range between the fovea (at $\theta = 0$ rad) and the ora serrata (at $\theta = \Theta =$

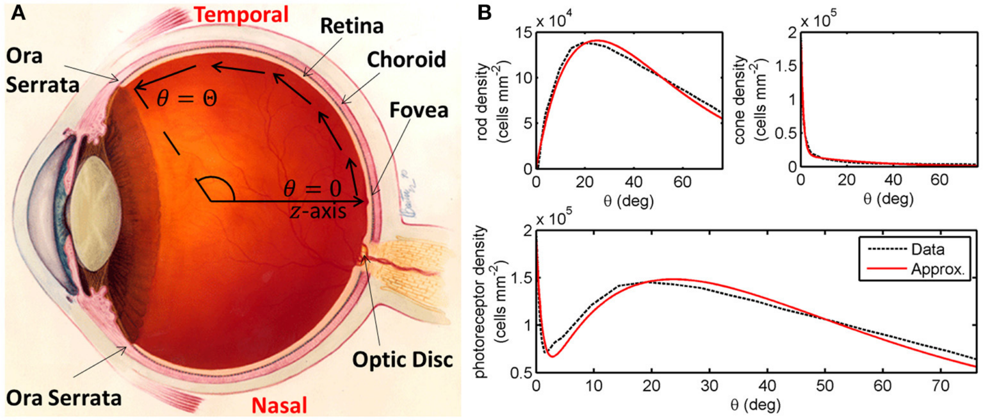

FIGURE 1 | Diagrams of the human eye and retinal photoreceptor distribution (reproduced, with permission, from Roberts et al., 2017). **(A)** Diagram of the (right) human eye, viewed in the transverse plane, illustrating the mathematical model geometry. The model is posed on a domain spanning the region between the foveal centre, at $\theta = 0$, and the ora serrata, at $\theta = \Theta$, along the temporal horizontal meridian, where θ measures the eccentricity. Figure originally reproduced, with modifications, from http://www.nei.nih.gov/health/coloboma/coloboma.asp, courtesy: National Eye Institute, National Institutes of Health (NEI/NIH). **(B)** Measured and fitted photoreceptor profiles, along the temporal horizontal meridian, in the human retina. Cone profile: $\tilde{\rho}_c(\theta) = B_1 e^{-b_1\theta} + B_2 e^{-b_2\theta}$, and rod profile: $\tilde{\rho}_r(\theta) = B_3 \theta e^{-b_3\theta}$ (see **Table 2** for dimensionless parameter values). The photoreceptor profile is the sum of the rod and cone profiles ($\tilde{\rho}_r(\theta) + \tilde{\rho}_c(\theta)$). Experimental data provided by Curcio and published in Curcio et al. (1990).

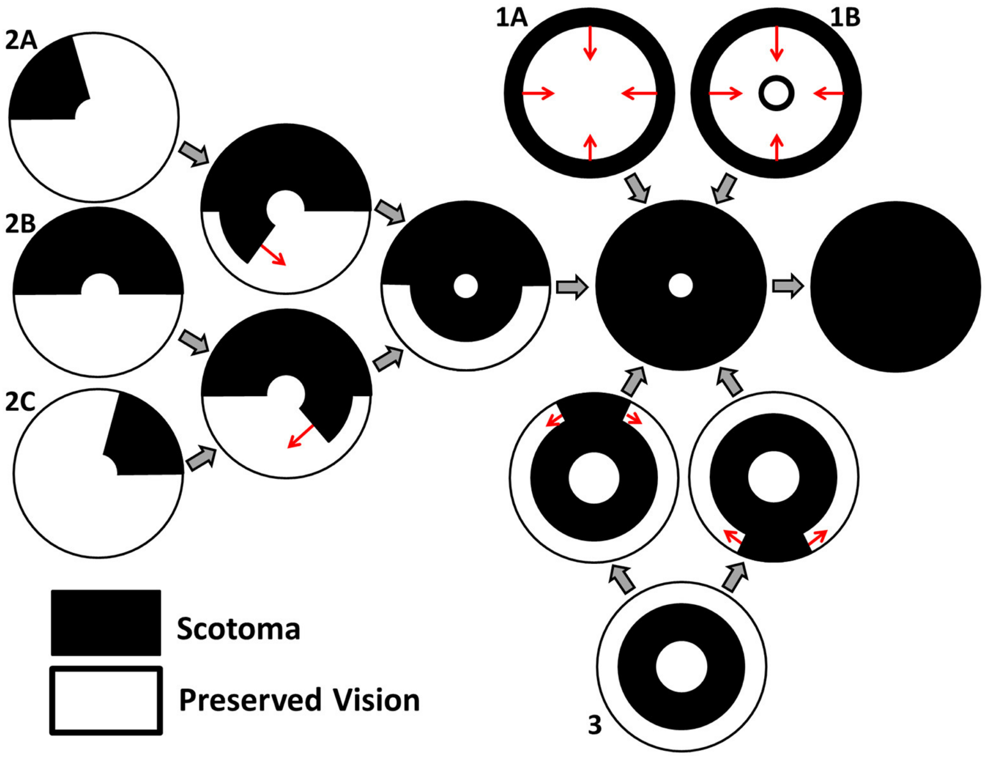

FIGURE 2 | Characteristic patterns of visual field loss in human RP (reproduced, with permission, from Roberts et al., 2018). Visual field loss patterns can be classified into three cases and six subcases (classification system described in Grover et al., 1998). Large gray arrows indicate transitions between stages of visual field loss and small red arrows indicate the direction of scotoma (blind spot) propagation. See text for details.

1.33 rad; see **Figure 1A**). We further simplify the model by non-dimensionalising; scaling the dependent and independent variables so that they and the resultant model parameters are dimensionless and hence unitless. This reduces the number of parameters (including eliminating R) and allows us to identify the dominant terms of the governing equations in the ensuing asymptotic analysis. For this reason, there are no units to be stated in **Figures 3–10**. For the full dimensional model and non-dimensionalisation see Roberts (2022).

We proceed directly to the dimensionless model, which consists of a system of PDEs in terms of the dependent variables: TF concentration, $f(\theta,t)$, rod photoreceptor density, $p_r(\theta,t)$, and cone photoreceptor density, $p_c(\theta,t)$; as functions of the independent variables: polar angle, scaled to lie in the range $0 \leq \theta \leq 1$, and time, $t > 0$ (see **Table 1**).

The TF equation is as follows

$$\frac{\partial f}{\partial t} = \underbrace{\frac{D_f}{\sin(\Theta\theta)}\frac{\partial}{\partial \theta}\left(\sin(\Theta\theta)\frac{\partial f}{\partial \theta}\right)}_{\text{diffusion}} + \underbrace{\alpha p_r}_{\text{production}} - \underbrace{\beta f p_c}_{\text{consumption}} - \underbrace{\eta f}_{\text{decay}}, \tag{1}$$

where $\partial f/\partial t$ is the rate of change in TF concentration over time and the parameters, D_f, the TF diffusivity, α, the rate of TF production by rods, β, the rate of TF consumption by cones, and η, the rate of TF decay, are positive constants. Trophic factor is free to diffuse across the retina through the interphotoreceptor matrix (Aït-Ali et al., 2015). We assume, in the absence of experimental evidence to the contrary, that all rods produce TF at an equal and constant rate, independent of the local TF concentration, such that the rate of TF production is directly proportional to the local rod density. Similarly, in the absence of further experimental evidence, we assume that all cones consume TF at an equal and constant rate for a given local TF concentration. Applying the physiological version of the Law of Mass Action, which states that the rate of a reaction is directly proportional to the product of the concentrations/densities of the reactants (Murray, 2002, in this case TF and cones), we assume that TF is consumed by cones at a rate directly proportional to the product of the local TF concentration and the local cone density. Lastly, we assume that TF decays exponentially, decreasing at a rate directly proportional to its local concentration, as has been shown to occur for a range of other proteins in living human cells (Eden et al., 2011).

The rod equation takes the following form

$$\frac{\partial p_r}{\partial t} = -\underbrace{\phi_r(\theta)p_r}_{\substack{\text{cell degeneration}\\ \text{(mutation-induced)}}}, \tag{2}$$

where $\partial p_r/\partial t$ is the rate of change in rod density over time and we allow the variable $\phi_r(\theta)$, the rate of mutation-induced rod degeneration, to vary spatially (functional forms defined in the Results section), or take a constant positive value, ϕ_r. Rods degenerate due to their expression of a mutant gene (Hamel, 2006; Hartong et al., 2006) and are assumed to do so exponentially, at a rate directly proportional to their local density, consistent with measurements of photoreceptor degeneration kinetics in mouse, rat and canine models of RP (Clarke et al., 2000). Unlike with cones, RdCVF does not serve a protective function for rods (Aït-Ali et al., 2015); therefore, their rate

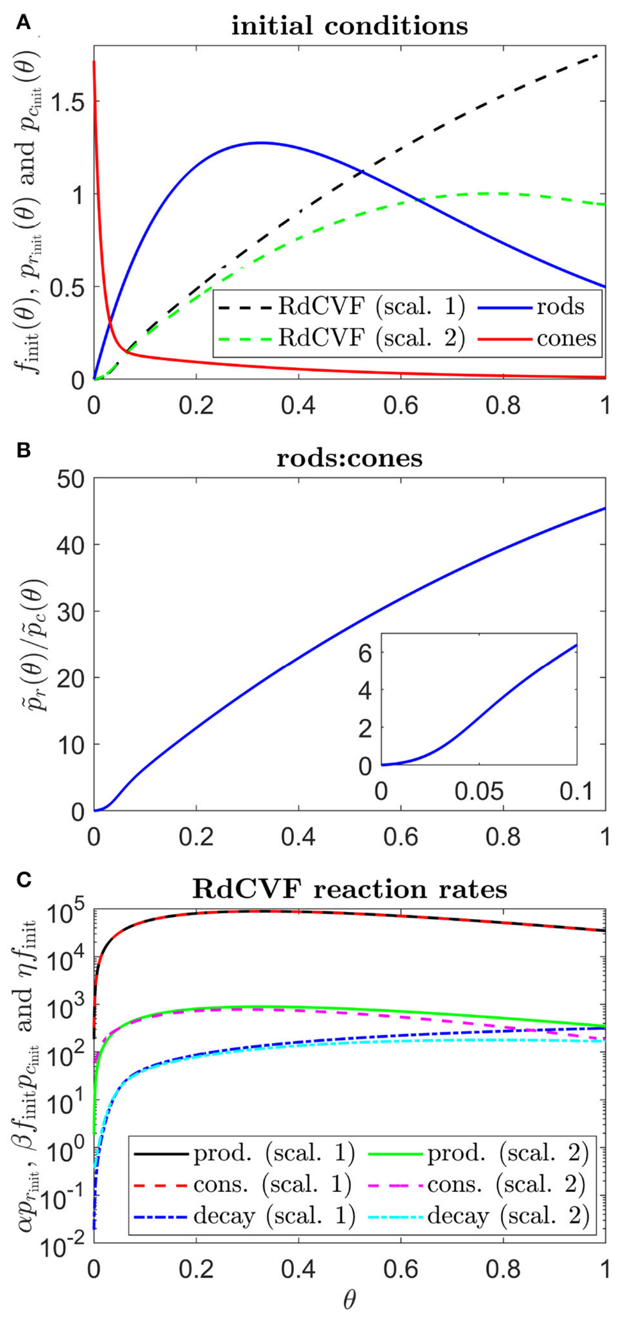

FIGURE 3 | Initial conditions, ratio of rods to cones and RdCVF reaction rates. **(A)** initial conditions used in all simulations, consisting of healthy rod and cone profiles and the corresponding RdCVF profiles under Scalings 1 and 2 (the legend applies to **(A)** only). **(B)** variation in the healthy rod:cone ratio, $\tilde{p}_r(\theta)/\tilde{p}_c(\theta)$, with eccentricity. **(C)** RdCVF production, consumption and decay rates under Scalings 1 and 2 (Equation (1), the legend applies to **(C)** only). To obtain $f_{\text{init}}(\theta)$ in **(A,C)**, Equations (1) and (4) were solved at steady-state using the finite difference method, with 4001 mesh points, where $p_r(\theta) = p_{r_{\text{init}}}(\theta)$ and $p_c(\theta) = p_{c_{\text{init}}}(\theta)$. Under Scaling 1, $\alpha = 7.01 \times 10^4$ and $\beta = 1.79 \times 10^6$, while under Scaling 2, $\alpha = 7.01 \times 10^2$ and $\beta = 1.79 \times 10^4$. Remaining parameter values as in **Table 2**.

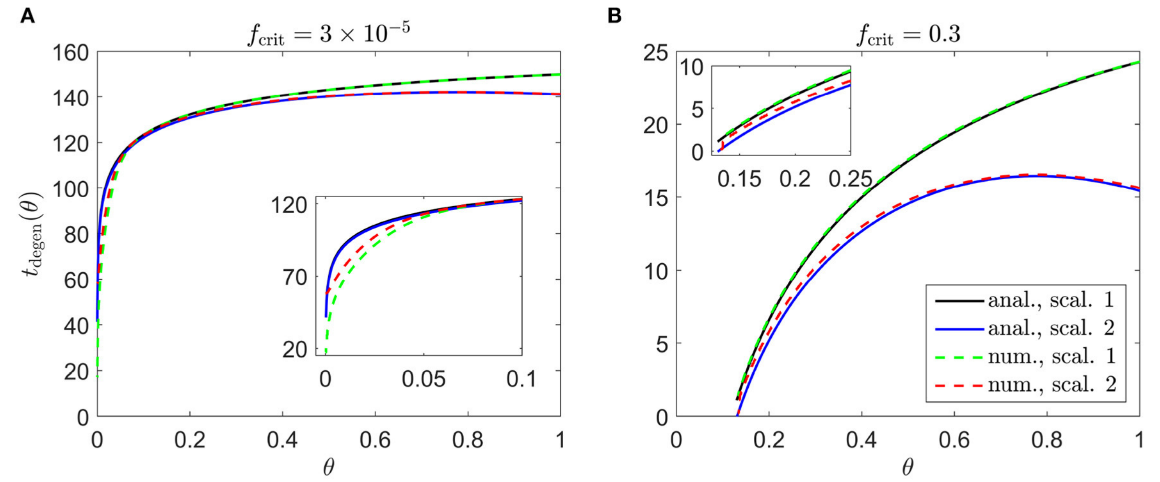

FIGURE 4 | Cone degeneration profiles. Graphs show the time, $t_{\text{degen}}(\theta)$, at which cones degenerate due to RdCVF deprivation, with constant rate of mutation-induced rod degeneration, $\phi_r = 7.33 \times 10^{-2}$, and constant TF threshold concentrations: $f_{\text{crit}} = 3 \times 10^{-5}$ **(A)** and $f_{\text{crit}} = 0.3$ **(B)**. The solid black and dashed green curves correspond to Scaling 1 ($\alpha = 7.01 \times 10^4$ and $\beta = 1.79 \times 10^6$), while the solid blue and dashed red curves correspond to Scaling 2 ($\alpha = 7.01 \times 10^2$ and $\beta = 1.79 \times 10^4$). The black and blue solid curves are analytical approximations, obtained by plotting Equations (6) and (9), respectively, while the green and red dashed curves are $p_c(\theta, t)/\tilde{p}_c(\theta) = 0.99$ contours, obtained by solving Equations (1–5) using the method of lines with 401 mesh points. **(A)** Simulation spans ~17.7 years in dimensional variables; **(B)** simulation spans ~2.8 years in dimensional variables. Insets show magnified portions of each graph. Cone degeneration initiates at the fovea ($\theta = 0$) in **(A)** and at $\theta = 0.13$ in **(B)**, spreading peripherally (rightwards) in both cases. Degeneration occurs earlier in **(B)** than in **(A)** and for Scaling 2 than for Scaling 1 (except near the fovea in **(A)**). Remaining parameter values as in **Table 2**.

of degeneration is independent of the TF concentration. We note that Equation (2) can be solved to yield $p_r(\theta, t) = p_{r_{\text{init}}}(\theta) e^{-\phi_r(\theta)t}$ (where $p_{r_{\text{init}}}(\theta)$, the initial value of $p_r(\theta, t)$, is defined below), provided there is no delay in onset or interruption of degeneration.

The cone equation is as follows

$$\frac{\partial p_c}{\partial t} = -\underbrace{p_c \lambda_2(f)}_{\substack{\text{cell degeneration} \\ \text{(TF starvation)}}}, \tag{3}$$

where $\partial p_c/\partial t$ is the rate of change in cone density over time. We define the Heaviside step function, $H(\cdot)$, such that

$$H(x) := \begin{cases} 0 & \text{if } x < 0, \\ 1 & \text{if } x \geq 0, \end{cases}$$

the function $\lambda_2(f)$ is given by

$$\lambda_2(f) = 1 - H(f - f_{\text{crit}}(\theta)),$$

where we allow the variable $f_{\text{crit}}(\theta)$, the TF threshold concentration, to vary spatially (functional forms defined in the Results section), or take a constant positive value, f_{crit}. Cone density is assumed to remain constant provided the local TF concentration, $f(\theta, t)$, remains in the healthy range at or above the critical threshold, f_{crit}, while cones are assumed to decay exponentially (due to TF starvation) at a rate directly proportional to their local density if $f(\theta, t)$ drops below this threshold, again consistent with Clarke et al. (2000)'s measurements of photoreceptor degeneration kinetics.

Having defined the governing [Equations (1–3)], we close the system by imposing boundary and initial conditions. We apply zero-flux boundary conditions at both ends of the domain,

$$\frac{\partial f}{\partial \theta}(0, t) = 0 = \frac{\partial f}{\partial \theta}(1, t), \tag{4}$$

where $\partial f/\partial \theta$ is the TF concentration gradient in the polar direction, such that there is no net flow of TF into or out of the domain. This is justified by symmetry at $\theta = 0$, while we assume that TF cannot escape from the retina where it terminates at the ora serrata ($\theta = 1$). The healthy rod and cone distributions are given by the following functions

$$\tilde{p}_r(\theta) = B_3 \theta e^{-b_3 \theta},$$
$$\tilde{p}_c(\theta) = B_1 e^{-b_1 \theta} + B_2 e^{-b_2 \theta},$$

where the values of the positive constants B_1, B_2, B_3, b_1, b_2, and b_3 are found by fitting to the mean of Curcio et al. (1990)'s measurements of healthy human rod and cone distributions along the temporal horizontal meridian using the Trust-Region Reflective algorithm in Matlab's curve fitting toolbox (see **Figure 1B**). Lastly, we impose the initial conditions

$$\begin{aligned} f(\theta, 0) &= f_{\text{init}}(\theta), \quad p_r(\theta, 0) = p_{r_{\text{init}}}(\theta) = \tilde{p}_r(\theta), \\ p_c(\theta, 0) &= p_{c_{\text{init}}}(\theta) = \tilde{p}_c(\theta), \end{aligned} \tag{5}$$

where $f_{\text{init}}(\theta)$ is the steady-state solution to Equations (1) and (4) with $p_r = p_{r_{\text{init}}}(\theta)$ and $p_c = p_{c_{\text{init}}}(\theta)$ (see **Figure 3A**). Thus, the retina starts in the healthy state in all simulations.

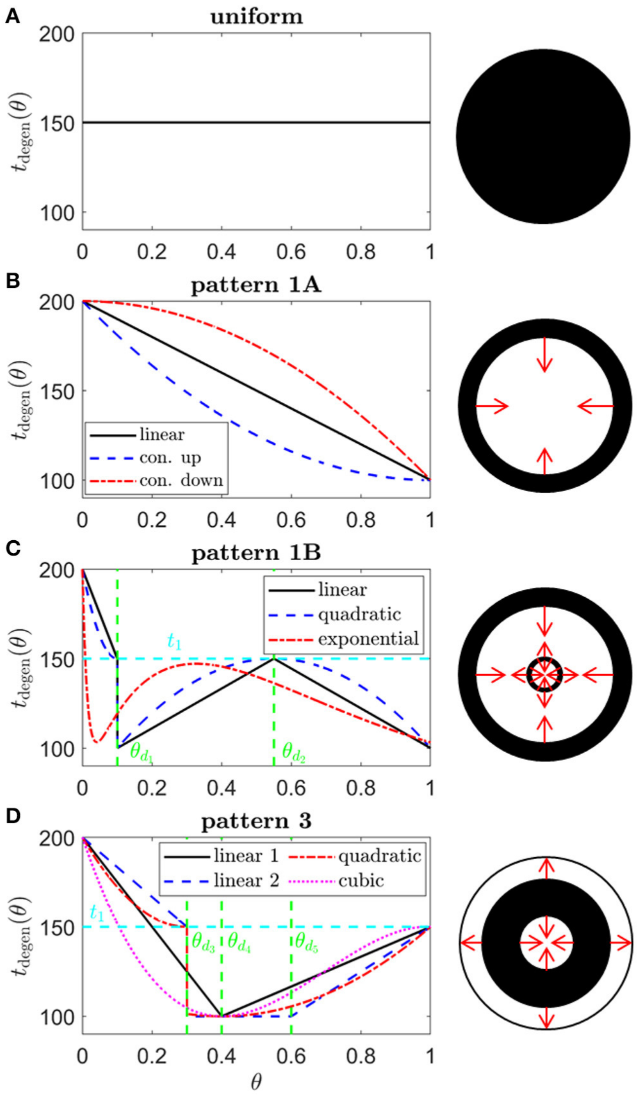

FIGURE 5 | Target cone degeneration profiles. Panels (left) show cone degeneration profiles, $t_{\text{degen}}(\theta)$, qualitatively replicating typical spatio-temporal patterns of visual field loss in RP: **(A)** Uniform, **(B)** Pattern 1A, **(C)** Pattern 1B and **(D)** Pattern 3. Visual field loss patterns directly correspond to cone degeneration patterns in these radially symmetric cases. We seek to replicate these patterns by finding appropriate $\phi_{r_{\text{inv}}}(\theta)$ and $f_{\text{crit}_{\text{inv}}}(\theta)$ profiles in **Figures 6–9**. Diagrams on the right show the corresponding 2D patterns of visual field loss — white regions: preserved vision, black regions: scotomas (blind spots), and red arrows: direction of scotoma propagation. Parameters: $t_0 = 100$ ($\sim$ 11.0 years), $t_1 = 150$ ($\sim$ 16.6 years), $t_2 = 200 \sim 22.1$ years, $\theta_{d_1} = 0.1$ ($\sim$ 7.6 degrees), $\theta_{d_2} = 0.55$ ($\sim$ 41.9 degrees), $\theta_{d_3} = 0.3$ ($\sim$ 22.9 degrees), $\theta_{d_4} = 0.4$ ($\sim$ 30.5 degrees) and $\theta_{d_5} = 0.6$ ($\sim$ 45.7 degrees). Cone degeneration profile formulas and parameters are given in **Table 3**. Remaining parameter values as in **Table 2**.

See **Table 2** for the dimensionless parameter values [see Roberts (2022) for dimensional values and justification of parameter values]. The model presented here simplifies that in Roberts (2022) in the following ways: it does not include treatment, cone outer segment regeneration, or initial patches of rod or cone loss, while mutation-induced rod loss is active for all simulations in this study. The present model also adds two new features to the previous model: allowing the rate of mutation-induced rod degeneration, $\phi_r(\theta)$, and the TF threshold concentration, $f_{\text{crit}}(\theta)$, to vary spatially, where before they were constant (or piecewise constant in the high f_{crit} subcase).

2.2. Numerical Solutions

Numerical (computational) solutions to Equations (1–5) were obtained using the method of lines (as in Roberts, 2022), discretising in space and then integrating in time. The time integration was performed using the Matlab routine `ode15s`, a variable-step, variable-order solver, designed to solve problems involving multiple timescales such as this (Matlab version R2020a was used here and throughout the paper). We used a relative error tolerance of 10^{-6} and an absolute error tolerance of 10^{-10}, with the remaining settings at their default values. The number of spatial mesh points employed varies between simulations, taking values of 26, 51, 101, 401, or 4,001. The upper bound of 4,001 mesh points was chosen such that the distance between mesh points corresponds to the average width of a photoreceptor. In each case the maximum computationally feasible mesh density was employed, all mesh densities being sufficient to achieve accurate results. The initial TF profile, $f(\theta, 0) = f_{\text{init}}(\theta)$, was calculated by discretising Equations (1) and (4) at steady-state, using a finite difference scheme, and solving the consequent system of nonlinear algebraic equations using the Matlab routine `fsolve` (which employs a Trust–Region–Dogleg algorithm) with $p_r = p_{r_{\text{init}}}(\theta)$ and $p_c = p_{c_{\text{init}}}(\theta)$.

2.3. Inverse Problem

Our previous modeling study of the TF hypothesis predicted patterns of cone degeneration which failed to match any known patterns in human RP (Roberts, 2022). In that study, we made the simplifying assumption that model parameters are spatially uniform, such that they do not vary with retinal eccentricity. While this is a reasonable assumption in most cases, we have reason to believe that two of the parameters—the rate of mutation-induced rod loss, ϕ_r, and the TF threshold concentration, f_{crit}—may vary spatially (see below), which could help account for *in vivo* patterns of retinal degeneration.

Rates of rod degeneration in human RP have not been studied in great detail. Thus far, histopathological examination of human RP retinas has revealed that rod degeneration is most severe in the mid-peripheral retina, with relative sparing of rods in the macula and far-periphery until later in the disease (Milam et al., 1998). It may be that this pattern varies depending upon the mutation involved and between individuals (cf. Huang et al., 2012 for which different spatial patterns of rod function loss occur in patients, all of whom have a mutation in the RPGR gene). The rate of decay of rod photoreceptors has also been shown to vary with retinal eccentricity in mouse and pig models of RP (Carter-Dawson et al., 1978; Li et al., 1998). Further, under healthy conditions, the RdCVF concentration at the centre of the retina (near $\theta = 0$) is much lower ($f(\theta, t) \sim O(10^{-5})$) than in the remainder of the retina (where $f(\theta, t) \sim O(0.1)$ to $O(1)$, see **Figure 3A**). Therefore, it is reasonable to assume

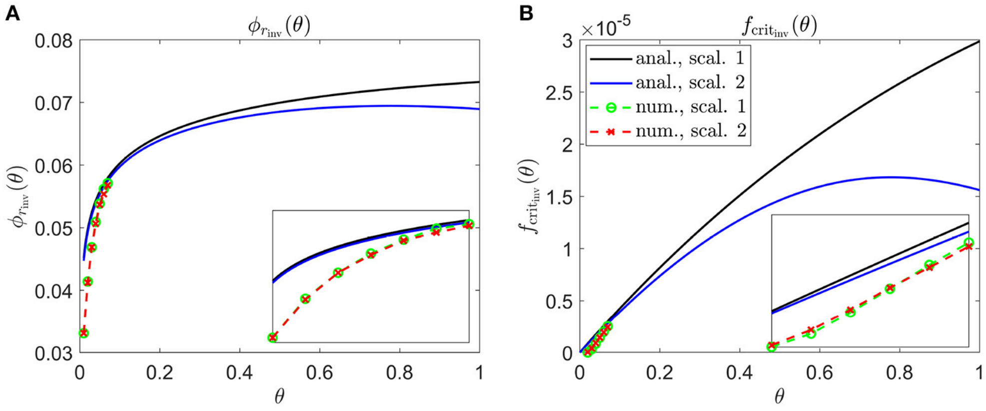

FIGURE 6 | Inverse mutation-induced rod degeneration rate and TF threshold concentration—Uniform target cone degeneration profile. **(A)** inverse mutation-induced rod degeneration rate, $\phi_{r_{\text{inv}}}(\theta)$ ($f_{\text{crit}} = 3 \times 10^{-5}$); **(B)** inverse TF threshold concentration, $f_{\text{crit}_{\text{inv}}}(\theta)$ ($\phi_r = 7.33 \times 10^{-2}$). The solid black and dashed green curves correspond to Scaling 1 ($\alpha = 7.01 \times 10^4$ and $\beta = 1.79 \times 10^6$), while the solid blue and dashed red curves correspond to Scaling 2 ($\alpha = 7.01 \times 10^2$ and $\beta = 1.79 \times 10^4$). The black and blue solid curves are analytical approximations to the inverses, obtained by plotting Equations (7) and (10), respectively **(A)**, and Equations (8) and (11) respectively **(B)**. The green and red dashed curves are numerical inverses, obtained by using the Matlab routines fminsearch **(A)** and patternsearch **(B)** to calculate the ϕ_r and f_{crit} profiles for which the contour described by $p_c(\theta, t)/\tilde{p}_c(\theta) = 0.99$ matches the target cone degeneration profile, $t_{\text{degen}}(\theta)$. Equations (1–5) were solved at each iteration using the method of lines, with 101 mesh points. Insets show magnified portions of each graph. Numerical inverses are calculated and plotted only at those locations (eccentricities) where the analytical inverse fails to generate a $t_{\text{degen}}(\theta)$ profile matching the target profile. Inverses are monotone increasing for Scaling 1, and increase initially for Scaling 2 before reaching a maximum and decreasing toward the ora serrata ($\theta = 1$). Numerical solutions reveal lower values of the inverses near the fovea ($\theta = 0$) than the analytical approximations suggest. Cone degeneration profile formulas and parameters are given in **Table 3**. Remaining parameter values as in **Table 2**.

that central retinal cones are able to cope with lower RdCVF concentrations than those toward the periphery, and hence that f_{crit} is also heterogeneous. To determine whether these heterogeneities could account for cone degeneration patterns in human RP, we formulate and solve something known as an *inverse problem*.

In an inverse problem we seek to determine the model input required to attain a known/desired output. In this case, the known output is the target cone degeneration profile, $t_{\text{degen}}(\theta)$, while the input is either the rate of mutation-induced rod loss profile, $\phi_r(\theta)$, or the TF threshold concentration profile, $f_{\text{crit}}(\theta)$, with corresponding inverses denoted as $\phi_r(\theta) = \phi_{r_{\text{inv}}}(\theta)$ and $f_{\text{crit}}(\theta) = f_{\text{crit}_{\text{inv}}}(\theta)$, respectively. When searching for $\phi_{r_{\text{inv}}}(\theta)$, we hold the TF threshold concentration constant at $f_{\text{crit}}(\theta) = f_{\text{crit}} = 3 \times 10^{-5}$, while, when searching for $f_{\text{crit}_{\text{inv}}}(\theta)$, we hold the rate of mutation-induced rod loss constant at $\phi_r(\theta) = \phi_r = 7.33 \times 10^{-2}$. The constant value of f_{crit} is chosen to lie just below the minimum steady-state value of $f(\theta)$, such that, in the absence of rod loss, cones remain healthy, while the constant value of ϕ_r is chosen to be one hundred times higher than the value that can be inferred from measurements in the healthy human retina (Curcio et al., 1993), placing the timescale of the resultant cone loss on the order of decades, in agreement with *in vivo* RP progression rates (Hamel, 2006; Hartong et al., 2006).

We consider a range of target cone degeneration profiles, summarized in **Figure 5** and **Table 3**, which qualitatively replicate visual field loss Patterns 1A, 1B, and 3 seen *in vivo* (and hence the corresponding *in vivo* cone degeneration patterns; taking the degeneration of the far-peripheral retina to occur in a radially symmetric manner in Pattern 3—see **Figure 2** and Grover et al., 1998). We do not consider patterns of type 2 (to be explored in a future study) as these cannot be replicated by a 1D model (since the radial symmetry, assumed by the 1D model, is broken by variation in the azimuthal/circumferential direction). For each degeneration pattern, we consider a set of sub-patterns to examine how this affects the shape of the inverses, allowing us to confirm that a modest change in the degeneration pattern results in a modest change in the inverses, while exploring both linear/piecewise linear profiles and more biologically realistic nonlinear (quadratic/cubic/exponential) patterns. We also consider a uniform target cone degeneration profile for comparison.

For each pattern, we consider the effect of two (biologically realistic) scalings for the rate of TF production by rods, α, and the rate of TF consumption by cones, β, upon the inverse profiles: (i) Scaling 1—for which $\alpha = 7.01 \times 10^4$ and $\beta = 1.79 \times 10^6$ as in Roberts (2022); and (ii) Scaling 2—for which $\alpha = 7.01 \times 10^2$ and $\beta = 1.79 \times 10^4$. Under Scaling 1, production and consumption of TF dominate over decay (with rate constant η), such that decay has a negligible effect upon the TF profile and model behavior. Under Scaling 2, TF production and consumption occur at a similar rate to decay, such that they balance each other, resulting in a different TF profile and model behavior (see **Figures 3A,C**). As discussed in Roberts (2022), none of α, β, or η have been measured. The decay rate, η, was chosen to match the measured decay rate of proteins in living human cells (Eden et al., 2011). Under Scaling 1, the consumption rate, β, is chosen such that it dominates over the decay rate (being a factor $\epsilon^{-1} = O(10^2)$ larger), while the production rate, α, is chosen to balance consumption (see the Analytical Inverse

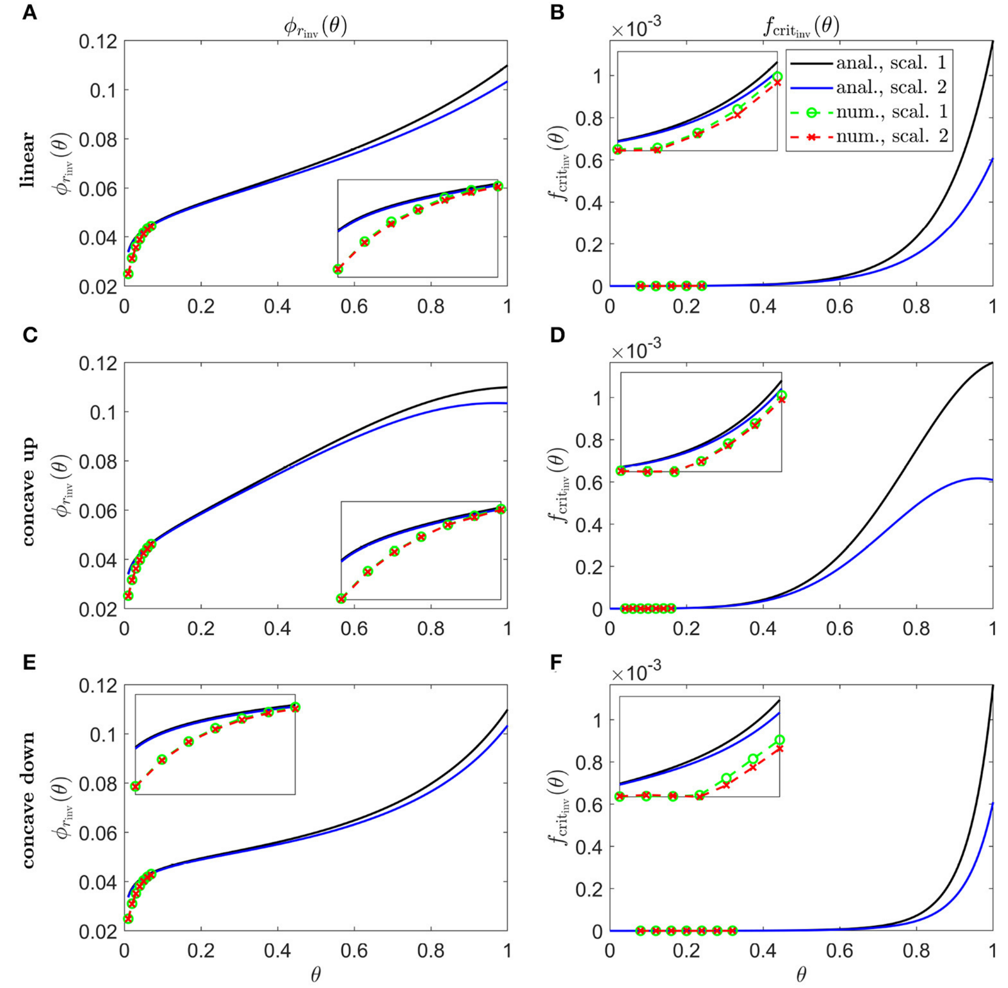

FIGURE 7 | Inverse mutation-induced rod degeneration rate and TF threshold concentration—Pattern 1A target cone degeneration profiles. **(A,C,E)** inverse mutation-induced rod degeneration rate, $\phi_{r_{\rm inv}}(\theta)$ ($f_{\rm crit} = 3 \times 10^{-5}$); **(B,D,F)** inverse TF threshold concentration, $f_{{\rm crit}_{\rm inv}}(\theta)$ ($\phi_r = 7.33 \times 10^{-2}$). **(A,B)** linear target cone degeneration profile, $t_{\rm degen}(\theta)$; **(C,D)** concave up quadratic $t_{\rm degen}(\theta)$ profile; **(E,F)** concave down quadratic $t_{\rm degen}(\theta)$ profile. The solid black and dashed green curves correspond to Scaling 1 ($\alpha = 7.01 \times 10^4$ and $\beta = 1.79 \times 10^6$), while the solid blue and dashed red curves correspond to Scaling 2 ($\alpha = 7.01 \times 10^2$ and $\beta = 1.79 \times 10^4$). The black and blue solid curves are analytical approximations to the inverses, obtained by plotting Equations (7) and (10), respectively, **(A,C,E)** and Equations (8) and (11), respectively, **(B,D,F)**. The green and red dashed curves are numerical inverses, obtained by using the Matlab routines fminsearch **(A,C,E)**, and patternsearch **(B,D,F)** to calculate the ϕ_r and $f_{\rm crit}$ profiles for which the contour described by $p_c(\theta, t)/\tilde{p}_c(\theta) = 0.99$ matches the target cone degeneration profile, $t_{\rm degen}(\theta)$. Equations (1–5) were solved at each iteration using the method of lines, with 26, 51, or 101 mesh points. Insets show magnified portions of each graph. Numerical inverses are calculated and plotted only at those locations (eccentricities) where the analytical inverse fails to generate a $t_{\rm degen}(\theta)$ profile matching the target profile. Inverses are monotone increasing functions for both scalings in **(A, B, E, F)**, and for Scaling 1 in **(C,D)** while the inverses increase initially for Scaling 2 before reaching a maximum and decreasing toward the ora serrata ($\theta = 1$) in **(C,D)**. Numerical solutions reveal lower values of the inverses near the fovea ($\theta = 0$) than the analytical approximations suggest. Cone degeneration profile formulas and parameters are given in **Table 3**. Remaining parameter values as in **Table 2**.

Section). This is a sensible scaling as it is likely that cones consume RdCVF at a much faster rate than that at which it decays. It is possible, however, that cones consume RdCVF at a similar rate to its decay rate, which is the scenario we consider in Scaling 2; reducing α and β by a factor of 100 ($\sim \epsilon^{-1}$) to bring consumption and production into balance with decay (see the Analytical Inverse Section).

We solve the inverse problem both analytically and numerically (computationally), as described in the Analytical Inverse and Numerical Inverse sections below. Analytical approximations are computationally inexpensive and provide deeper insight into model behavior, while numerical solutions, though computationally intensive, are more accurate.

2.3.1. Analytical Inverse

Less mathematically inclined readers may wish to skip over the following derivation and proceed to the resulting Equations (6–11) and surrounding explanatory text. To derive analytical (algebraic) approximations for the inverses, $\phi_{r_{\rm inv}}(\theta)$ and $f_{{\rm crit}_{\rm inv}}(\theta)$, we perform an asymptotic analysis, seeking the leading order behavior of Equations (1–5). In other words, we are simplifying our equations, making it possible to solve them algebraically (by

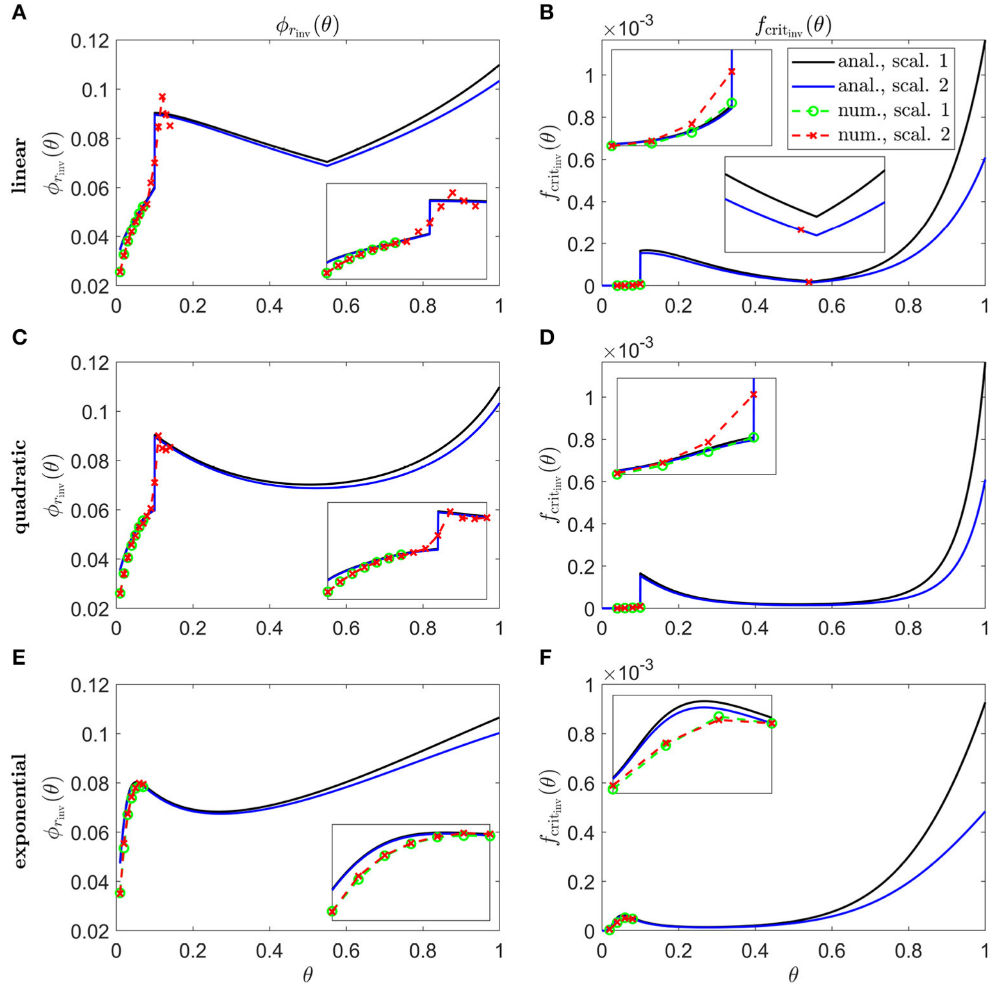

FIGURE 8 | Inverse mutation-induced rod degeneration rate and TF threshold concentration—Pattern 1B target cone degeneration profiles. **(A,C,E)** inverse mutation-induced rod degeneration rate, $\phi_{r_{\mathrm{inv}}}(\theta)$ ($f_{\mathrm{crit}} = 3 \times 10^{-5}$); **(B,D,F)** inverse TF threshold concentration, $f_{\mathrm{crit}_{\mathrm{inv}}}(\theta)$ ($\phi_r = 7.33 \times 10^{-2}$). **(A,B)** linear target cone degeneration profile, $t_{\mathrm{degen}}(\theta)$; **(C,D)** quadratic $t_{\mathrm{degen}}(\theta)$ profile; **(E,F)** exponential $t_{\mathrm{degen}}(\theta)$ profile. The solid black and dashed green curves correspond to Scaling 1 ($\alpha = 7.01 \times 10^4$ and $\beta = 1.79 \times 10^6$), while the solid blue and dashed red curves correspond to Scaling 2 ($\alpha = 7.01 \times 10^2$ and $\beta = 1.79 \times 10^4$). The black and blue solid curves are analytical approximations to the inverses, obtained by plotting Equations (7) and (10), respectively, **(A,C,E)**, and Equations (8) and (11), respectively, **(B,D,F)**. The green and red dashed curves are numerical inverses, obtained by using the Matlab routines fminsearch **(A,C,E)**, and patternsearch **(B,D,F)** to calculate the ϕ_r and f_{crit} profiles for which the contour described by $p_c(\theta, t)/\tilde{p}_c(\theta) = 0.99$ matches the target cone degeneration profile, $t_{\mathrm{degen}}(\theta)$. Equations (1–5) were solved at each iteration using the method of lines, with 51 or 101 mesh points. Insets show magnified portions of each graph. Numerical inverses are calculated and plotted only at those locations (eccentricities) where the analytical inverse fails to generate a $t_{\mathrm{degen}}(\theta)$ profile matching the target profile. Inverses resemble vertically flipped versions of the $t_{\mathrm{degen}}(\theta)$ profiles. Numerical solutions reveal lower values of the inverses near the fovea ($\theta = 0$) than the analytical approximations suggest and higher values in some regions away from the fovea in **(A–D)**. Cone degeneration profile formulas and parameters are given in **Table 3**. Remaining parameter values as in **Table 2**.

hand), by only including those terms (corresponding to specific biological processes, e.g., TF production) which dominate the behavior of the solution, where the method known as "asymptotic analysis" enables us to rationally identify these dominant terms. Proceeding as in Roberts (2022) (where we considered a steady-state problem), we choose $\epsilon = O(10^{-2})$ and scale the parameters $\eta = \epsilon^{-1}\eta'$ and $b_1 = \epsilon^{-1}b_1'$, introducing the new scaling $\phi_r(\theta) = \epsilon\phi_r'(\theta)$, as we study the time-dependent problem here (where dashes $'$ denote scaled variables and parameters). We consider two possible (biologically realistic) scalings on α and β: (i) Scaling 1—for which $\alpha = \epsilon^{-2}\alpha'$ and $\beta = \epsilon^{-3}\beta'$ as in Roberts (2022) (corresponding to $\alpha = 7.01 \times 10^4$ and $\beta = 1.79 \times 10^6$); and (ii) Scaling 2—for which $\alpha = \epsilon^{-1}\alpha'$ and $\beta = \epsilon^{-2}\beta'$ (corresponding to $\alpha = 7.01 \times 10^2$ and $\beta = 1.79 \times 10^4$). All remaining parameters are assumed to be $O(1)$. We also scale the dependent variable $p_c(\theta, t) = \epsilon p_c'(\theta, t)$, and assume $f(\theta, t) = O(1)$ and $p_r(\theta, t) = O(1)$.

Applying the above scalings and dropping the dashes (working with the scaled versions of the variables and parameters, but omitting the dashes $'$ for notational convenience), Equation

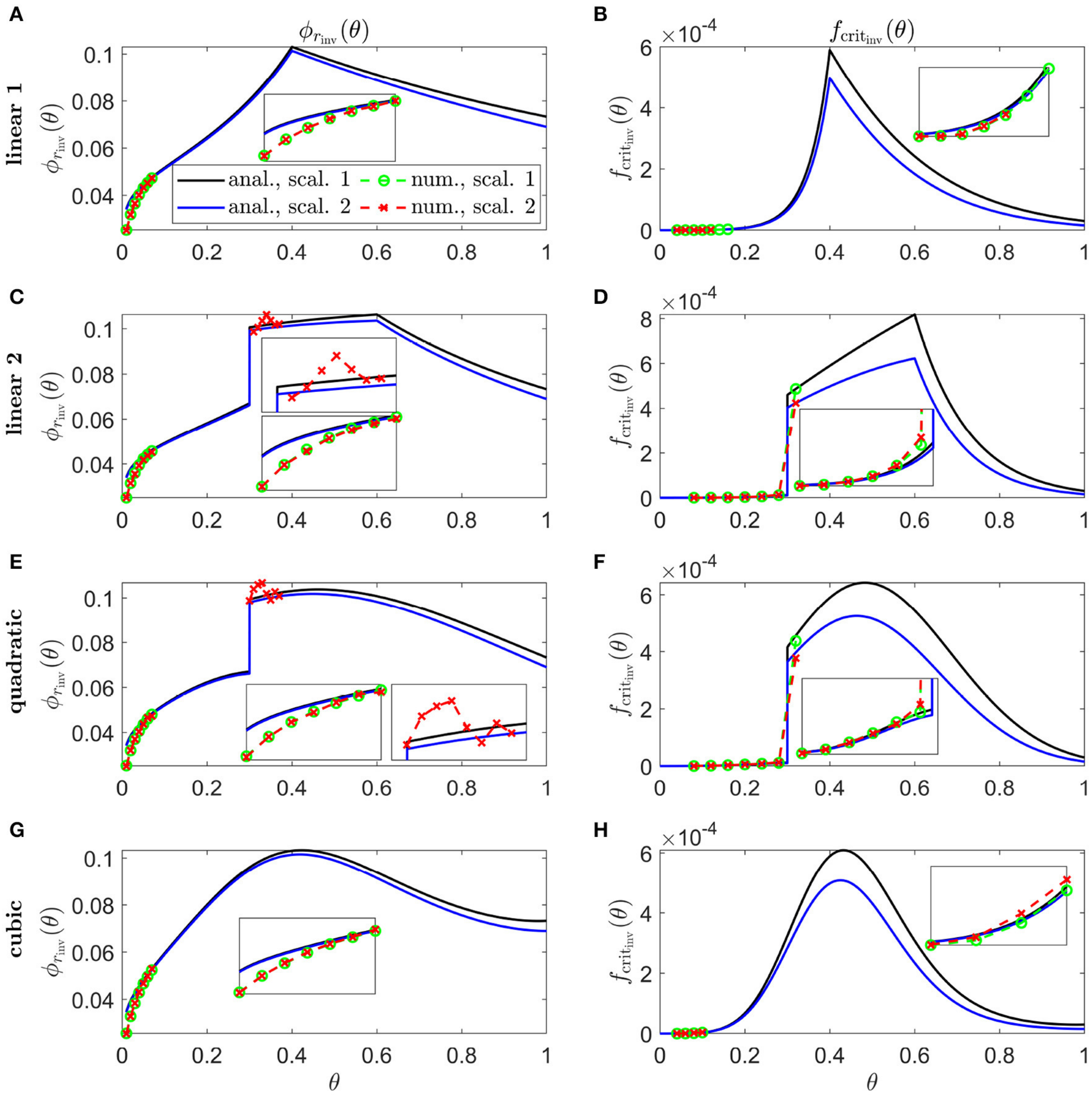

FIGURE 9 | Inverse mutation-induced rod degeneration rate and TF threshold concentration—Pattern 3 target cone degeneration profiles. **(A,C,E,G)** inverse mutation-induced rod degeneration rate, $\phi_{r_{\rm inv}}(\theta)$ ($f_{\rm crit} = 3 \times 10^{-5}$); **(B,D,F,H)** inverse TF threshold concentration, $f_{{\rm crit}_{\rm inv}}(\theta)$ ($\phi_r = 7.33 \times 10^{-2}$). **(A,B)** linear 1 target cone degeneration profile, $t_{\rm degen}(\theta)$; **(C,D)** linear 2 $t_{\rm degen}(\theta)$ profile; **(E,F)** quadratic $t_{\rm degen}(\theta)$ profile; **(G,H)** cubic $t_{\rm degen}(\theta)$ profile. The solid black and dashed green curves correspond to Scaling 1 ($\alpha = 7.01 \times 10^4$ and $\beta = 1.79 \times 10^6$), while the solid blue and dashed red curves correspond to Scaling 2 ($\alpha = 7.01 \times 10^2$ and $\beta = 1.79 \times 10^4$). The black and blue solid curves are analytical approximations to the inverses, obtained by plotting Equations (7) and (10) respectively **(A,C,E,G)**, and Equations (8) and (11), respectively, **(B,D,F,H)**. The green and red dashed curves are numerical inverses, obtained by using the Matlab routines fminsearch **(A,C,E,G)**, and patternsearch **(B,D,F,H)** to calculate the ϕ_r and $f_{\rm crit}$ profiles for which the contour described by $p_c(\theta, t)/\tilde{p}_c(\theta) = 0.99$ matches the target cone degeneration profile, $t_{\rm degen}(\theta)$. Equations (1–5) were solved at each iteration using the method of lines, with 26, 51 or 101 mesh points. Insets show magnified portions of each graph. Numerical inverses are calculated and plotted only at those locations (eccentricities) where the analytical inverse fails to generate a $t_{\rm degen}(\theta)$ profile matching the target profile. Inverses resemble vertically flipped versions of the $t_{\rm degen}(\theta)$ profiles. Numerical solutions reveal lower values of the inverses near the fovea ($\theta = 0$) than the analytical approximations suggest and higher values in some regions away from the fovea in **(C–F,H)**. Cone degeneration profile formulas and parameters are given in **Table 3**. Remaining parameter values as in **Table 2**.

(2) becomes

$$\frac{\partial p_r}{\partial t} = -\epsilon \phi_r(\theta) p_r.$$

Thus, on this (fast) timescale, the rod density is constant. Since we are interested in the timescale upon which rods degenerate, we scale time as $t' = \epsilon t$ such that the decay term enters the dominant balance. Thus, on this slow timescale, after dropping the dashes, we have that

$$\frac{\partial p_r}{\partial t} = -\phi_r(\theta) p_r,$$

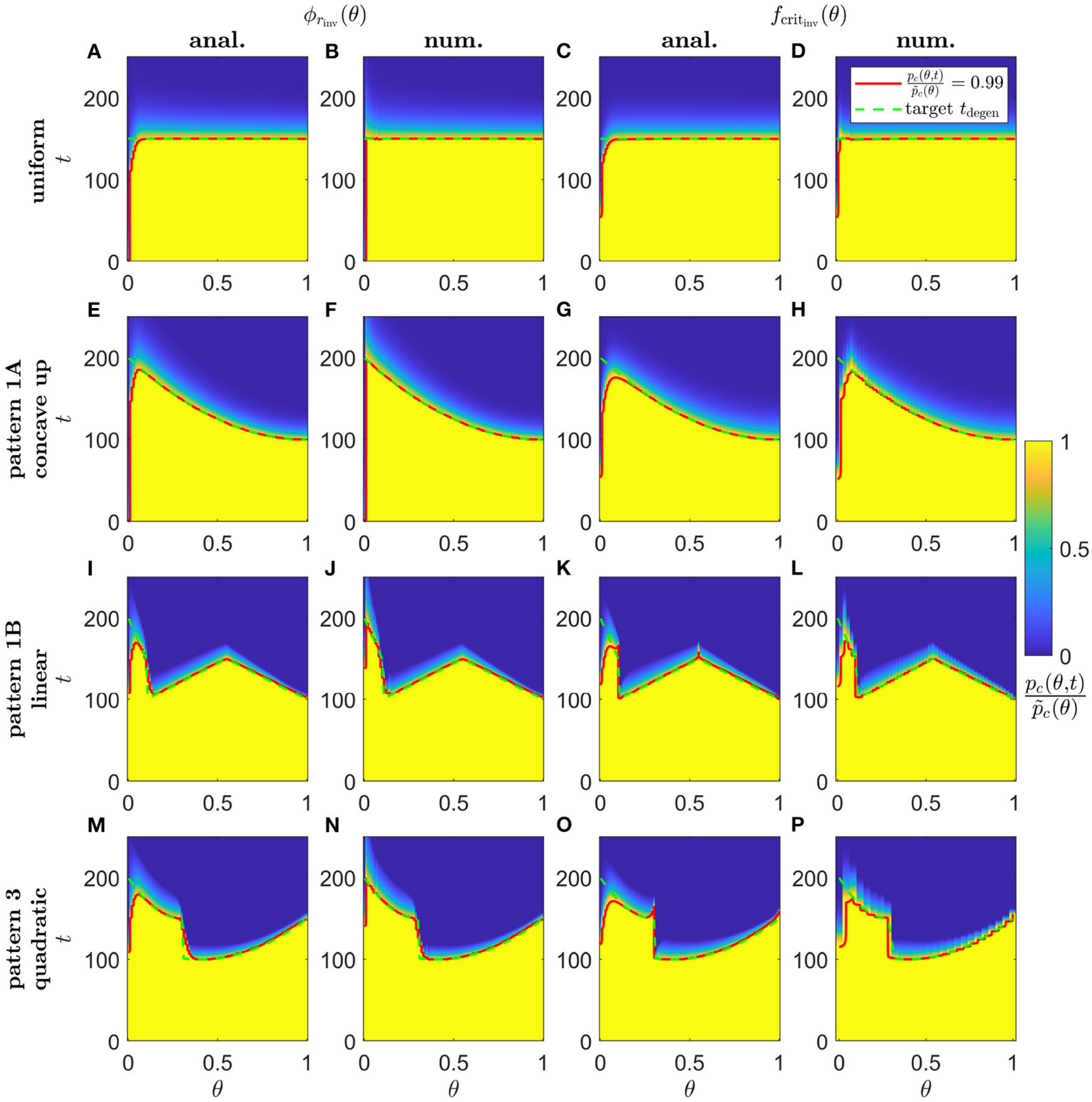

FIGURE 10 | Simulations of proportional cone loss for a range of inverse mutation-induced rod degeneration rates and TF threshold concentrations. Plots show the proportion of cones remaining compared to local healthy values, $p_c(\theta,t)/\tilde{p}_c(\theta)$, across space and over time. **(A,E,I,M)** analytical inverse mutation-induced rod degeneration rate, $\phi_{r_{\text{inv}}}(\theta)$ ($f_{\text{crit}} = 3 \times 10^{-5}$); **(B,F,J,N)** numerical $\phi_{r_{\text{inv}}}(\theta)$ ($f_{\text{crit}} = 3 \times 10^{-5}$); **(C,G,K,O)** analytical inverse TF threshold concentration, $f_{\text{crit}_{\text{inv}}}(\theta)$ ($\phi_r = 7.33 \times 10^{-2}$); **(D,H,L,P)** numerical $f_{\text{crit}_{\text{inv}}}(\theta)$ ($\phi_r = 7.33 \times 10^{-2}$). **(A–D)** Uniform target cone degeneration profile, $t_{\text{degen}}(\theta)$, with Scaling 1 ($\alpha = 7.01 \times 10^4$ and $\beta = 1.79 \times 10^6$); **(E–H)** Pattern 1A quadratic concave up $t_{\text{degen}}(\theta)$ profile with Scaling 1; **(I–L)** Pattern 1B linear $t_{\text{degen}}(\theta)$ profile with Scaling 2 ($\alpha = 7.01 \times 10^2$ and $\beta = 1.79 \times 10^4$); **(M–P)** Pattern 3 quadratic $t_{\text{degen}}(\theta)$ profile with Scaling 2. Equations (1–5) were solved using the method of lines, with 26, 51 or 101 mesh points. Analytical and numerical $\phi_{r_{\text{inv}}}(\theta)$ and $f_{\text{crit}_{\text{inv}}}(\theta)$ are as plotted in **Figures 5–8**. Solid red curves denote the contours along which $p_c(\theta,t)/\tilde{p}_c(\theta) = 0.99$, while dashed green curves show the target $t_{\text{degen}}(\theta)$ profiles. Cone degeneration profiles generally show good agreement with the target $t_{\text{degen}}(\theta)$ profiles. There is some divergence from $t_{\text{degen}}(\theta)$ for the analytical inverses near the fovea ($\theta = 0$) and at discontinuous or nonsmooth portions of $t_{\text{degen}}(\theta)$; this is mostly corrected by the numerical inverses. Cone degeneration profile formulas and parameters are given in **Table 3**. Remaining parameter values as in **Table 2**.

such that, at leading order, $p_{r_0}(\theta,t) = p_{r_{\text{init}_0}}(\theta)e^{-\phi_r(\theta)t} = B_3\theta e^{-b_3\theta}e^{\phi_r(\theta)t}$.

We are interested here in the regime in which cones have not yet degenerated, thus, we assume the leading order cone density remains constant at $p_{c_0}(\theta) = p_{c_{\text{init}_0}}(\theta) = B_2e^{-b_2\theta}$.

Applying Scaling 1 and the slow timescale to Equation (1), we obtain

$$\epsilon\frac{\partial f}{\partial t} = D_f\frac{\partial^2 f}{\partial\theta^2} + D_f\Theta\cot(\Theta\theta)\frac{\partial f}{\partial\theta} + \epsilon^{-2}\alpha p_r - \epsilon^{-2}\beta p_c f - \epsilon^{-1}\eta f.$$

Since the TF dynamics occur on a faster timescale than mutation-induced rod loss, we make a quasi-steady-state approximation (QSSA), assuming that the TF concentration instantaneously takes its steady-state profile, for any given rod density profile, as the rods degenerate ($\epsilon\partial_t f \sim 0$). Thus, at leading order, we obtain

$$f_{0_{\text{QSSA}}}(\theta) = \frac{\alpha p_{r_0}(\theta, t)}{\beta p_{c_0}(\theta)}.$$

Rearranging this expression and assuming that cone degeneration initiates when $f_{0_{\text{QSSA}}}(\theta) = f_{\text{crit}}(\theta)$, we obtain the cone degeneration time profile,

$$t_{\text{degen}}(\theta) = \frac{1}{\phi_r(\theta)}\left(\log\left(\frac{\alpha B_3}{\beta B_2 f_{\text{crit}}(\theta)}\theta\right) - (b_3 - b_2)\theta\right), \tag{6}$$

the inverse mutation-induced rod degeneration rate profile,

$$\phi_{r_{\text{inv}}}(\theta) = \frac{1}{t_{\text{degen}}(\theta)}\left(\log\left(\frac{\alpha B_3}{\beta B_2 f_{\text{crit}}}\theta\right) - (b_3 - b_2)\theta\right), \tag{7}$$

and the inverse TF threshold concentration profile,

$$f_{\text{crit}_{\text{inv}}}(\theta) = \frac{\alpha B_3}{\beta B_2}\theta e^{-((b_3 - b_2)\theta + \phi_r t_{\text{degen}}(\theta))}. \tag{8}$$

Alternatively, if we apply Scaling 2 and the slow timescale to Equation (1) we obtain

$$\epsilon\frac{\partial f}{\partial t} = D_f\frac{\partial^2 f}{\partial \theta^2} + D_f \Theta \cot(\Theta\theta)\frac{\partial f}{\partial \theta} + \epsilon^{-1}\alpha p_r - \epsilon^{-1}\beta p_c f - \epsilon^{-1}\eta f,$$

with the TF decay term, ηf, now entering the dominant balance. Applying the QSSA and proceeding as above we find

$$f_{0_{\text{QSSA}}}(\theta) = \frac{\alpha p_{r_0}(\theta, t)}{\beta p_{c_0}(\theta) + \eta},$$

with cone degeneration time profile,

$$t_{\text{degen}}(\theta) = \frac{1}{\phi_r(\theta)}\left(\log\left(\frac{\alpha B_3}{(\beta B_2 + \eta e^{b_2\theta}) f_{\text{crit}}(\theta)}\theta\right) - (b_3 - b_2)\theta\right), \tag{9}$$

inverse mutation-induced rod degeneration rate profile,

$$\phi_{r_{\text{inv}}}(\theta) = \frac{1}{t_{\text{degen}}(\theta)}\left(\log\left(\frac{\alpha B_3}{(\beta B_2 + \eta e^{b_2\theta}) f_{\text{crit}}}\theta\right) - (b_3 - b_2)\theta\right), \tag{10}$$

and inverse TF threshold concentration profile,

$$f_{\text{crit}_{\text{inv}}}(\theta) = \frac{\alpha B_3}{(\beta B_2 + \eta e^{b_2\theta})}\theta e^{-((b_3 - b_2)\theta + \phi_r t_{\text{degen}}(\theta))}. \tag{11}$$

These equations reveal how the inverses, $\phi_{r_{\text{inv}}}(\theta)$ and $f_{\text{crit}_{\text{inv}}}(\theta)$, are influenced by our choices for fixed values of f_{crit} and ϕ_r, respectively. As can be seen from Equations (7) and (10), $\phi_{r_{\text{inv}}}(\theta)$ is inversely and monotonically related to f_{crit}, such that as f_{crit} increases, $\phi_{r_{\text{inv}}}(\theta)$ decreases. Similarly, $f_{\text{crit}_{\text{inv}}}(\theta)$ and ϕ_r are inversely and monotonically related in Equations (8) and (11), such that as ϕ_r increases, $f_{\text{crit}_{\text{inv}}}(\theta)$ decreases. Lastly, as would be expected intuitively, $t_{\text{degen}}(\theta)$, $\phi_{r_{\text{inv}}}(\theta)$ and $f_{\text{crit}_{\text{inv}}}(\theta)$ all increase monotonically with increasing TF production, α, and decrease monotonically with increasing TF consumption, β, and TF decay η [Equations (6–8) and (9–11)].

2.3.2. Numerical Inverse

The numerical inverse is calculated by repeatedly solving the forward problem [Equations (1–5)] for different values of the input ($\phi_r(\theta)$ or $f_{\text{crit}}(\theta)$), with the aim of converging upon the inverse ($\phi_{r_{\text{inv}}}(\theta)$ or $f_{\text{crit}_{\text{inv}}}(\theta)$). To find $\phi_{r_{\text{inv}}}(\theta)$, we use the Matlab routine `fminsearch` (which uses a simplex search method), while to obtain $f_{\text{crit}_{\text{inv}}}(\theta)$ the Matlab routine `patternsearch` (which uses an adaptive mesh technique) was found to be more effective. In both cases, the objective function (the quantity we are seeking to minimise) was taken as the sum of squares of the difference between the target cone degeneration profile, $t_{\text{degen}}(\theta)$, and the contour described by $p_c(\theta, t)/\tilde{p}_c(\theta) = 0.99$ (along which cone degeneration is deemed to have initiated). Equations (1–5) were solved at each iteration as described in the Numerical Solutions section. Numerical inverses were calculated only at those locations (eccentricities) where the analytical inverse failed to generate a $t_{\text{degen}}(\theta)$ profile matching the target profile, the analytical inverse being assumed to hold at all other eccentricities.

3. RESULTS

We begin by calculating the cone degeneration profiles, $t_{\text{degen}}(\theta)$, in the case where both the rate of mutation induced rod degeneration, ϕ_r, and the TF threshold concentration, f_{crit}, are spatially uniform (or piecewise constant). We set the standard value for $\phi_r = 7.33 \times 10^{-2}$ and consider the subcases (i) $f_{\text{crit}} = 3 \times 10^{-5}$ for $0 \leq \theta \leq 1$ (**Figure 4A**), and (ii) $f_{\text{crit}} = 0.3$ for $\theta > 0.13$ while $f_{\text{crit}} = 3 \times 10^{-5}$ for $\theta \leq 0.13$ (**Figure 4B**), as were explored in Roberts (2022). These subcases correspond to the situation in which the TF threshold concentration lies beneath the minimum healthy TF value at all retinal locations (i), and the situation in which foveal cones are afforded special protection compared to the rest of the retina, such that they can withstand lower TF concentrations (ii). For notational simplicity, we shall refer to subcase (ii) simply as $f_{\text{crit}} = 0.3$ in what follows. As with **Figures 6–9**, we consider both Scaling 1 and Scaling 2 (see Inverse Problem) on the rate of TF production by rods, α, and the rate of TF consumption by cones, β, calculating both analytical and numerical solutions.

Cone degeneration initiates at the fovea ($\theta = 0$) in **Figure 4A** and at $\theta = 0.13$ in **Figure 4B**, spreading peripherally (rightwards) in both cases, while degeneration also initiates at the ora serrata ($\theta = 1$) under Scaling 2 in both **Figures 4A,B**, spreading centrally. Degeneration occurs earlier in **Figure 4B** than in **Figure 4A** and earlier for Scaling 2 than for Scaling 1 (except near the fovea in **Figure 4A**). Numerical and analytical solutions agree well, only diverging close to the fovea in **Figure 4A**, where the analytical solution breaks down. None of these patterns of degeneration match those seen *in vivo* (see **Figure 2**).

In **Figures 6–9**, we calculate the $\phi_r(\theta) = \phi_{r_{\text{inv}}}(\theta)$ and $f_{\text{crit}}(\theta) = f_{\text{crit}_{\text{inv}}}(\theta)$ profiles required to qualitatively replicate the cone degeneration profiles, $t_{\text{degen}}(\theta)$, observed *in vivo* (**Figure 5**), by solving the associated inverse problems (see Inverse Problem). As noted in the Inverse Problem section, when searching for $\phi_{r_{\text{inv}}}(\theta)$, we hold the TF threshold concentration constant at $f_{\text{crit}}(\theta) = f_{\text{crit}} = 3 \times 10^{-5}$, while, when searching for $f_{\text{crit}_{\text{inv}}}(\theta)$, we hold the rate of mutation-induced rod loss constant at $\phi_r(\theta) = \phi_r = 7.33 \times 10^{-2}$. Analytical inverses are plotted across the domain ($0 \leq \theta \leq 1$), while numerical inverses are calculated and plotted only at those locations (eccentricities) where the analytical inverse fails to generate a $t_{\text{degen}}(\theta)$ profile matching the target profile (as determined by visual inspection, the $t_{\text{degen}}(\theta)$ and target profiles being visually indistinguishable outside of these regions).

In **Figure 6**, we calculate inverses for a Uniform degeneration profile. While this pattern is not typically observed in humans, we consider this case as a point of comparison with the non-uniform patterns explored in **Figures 7–9**. Both inverses, $\phi_{r_{\text{inv}}}(\theta)$ and $f_{\text{crit}_{\text{inv}}}(\theta)$, are monotone increasing for Scaling 1, and increase initially for Scaling 2 before reaching a maximum and decreasing toward the ora serrata (at $\theta = 1$). Consequently, Scaling 1 and 2 inverses, while close near the fovea ($\theta = 0$), diverge toward the ora serrata, this effect being more prominent for $f_{\text{crit}_{\text{inv}}}(\theta)$. The inverse profiles have a similar shape to the $t_{\text{degen}}(\theta)$ profiles in **Figure 4** (see Discussion). Numerical solutions reveal lower values of the inverses near the fovea, where the analytical approximations break down.

Inverses for linear (**Figures 7A,B**), concave up (quadratic) (**Figures 7C,D**) and concave down (quadratic) (**Figures 7E,F**) Pattern 1A degeneration profiles are shown in **Figure 7**. Inverses are monotone increasing functions for both Scalings 1 and 2 in **Figures 7A–F** and for Scaling 1 in **Figures 7C,D**, while the inverses increase initially for Scaling 2 before reaching a maximum and decreasing toward the ora serrata in **Figures 7C,D**. Numerical solutions reveal lower values of the inverses near the fovea, where the analytical approximations break down.

Figure 8 shows inverses for linear (**Figures 8A,B**), quadratic (**Figures 8C,D**) and exponential (**Figures 8E,F**) Pattern 1B degeneration profiles. Inverses resemble vertically flipped versions of the $t_{\text{degen}}(\theta)$ profiles in **Figure 5C** (see Discussion). Numerical solutions reveal lower values of the inverses near the fovea, where the analytical approximations break down, and higher values in some regions away from the fovea in **Figures 8A–D**. The discontinuities in the linear and quadratic cases are biologically unrealistic, though consistent with the idealised qualitative target cone degeneration patterns in **Figure 5C**.

In **Figure 9**, we calculate inverses for linear 1 (**Figures 9A,B**), linear 2 (**Figures 9C,D**), quadratic (**Figures 9E,F**), and cubic (**Figures 9G,H**) Pattern 3 degeneration profiles. Inverses resemble vertically flipped versions of the $t_{\text{degen}}(\theta)$ profiles in **Figure 5D** (see Discussion). Numerical solutions reveal lower values of the inverses near the fovea, where the analytical approximations break down, and higher values in some regions away from the fovea in **Figures 9C–F,H**. Similarly to **Figure 8**, the discontinuities in the linear 2 and quadratic cases are biologically unrealistic, though consistent with the idealised qualitative target cone degeneration patterns in **Figure 5D**.

TABLE 1 | Variables employed in the non-dimensional mathematical model [Equations (1–5)].

Variable	Description
θ	Eccentricity
t	Time
$f(\theta, t)$	Trophic factor concentration
$p_r(\theta, t)$	Rod density
$p_c(\theta, t)$	Cone density

TABLE 2 | Parameters employed in the non-dimensional mathematical model [Equations (1–5)]. Values are given to three significant figures (radians are dimensionless).

Parameter	Description	Value
Θ	Eccentricity of the ora serrata	1.33 rad
D_f	Trophic factor diffusivity	0.237
α	Rate of trophic factor production by rods	7.01×10^2 or 7.01×10^4
β	Rate of trophic factor consumption by cones	1.79×10^4 or 1.79×10^6
η	Rate of trophic factor decay	1.79×10^2
ϕ_r	Rate of mutation-induced rod degeneration	7.33×10^{-2}
f_{crit}	Trophic factor threshold concentration	3×10^{-5} or 0.3
B_1	Cone profile parameter	1.56
B_2	Cone profile parameter	0.158
B_3	Rod profile parameter	10.6
b_1	Cone profile parameter	71.8
b_2	Cone profile parameter	2.67
b_3	Rod profile parameter	3.06

Lastly, in **Figure 10**, we show simulation results of proportional cone loss for analytical and numerical $\phi_{r_{\text{inv}}}(\theta)$ and $f_{\text{crit}_{\text{inv}}}(\theta)$, for Uniform (Scaling 1, **Figures 10A–D**), concave up Pattern 1A (Scaling 1, **Figures 10E–H**), linear Pattern 1B (Scaling 2, **Figures 10I–L**) and quadratic Pattern 3 (Scaling 2, **Figures 10M–P**) target degeneration profiles. Cone degeneration profiles generally show good agreement with the target $t_{\text{degen}}(\theta)$ profiles. There is some divergence from $t_{\text{degen}}(\theta)$ for the analytical inverses near the fovea and at discontinuous or nonsmooth portions of $t_{\text{degen}}(\theta)$; this is mostly corrected by the numerical inverses. This correction is not perfect near the centre of the fovea, where cones still degenerate earlier than the target profiles. This occurs because it is necessary to replace the Heaviside step function in $\lambda_2(f)$ [see Equation (3)] with a hyperbolic tanh function to satisfy the smoothness requirements for the numerical solver, with the result that the initiation of cone degeneration is sensitive to the low TF concentrations ($f(\theta, t) < 10^{-4}$) in that region.

4. DISCUSSION

The spatio-temporal patterns of retinal degeneration observed in human retinitis pigmentosa (RP) are well characterised; however,

TABLE 3 | Target cone degeneration profiles, $t_{\text{degen}}(\theta)$.

Degeneration pattern	Sub-pattern	Cone degeneration time ($t_{\text{degen}}(\theta)$)
Uniform	—	t_1
Pattern 1A	Linear	$t_2 - (t_2 - t_0)\theta$
	Quadratic (concave up)	$(t_2 - t_0)(\theta - 1)^2 + t_0$
	Quadratic (concave down)	$t_2 - (t_2 - t_0)\theta^2$
Pattern 1B	Linear	$t_2 - \frac{(t_2 - t_1)}{\theta_{d_1}}\theta$ if $\theta \leq \theta_{d_1}$
		$t_0 + \frac{(t_1 - t_0)}{(\theta_{d_2} - \theta_{d_1})}(\theta - \theta_{d_1})$ if $\theta_{d_1} < \theta \leq \theta_{d_2}$
		$t_1 + \frac{(t_1 - t_0)}{(1 - \theta_{d_2})}(\theta_{d_2} - \theta)$ if $\theta \geq \theta_{d_2}$
	Quadratic	$\frac{(t_2 - t_1)}{\theta_{d_1}^2}(\theta - \theta_{d_1})^2 + t_1$ if $\theta \leq \theta_{d_1}$
		$t_1 - \frac{(t_1 - t_0)}{(\theta_{d_2} - 1)^2}(\theta - \theta_{d_2})^2$ if $\theta > \theta_{d_1}$
	Exponential	$A_1 e^{-a_1\theta} + A_2\theta e^{-a_2\theta} + A_3$
Pattern 3	Linear 1	$t_2 - \frac{(t_2 - t_0)}{\theta_{d_4}}\theta$ if $\theta \leq \theta_{d_4}$
		$t_0 + \frac{(t_1 - t_0)}{(1 - \theta_{d_4})}(\theta - \theta_{d_4})$ if $\theta \geq \theta_{d_4}$
	Linear 2	$t_2 - \frac{(t_2 - t_1)}{\theta_{d_3}}\theta$ if $\theta \leq \theta_{d_3}$
		t_0 if $\theta_{d_3} < \theta \leq \theta_{d_5}$
		$t_0 + \frac{(t_1 - t_0)}{(1 - \theta_{d_5})}(\theta - \theta_{d_5})$ if $\theta \geq \theta_{d_5}$
	Quadratic	$\frac{(t_2 - t_1)}{\theta_{d_3}^2}(\theta - \theta_{d_3})^2 + t_1$ if $\theta \leq \theta_{d_3}$
		$\frac{(t_1 - t_0)}{(1 - \theta_{d_4})^2}(\theta - \theta_{d_4})^2 + t_0$ if $\theta > \theta_{d_3}$
	Cubic	$C_3\theta^3 + C_2\theta^2 + C_1\theta + C_0$

Parameter values*

$$t_0 = 100 \quad t_1 = 150 \quad t_2 = 200 \quad \theta_{d_1} = 0.1 \quad \theta_{d_2} = 0.55$$

$$\theta_{d_3} = 0.3 \quad \theta_{d_4} = 0.4 \quad \theta_{d_5} = 0.6 \quad A_1 = 125 \quad A_2 = 600$$

$$A_3 = 75 \quad a_1 = 71.8 \quad a_2 = 3.06$$

$$C_0 = t_2 = 200$$

$$C_1 = \frac{-2(t_2 - t_0) + 3(t_2 - t_0)\theta_{d_4} - (t_2 - t_1)\theta_{d_4}^3}{\theta_{d_4}(1 - \theta_{d_4})^2} = -5.78 \times 10^2$$

$$C_2 = \frac{(t_2 - t_0) - 3(t_2 - t_0)\theta_{d_4}^2 + 2(t_2 - t_1)\theta_{d_4}^3}{\theta_{d_4}^2(1 - \theta_{d_4})^2} = 1.01 \times 10^3$$

$$C_3 = \frac{-(t_2 - t_0) + 2(t_2 - t_0)\theta_{d_4} - (t_2 - t_1)\theta_{d_4}^2}{\theta_{d_4}^2(1 - \theta_{d_4})^2} = -4.86 \times 10^2$$

**We choose θ_{d_1} and θ_{d_2} such that $\theta_{d_2} = (\theta_{d_1} + 1)/2$, so that θ_{d_2} lies halfway between $\theta = \theta_{d_1}$ and $\theta = 1$.*

the mechanistic explanation for these patterns has yet to be conclusively determined. In this paper, we have formulated a one-dimensional (1D) reaction-diffusion partial differential equation (PDE) model (modified from Roberts, 2022) to predict RP progression under the trophic factor (TF) hypothesis. Using this model, we solved inverse problems to determine the rate of mutation-induced rod loss profiles, $\phi_r(\theta) = \phi_{r_{\text{inv}}}(\theta)$, and TF threshold concentration profiles, $f_{\text{crit}}(\theta) = f_{\text{crit}_{\text{inv}}}(\theta)$, that would be required to generate spatio-temporal patterns of cone degeneration qualitatively resembling those observed *in vivo*, were the TF mechanism solely responsible for RP progression. In reality, multiple mechanisms (including oxidative damage and metabolic dysregulation, Travis et al., 1991; Valter et al., 1998; Stone et al., 1999; Punzo et al., 2009, 2012) likely operate in tandem to drive the initiation and propagation of retinal degeneration in RP. By using mathematics to isolate the TF mechanism, in a way that would be impossible to achieve experimentally, we are able to determine the conditions under which the TF mechanism alone would recapitulate known phenotypes. Having identified these conditions, this paves the way for future biomedical and experimental studies to test our predictions.

Other mechanisms may give rise to spatio-temporal patterns of retinal degeneration different from those predicted for the TF mechanism and may do so using fewer assumptions. For example, our previous work on oxygen toxicity in RP demonstrated that this mechanism can replicate visual field loss Pattern 1 (especially 1B) and the late far-peripheral degeneration stage of Pattern 3, without imposing heterogeneities on the rod decay rate or photoreceptor susceptibility to oxygen toxicity (Roberts et al., 2017, 2018). Further, we hypothesise that the toxic substance hypothesis (in which dying rods release a chemical which kills neighbouring photoreceptors) is best able to explain the early mid-peripheral loss of photoreceptors in Patterns 2 and 3, given the high density of rods in this region. In future work, we will explore the toxic substance and other hypotheses, ultimately combining them together in a more comprehensive modeling framework, aimed at explaining and predicting all patterns of retinal degeneration in RP.

Spatially uniform $\phi_r(\theta)$ and $f_{\text{crit}}(\theta)$ profiles fail to replicate any of the *in vivo* patterns of degeneration (**Figure 4**), showing that heterogenous profiles are required, all else being equal. Throughout this article, we have considered two scalings on the rate of TF production by rods, α, and the rate of TF consumption by cones, β (denoted as Scalings 1 and 2, see the Inverse Problem section for details). Under Scaling 1, the rod:cone ratio (**Figure 3B**) dominates the model behavior [see Equation (6)], leading to a monotone, central to peripheral pattern of degeneration, while under Scaling 2, the trophic factor decay term, ηf, enters the dominant balance [see Equation (9)], such that degeneration initiates at both the fovea and (later) at the ora serrata, the degenerative fronts meeting in the mid-/far-periphery (**Figure 4**).

As discussed in the Inverse Problem section, the rate of mutation-induced rod loss, $\phi_r(\theta)$, is known to be spatially heterogeneous in humans with RP (Milam et al., 1998). The $\phi_r(\theta)$ profile predicted for Pattern 3 is consistent with the preferential loss of rods in the mid-peripheral retina noted by Milam et al. (1998) for human RP. A more extensive biomedical investigation is required to characterise quantitatively the diversity of $\phi_r(\theta)$ profiles across individuals and for different mutations. This would make it possible to determine if the $\phi_r(\theta)$ profiles predicted by our model for cone degeneration Patterns 1A and 1B are realised in human RP patients with those cone degeneration patterns. To the best of our knowledge, we are the first to suggest that the intrinsic susceptibility of cones to RdCVF deprivation, characterised in our models by the TF threshold concentration, $f_{\text{crit}}(\theta)$, may vary across the retina. Assuming it does vary, what might account for this phenomenon? There is a precedent for special protection being provided to localised parts of the retina. For example, experiments in mice have found that production of basic fibroblast growth factor (bFGF) and glial fibrillary acidic protein (GFAP) is permanently upregulated along the retinal edges, at the ora serrata and optic disc, to protect against elevated stress in these regions (Mervin and Stone, 2002; Stone et al., 2005). Similarly, in the human retina, rods (though not cones) contain bFGF, with a concentration gradient increasing toward the periphery (Li et al., 1997, potentially explaining the relative sparing of rods often observed at the far-periphery). By analogy, we speculate that, in the human retina, cone protective factors may be upregulated at the fovea to compensate for the low RdCVF concentrations in that region, lowering the local value of $f_{\mathrm{crit}}(\theta)$. This hypothesis awaits experimental confirmation.

We solved the inverse functions, $\phi_{r_{\mathrm{inv}}}(\theta)$ and $f_{\mathrm{crit}_{\mathrm{inv}}}(\theta)$, both analytically (algebraically) and numerically (computationally). Analytical solutions are approximations; however, they have the advantage of being easier to compute (increasing their utility for biomedical researchers) and provide a more intuitive understanding of model behavior, while numerical solutions are more accurate, though computationally expensive. We calculated the inverses for a range of target cone degeneration profiles, consisting of a Uniform profile and profiles which qualitatively replicate those found *in vivo*: Pattern 1A, Pattern 1B and Pattern 3 (Pattern 2 being inaccessible to a 1D model; see **Figure 5** and **Table 3**).

The shapes of the inverse functions are determined partly by the rod and cone distributions, $\tilde{p}_r(\theta)$ and $\tilde{p}_c(\theta)$, and partly by the target cone degeneration profile, $t_{\mathrm{degen}}(\theta)$ [see Equations (7,8,10,11)]. As such, in the Uniform case (**Figure 6**), the Scaling 1 inverse profiles take a similar shape to the rod:cone ratio (**Figure 3B**), the inverses being lower toward the fovea to compensate for the smaller rod:cone ratio and hence lower supply of TF to each cone. The Scaling 2 inverse profiles follow a similar trend but decrease toward the ora serrata after peaking in the mid-/far-periphery due to the greater influence of the trophic factor decay term under this scaling. Interestingly, the shapes of these inverse profiles bear a striking resemblance to the cone degeneration profiles for spatially uniform $\phi_r(\theta)$ and $f_{\mathrm{crit}}(\theta)$ (**Figure 4**). This is because lower values of the inverses are required to delay degeneration, in those regions where cones would otherwise degenerate earlier, to achieve a uniform degeneration profile. The inverse functions resemble vertically flipped versions of the target cone degeneration profiles for Patterns 1A, 1B and 3 (**Figures 7**, **8**), this being more apparent for Patterns 1B and 3 due to their more distinctive shapes. This makes sense since lower inverse values are required for later degeneration times. Scaling 2 inverses typically lie below Scaling 1 inverses, compensating for the fact that degeneration generally occurs earlier under Scaling 2 than under Scaling 1 for any given $\phi_r(\theta)$ and $f_{\mathrm{crit}}(\theta)$.

Analytical inverses give rise to cone degeneration profiles that accurately match the target cone degeneration profiles, except near the fovea (centred at $\theta = 0$, where the validity of the analytical approximation breaks down) and where the target $t_{\mathrm{degen}}(\theta)$ profile is nonsmooth or discontinuous (i.e. linear and quadratic Pattern 1B, and linear 1, linear 2 and quadratic Pattern 3; see **Figure 10** for examples). Numerical inverses improve accuracy in these regions, consistently taking lower values near the fovea, delaying degeneration where it occurs prematurely under the analytical approximation.

We have assumed throughout this study that at least one of $\phi_r(\theta)$ and $f_{\mathrm{crit}}(\theta)$ is spatially uniform. It is possible, however, that both vary spatially. In this case there are no unique inverses; however, if the profile for one of these functions could be measured experimentally, then the inverse problem for the remaining function could be solved as in this paper.

This work could be extended both experimentally and theoretically. Experimental and biomedical studies could measure how the rate of mutation-induced rod loss and TF threshold concentration vary with location in the retina, noting the spatio-temporal pattern of cone degeneration and comparing with the inverse $\phi_{r_{\mathrm{inv}}}(\theta)$ and $f_{\mathrm{crit}_{\mathrm{inv}}}(\theta)$ profiles predicted by our models. Curcio et al. (1993) have previously measured variation in the rate of rod loss in normal (non-RP) human retinas (where rods degenerated most rapidly in the central retina); a similar approach could be taken to quantify the rate of rod loss in human RP retinas. The parameter f_{crit} is less straightforward to measure. Léveillard et al. (2004) incubated cone-enriched primary cultures from chicken embryos with glutathione S-transferase-RdCVF (GST-RdCVF) fusion proteins, doubling the number of living cells per plate compared with GST alone. If experiments of this type could be repeated for a range of controlled RdCVF concentrations, then the value of f_{crit} could be identified. Determining the spatial variation of $f_{\mathrm{crit}}(\theta)$ in a foveated human-like retina may not be possible presently; however, the recent development of retinal organoids provides promising steps in this direction (O'Hara-Wright and Gonzalez-Cordero, 2020; Fathi et al., 2021). If organoids could be developed with a specialised macular region, mirroring that found *in vivo*, then the minimum RdCVF concentration required to maintain cones in health could theoretically be tested at a variety of locations. Further, the distribution of RdCVF, predicted in our models, could theoretically be measured in post-mortem human eyes using fluorescent immunohistochemistry, as was done for the protein neuroglobin by Ostojić et al. (2008) and Rajendram and Rao (2007), and perhaps also fluorescent immunocytochemistry as was done for bFGF by Li et al. (1997). In particular, it would be interesting to see if RdCVF concentration varies with retinal eccentricity as starkly as our model predicts, with extremely low levels in the fovea.

In future work, we will extend our mathematical model to two spatial dimensions, accounting for variation in the azimuthal/circumferential dimension (allowing us to capture radially asymmetric aspects of visual field loss Patterns 2 and 3, and to account for azimuthal variation in the rod and cone distributions), and use quantitative target cone degeneration patterns derived from SD-OCT imaging of RP patients (e.g., as in Escher et al., 2012). We will also adapt the model to consider animal retinas for which the photoreceptor distribution has been well characterised (e.g., rats, mice and pigs, Chandler et al., 1999; Gaillard et al., 2009; Ortín-Martínez et al., 2014).

In conclusion, we have formulated and solved a mathematical inverse problem to determine the rate of mutation-induced rod loss and TF threshold concentration profiles required to explain the spatio-temporal patterns of retinal degeneration observed in human RP. Inverse profiles were calculated for a set of qualitatively distinct degeneration patterns, achieving a close match with the target cone degeneration profiles. Predicted inverse profiles await future experimental verification.

DATA AVAILABILITY STATEMENT

The raw data supporting the conclusions of this article will be made available by the authors, without undue reservation.

AUTHOR CONTRIBUTIONS

PR: conceptualisation, methodology, software, validation, formal analysis, investigation, data curation, writings–original draft, writings–review and editing, visualisation, and project administration.

FUNDING

PR was funded by BBSRC (BB/R014817/1).

ACKNOWLEDGMENTS

PR thanks Tom Baden for allowing the time to pursue this research. PR also thanks the reviewers for their helpful and insightful comments.

REFERENCES

Aït-Ali, N., Fridlich, R., Millet-Puel, G., Clérin, E., Delalande, F., Jaillard, C., et al. (2015). Rod-derived cone viability factor promotes cone survival by stimulating aerobic glycolysis. *Cell* 161, 817–832. doi: 10.1016/j.cell.2015.03.023

Birtel, J., Gliem, M., Mangold, E., Müller, P. L., Holz, F. G., Neuhaus, C., et al. (2018). Next-generation sequencing identifies unexpected genotype-phenotype correlations in patients with retinitis pigmentosa. *PLoS ONE* 13, e0207958. doi: 10.1371/journal.pone.0207958

Burns, J., Clarke, G., and Lumsden, C. J. (2002). Photoreceptor death: Spatiotemporal patterns arising from one-hit death kinetics and a diffusible cell death factor. *Bull. Math. Biol.* 64, 1117–1145. doi: 10.1006/bulm.2002.0320

Camacho, E. T., Brager, D., Elachouri, G., Korneyeva, T., Millet-Puel, G., Sahel, J. A., et al. (2019). A mathematical analysis of aerobic glycolysis triggered by glucose uptake in cones. *Sci. Rep.* 9, 4162. doi: 10.1038/s41598-019-39901-z

Camacho, E. T., Colón Vélez, M. A., Hernández, D. J., Bernier, U. R., van Laarhoven, J., and Wirkus, S. (2010). A mathematical model for photoreceptor interactions. *J. Theor. Biol.* 267, 638–646. doi: 10.1016/j.jtbi.2010.09.006

Camacho, E. T., Dobreva, A., Larripa, K., Rădulescu, A., Schmidt, D., and Trejo, I. (2021). *Mathematical Modeling of Retinal Degeneration: Aerobic Glycolysis in a Single Cone*, volume 22 of *Association for Women in Mathematics Series* Cham: Springer International Publishing, 135–178.

Camacho, E. T., Lenhart, S., Melara, L. A., Villalobos, M. C., and Wirkus, S. (2020). Optimal control with MANF treatment of photoreceptor degeneration. *Math. Med. Biol.* 37, 1–21. doi: 10.1093/imammb/dqz003

Camacho, E. T., Léveillard, T., Sahel, J. A., and Wirkus, S. (2016a). Mathematical model of the role of RdCVF in the coexistence of rods and cones in a healthy eye. *Bull. Math. Biol.* 78, 1394–1409. doi: 10.1007/s11538-016-0185-x

Camacho, E. T., Melara, L. A., Villalobos, M. C., and Wirkus, S. (2014). Optimal control in the treatment of retinitis pigmentosa. *Bull. Math. Biol.* 76, 292–313. doi: 10.1007/s11538-013-9919-1

Camacho, E. T., Punzo, C., and Wirkus, S. A. (2016b). Quantifying the metabolic contribution to photoreceptor death in retinitis pigmentosa via a mathematical model. *J. Theor. Biol.* 408, 75–87. doi: 10.1016/j.jtbi.2016.08.001

Camacho, E. T., Radulescu, A., and Wirkus, S. (2016c). Bifurcation analysis of a photoreceptor interaction model for retinitis pigmentosa. *Commun. Nonlin. Sci. Numer. Simulat.* 38, 267–276. doi: 10.1016/j.cnsns.2016.02.030

Camacho, E. T., and Wirkus, S. (2013). Tracing the progression of retinitis pigmentosa via photoreceptor interactions. *J. Theor. Biol.* 317, 105–118. doi: 10.1016/j.jtbi.2012.09.034

Carter-Dawson, L. D., LaVail, M. M., and Sidman, R. L. (1978). Differential effect of the rd mutation on rods and cones in the mouse retina. *Invest. Ophthalmol. Vis. Sci.* 17, 489–498.

Chandler, M. J., Smith, P. J., Samuelson, D. A., and Mackay, E. O. (1999). Photoreceptor density of the domestic pig retina. *Vet. Ophthalmol.* 2, 179–184. doi: 10.1046/j.1463-5224.1999.00077.x

Clarke, G., Collins, R. A., Leavitt, B. R., Andrews, D. F., Hayden, M. R., Lumsden, C. J., and McInnes, R. R. (2000). A one-hit model of cell death in inherited neuronal degenerations. *Nature* 406, 195–199. doi: 10.1038/35018098

Colón Vélez, M. A., Hernández, D. J., Bernier, U. R., van Laarhoven, J., and Camacho, E. T. (2003). *Mathematical Models for Photoreceptor Interactions*. Technical Report, Cornell University, Department of Biological Statistics and Computational Biology.

Coussa, R. G., Basali, D., Maeda, A., DeBenedictis, M., and Traboulsi, E. I. (2019). Sector retinitis pigmentosa: report of ten cases and a review of the literature. *Mol. Vis.* 25, 869–889.

Curcio, C. A., Millican, C. L., Allen, K. A., and Kalina, R. E. (1993). Aging of the human photoreceptor mosaic: evidence for selective vulnerability of rods in central retina. *Invest. Ophthalmol. Vis. Sci.* 34, 3278–3296.

Curcio, C. A., Sloan, K. R., Kalina, R. E., and Hendrickson, A. E. (1990). Human photoreceptor topography. *J. Comp. Neurol.* 292, 497–523. doi: 10.1002/cne.902920402

Daiger, S. P., Bowne, S. J., and Sullivan, L. S. (2007). Perspective on genes and mutations causing retinitis pigmentosa. *Arch. Ophthalmol.* 125, 151–158. doi: 10.1001/archopht.125.2.151

Eden, E., Geva-Zatorsky, N., Issaeva, I., Cohen, A., Dekel, E., Danon, T., et al. (2011). Proteome half-life dynamics in living human cells. *Science* 331, 764–768. doi: 10.1126/science.1199784

Escher, P., Tran, H. V., Vaclavik, V., Borruat, F. X., Schorderet, D. F., and Munier, F. L. (2012). Double concentric autofluorescence ring in NR2E3-p.G56R-linked autosomal dominant retinitis pigmentosa. *Invest. Ophthalmol. Vis. Sci.* 53, 4754–4764. doi: 10.1167/iovs.11-8693

Fathi, M., Ross, C. T., and Hosseinzadeh, Z. (2021). Functional 3-dimensional retinal organoids: technological progress and existing challenges. *Front. Neurosci.* 15, 668857. doi: 10.3389/fnins.2021.668857

Fintz, A. C., Audo, I., Hicks, D., Mohand-Saïd, S., Léveillard, T., and Sahel, J. (2003). Partial characterization of retina-derived cone neuroprotection in two culture models of photoreceptor degeneration. *Invest. Ophthalmol. Vis. Sci.* 44, 818–825. doi: 10.1167/iovs.01-1144

Gaillard, F., Kuny, S., and Sauvé, Y. (2009). Topographic arrangement of S-cone photoreceptors in the retina of the diurnal nile grass rat (arvicanthis niloticus). *Invest. Ophthalmol. Vis. Sci.* 50, 5426–5434. doi: 10.1167/iovs.09-3896

Ge, Z., Bowles, K., Goetz, K., Scholl, H. P. N., Wang, F., Wang, X., et al. (2015). NGS-based molecular diagnosis of 105 eyegene® probands with retinitis pigmentosa. *Sci. Rep.* 5, 18287. doi: 10.1038/srep18287

Grover, S., Fishman, G. A., and Brown Jr, J. (1998). Patterns of visual field progression in patients with retinitis pigmentosa. *Ophthalmology* 105, 1069–1075. doi: 10.1016/S0161-6420(98)96009-2

Gupta, N., Brown, K. E., and Milam, A. H. (2003). Activated microglia in human retinitis pigmentosa, late-onset retinal degeneration, and age-related macular degeneration. *Exp. Eye Res.* 76, 463–471. doi: 10.1016/S0014-4835(02)00332-9

Haer-Wigman, L., van Zelst-Stams, W. A. G., Pfundt, R., van den Born, L. I., Klaver, C. C. W., Verheij, J. B. G. M., et al. (2017). Diagnostic exome sequencing in 266 dutch patients with visual impairment. *Eur. J. Hum.* 25, 591–599. doi: 10.1038/ejhg.2017.9

Hamel, C. (2006). Retinitis pigmentosa. *Orphanet. J. Rare Dis.* 1, 40. doi: 10.1186/1750-1172-1-40

Hartong, D. T., Berson, E. L., and Dryja, T. P. (2006). Retinitis pigmentosa. *Lancet* 368, 1795–1809. doi: 10.1016/S0140-6736(06)69740-7

Huang, W. C., Wright, A. F., Roman, A. J., Cideciyan, A. V., Manson, F. D., Gewaily, D. Y., et al. (2012). RPGR-associated retinal degeneration in human X-linked RP and a murine model. *Invest. Ophthalmol. Vis. Sci.* 53, 5594–5608. doi: 10.1167/iovs.12-10070

Léveillard, T., Mohand-Saïd, S., Lorentz, O., Hicks, D., Fintz, A. C., Clérin, E., et al. (2004). Identification and characterization of rod-derived cone viability factor. *Nat. Genet.* 36, 755–759. doi: 10.1038/ng1386

Léveillard, T. and Sahel, J. A. (2017). Metabolic and redox signaling in the retina. *Cell. Mol. Life Sci.* 74, 3649–3665. doi: 10.1007/s00018-016-2318-7

Li, Z. Y., Chang, J. H., and Milam, A. H. (1997). A gradient of basic fibroblast growth factor in rod photoreceptors in the normal human retina. *Vis. Neurosci.* 14, 671–679.

Li, Z. Y., Wong, F., Chang, J. H., Possin, D. E., Hao, Y., Petters, R. M., and Milam, A. H. (1998). Rhodopsin transgenic pigs as a model for human retinitis pigmentosa. *Invest. Ophthalmol. Vis. Sci.* 39, 808–819.

Mei, X., Chaffiol, A., Kole, C., Yang, Y., Millet-Puel, G., Clérin, E., et al. (2016). The thioredoxin encoded by the rod-derived cone viability factor gene protects cone photoreceptors against oxidative stress. *Antiox. Redox Signal.* 24, 909–923. doi: 10.1089/ars.2015.6509

Mervin, K., and Stone, J. (2002). Developmental death of photoreceptors in the C57BL/6J mouse: association with retinal function and self-protection. *Exp. Eye Res.* 75, 703–713. doi: 10.1006/exer.2002.2063

Milam, A. H., Zong, Y. L., and Fariss, R. N. (1998). Histopathology of the human retina in retinitis pigmentosa. *Prog. Retin. Eye Res.* 17, 175–205.

Mohand-Saïd, S., Deudon-Combe, A., Hicks, D., Simonutti, M., Forster, V., Fintz, A. C., et al. (1998). Normal retina releases a diffusible factor stimulating cone survival in the retinal degeneration mouse. *Proc. Natl. Acad. Sci.* 95, 8357–8362.

Mohand-Saïd, S., Hicks, D., Dreyfus, H., and Sahel, J. A. (2000). Selective transplantation of rods delays cone loss in a retinitis pigmentosa model. *Arch. Ophthalmol.* 118, 807–811. doi: 10.1001/archopht.118.6.807

Mohand-Saïd, S., Hicks, D., Simonutti, M., Tran-Minh, D., Deudon-Combe, A., Dreyfus, H., et al. (1997). Photoreceptor transplants increase host cone survival in the retinal degeneration (rd) mouse. *Ophthalmic Res.* 29, 290–297.

Murray, J. D. (2002). *Mathematical Biology I: An Introduction, Interdisciplinary Applied Mathematics. 3rd Edn*. New York, NY; Berlin; Heidelberg; Barcelona; Hong Kong; London; Milan; Paris; Singapore; Tokyo: Springer.

Newton, F., and Megaw, R. (2020). Mechanisms of photoreceptor death in retinitis pigmentosa. *Genes* 11, 1120. doi: 10.3390/genes11101120

O'Hara-Wright, M., and Gonzalez-Cordero, A. (2020). Retinal organoids: a window into human retinal development. *Development* 147, dev189746. doi: 10.1242/dev.189746

Ortín-Martínez, A., Nadal-Nicolás, F. M., Jiménez-López, M., Alburquerque-Béjar, J. J., Nieto-López, L., García-Ayuso, D., et al. (2014). Number and distribution of mouse retinal cone photoreceptors: differences between an albino (Swiss) and a pigmented (C57/BL6) strain. *PLoS ONE* 9, e102392. doi: 10.1371/journal.pone.0102392

Ostojić, J., Grozdanić, S. D., Syed, N. A., Hargrove, M. S., Trent, J. T., Kuehn, M. H., et al. (2008). Patterns of distribution of oxygen-binding globins, neuroglobin and cytoglobin in human retina. *Arch. Ophthalmol.* 126, 1530–1536. doi: 10.1001/archopht.126.11.1530

Oyster, C. W. (1999). *The Human Eye: Structure and Function*. Sunderland, MA: Sinauer Associates Inc.

Punzo, C., Kornacker, K., and Cepko, C. L. (2009). Stimulation of the insulin/mTOR pathway delays cone death in a mouse model of retinitis pigmentosa. *Nat. Neurosci.* 12, 44–52. doi: 10.1038/nn.2234

Punzo, C., Xiong, W., and Cepko, C. L. (2012). Loss of daylight vision in retinal degeneration: are oxidative stress and metabolic dysregulation to blame? *J. Biol. Chem.* 287, 1642–1648. doi: 10.1074/jbc.R111.304428

Rajendram, R., and Rao, N. A. (2007). Neuroglobin in normal retina and retina from eyes with advanced glaucoma. *Br. J. Ophthalmol.* 91, 663–666. doi: 10.1136/bjo.2006.093930

Ripps, H. (2002). Cell death in retinitis pigmentosa: gap junctions and the 'bystander' effect. *Exp. Eye Res.* 74, 327–336. doi: 10.1006/exer.2002.1155

Roberts, P. A. (2022). Mathematical models of retinitis pigmentosa: The trophic factor hypothesis. *J. Theor. Biol.* 534, 110938. doi: 10.1016/j.jtbi.2021.110938

Roberts, P. A., Gaffney, E. A., Luthert, P. J., Foss, A. J. E., and Byrne, H. M. (2016a). Mathematical and computational models of the retina in health, development and disease. *Prog. Retin. Eye. Res.* 53, 48–69. doi: 10.1016/j.preteyeres.2016.04.001

Roberts, P. A., Gaffney, E. A., Luthert, P. J., Foss, A. J. E., and Byrne, H. M. (2016b). Retinal oxygen distribution and the role of neuroglobin. *J. Math. Biol.* 73, 1–38. doi: 10.1007/s00285-015-0931-y

Roberts, P. A., Gaffney, E. A., Luthert, P. J., Foss, A. J. E., and Byrne, H. M. (2017). Mathematical models of retinitis pigmentosa: the oxygen toxicity hypothesis. *J. Theor. Biol.* 425, 53–71. doi: 10.1016/j.jtbi.2017.05.006

Roberts, P. A., Gaffney, E. A., Whiteley, J. P., Luthert, P. J., Foss, A. J. E., and Byrne, H. M. (2018). Predictive mathematical models for the spread and treatment of hyperoxia-induced photoreceptor degeneration in retinitis pigmentosa. *Invest. Ophthalmol. Vis. Sci.* 59, 1238–1249. doi: 10.1167/iovs.17-23177

Stone, J., Maslim, J., Valter-Kocsi, K., Mervin, K., Bowers, F., Chu, Y., et al. (1999). Mechanisms of photoreceptor death and survival in mammalian retina. *Prog. Retin. Eye Res.* 18, 689–735. doi: 10.1016/S1350-9462(98)00032-9

Stone, J., Mervin, K., Walsh, N., Valter, K., Provis, J. M., and Penfold, P. L. (2005). "Photoreceptor stability and degeneration in mammalian retina: lessons from the edge," in *Macular Degeneration*, eds P. Penfold, and J. Provis Berlin: Springer, 149–165.

Travis, G. H., Sutcliffe, J. G., and Bok, D. (1991). The retinal degeneration slow (rds) gene product is a photoreceptor disc membrane-associated glycoprotein. *Neuron* 6, 61–70.

Valter, K., Maslim, J., Bowers, F., and Stone, J. (1998). Photoreceptor dystrophy in the RCS rat: roles of oxygen, debris, and bFGF. *Invest. Ophthalmol. Vis. Sci.* 39, 2427–2442.

Wifvat, K., Camacho, E. T., Wirkus, S., and Léveillard, T. (2021). The role of RdCVFL in a mathematical model of photoreceptor interactions. *J. Theor. Biol.* 520, 110642. doi: 10.1016/j.jtbi.2021.110642

Yang, Y., Mohand-Said, S., Danan, A., Simonutti, M., Fontaine, V., Clérin, E., et al. (2009). Functional cone rescue by RdCVF protein in a dominant model of retinitis pigmentosa. *Mol. Ther.* 17, 787–795. doi: 10.1038/mt.2009.28

Conflict of Interest: The author declares that the research was conducted in the absence of any commercial or financial relationships that could be construed as a potential conflict of interest.

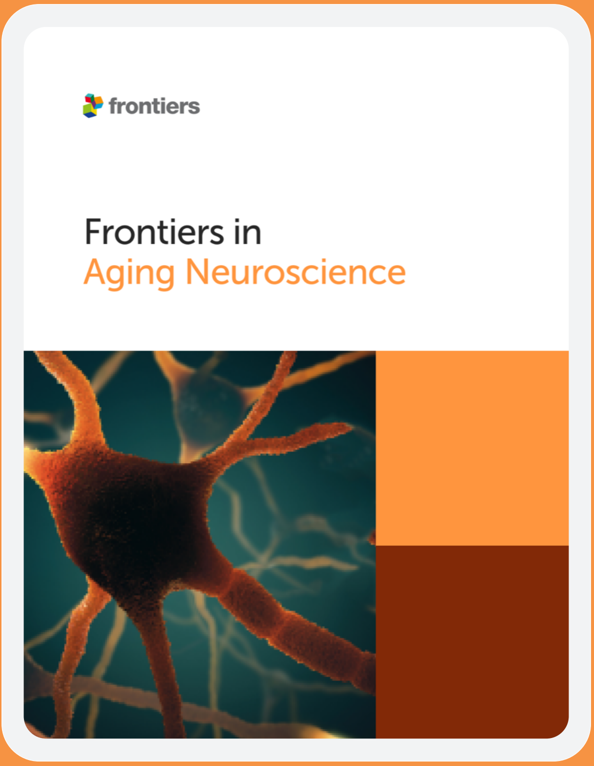

frontiers

Frontiers in
Aging Neuroscience

Frontiers

Avenue du Tribunal-Fédéral 34
1005 Lausanne, Switzerland
frontiersin.org

Contact us

+41 (0)21 510 17 00
frontiersin.org/about/contact